

Machine Learning Metamodel and Multi-Fidelity Neural Network for Guided Wave-Based Structural Health Monitoring and Prognostics

Thesis submitted to the University of Nottingham

for the degree of

Doctor of Philosophy

2025

by

Balaji Chandran

Student ID: 20303758

Supervised by:

Dr. Madhup Pandey

Centre for Structural Engineering and Informatics (CSEI)

Faculty of Engineering

Department of Mechanical Engineering

University of Nottingham

Declaration

I hereby declare that this thesis is my own original work and has not been submitted in substantially the same form for the award of a higher degree elsewhere. All sources used have been properly acknowledged through appropriate referencing.

This thesis is submitted to the University of Nottingham in partial fulfilment of the requirements for the degree of Doctor of Philosophy. It represents the results of work carried out during my period of registration as a doctoral student in the Faculty of Engineering.

To the best of my knowledge, the content presented is accurate, and the data and analyses have been conducted with academic integrity.

Balaji Chandran
25-09-2025

Acknowledgements

First and foremost, I would like to express my sincere gratitude to my supervisors, Dr. Madhup Pandey (Primary Supervisor), Dr. Dimitrios Chronopoulos (External) and Dr. Jelena Ninic (External), for their invaluable guidance, constant support, and constructive feedback throughout the course of my PhD. Their expertise and motivation have been crucial in shaping the direction of this research. I would also like to thank my co-supervisor Dr. Carlos Osorio Sandoval, for his support and encouragement.

This journey would not have been possible without the unconditional love and support of my family. My deepest thanks to my wife, Abinaya, whose patience, understanding, and sacrifices have been a bedrock during the challenging moments of this journey. I also thank my son, Bodhik, whose love and joyful energy have been a source of daily motivation and happiness. To my parents and siblings, your lifelong encouragement and belief in me have been instrumental in every step I have taken.

I gratefully acknowledge the Government of India for sponsoring my doctoral studies. Without this financial support, it would have been impossible to achieve this.

I also wish to thank my colleagues and friends at the Aerospace Technology Centre (ATC) and the Centre for Structural Engineering and Informatics (CSEI) Research Group, University of Nottingham, for creating a supportive and intellectually stimulating environment. The

regular seminar meetings helped me grow professionally.

The wider academic and support community at the University of Nottingham deserves recognition for their roles in grooming me academically through various doctoral training programmes, short courses, and seminars. These opportunities significantly enhanced my research and teaching capabilities.

Special thanks go to the technical staff, administrative teams, and library services, who ensured smooth day-to-day operations and access to essential resources.

Finally, to all those who, in one way or another, contributed to this beautiful journey, your support, whether direct or indirect, is truly appreciated.

Thank you all.

Abstract

This thesis presents a machine learning based framework for ultrasonic structural health monitoring (SHM) aimed at damage prediction, localization, and remaining useful life (RUL) estimation in engineering structures. Guided ultrasonic waves, particularly Lamb waves, are well suited for SHM due to their long range propagation and sensitivity to small defects. However, the interpretation of guided wave responses across varying structural configurations, materials, and damage scenarios remains challenging, motivating the use of data-driven approaches.

In the initial phase of this study, a metamodel was developed comprising deterministic machine learning models including Polynomial Regression (PR), Artificial Neural Networks (ANN), and Support Vector Machines (SVM), alongside probabilistic models like Bayesian Regression (BR), and Stochastic Gradient Descent (SGD). The metamodel is designed to benchmark and select the most suitable learning algorithm based on dataset-specific performance metrics. Training data are derived from guided-wave experiments and corresponding finite element simulations of aluminium plates containing circular and slotted hole damage of varying sizes. Lamb waves are excited using tone-burst signals in the frequency range 300–500 kHz, and responses are recorded using a four-sensor network. Damage-sensitive features, namely time-of-flight and peak amplitude, are extracted and combined to form a damage index (DI), which serves as the primary learning target. Results show that ANN performs best

when trained on limited experimental data, while SVM achieves superior performance when trained on fused experimental–simulation datasets.

Although the metamodel provides valuable insight, directly combining low-fidelity simulation data with high-fidelity experimental data limits robustness. To address this, the second phase of this research introduces a Multi-Fidelity Neural Network (MFNN) framework that hierarchically integrates numerical simulations and experimental measurements. Finite element models are first validated against experimental waveforms using time alignment and amplitude scaling to ensure consistency. Within the MFNN architecture, simulation data provide broad coverage of the design space, while experimental data are used to learn a corrective residual that aligns predictions with physical reality.

The MFNN demonstrates improved accuracy and robustness compared with the metamodel, particularly under limited experimental data conditions. Beyond damage severity estimation, the MFNN framework was extended to support damage localization through DI–based projection and remaining useful life estimation by coupling damage index trajectories with physics-informed fatigue models. The resulting prognostic trends remained physically consistent, demonstrating the suitability of the proposed framework for integrated detection, localization, and RUL estimation within ultrasonic SHM. Overall, this thesis contributes a novel metamodel and multi-fidelity neural network based framework for ultrasonic SHM, offering scalable, accurate and efficient solutions for structural diagnostics and prognostics.

Contents

Declaration **1**

Acknowledgements **2**

Abstract **4**

1 Introduction **17**

1.1 Background and Motivation *17*

1.2 Problem Statement *18*

1.3 Research Aim and Objectives *19*

1.4 Methodological Overview *22*

1.5 Thesis Organization *24*

2 Literature Review **26**

2.1 Overview of Structural Health Monitoring Frameworks *26*

2.2 Ultrasonic Guided wave techniques in SHM *30*

2.2.1 Damage Types Selection and Characterization 34

2.2.2 Signal Processing and Feature Extraction in Time Domain 37

2.3 Machine Learning for Structural Diagnostics *41*

2.3.1 Deterministic ML Models for Damage Prediction . . 45

2.3.2 Probabilistic Approaches for Damage Inference 46

2.3.3 Comparative Studies and Model Selection 47

2.3.4 Metamodelling Strategies for Adaptive Model Selection 51

2.4 Multi-fidelity Frameworks for Data Fusion *54*
2.4.1 Concept and Architecture 55
2.5 Prognostics and Remaining Useful Life Estimation *61*
2.5.1 Physics-Based Approaches to RUL Estimation 62
2.5.2 Data-Driven Approaches to RUL Estimation 67
2.5.3 Integrating Data-Driven Models with Fatigue Physics 74

3 Methodology **77**
3.1 Synopsis of the Proposed Approach *77*
3.2 Data Collection Using Lamb Waves *83*
3.2.1 Experimental Data Acquisition (High-Fidelity) 83
3.2.2 Numerical Simulation and Data Generation (Low-Fidelity) 85
3.2.3 Data Alignment and Preprocessing 85
3.3 Feature Extraction and Damage Index formulation *87*
3.4 Machine Learning for Damage Prediction, Localization, and RUL Estimation *93*

4 Model development **98**
4.1 Experimental Modelling *98*
4.2 Analytical Modelling *107*

5 Validation of Analytical Models **112**
5.1 Specimens, instrumentation and data coverage *113*
5.2 Validation metrics *114*
5.3 Representative waveform comparisons and Validation sample *116*
5.4 Statistical analysis and interpretation *119*
5.5 Discussion of Validation Results *121*

6 Application of Machine Learning Models **123**

6.1 Metamodel Development Using Deterministic and Probabilistic Approaches 124
6.1.1 Dataset preparation and normalization 124
6.1.2 Deterministic and probabilistic models 125
6.1.3 Balanced sampling strategy and performance comparison 126
6.1.4 MFNN over Metamodel 127
6.2 Multi-Fidelity Neural Network for Prediction of Damage, Location, and RUL Estimation 129
6.2.1 MFNN Architecture and Formulation 130
6.2.2 Dataset Preparation, Normalization and Sampling . . 133
6.2.3 Training Methodology and Convergence 135
6.2.4 Methodological Robustness and Design Attributes . . 136

7 Results & Discussion 138
7.1 Damage Detection 139
7.1.1 Preliminary Model Screening using Experimental Dataset only 139
7.1.2 Metamodel with both deterministic and probabilistic learners on the fused experimental and simulation datasets 142
7.1.3 Damage prediction using Multi-Fidelity Neural Network 144
7.1.4 Narrative of observations across stages 145
7.2 Damage Localization using MFNN 147
7.3 Prediction of Remaining Useful life 150
7.4 Frequency dependence of the Damage Index 153
7.5 Effect of Defect Size on Damage Index 154
7.6 Advantages of Multi-Fidelity Integration 155

7.6.1 Improved Data Efficiency 155
7.6.2 Robustness Across Configurations 156
7.7 Challenges in Framework Design and Strategic Mitigation . . 156
7.8 Relevance of MFNN to SHM Practice 159

8 Conclusion & Future Scope 161
8.1 Conclusions 161
8.2 Operational Challenges and Remedial Measures 164
8.2.1 Sensor Coupling and Signal Quality 164
8.2.2 Boundary Conditions in Experiments 165
8.2.3 Environmental and Ambient Noise 165
8.2.4 Geometrical Defect Accuracy 166
8.2.5 Simulation Assumptions and Real-World Deviations . 167
8.2.6 Data Volume and Machine Learning Compatibility . 168
8.2.7 Time Constraints and Trial Management 168
8.3 Future Scope 169

9 Appendix 171

List of Figures

2.1 Schematic of a general SHM system 27
2.2 Lamb wave propagation in a plate-like structure [1] 28
2.3 Comparison between deterministic and probabilistic model outputs Rezaee et al. (2015)[2] 48
2.4 Schematic of a Multi-Fidelity Neural Network (MFNN) architecture used in SHM. 57

3.1 Flowchart of the proposed research methodology: Phase 1 (ML Metamodel for SHM) and Phase 2 (Multi-Fidelity Neural Network for SHM) 82
3.2 Difference in the ToFs between the incident diagnostic wave and the damage-scattered wave [3] [4] 90
3.3 Time-of-Flight (ToF) alignment for the 5 mm circular hole damage case 91
3.4 End-to-end workflow illustrating MFNN-based Damage Index prediction and physics-informed RUL inference. 96

4.1 Experimental setup consists of: (i) specimen (Aluminium plate) with a circular hole, (ii) sensor attachments for signal transmission and reception, (iii) a function generator to provide the excitation signal, and (iv) a digital oscilloscope for visualizing and acquiring the sensor data 99
4.2 Sample three-cycle tone burst excitation signal at Sensor S1 (400 kHz) 100

4.3 Sensor arrangement on the aluminium plate (All dimensions are in mm) 101
4.4 Illustration of a 5 mm Circular hole damage model 105
4.5 Illustration of a 5 mm x 15 mm Slotted hole damage model . 105

5.1 Comparison of experimental and simulated guided wave signals for the pristine 1.5 mm plate 116
5.2 Comparison of experimental and simulated guided wave signals for a 5 mm circular hole in a 1.5 mm aluminium plate at 500 kHz 117
5.3 Comparison of experimental and simulated guided wave signals for 12 mm × 4 mm slotted hole damage in a 0.9 mm aluminium plate at 500 kHz 118

7.1 Prediction performance and residual behaviour of the baseline ANN trained on limited experimental dataset for 4 mm circular hole damage 140
7.2 Prediction performance and residual behaviour of the baseline ANN trained on limited experimental dataset for 5 mm circular hole damage 140
7.3 Prediction performance and residual behaviour of the best-performing model (ANN) within the deterministic metamodel, trained exclusively on the experimental dataset for Circular hole damage 141
7.4 Comparative damage prediction performance of the developed Metamodel algorithms a) PR b) SVM c) ANN d) BR e) SGD 143
7.5 MFNN performance showing error convergence and prediction accuracy 145

7.6 Predicted DI-based damage localization heatmaps generated using MFNN. Left: Localization for a 5 mm circular hole damage. Right: Localization for a 15 mm x 5 mm slotted hole damage 149
7.7 DI-based degradation trajectories inferred from MFNN predictions and validated through analytical consistency with established S–N fatigue life trends for circular and slotted damage configurations. 152
7.8 Variation of Damage Index with excitation frequency. Actual experimental values are compared with model predictions, showing strong agreement and frequency-dependent clustering. 153
7.9 Variation of Damage Index with increasing damage size for circular and slotted hole defects. The trend confirms that larger damage leads to higher DI, validating the physical relevance of the metric. 154

9.1 Illustration of symmetric Lamb wave motion, where upper and lower surface displacements are in phase [5]. 173
9.2 Illustration of antisymmetric Lamb wave motion, with surface displacements out of phase [5]. 173
9.3 Dispersion curves for a 1-mm-thick aluminium alloy 1100: (a) phase velocity and (b) group velocity [6, 4]. 174

List of Tables

3.1 Comparative evaluation of potential damage features. Features selected for this study are highlighted. 88

5.1 Experimental Setup Details of Aluminium Plates 113

5.2 Simulation Setup Details of Aluminium Plates 114

5.3 Per-plate summary of simulation errors relative to experiments, including specimen details. 115

5.4 Validation results at 500 kHz for Sensor S3 across all seven plates. Columns show experimental and simulation values of time of flight (ToF), peak amplitude, and damage index (DI). 119

6.1 Rationale for Selection of Machine Learning Models 125

7.1 Performance metrics (RMSE and R^2) of the constituent machine learning models in the Metamodel trained on the fused experimental-simulation dataset. 144

7.2 Quantitative performance benchmark comparing the global accuracy of the best single-fidelity metamodel (SVM) against the Multi-Fidelity Neural Network (MFNN). 146

7.3 Summary of key challenges encountered in this research and corresponding mitigation strategies adopted. 158

9.1 Model Configuration and Hyperparameters 185

9.2 Normalized ToF, Peak Amp, and DI values from experimental and simulation data for Plate 1 to Plate 7. 186
9.3 Comprehensive Metamodel Prediction Results. 198
9.4 MFNN prediction results 244

List of Abbreviations

SHM	Structural Health Monitoring
NDT	Non-Destructive Testing
ML	Machine Learning
MFNN	Multi-Fidelity Neural Network
ANN	Artificial Neural Network
SVM	Support Vector Machines
PR	Polynomial Regression
BR	Bayesian Regression
SGD	Stochastic Gradient Descent
RUL	Remaining Useful Life
ToF	Time of Flight
DI	Damage Index
LF	Low Fidelity
HF	High Fidelity
MSE	Mean Square Error
RMSE	Root Mean Square Error
EOV	Environmental and Operational Variability
NDE	Non-Destructive Evaluation
EMAT	Electro-Magnetic Acoustic Transducer
PZT	Lead Zirconate Titanate
CNN	Convolutional Neural Network

UGW	Ultrasonic Guided Waves
PCA	Principal Component Analysis
SHAP	Shapley Additive Explanations
XAI	Expandable AI
GPR	Gaussian Process Regression
RNN	Recurrent Neural Network
LSTM	Long Short-Term Memory Networks
LIME	Local Interpretable Model-agnostic Explanations
PWAS	Piezo-electric Wafer Active Sensors
FE	Finite Element
MAE	Mean Absolute Error
MLP	Multi-Layer Perceptron
PSO	Particle Swarm Optimization
MEMS	Micro Electro-Mechanical Systems
Amp	Amplitude
FBG	Fiber Bragg Gratings
SPR	Statistical Pattern Recognition

Chapter 1 Introduction

1.1 Background and Motivation

Structural Health Monitoring (SHM) has become a crucial technology in modern engineering, particularly in high-stakes industries such as aerospace, marine, and civil infrastructure. SHM enables early detection of structural degradation, thus preventing catastrophic failures and reducing maintenance costs. Traditional Non-Destructive Testing (NDT) methods, although well-established, are typically labor-intensive, infrequent, and reliant on manual inspection. These limitations hinder their suitability for real-time and scalable applications.

Among advanced NDT methods, ultrasonic guided waves, especially Lamb waves, are of growing interest in sectors such as aerospace for fuselage lap-joint inspection, energy for long-range pipeline monitoring, and civil infrastructure for rail track assessment. They are preferred due to their ability to travel long distances with minimal energy loss and interact sensitively with defects such as cracks, holes, delamination, and corrosion. However, interpreting Lamb wave signals remains complex due to multi-mode dispersion, reflections, and the influence of geometric and material variations.

To overcome these challenges, machine learning (ML) techniques offer promising capabilities in learning patterns and relationships in high-dimensional data without requiring explicit analytical models. In

particular, ML can be used to process the structural health information obtained from the damage-sensitive features, classify damage types, localize defects, and even predict structural degradation over time.

In this context, the present research aims to design an SHM framework that integrates ultrasonic guided waves with machine learning models for prediction and localization of damage and also to estimate the Remaining Useful Life (RUL) of structures. The first phase introduces a metamodel built from a combination of deterministic and probabilistic machine learning algorithms: Artificial Neural Networks (ANN), Support Vector Machines (SVM), Polynomial Regression (PR), Bayesian Regression (BR), and Stochastic Gradient Descent (SGD). The second phase leverages a more sophisticated approach: a Multi-Fidelity Neural Network (MFNN) model that combines high-fidelity experimental data with low-fidelity numerical simulations to enhance prediction accuracy while reducing dependency on extensive experimental testing.

1.2 Problem Statement

Despite significant progress in SHM and machine learning, several challenges remain unresolved:

- **Model Generalization:** Many ML models struggle to generalize across different materials, sensor configurations, and damage types. This limits their practical application in diverse real-world conditions.
- **Data Limitations:** A fundamental trade-off exists between data availability and physical accuracy. Experimental data captures realistic wave behavior but is expensive and limited. Conversely, numerical simulations are scalable and abundant but suffer from physical bias due to simplifying assumptions. The critical research

gap is the lack of a unified framework to collectively leverage both sources, hindering the ability to combine experimental fidelity with computational scalability for robust diagnostics.

- **Limited Prognostics:** Most ML-based SHM methods focus on classification or regression, with limited attention given to predicting the RUL of damaged structures.
- **Simulation-Experiment Gap:** Discrepancies between simulation and experimental data hinder the direct use of numerical models in real-time monitoring applications.

To address these challenges, this thesis develops a two-stage framework: first, a dynamic metamodel that benchmarks multiple machine learning models to identify the best-performing approach under different conditions; and second, a Multi-Fidelity Neural Network (MFNN) that fuses low-fidelity simulations with high-fidelity experiments to improve predictive accuracy and extend applicability to prognostics.

1.3 Research Aim and Objectives

The overarching aim of this research is to develop, evaluate, and benchmark a data-driven Structural Health Monitoring (SHM) framework that integrates ultrasonic guided wave physics with advanced machine learning strategies, specifically Metamodels and Multi-Fidelity Neural Networks (MFNN), to achieve robust structural damage diagnostics and prognostics.

To achieve this aim, the research is structured around the following specific objectives:

1. **Development of High-Fidelity and Low-Fidelity Datasets:**

- To conduct experimental guided wave propagation tests on aluminium plates with varying thicknesses and damage configurations (circular and slotted holes) to generate high-fidelity (HF) reference data.
- To develop and validate a finite element (FE) simulation model in ABAQUS that accurately replicates the experimental wave physics, serving as a scalable source of low-fidelity (LF) data.

2. **Feature Extraction and Damage Index Formulation:**

   - To extract damage-sensitive features, specifically Time-of-Flight (ToF) shifts and Peak Amplitude attenuation, from time-domain signals.
   - To formulate a unified Damage Index (DI) that quantifies structural degradation across different damage geometries and sensor paths.

3. **Development of a Machine Learning Metamodel (Phase 1):**

   - To design, train, and benchmark a dynamic Metamodel framework comprising both deterministic algorithms (Polynomial Regression, SVM, ANN) and probabilistic algorithms (Bayesian Ridge, SGD) in order to identify the optimal modeling strategy for varying data complexities.

4. **Development of a Multi-Fidelity Neural Network (Phase 2):**

   - To design a Multi-Fidelity Neural Network (MFNN) architecture capable of fusing abundant low-fidelity simulation data with sparse high-fidelity experimental data.
   - To demonstrate that the MFNN can correct simulation biases and outperform single-fidelity models in terms of prediction

accuracy.

5. **Extension to Damage Localization and Prognostics:**

    - To develop a Damage Index-based imaging framework for the spatial localization of structural defects.
    - To develop a physics-informed RUL estimation framework by mapping predicted Damage Indices to established S-N fatigue life curves.

Research Hypotheses To provide a logical structure for the proposed methodologies, this thesis tests the following three core research hypotheses:

- **Hypothesis 1 (The Metamodel Hypothesis):** No single machine learning algorithm is universally optimal for all SHM data scenarios. A Metamodel framework that dynamically selects between deterministic and probabilistic models based on data characteristics will yield higher robustness than any individual static model.
- **Hypothesis 2 (The Multi-Fidelity Hypothesis):** Machine learning models trained solely on experimental data suffer from sparsity, while those trained on simulations suffer from physical bias. A Multi-Fidelity Neural Network (MFNN) that learns a residual correction function between simulation and experiment will achieve superior prediction accuracy compared to models trained on either dataset alone.
- **Hypothesis 3 (The Physics-Informed Prognostics Hypothesis):** The evolution of guided wave-based Damage Indices (DI) follows a degradation trajectory consistent with theoretical material fatigue

behavior, thereby enabling data-driven Remaining Useful Life (RUL) estimation.

1.4 Methodological Overview

This research adopts a Design Science Research (DSR) methodology supported by abductive reasoning, in which machine learning artefacts are systematically designed, evaluated, and refined to address a practical Structural Health Monitoring (SHM) problem. The methodological structure is organised into two sequential phases, where each phase builds on the findings and limitations identified in the preceding stage to progressively advance the research objectives.

The first phase focuses on the development and evaluation of a machine learning metamodel to establish a reliable diagnostic baseline for damage severity prediction. Guided wave data is collected from aluminium plates using tone burst excitation across a frequency range of 300–500 kHz. A square sensor configuration is employed, consisting of one actuator and three sensors arranged symmetrically around the damage region.

Artificial damage is introduced in the form of circular holes (4–8 mm diameter) and slotted defects (e.g., 12×4 mm, 15×5 mm, and 18×6 mm) in the centre of the plate. These dimensions were selected to represent realistic damage severities encountered in service conditions. Circular holes simulate rivet hole degradation or localized corrosion pitting, while slotted defects with approximately 3:1 aspect ratios represent elongated fatigue cracks or anisotropic damage. Furthermore, these damage sizes fall within the wavelength sensitivity range of the selected excitation frequencies, enabling meaningful assessment of detection capability and damage progression.

The recorded ultrasonic signals are processed to extract damage-sensitive features, specifically Time of Flight shifts and Peak Amplitude attenuation.

In parallel, the numerical models are developed in ABAQUS using a three-cycle tone burst excitation with a Hann window. Material properties, boundary conditions, and sensor configurations are matched to the experimental setup. The simulated wave responses are evaluated against experimental data using Time of Flight and amplitude error metrics, and adaptive amplitude scaling is applied to reduce systematic discrepancies between numerical and experimental responses.

A machine learning Metamodel comprising deterministic algorithms (Polynomial Regression, Artificial Neural Networks, and Support Vector Machines) and probabilistic algorithms (Bayesian Ridge Regression and Stochastic Gradient Descent) is then developed. These models are benchmarked using quantitative performance metrics such as Mean Square Error (MSE) and Root Mean Square Error (RMSE). This comparative evaluation enables identification of the most robust predictive strategy under varying data conditions, revealing both the strengths and limitations of single-fidelity learning approaches.

The second phase is motivated by the limitations identified in Phase 1, particularly the trade-off between experimental data scarcity and simulation bias. To address this, a Multi-Fidelity Neural Network (MFNN) framework is introduced. The MFNN leverages abundant low-fidelity simulation data to learn the baseline wave–damage relationship, while sparse high-fidelity experimental data is incorporated during training to correct simulation bias and improve predictive accuracy. This abductive design step reflects the hypothesis that combining complementary data sources provides a more effective explanation of observed discrepancies than relying on either source alone.

Once validated for damage severity prediction, the MFNN framework is extended to damage localization through probabilistic imaging, demonstrating the ability to infer spatial defect information without

dense sensor arrays. Finally, the predicted Damage Index progression is qualitatively mapped to established fatigue S–N behaviour to provide early-stage Remaining Useful Life insight. This progression ensures that each methodological step logically advances the research objectives and follows the hierarchical structure of SHM, from diagnostics to prognostics.

1.5 Thesis Organization

The remainder of the thesis is structured as follows:

- **Chapter 2: Literature Review** – Reviews SHM techniques, Lamb wave theory, machine learning models, and multi-fidelity learning strategies used in damage detection, localization, and RUL estimation.
- **Chapter 3: Methodology** – Describes the detailed workflow for data collection, feature extraction, model training, validation, and prediction of damage, location, and RUL estimation.
- **Chapter 4: Model Development** – Presents the experimental setup and finite element simulation modelling in ABAQUS.
- **Chapter 5: Validation of Analytical Models** – Reports validation of simulated and experimental results, confirming fidelity of guided wave modelling.
- **Chapter 6: Application of Machine Learning Models** – Presents the application of the metamodel and MFNN frameworks, including architectures, dataset preparation, training procedures, and validation.
- **Chapter 7: Results & Discussion** – Discusses the findings, comparative analysis, advantages, and limitations of the approaches.

- **Chapter 8: Conclusion & Future Scope** – Summarizes the contributions and outlines potential directions for future research.
- **Appendices** – Appendix A provides supplementary material for ultrasonics, Appendix B for ML, Appendix C includes complete datasets of results and Appendix D has the source codes for reproducibility. These include supporting concepts, equations, figures, tables, complete dataset and other results.
- **Bibliography** – Lists all sources cited in this thesis.

Chapter 2 Literature Review

2.1 Overview of Structural Health Monitoring Frameworks

SHM is a multidisciplinary field focused on the continuous or periodic assessment of structures using sensory data and intelligent decision-making techniques [7]. It involves the acquisition, processing, and interpretation of data from a variety of sensors embedded or mounted on structural components to detect and quantify damage, assess structural integrity, and estimate remaining useful life [8]. SHM systems are widely used in critical infrastructure such as aircraft, bridges, wind turbines, pipelines, and offshore platforms where structural failure can lead to catastrophic consequences [9].

The primary motivation for SHM stems from the need to ensure safety and reliability while reducing life-cycle costs [10]. Traditional maintenance strategies, such as scheduled or reactive maintenance are often inefficient and may not detect incipient damage in time [11]. SHM systems, in contrast, enable condition-based maintenance by offering real-time or near-real-time insights into the structural state [12]. This allows maintenance to be performed only when needed, thereby extending the lifespan of the structure and reducing downtime [13].

Figure 2.1 illustrates the general framework of a structural health

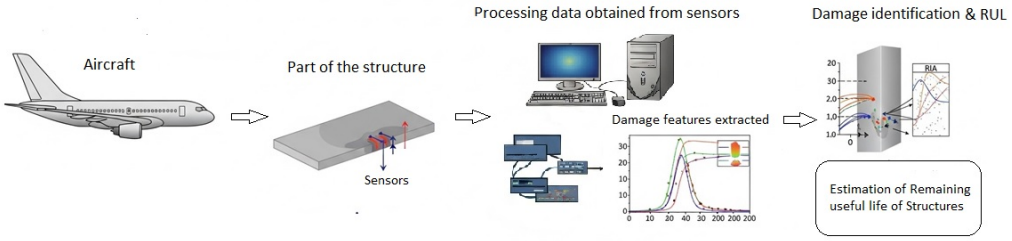


Figure 2.1: Schematic of a general SHM system

monitoring (SHM) system. The process begins with guided wave excitation and sensing in a structure, followed by signal processing to extract relevant features. These features are then used as inputs to machine learning models that enable damage detection, localization, and prognostic assessments such as RUL estimation. This schematic highlights the flow of information from physical measurements to decision-making, providing context for the machine learning approaches developed in this thesis.

At the core of SHM lies the principle of damage detection, which may include the identification of cracks, corrosion, delamination, or other forms of degradation [14]. The damage detection process is generally categorized into four levels:

Detection – identifying whether damage is present [15].

Localization – determining where the damage is located [16].

Quantification – assessing the severity of the damage [17].

Prognosis – predicting the remaining useful life or time to failure [18].

Several technologies are employed in SHM, including strain gauges [19], accelerometers [20], fiber Bragg grating sensors [21], and piezoelectric sensors [22]. The choice of sensing technology often depends on the target structure and its operating conditions. For example, strain gauges are frequently used for monitoring local stress concentrations in bridges and civil structures, while accelerometers are widely adopted in rotating machinery and wind turbines to capture dynamic vibration

responses. Fiber Bragg gratings, due to their immunity to electromagnetic interference, are increasingly integrated into large-scale composite structures such as aircraft wings and offshore platforms. Of particular relevance in this thesis is the use of piezoelectric transducers for ultrasonic guided wave-based monitoring [23]. These sensors can both excite and receive Lamb waves, ultrasonic signals that propagate along thin-walled structures such as aircraft fuselage panels, aluminium plates, or pipeline walls, where early detection of cracks or corrosion is critical [24]. This dual functionality makes them ideal for embedded or surface-mounted SHM systems across aerospace, energy, and civil engineering applications [25].

The typical SHM process using guided waves involves: actuation of the structure using tone burst signals or chirp waves [26], signal propagation through the material, interaction of the waves with defects or boundaries, detection of changes in time-of-flight (ToF), amplitude, or phase of the received signal [27], changes in wave characteristics indicate the presence and possibly the severity of damage. For instance, a reduction in peak amplitude or a delay in ToF may suggest wave scattering caused by a defect [28].

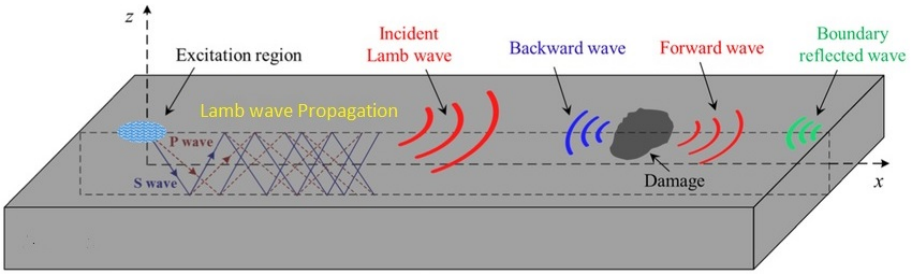


Figure 2.2: Lamb wave propagation in a plate-like structure [1]

Figure 2.2 depicts the propagation of Lamb waves in a thin plate-like structure. The figure emphasizes the multimodal nature of guided waves, showing how symmetric and antisymmetric modes travel with different group velocities. Such behaviour underpins the sensitivity of Lamb waves to

structural damage, as defects alter wave speed, attenuation, and scattering. This forms the theoretical foundation for the damage indices employed in this work, where deviations in time-of-flight and amplitude are directly related to wave–damage interactions.

To improve the reliability of SHM, signal processing techniques such as Fourier transforms [29], wavelet analysis [30], and Hilbert–Huang transforms [31] are used to filter noise and extract meaningful features. These features are then interpreted using data-driven methods, often involving machine learning (ML) or deep learning techniques, which can handle high-dimensional data and learn complex nonlinear relationships [32].

In this research, SHM is extended beyond conventional monitoring by incorporating machine learning based metamodels and multi-fidelity neural networks (MFNNs) to predict damage evolution and remaining useful life [33]. The concept of integrating ML into SHM has gained significant traction due to the availability of high-resolution sensor data and computational advancements [34]. ML algorithms can be trained using both experimental (high-fidelity) and simulated (low-fidelity) data to estimate damage location and severity with high accuracy [35].

Moreover, the SHM system designed in this thesis uses a round-robin sensor configuration on an aluminum plate with different damage scenarios, including circular and slotted holes. [24]. This allows the development of a rich feature space for training ML models. The extracted features such as time delay, energy loss, and damage index values are mapped to damage size or type using regression and classification algorithms [36].

A key challenge in SHM is environmental and operational variability (EOV), which can affect signal quality and lead to false positives or negatives [37]. Temperature changes, loading conditions, or sensor aging can introduce inconsistencies [38]. Techniques such as baseline signal

subtraction, normalization, and adaptive thresholding are employed to mitigate these effects [39]. Additionally, multi-sensor data fusion improves robustness by combining data from several sources to reach a consensus [40]. Another essential part of SHM is validation and verification. The performance of the monitoring system must be evaluated using metrics such as precision, recall, accuracy, and RMSE [41]. In the thesis, validation is achieved by comparing predictions from the ML metamodels and MFNNs with experimental results obtained from ultrasonic inspection of damaged plates [25].

Furthermore, the SHM system developed in this study supports remaining useful life estimation, which goes beyond identifying damage to forecasting how long the structure can safely function [42]. This is achieved by analyzing trends in the extracted features over time and fitting them to degradation models using the trained ML algorithms [43].

In summary, Structural Health Monitoring is an evolving field that plays a pivotal role in ensuring the structural safety and integrity of critical assets [7]. Its effectiveness is significantly enhanced through the use of advanced sensors, guided wave techniques, intelligent algorithms, and hybrid data sources [23]. The current research contributes to SHM by proposing a machine learning metamodel and a multi-fidelity data-driven framework for early damage detection and prognostics, demonstrating its potential for real-time implementation in aerospace and other safety critical applications [35].

2.2 Ultrasonic Guided wave techniques in SHM

Ultrasonics has emerged as a fundamental non destructive evaluation (NDE) technique in Structural Health Monitoring (SHM) due to its ability to detect internal flaws, measure material properties, and characterize

damage progression in engineering structures. Operating at frequencies above 20 kHz, ultrasonic methods enable precise detection of minute structural anomalies, including cracks, delamination, voids, and material discontinuities that are often invisible to visual inspection techniques. Among ultrasonic techniques, guided waves such as Lamb waves are particularly attractive for SHM of large and thin-walled structures, such as aircraft fuselage panels and composite laminates, because of their long range propagation capabilities and sensitivity to small defects [44]. Ultrasonic waves are influenced by material properties, geometry, and boundary conditions, making them ideal for evaluating structural integrity in real-time without compromising operational performance.

The generation and detection of ultrasonic waves in SHM systems are typically achieved using piezoelectric transducers, laser ultrasonics, or electromagnetic acoustic transducers (EMATs), depending on application requirements and material compatibility [45]. Piezoelectric transducers remain the most commonly used due to their simplicity, affordability, and ability to operate at various frequencies. These transducers convert electrical energy into mechanical vibrations and vice versa, facilitating the emission and reception of ultrasonic waves. When attached to a structure's surface, they can continuously monitor for changes in wave propagation characteristics, which are indicative of damage. Ultrasonic inspection techniques can be broadly categorized into contact and non-contact methods. Contact-based techniques are reliable but require coupling agents and consistent sensor placement, while non-contact methods offer flexibility at the cost of reduced signal strength and increased complexity [46].

A key feature of ultrasonic SHM is the use of Lamb waves, which are guided elastic waves that propagate along thin structures such as plates or shells. Lamb waves consist of symmetric and antisymmetric modes, each

with different displacement characteristics and sensitivities to damage. The selection of mode and frequency is critical because dispersion effects can distort signals and complicate data interpretation [47][48]. Typically, a tone burst signal is used for excitation to confine the frequency content and reduce dispersion. A more detailed mathematical derivation of the Lamb wave dispersion equations and the fundamental principles of the sensors used is included in Appendix A. Parameters such as group velocity, phase velocity, and signal amplitude are monitored to identify structural anomalies. The arrival time (or Time-of-Flight) and amplitude reduction due to scattering or absorption by damage serve as important diagnostic features. These characteristics are used in both baseline and baseline-free methods to identify deviations in wave patterns caused by structural degradation [49][50].

The signal processing of ultrasonic data plays a crucial role in enhancing sensitivity and reducing false alarms. Techniques such as Short-Time Fourier Transform (STFT), Wavelet Transform, Hilbert-Huang Transform (HHT), and Empirical Mode Decomposition (EMD) are widely applied to extract useful features from the received signals [51]. The choice of processing method depends on the type of signal, noise level, and desired information. Wavelet analysis, for example, is beneficial for non-stationary signals, allowing the decomposition of ultrasonic signals into time-frequency components for better identification of damage-induced changes. Feature extraction is essential for downstream machine learning models, where data-driven algorithms are trained to associate signal patterns with structural conditions.

In complex structural configurations, multiple sensors are deployed in arrays to perform full-field monitoring using techniques like time reversal, imaging algorithms, and phased array approaches. Phased array ultrasonics, commonly used in aerospace and pipeline monitoring, allows

for beam steering and focusing to improve spatial resolution and accuracy [52] [53]. Imaging techniques such as Synthetic Aperture Focusing Technique (SAFT), Total Focusing Method (TFM), and Delay-and-Sum algorithms are also employed to reconstruct the location and size of damage. These methods are particularly valuable for visualizing internal defects in multilayered or inaccessible regions of structures. Sensor networks configured in a pitch-catch or pulse-echo mode allow for directional analysis of wave propagation, further enhancing the ability to detect and localize damage.

Temperature variation, material anisotropy, and structural complexity present challenges in ultrasonic SHM. Temperature-induced changes can affect wave speed and signal amplitude, leading to misinterpretation of results. Compensation strategies include baseline signal correction, differential measurements, and machine learning-based compensation algorithms [54]. In composite structures, anisotropy and heterogeneous properties can result in mode conversion and attenuation, complicating wave interpretation. Research is ongoing to optimize sensor placement, excitation frequency, and signal processing to mitigate these effects and improve reliability.

The integration of ultrasonics with machine learning techniques has greatly enhanced SHM capabilities by enabling automated and accurate interpretation of complex signals. Data driven approaches can classify damage types, predict their evolution, and assess the remaining useful life (RUL) of structures based on extracted ultrasonic features. Supervised learning models are trained using labeled datasets generated from experimental or simulated tests, while unsupervised models identify anomalies without prior labels. Feature engineering using ultrasonic data provides crucial inputs such as time of flight, energy loss, frequency shift, and scattering coefficients. Hybrid models that combine physical insights

from wave propagation with machine learning predictions offer improved accuracy and robustness [7] [55].

Recent advancements in wireless sensing, embedded systems, and cloud computing have facilitated real-time ultrasonic SHM systems for remote monitoring of critical infrastructures such as bridges, wind turbines, and aircraft. These systems offer scalable and low-cost solutions, reducing the need for periodic manual inspections and enhancing safety. The continuous evolution of ultrasonic technologies, including laser ultrasonics, piezo-composite sensors, and high-frequency transducers, continues to expand their application in SHM. As a mature and reliable NDE tool, ultrasonics remains at the forefront of smart monitoring systems, enabling proactive maintenance strategies and supporting the shift from schedule-based to condition-based maintenance.

2.2.1 Damage Types Selection and Characterization

Understanding the influence of damage geometry on ultrasonic wave propagation is critical in structural health monitoring (SHM), especially when using guided waves for damage detection and characterization [3] [44]. Damage in engineering structures can appear in many forms ranging from fatigue cracks and delamination to drilled holes and corrosion pits—each influencing wave scattering, mode conversion, and attenuation in unique ways [56] [50] [47] [48]. In the present research, a focused investigation has been undertaken on circular and slotted hole damage types[45] [57]. These selections are driven by practical considerations, analytical clarity, and their relevance to aerospace structural components [58].

Circular and slotted hole defects offer several distinct advantages when studying guided wave propagation. First, circular holes, due to their symmetric geometry, serve as ideal candidates for baseline studies in wave

scattering and interaction [59] [60]. They generate isotropic reflection and diffraction patterns, simplifying the analysis of signal features such as amplitude reduction, time of flight delays, and frequency content variation [52]. This symmetry makes it easier to model the interaction using analytical or numerical methods and validate them experimentally [56] [50]. In aerospace structures, circular holes often occur as fastener locations, service access points, or manufacturing defects [24]. Their deterioration over time due to fatigue, corrosion, or overloading can be precursors to critical failure. Thus, the circular damage cases in this research not only simplify the experimental and modeling procedures but also mirror real-world degradation scenarios [3].

slotted hole defects, on the other hand, introduce controlled anisotropy into the problem [61] [62] [63]. Unlike circular holes, slotted hole damages cause directional variations in wave scattering, depending on the orientation of the damage [64] [65]. This anisotropic behavior closely mimics the characteristics of actual fatigue cracks or delaminated regions, especially those that exhibit a preferred growth direction [66]. In the current study, slotted hole damage with varying aspect ratios and orientations is used to simulate more realistic damage profiles while still maintaining control over geometric parameters. This helps in evaluating the robustness of feature extraction methods and the generalizability of machine learning models [67]. From an engineering standpoint, slotted hole notches or defects can result from wear, erosion, or improper machining, all of which are relevant to aerospace and mechanical components under cyclic stress [56] [50].

Another reason for selecting these specific damage types lies in the feasibility of parameterized studies. Circular and slotted hole damages can be easily scaled (in diameter, aspect ratio, or area) and systematically placed across the plate, making it easier to generate training datasets for supervised learning algorithms [56] [50]. The use of tone burst excitations

and round-robin sensor configurations further enhances the spatial coverage and data richness [3]. In experiments, this allowed for repeatable testing of identical damage conditions, which is essential when calibrating the effects of damage size and type on signal features like peak amplitude and time-of-flight [52].

Moreover, the combined use of circular, and slotted hole damages bridges the gap between controlled laboratory conditions and complex real-world problems [44]. While circular damages offer analytical tractability and repeatability, the inclusion of slotted hole damages introduces irregularities that test the robustness of diagnostic algorithms [57]. The result is a more balanced and generalizable SHM framework that performs well across a spectrum of defect types. This approach aligns with recent studies that emphasize the need for hybrid datasets, combining idealized and realistic damage for training deep learning or statistical models in structural diagnostics [3] [68].

From a practical perspective, this selection strategy is also resource efficient. Experimental realization of circular and slotted holes using precision drilling tools is straightforward, with minimal variation across repeated trials [59]. Conversely, cracks are inherently stochastic and difficult to reproduce with consistent geometry, orientation, or depth. Attempting to generate artificial cracks in laboratory conditions often leads to undesirable uncertainties in size and propagation path, which can introduce noise in machine learning pipelines [67][45].

In conclusion, the use of circular and slotted hole damages represents a methodologically sound and practically relevant strategy [58] [56] [50]. It ensures a clean separation between training and validation datasets while leveraging the strengths of both experimental accuracy and simulation versatility. The resulting data, rich in variability and interpretability, feed into the machine learning metamodel to classify, quantify, and localize

damage. This hybrid approach, grounded in physics and data-driven modeling, makes the research more robust and applicable to aerospace SHM challenges [3] [68].

2.2.2 Signal Processing and Feature Extraction in Time Domain

Processing lamb wave signals is always a challenging one. Time domain analysis plays a pivotal role in ultrasonic guided wave-based Structural Health Monitoring (SHM), offering a direct and intuitive method to interpret the wave signals collected from structures [44] [3]. In SHM systems, ultrasonic waves are typically generated using piezoelectric transducers and transmitted through structural materials. These waves interact with defects, altering the received signals in characteristic ways that are both quantifiable and diagnostically meaningful [45] [52]. Time domain approaches involve evaluating temporal signal characteristics such as arrival time, peak amplitude, time of flight (ToF), signal duration, and waveform shape features that often serve as the first indicators of damage [47] [48] [49] [50]. The minimal computational burden of time domain processing, combined with its physical interpretability, has ensured its continued use in both experimental and simulation based SHM studies [60] [65].

In the present research, time domain analysis underpins the feature extraction process used to identify and localize different types of structural damage. Each defect type interacts with ultrasonic waves in distinct ways, which are reflected in the temporal signal profile [69] [44] [63]. For instance, circular holes typically lead to symmetric amplitude reductions and delayed arrivals due to uniform scattering [70] [49] [50]. Hong et al.(2014)[64] experimentally demonstrated that wavefronts interacting with

circular defects preserve isotropy, with reflections distributed evenly in all directions. In contrast, slotted hole damages produce anisotropic effects, causing directional variation in both amplitude and ToF depending on slot orientation [64] [65] [66]. Liu et al.(2012)[66] confirmed through guided wave simulations and experiments that scattering intensity is strongly dependent on the major axis of the slot, with significant differences observed when the wave vector is parallel versus perpendicular to the defect. Cracks introduce even more complex phenomena such as nonlinear scattering, waveform distortion, and mode conversion. Lin et al.(2001)[71], Yuan et al.(2008)[72] and Azar et al.(2021)[67] reported that guided waves interacting with cracks exhibit multiple reflections from the crack tips and mode conversion into secondary wave modes, highlighting the challenge of distinguishing such features in noisy experimental environments.

Among all time domain features, Time of Flight (ToF) is arguably the most widely utilized. It denotes the duration taken by the wave to travel from transmitter to receiver and can be mathematically expressed as

$$\Delta t = t_{\text{damaged}} - t_{\text{pristine}}, \tag{2.1}$$

where t_{pristine} and t_{damaged} are the arrival times of the main wave packet envelope peak in the pristine and damaged cases, respectively. Under pristine conditions, ToF remains consistent and predictable, being determined by the material's elastic properties and geometry [52] [58]. However, the presence of defects typically causes delays, as the wavefront may scatter, reflect, or even reroute around discontinuities [49] [50]. By comparing damaged ToF values against those from baseline (undamaged) cases, damage presence and proximity can be inferred. This approach is particularly effective in sensor configurations like round-robin and pitch-catch, where overlapping sensing paths increase detection reliability

[3] [45].

Another fundamental time domain metric is the peak amplitude of the received wave. The analytic signal $\tilde{s}(t)$ can be obtained using the Hilbert transform $\mathcal{H}\{\cdot\}$, and its envelope is defined as

$$E(t) = \left| s(t) + j\,\mathcal{H}\{s(t)\} \right|, \tag{2.2}$$

with the peak amplitude given by

$$A_{\max} = \max_{t} E(t). \tag{2.3}$$

Damage in a structure often leads to a decrease in amplitude due to energy losses via scattering, absorption, or conversion into other wave modes [47] [48] [61] [73]. In this study, amplitude is used alongside ToF to develop Damage Indices (DIs) that serve as input features to machine learning algorithms for classification and regression. The low computational requirements of peak amplitude extraction make it especially suitable for real time SHM systems [60] [66]. However, amplitude is sensitive to extrinsic variables like sensor bonding conditions, material anisotropy, or ambient temperature changes, necessitating careful signal normalization and calibration, both of which are implemented in this work [58] [64] [65].

Time domain waveform shape analysis also provides rich information. The emergence of secondary peaks, signal elongation, and waveform skew can all signal the presence of damage [63] [67]. Particularly in the case of simulated slotted hole damage model in Abaqus, waveforms display multiple reflections from crack tips and altered propagation paths that distort the original waveform [71] [72]. For circular hole damage, asymmetric signal broadening offers additional clues regarding orientation and severity. In this research, full waveform analysis is conducted on raw experimental data before feature extraction to capture such subtleties.

A significant advantage of time domain analysis is its non parametric, model free nature. It operates directly on raw signal data without requiring spectral transformation or wavelet decomposition [44][3]. This makes it highly suitable for early diagnostics, field deployments, and quick look inspections. In the present work, the raw signals are normalized to a [0.1, 0.9] range to mitigate scaling inconsistencies and improve neural network performance. From these signals, features such as peak amplitude, ToF, rise time, and duration are extracted for various sensor–frequency combinations. These features are then used to generate DIs across multiple locations and excitation frequencies, forming a robust and multi-dimensional feature space [45] [68].

Nevertheless, time domain analysis is not without challenges. One major issue is wave mode overlap, especially in dispersive media or at high excitation frequencies, where multiple Lamb modes coexist and interfere [52] [58]. Such interference can obscure the diagnostic features and reduce the signal to noise ratio. In this research, this problem is mitigated through the use of narrowband tone burst excitations and careful frequency selection based on modal dispersion studies. Additionally, sensor placement is optimized to ensure modal separation and avoid destructive interference [61] [74].

Environmental variability is another challenge. Factors such as temperature drift, loading conditions, and humidity can alter wave velocity and attenuation, leading to false positives [66][67]. While the current study is conducted under controlled laboratory conditions and idealized simulations, future work may incorporate compensation strategies such as temperature normalization, baseline subtraction, or adaptive filtering.

Time domain features are also crucial for validation. In this research, simulation results from Abaqus are validated against experimental data

using ToF and amplitude benchmarks. This alignment confirms the fidelity of the simulation model and justifies its use as low fidelity input to the multi-fidelity neural network (MFNN) framework used in the machine learning phase [68] [71] [72].

In conclusion, time domain analysis forms the cornerstone of signal processing in this research. Its blend of simplicity, interpretability, and diagnostic richness makes it an excellent choice for guided wave SHM applications. Whether dealing with symmetric holes, anisotropic slotted hole defects, or complex cracks, time domain features offer a powerful and scalable toolset. The integration of ToF, peak amplitude, and waveform morphology into machine learning pipelines ensures that SHM systems can be both sensitive and generalizable across a wide range of structural scenarios.

2.3 Machine Learning for Structural Diagnostics

The integration of ML into SHM has revolutionized the field by enabling predictive analytics and automated decision-making. ML algorithms can process vast amounts of sensor data to identify patterns indicative of structural issues, thereby complementing traditional physics-based approaches that often struggle with scalability and environmental variability [37, 55]. The application of ML to SHM can be traced back to the late 1990s and early 2000s, when statistical pattern recognition (SPR) methods were first employed to automate damage detection in complex structures. The motivation was clear: purely physics-based models were insufficient for large or intricate systems subjected to variable environmental and operational conditions. Early work focused on vibration signals and acoustic emissions, laying the foundation for today's sophisticated data-driven methods.

One of the seminal contributions came from Worden and Manson [8], who applied Principal Component Analysis (PCA) and Mahalanobis distance for damage detection. PCA reduced the dimensionality of sensor data while preserving variance, and Mahalanobis distance quantified deviations from baseline states. This unsupervised approach allowed for subtle damage detection without requiring labeled data, an advantage where ground truth is difficult to obtain. Around the same time, Sohn et al. (2001) [75] introduced novelty detection strategies using autoregressive models with exogenous inputs (ARX). These methods forecasted structural responses and flagged deviations, while also incorporating environmental compensation for variables such as temperature and humidity. Their work underscored the need for SHM systems that could distinguish damage from benign environmental effects.

Machine learning methods for SHM can broadly be categorized into supervised and unsupervised approaches. Supervised learning, including regression and classification models, relies on labelled datasets such as pristine and damaged waveforms, whereas unsupervised methods such as clustering identify structural changes without prior labels [76]. Within supervised methods, deterministic models such as polynomial regression (PR), support vector machines (SVMs), and artificial neural networks (ANNs) have been extensively applied to predict damage indices or classify damage types. Probabilistic approaches, including Bayesian Ridge (BR) and stochastic gradient descent (SGD), provide an additional layer of uncertainty quantification. Convolutional Neural Networks (CNNs) represent a deep learning extension of neural networks, where spatially correlated features of guided wave responses are automatically extracted for classification of damage states in composite and metallic structures [18]. Supervised methods gained traction as researchers amassed labeled datasets from laboratory experiments. For example, Verstraete et al.

(2003) [77] demonstrated the utility of SVMs in classifying damage types and locations from modal and acoustic data. The key advantage of SVMs was strong generalization with limited training data, making them attractive in aerospace SHM where large experimental datasets are expensive. Parallel efforts explored artificial neural networks. Sohn et al. (2000) [78] used multilayer perceptrons to classify damage severity in composite beams, showing that even shallow networks could capture nonlinear mappings between sensor features and structural states. Bayesian methods also emerged during this period to explicitly handle uncertainty. Beck and Katafygiotis (1998) [79] employed Bayesian updating for system identification, while Papadimitriou (2004) [80] applied Bayesian inference to damage localization. These efforts illustrated the value of probabilistic reasoning in SHM.

The early 2000s also saw an emphasis on combining feature extraction with ML. Techniques such as Fourier and Wavelet Transforms, as well as statistical descriptors like skewness, kurtosis, and entropy, were widely used to transform raw time series into feature vectors [81]. These were then fed into regression or classification algorithms, establishing the standard SHM pipeline of preprocessing, feature extraction, and model training. Modal data and vibration-based monitoring were also prominent. Yan et al. (2005) [82] used frequency response functions as ML inputs for crack detection in beams and plates. Their comparative study of models highlighted the trade-off between model complexity and interpretability—insights that later informed ensemble and metamodel approaches. Importantly, ML applications were often domain-specific. Doebling et al. (1998) [83] reviewed bridge and civil infrastructure applications, while Giurgiutiu and Rogers (2002) [84] demonstrated aerospace use cases with piezoelectric sensors. Such studies underscored the need for customized feature sets and ML strategies tailored to different

materials and structures.

Ultrasonic guided waves (UGWs), especially Lamb waves, are widely used in SHM due to their sensitivity to small defects and long-range propagation in thin-walled structures. However, UGW signals are dispersive, complex, and sensitive to boundary conditions, making interpretation challenging. ML has been increasingly integrated to extract damage-relevant features from these high-dimensional time series. Early applications were feature-based. Raghavan and Cesnik (2007) [49, 50] localized defects in aluminium plates by training classifiers on time-of-flight (ToF) and amplitude reduction features. Sohn et al. (2004) [51] extended this by training ANNs on time- and frequency-domain features to classify damage in composite plates. With advances in computational power, more recent studies moved toward deep learning, which automated feature extraction and improved robustness. Yang et al. (2020) [85] employed CNNs on ultrasonic images generated from wavefield data, achieving higher accuracy than hand-crafted features, especially under noisy conditions. Abbassi et al. (2023) [86] applied unsupervised PCA and autoencoders for anomaly detection under varying temperature, enabling label-free monitoring. Transfer learning has also emerged: Zhang et al. (2023) [87] showed that pretrained CNNs fine-tuned with small datasets can deliver high accuracy when experimental data are scarce.

The field has recently shifted toward hybrid and multi-fidelity ML. Pop et al. (2024) [88] combined experimental and simulated UGW data in a deep network for carbon fiber SHM, demonstrating improved generalization. Explainable AI (XAI) has also entered SHM: Li et al. (2024) [89] used SHAP values with CNNs trained on guided wave spectrograms, improving interpretability and trust in aerospace applications.

In summary, ML techniques in SHM evolved from early statistical and

shallow learning models (PCA, ARX, SVMs, ANNs, Bayesian inference) to modern deep and hybrid frameworks. In UGW-based SHM, progress has moved from feature-engineered approaches to end-to-end deep learning, with current innovations including multi-fidelity learning, transfer learning, and explainable AI. These advances highlight the maturity of ML in SHM and motivate the use of metamodels and MFNNs in this thesis.

2.3.1 Deterministic ML Models for Damage Prediction

The choice of machine learning (ML) models in Structural Health Monitoring (SHM) significantly influences system performance, especially in contexts with noisy sensor data, variable operating conditions, and limited labeled datasets. A useful classification of ML models is into deterministic and probabilistic frameworks. Deterministic models map inputs to outputs with fixed parameters, offering predictability and computational efficiency. In contrast, probabilistic models incorporate uncertainty, providing not only predictions but also estimates of confidence, making them valuable in risk sensitive SHM applications.

Deterministic ML models are widely used in SHM due to their robustness, ease of implementation, and interpretability. Common examples include Polynomial Regression (PR), Support Vector Machines (SVM), and Artificial Neural Networks (ANNs).

Polynomial Regression (PR) models fit nonlinear relationships between extracted features, such as time of flight, amplitude, or damage index and the corresponding structural condition using polynomial basis functions. While computationally inexpensive, PR is limited by its sensitivity to overfitting and poor generalization to unseen data when high-degree polynomials are used [90].

Support Vector Machines (SVM) offer better generalization by finding an optimal hyperplane that maximizes the margin between classes or

minimizes the regression error within a specified tolerance [91]. SVMs have been applied in SHM to classify damage states in composite structures using features extracted from Lamb wave responses [92]. Their effectiveness is especially notable in small datasets, though their performance declines when scaling to high-dimensional or large scale data.

Artificial Neural Networks (ANNs), particularly feedforward and multilayer perceptron architectures, are among the most widely used deterministic models in SHM. They are capable of modeling complex, nonlinear relationships and are well suited to time domain or frequency domain signal features extracted from ultrasonic guided waves. Zhang et al. (2021)[93] demonstrated the use of ANNs for predicting delamination in composite laminates using guided wave amplitude and arrival time data. ANNs are, however, data hungry and prone to overfitting without regularization.

2.3.2 Probabilistic Approaches for Damage Inference

Probabilistic machine learning model account for uncertainties and variabilities in data, offering a probabilistic assessment of structural health, making them suitable for SHM applications under varying environmental or operational conditions. Two prominent techniques in this category are Bayesian Regression (BR) and Stochastic Gradient Descent (SGD) (when interpreted from a probabilistic optimization perspective).

Bayesian Regression provides a full posterior distribution over model parameters, enabling uncertainty quantification in predictions. Its advantage lies in offering not only a predicted damage state but also the confidence interval around the prediction [94]. Housner et al. (2020) [95] used Bayesian linear models for uncertainty aware crack localization in structural plates, showing that probabilistic models could outperform

deterministic ones when data variability is high or when training data is sparse.

Stochastic Gradient Descent (SGD), commonly used for optimizing complex loss landscapes in deep learning, is probabilistic in nature when considered in the context of noisy updates and learning under uncertainty. SGD is particularly effective in large scale SHM datasets where full batch optimization is computationally prohibitive. Li and Li (2023) [96] demonstrated its use in damage regression tasks on large experimental guided wave datasets, where SGD outperformed traditional batch learners in training time and convergence stability.

Probabilistic models also integrate well with multi-fidelity modeling frameworks. For instance, Gaussian Process Regression (GPR), a Bayesian nonparametric approach, is frequently used to combine high-fidelity experimental data with low-fidelity simulation data for damage prediction. Xu et al. (2024) [97] employed GPR to fuse Abaqus simulations and real sensor signals for delamination detection, achieving improved prediction accuracy and uncertainty calibration.

2.3.3 Comparative Studies and Model Selection

The deterministic vs probabilistic model trade off in SHM involves considerations of data size, computational resources, and the criticality of uncertainty quantification. Deterministic models offer fast inference and simplicity, making them suitable for real time monitoring in resource constrained systems. They provide specific outputs for given inputs, making them suitable for scenarios where system behavior is well understood. These models are often used in SHM for tasks like damage classification and localization. However, probabilistic models provide richer information for decision making and risk management, which is critical in aerospace or nuclear SHM systems.

Recent studies suggest hybrid approaches using deterministic models for feature extraction and probabilistic models for final inference, may offer the best of both worlds. For example, a feedforward ANN may transform raw time domain signals into high dimensional latent features, which are then passed to a Bayesian decision model for probabilistic prediction of damage location and severity. Given an input signal $\mathbf{x}$, a feedforward ANN produces a latent representation $\mathbf{z} = f_{\text{ANN}}(\mathbf{x}; \Theta)$, where Θ are the network parameters. This latent vector $\mathbf{z}$ is then treated as the input to a Bayesian decision model, where the posterior probability of damage state d is given as:

$$P(d \mid \mathbf{z}) = \frac{P(\mathbf{z} \mid d)P(d)}{\sum_{d'} P(\mathbf{z} \mid d')P(d')}. \tag{2.4}$$

This formulation allows deterministic feature extraction from the ANN to be coupled with probabilistic prediction of location and severity.

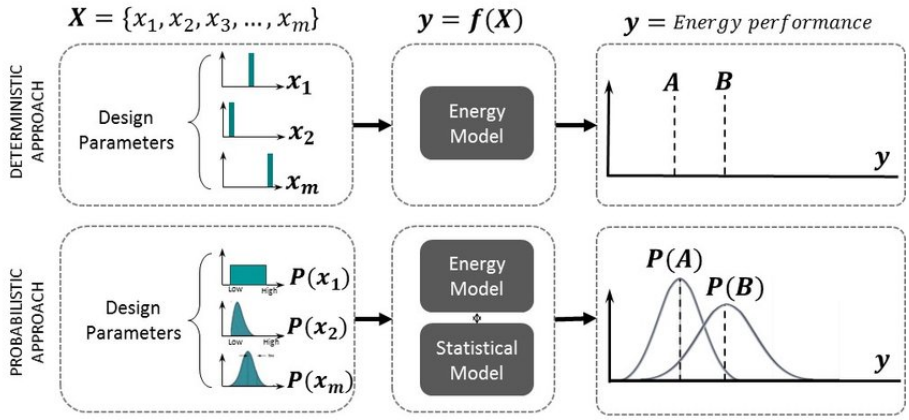


Figure 2.3: Comparison between deterministic and probabilistic model outputs Rezaee et al. (2015)[2]

Figure 2.3 compares the outputs of deterministic and probabilistic machine learning models, as presented by Rezaee et al.(2015). Deterministic models, such as polynomial regression, SVM, or standard ANNs, provide a single best-fit prediction for each input, without accounting for uncertainty. This makes them straightforward and

interpretable, but potentially overconfident when data are scarce or noisy. In contrast, probabilistic models such as Bayesian Ridge Regression or stochastic methods provide not only a central estimate but also a confidence interval around the prediction. The figure illustrates this distinction: the deterministic model tracks the data trend closely but offers no information about reliability, while the probabilistic model captures both the mean behavior and the associated uncertainty bands. This capability is particularly valuable in SHM applications where experimental variability and environmental noise are unavoidable.

The effectiveness of ML in SHM hinges significantly on the selection of suitable models that align with the nature of the sensor data and the diagnostic task. In the context of ultrasonic guided wave based SHM, where signals are complex, nonlinear, and susceptible to environmental variability, multiple ML models often show varying strengths and weaknesses. As a result, recent research has moved toward the use of metamodels integrated frameworks that evaluate and combine multiple ML algorithms to enhance prediction accuracy and robustness across diverse structural conditions. For example, Perdikaris et al. [68] applied a multi-fidelity regression framework to aeroelastic systems, demonstrating improved predictive accuracy compared to single-fidelity models. Similarly, Azar et al. [67] combined SVM and ANN predictions for composite plate SHM, showing that an ensemble outperformed either model alone in classifying delamination size. More recently, Yuan et al. [72] employed hybrid probabilistic-deterministic metamodels to improve generalization in damage localization tasks under varying loading conditions. These examples underline that integrated metamodel frameworks are increasingly adopted to enhance accuracy and robustness across diverse structural conditions.

This section reviews comparative studies of ML models in SHM and

motivates the development of a metamodel framework comprising both deterministic and probabilistic models. The comparative evaluation of ML algorithms in SHM is crucial due to the wide variability in data characteristics, such as noise, dimensionality, missing values, and heteroscedasticity. Worden et al. (2007) [98] emphasized that no single model universally outperforms others across all SHM tasks, advocating for empirical model comparisons under different experimental setups. Chou et al. (2022) [99] demonstrated that ensemble evaluations of SVM, ANN, Decision Trees, and Random Forests yielded performance differences of up to 15% in damage classification accuracy depending on environmental noise, training data size, and sensor placement.

Additionally, data modality plays a role in model performance. For instance, vibration data collected in frequency domain are often more compatible with linear models like PR, while time domain ultrasonic signals favor non linear models such as ANN or Gaussian Process Regression (GPR) [100] [18]. Thus, comparative studies are essential not only for model benchmarking but also for ensuring that the final selection aligns with data structure and task complexity.

Numerous comparative studies validate this metamodel strategy. Li et al. (2014) [101]compared PR, ANN, and GPR on a dataset of ultrasonic waveforms for crack detection. While PR showed lower computational cost, ANN consistently outperformed others in terms of predictive accuracy. GPR, despite its ability to quantify uncertainty, was found computationally expensive for large datasets. Similar findings were reported by Lin et al. (2022) [102], who emphasized that SVMs work well on small, balanced datasets but tend to underperform in high-dimensional setups with noisy labels.

Probabilistic models were particularly valuable for confidence estimation and decision support. For example, BR was used by Wang

and Sun (2020) [32] to assess uncertainty bounds in damage localization, showing improved performance in scenarios with limited labeled training data. Meanwhile, SGD's role in optimizing model parameters with minimal computational overhead made it a strong baseline in online SHM systems.

2.3.4 Metamodelling Strategies for Adaptive Model Selection

A metamodel refers to a high level strategy that combines predictions from multiple base models or selects the best performing model dynamically based on defined criteria. This approach enhances model generalization, mitigates individual weaknesses, and provides a more stable decision-making process under uncertain or evolving structural states.

In this research, a metamodel framework is developed that integrates three deterministic ML models: Polynomial Regression (PR), Support Vector Machines (SVM), Artificial Neural Networks (ANN)—and two probabilistic models, Bayesian Regression (BR) and Stochastic Gradient Descent (SGD). Each model is trained and evaluated independently using extracted features such as time of flight and amplitude based damage index, and signal envelope characteristics from guided wave signals. Model performance was evaluated using standard metrics. The Root Mean Square Error (RMSE) is defined as:

$$\text{RMSE} = \sqrt{\frac{1}{N}\sum_{i=1}^{N}(y_i - \hat{y}_i)^2}, \tag{2.5}$$

where y_i and $\hat{y}_i$ denote true and predicted values, respectively. The

coefficient of determination (R^2) is given by:

$$R^2 = 1 - \frac{\sum_{i=1}^{N}(y_i - \hat{y}_i)^2}{\sum_{i=1}^{N}(y_i - \bar{y})^2}, \tag{2.6}$$

where $\bar{y}$ is the mean of the observed values. Together, RMSE measures prediction accuracy in absolute terms, while R^2 captures the proportion of variance explained by the model.

The model with the best score on a given metric is selected as the local predictor. Alternatively, an ensemble version of the metamodel may perform a weighted average of outputs, where weights are inversely proportional to each model's validation error (as done by [103]). This helps smooth the predictions and makes the system more robust to model variance. In ensemble implementations of the metamodel, predictions $\hat{y}_j$ from individual models M_j are combined as:

$$\hat{y}_{\text{ens}} = \sum_{j=1}^{k} w_j \hat{y}_j, \quad w_j = \frac{1/E_j}{\sum_{l=1}^{k}(1/E_l)}, \tag{2.7}$$

where E_j is the validation error of model M_j. This ensures that models with lower errors contribute more heavily to the final prediction.

In the current thesis work, ANN emerged as the most consistently accurate model across experimental and simulation datasets. Despite requiring more training time and hyperparameter tuning, its ability to model complex nonlinear relationships and adapt to diverse data distributions proved crucial. The comparative evaluation confirmed that ANN achieved the lowest RMSE and highest generalization performance, particularly when used with normalized features and optimized architecture.

This insight justifies the decision to advance the metamodel into a Multi-Fidelity Neural Network (MFNN) framework, wherein the ANN

forms the backbone for combining high-fidelity (experimental) and low-fidelity (simulation) data. MFNN leverages the flexibility of ANN and the efficiency of multi-fidelity learning to provide scalable, interpretable, and generalizable SHM solutions.

The comparative evaluation of deterministic and probabilistic models underpins the motivation for building a hybrid metamodel. Each model contributes unique strengths: PR's simplicity, SVM's precision, ANN's adaptability, BR's uncertainty estimation, and SGD's optimization efficiency. By integrating them within a unified selection and aggregation framework, the metamodel balances performance and reliability. The selection of ANN as the preferred model further enhances the system's capability to adapt to hybrid datasets, setting the stage for the subsequent application of MFNN in the research.

Metamodels serve as simplified representations of complex systems, facilitating faster computations and analyses. In SHM, ML-based metamodels can approximate the behavior of structures under various conditions, enabling efficient simulations and assessments without the need for exhaustive physical testing. The metamodel analysis provided critical insights into the relative strengths and weaknesses of deterministic and probabilistic machine learning approaches. However, all metamodels were limited by their reliance on single fidelity data. Simulation-only models risked bias from numerical idealizations, while purely experimental models suffered from data scarcity. The direct integration of experimental and simulated data is often suboptimal and can lead to inaccuracies. These findings motivated the development of a Multi-Fidelity Neural Network (MFNN) framework, specifically designed to integrate low-fidelity simulation data with high-fidelity experimental data in order to achieve both scalability and physical realism.

2.4 Multi-fidelity Frameworks for Data Fusion

In data-driven Structural Health Monitoring (SHM), one of the most significant challenges is the limited availability of high-fidelity experimental data, which are expensive and time-consuming to collect. Conversely, low-fidelity simulation data, such as those from finite element models (e.g., Abaqus), are more readily available but may lack realism due to simplifying assumptions or idealizations. Multi-Fidelity Machine Learning (MFML), and more specifically Multi-Fidelity Neural Networks (MFNNs), offer a systematic way to combine both types of data, leveraging the quantity of simulations and the quality of experiments to improve model accuracy and generalization.

MFNNs are hierarchical learning architectures that integrate low-fidelity (LF) and high-fidelity (HF) datasets into a unified predictive framework. In the context of ultrasonic guided wave based SHM, MFNNs can significantly enhance the predictive capabilities of machine learning models by using simulations (e.g., with circular hole, slotted hole, and crack damage) to learn general structural behavior, and experiments (e.g., with circular and slotted hole damage) to refine and calibrate predictions. This dual approach is motivated by the observation that models trained solely on simulations often underperform when exposed to real-world data, while purely experimental approaches are limited by data scarcity.

Recent studies illustrate this balance. Perdikaris et al. (2017) [104] pioneered nonlinear information fusion using deep residual networks, showing that MFNNs could outperform single-fidelity models when the simulation-experiment gap is significant. Their approach corrected biases in low-fidelity aerodynamic simulations using sparse experimental data, highlighting the potential for similar correction in guided wave propagation where boundary and bonding effects are not captured by finite element

models. Zhu et al. (2020) [105] applied MFNNs to impact localization in composites, reporting over 30% improvement in accuracy compared to single-fidelity ANNs. Importantly, they demonstrated that MFNNs could generalize across geometries, a finding directly relevant to SHM of structures with varying thicknesses or defect sizes. Wu et al. (2021) [106] extended the approach to pipeline corrosion monitoring, where thousands of synthetic signals were combined with a small number of ultrasonic measurements, achieving robust classification despite strong environmental noise. These examples confirm that MFNNs not only enhance predictive performance but also provide resilience to variability, a critical requirement for SHM in aerospace and civil engineering.

However, these successes also highlight limitations. Perdikaris et al.[104] showed improved accuracy but required careful data alignment between LF and HF sources, a step often non-trivial in SHM where sensor placement may differ between simulations and experiments. Zhu et al.[105] reported reduced accuracy when experimental coverage was too sparse, suggesting that MFNNs cannot fully substitute experiments but only complement them. Wu et al.[106] emphasized computational cost, as large LF datasets combined with residual learning can increase training time. These points underline that while MFNNs are promising, their implementation requires careful preprocessing, balanced sampling, and computational resource management.

2.4.1 Concept and Architecture

A standard MFNN comprises two neural sub-networks, a low-fidelity branch trained on simulations to capture broad signal–damage relationships, and a high-fidelity branch that refines predictions using limited experimental data. One widely adopted design is residual learning, where the HF network learns the correction between LF predictions and

ground truth [68]. This enables efficient transfer of simulation-informed patterns while anchoring results in experimental realism.

Other architectures have also been proposed. Raissi et al. (2019) [107] integrated physics-informed constraints into MFNNs to infer stress fields from sparse strain data, ensuring that outputs obey governing equations. Kennedy and O'Hagan (2000) [108], although predating deep learning, laid the statistical foundation by formulating hierarchical Gaussian process models, inspiring today's deep MFNN formulations. More recently, Guo et al. (2022) [109] demonstrated a multi-branch MFNN for vibration-based SHM of wind turbine blades, where simulation-informed features of mode shapes were corrected by experimental vibration measurements, achieving higher accuracy than baseline neural networks. These works collectively show that MFNNs are not tied to one architecture but represent a family of strategies for hierarchical data fusion.

The MFNN architecture developed in this work is directly motivated by the practical need to integrate abundant low-fidelity (LF) finite element data with scarce but highly reliable high-fidelity (HF) experimental data. The code implements a dual-branch network design, where LF and HF information are first independently processed and subsequently fused into a joint predictive model. This ensures that the general patterns learned from simulations guide the learning process, while experimental data provide fine-tuning and correction.

Figure 2.4 illustrates the MFNN architecture adopted in this thesis. The low-fidelity (LF) branch is first trained on extensive simulation data to establish a baseline representation of wave–damage interactions. Its predictions are then concatenated with high-fidelity (HF) experimental inputs, forming the fusion stage of the network. The HF branch refines these fused features, learning corrective mappings that align simulation-informed generalization with experimentally validated

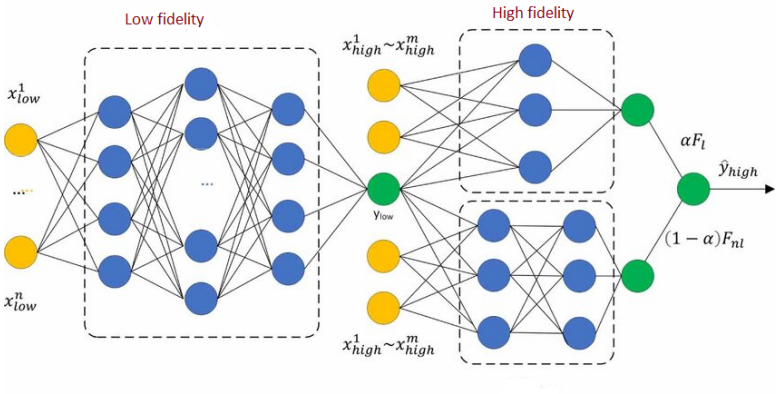


Figure 2.4: Schematic of a Multi-Fidelity Neural Network (MFNN) architecture used in SHM.

precision.

Formally, let $\mathbf{X}_{LF}$ and $\mathbf{y}_{LF}$ denote the inputs and outputs of the LF dataset, and $\mathbf{X}_{HF}$ and $\mathbf{y}_{HF}$ represent the HF dataset. The LF branch of the network approximates the mapping:

$$f_{LF} : \mathbf{X}_{LF} \mapsto \hat{\mathbf{y}}_{LF}, \tag{2.8}$$

while the HF branch is trained to learn a correction function that adjusts LF predictions to match HF observations. In the dual-branch MFNN, this is expressed as:

$$f_{HF} : [\mathbf{X}_{HF}, f_{LF}(\mathbf{X}_{HF})] \mapsto \hat{\mathbf{y}}_{HF}, \tag{2.9}$$

where the concatenation of HF inputs and LF predictions provides the fused input to the HF branch. This formulation allows the network to explicitly leverage the LF model as prior knowledge.

The LF branch in the code is structured as a fully connected feedforward network, comprising multiple dense layers with nonlinear activation functions (Rectified Linear Units, ReLU). The HF branch mirrors this structure but with fewer parameters, reflecting the smaller dataset size. Both branches are trained using mean squared error (MSE)

as the loss function, consistent with regression-based SHM tasks. The LF branch is first trained independently on the full set of simulation data until convergence. Its weights are then frozen, and the HF branch is trained using experimental data, with LF predictions serving as additional input features. This staged training ensures that the LF model captures broad structural trends, while the HF model specializes in correcting systematic biases.

Scaling and normalization play an essential role in this architecture. Both LF and HF inputs are standardized using consistent preprocessing pipelines to ensure compatibility across fidelities. Outputs are likewise normalized between fixed bounds, avoiding bias introduced by differing magnitudes of simulation and experimental responses. During inference, the LF network provides baseline predictions, and the HF network refines them, ensuring robustness even when experimental data are sparse.

The MFNN training strategy is also carefully designed to prevent overfitting to the small HF dataset. Early stopping criteria are applied, and the HF branch is trained with dropout regularization, reducing the risk of memorization. Furthermore, performance is evaluated using Root Mean Square Error (RMSE) and the coefficient of determination (R^2), with scatter plots of predicted versus true values saved at each run. A 45-degree reference line is used in these plots to visually assess model calibration.

A notable implementation detail is the explicit handling of dataset alignment. While LF simulations cover all possible combinations of thickness, frequency, damage size, and sensor positions, HF experiments are only available for a restricted set of seven aluminum plates. The code resolves this mismatch by mapping HF samples to their corresponding LF counterparts based on thickness and damage descriptors. When HF data are missing for certain configurations, the LF model still provides

predictions, but no correction is applied. This reflects the real-world constraint that experiments cannot practically cover the full parameter space.

The final output of the MFNN is thus a two-step corrected prediction:

$$\hat{\mathbf{y}} = f_{HF}(\mathbf{X}_{HF}, f_{LF}(\mathbf{X}_{HF})), \tag{2.10}$$

which integrates both fidelity levels into a coherent framework. This structure ensures that the LF data contribute generalizable physics-informed patterns, while the HF data enforce empirical accuracy, striking a balance between data abundance and data reliability.

The MFNN framework developed in this thesis embodies a structured approach to fusing simulation and experimental data for SHM. Its dual-branch design, staged training, and data alignment strategies address the key challenges of limited experimental availability and simulation bias. By implementing robust preprocessing, regularization, and evaluation strategies, the architecture achieves a balance between exploiting abundant simulations and refining predictions with scarce experimental evidence. This provides a technically rigorous and practically feasible methodology, contributing to the growing body of MFNN applications in engineering.

Applications in SHM

Applications of MFNNs in SHM remain emergent but growing. Zhu et al. (2020) showed MFNNs outperforming single ANNs for composite impact damage localization. Wu et al. (2021) applied MFNNs for corrosion in steel pipelines, reporting robust classification under variable noise. Guo et al. (2022) extended the framework to vibration-based turbine blade monitoring, while Pop et al. (2024) [88] recently demonstrated a wireless UGW SHM system using MFNNs, significantly improving

fatigue crack detection accuracy compared to conventional ANNs. These studies collectively demonstrate that MFNNs are not limited to guided waves but are generalizable across sensing modalities. Yet challenges remain, including computational scalability and sensitivity to misaligned simulation-experiment domains.

In the context of this thesis, MFNNs are implemented using LF features extracted from Abaqus simulations (time of flight, peak amplitude, damage indices) and HF features extracted from experiments on aluminum plates with circular and slotted holes. The LF network captures the general influence of damage on Lamb waves, while the HF network refines predictions to account for bonding variability, sensor noise, and geometric tolerances. Compared to deterministic and probabilistic metamodels, the MFNN achieves lower RMSE, higher R^2, and better generalization to unseen cases, validating its suitability for SHM.

The literature highlights that MFNNs represent a critical advance in SHM. They leverage abundant simulations without discarding experimental realism, address the limitations of single-fidelity ML, and provide a pathway for scalable, accurate, and physically grounded predictions. While challenges in data alignment and computational cost remain, the reviewed studies and this thesis demonstrate that MFNNs are a powerful framework for next-generation SHM.

While the MFNN framework substantially improved the prediction of damage indices by combining LF and HF datasets, SHM ultimately requires not only diagnostics but also prognostics. In practice, the value of SHM lies in predicting how long a structure can continue to perform safely after damage initiation. This is expressed as the Remaining Useful Life (RUL). To establish this connection, the outputs of the MFNN, Damage Indices derived from guided wave features, are mapped to fatigue-life models. By grounding the machine learning predictions in established

fatigue relationships, the framework provides both accurate damage detection and actionable life prediction. This forms the basis of the next section.

2.5 Prognostics and Remaining Useful Life Estimation

In SHM, detecting and localizing damage is only the first step; the ultimate goal is to assess how long the structure can safely continue to operate. This concept is formalized as the Remaining Useful Life (RUL). Estimation of RUL provides the bridge between diagnostics and prognostics, allowing maintenance decisions to be planned based on predicted fatigue life rather than reactive inspections.

The accurate prediction of RUL is a central aspect of SHM, as it directly informs maintenance planning, safety management, and life-cycle cost optimization. For aerospace, automotive, and civil engineering applications, reliable RUL estimation enables operators to replace components before catastrophic failure while minimizing unnecessary downtime [110, 111]. Over the past decades, a wide spectrum of approaches has emerged, broadly categorized into physics-based models and data-driven methods.

Although the experimental specimens investigated in this thesis are not subjected to cyclic fatigue loading, the guided wave-based Damage Index (DI) trajectories provide a degradation proxy that can be mapped to fatigue life through physics-informed calibration. This ensures that the use of fatigue-based models, such as S–N curves, remains meaningful in the present context by anchoring machine learning predictions of DI to established fatigue lifetimes.

This section reviews the methodologies for RUL estimation in literature and situates the contributions of the present work, which

integrates ultrasonic guided wave features, Multi-Fidelity Neural Networks (MFNN), and validation using S–N curve theory.

2.5.1 Physics-Based Approaches to RUL Estimation

Physics-based approaches form the historical foundation of fatigue life prediction and remain central to safety-critical engineering disciplines. These models rely on fundamental principles of fracture mechanics, elasticity, and material science to predict the evolution of cracks or defects under cyclic loading. In structural health monitoring (SHM), such models provide interpretability and physical grounding, linking observed damage progression to well-established fatigue theories [112, 113]. The most commonly employed categories include fatigue crack growth laws, S-N (Wöhler) curves, and continuum damage mechanics. This subsection provides a detailed review of these methodologies, with emphasis on their mathematical formulations, assumptions, and applicability to the present study.

Paris' law is one of the earliest and most widely adopted models for fatigue crack growth, first introduced by Paris and Erdogan [114, 115]. The law relates the rate of crack extension per loading cycle (da/dN) to the applied stress intensity factor range (ΔK):

$$\frac{da}{dN} = C(\Delta K)^m, \tag{2.11}$$

where a is the crack length, N is the number of cycles, $\Delta K = K_{\max} - K_{\min}$ is the range of the stress intensity factor, and C and m are empirical material constants determined through fatigue testing. The stress intensity factor itself is given by:

$$K = \sigma\sqrt{\pi a}Y(a/W), \tag{2.12}$$

where σ is the applied nominal stress, W is a characteristic geometry dimension (e.g., plate width), and $Y(a/W)$ is a dimensionless geometry correction factor.

Paris' Law is valid primarily in the so-called "Region II" of crack growth, where the relationship between $\frac{da}{dN}$ and ΔK is log-linear. In Region I (near-threshold) and Region III (rapid growth to failure), other mechanisms dominate, requiring extensions such as the Forman model:

$$\frac{da}{dN} = \frac{C(\Delta K)^m}{(1-R)\Delta K_c - \Delta K}, \tag{2.13}$$

where $R = K_{\min}/K_{\max}$ is the load ratio, and ΔK_c is the critical stress intensity factor range [116]. Similarly, the NASGRO equation incorporates threshold effects, crack closure, and near-fracture toughness phenomena [117]. These extensions expand the applicability of crack growth laws to variable amplitude loading, which is common in aerospace structures [118].

Despite its popularity, Paris' Law has notable limitations. It assumes that fatigue life is governed entirely by crack propagation, neglecting crack initiation. For metallic structures with small pre-existing defects, this assumption may be justified, but in cases involving notches or large holes, as in the present study, initiation dominates the fatigue process. Consequently, alternative models such as S–N curves provide more relevant predictions.

To address variability and uncertainty, modern fatigue crack growth models often treat crack evolution as a stochastic process. **Probabilistic Fracture Mechanics** frameworks describe growth as:

$$da = C(\Delta K)^m dN + \sigma_w dW, \tag{2.14}$$

where the first term captures deterministic Paris-type growth, and the second term models randomness through a Wiener process dW with

variance σ_w^2 [119, 120]. Such probabilistic formulations are increasingly adopted in aerospace lifing due to their ability to quantify risk.

Other advances include **Phase-Field Fracture Models**, which regularize discontinuities and allow the simulation of crack initiation, propagation, and branching in a unified framework. The total energy functional combines elastic energy with a fracture energy term:

$$\mathcal{F}(u, D) = \int_{\Omega} \left[g(D)\psi(\varepsilon(u)) + G_c \gamma(D, \nabla D) \right] d\Omega, \tag{2.15}$$

where u is displacement, D a damage variable, G_c fracture toughness, and γ a crack density functional [121, 122]. These methods provide rich physical fidelity but remain computationally intensive for online SHM applications.

Continuum Damage Mechanics (CDM) extends fatigue modeling by introducing a scalar damage variable $D \in [0, 1]$ that represents the progressive degradation of material stiffness. In this framework, effective stress is defined as:

$$\sigma = \frac{\tilde{\sigma}}{1 - D}, \tag{2.16}$$

where $\tilde{\sigma}$ is the applied stress. Damage evolution laws are then postulated, such as:

$$\frac{dD}{dN} = f(\sigma, N), \tag{2.17}$$

where f is a function of stress and cycle count [123]. CDM provides a unifying framework capable of describing both crack initiation and propagation, but it requires detailed parameter identification and often lacks closed-form solutions. For SHM, CDM offers interpretability but is computationally intensive compared to empirical models.

S-N Curve, introduced by Wöhler in the 19th century, remains one of the most widely used tools for fatigue design and life prediction [124]. It represents the empirical relationship between the applied stress amplitude (S) and the number of cycles to failure (N). The general form of the equation is:

$$S^m N = C', \tag{2.18}$$

where m and C' are material constants determined experimentally. Equation 2.18 is typically linearized by plotting $\log S$ against $\log N$, yielding a straight line in log–log space:

$$\log S = \log C' - m \log N. \tag{2.19}$$

The slope m indicates the sensitivity of fatigue life to stress amplitude, while C' reflects material resistance to fatigue. For many high-strength aerospace alloys, m ranges between 5 and 12, depending on loading mode and environmental conditions [125, 126].

A key concept associated with S–N curves is the fatigue limit (or endurance limit), defined as the stress amplitude below which the material can theoretically sustain an infinite number of cycles without failure. For steels, this limit is often well defined; however, in aluminum alloys, the S–N curve decreases continuously, implying that no true endurance limit exists [112]. Instead, a practical fatigue strength corresponding to 10^7 or 10^8 cycles is typically reported.

In metallic plate structures such as those considered in this thesis, fatigue is the dominant failure mechanism. Under repeated cyclic loading, microstructural damage initiates and accumulates, eventually leading to crack formation and growth. This progressive degradation alters guided wave propagation characteristics, making it detectable through

signal-based features. Although the experimental specimens in this work were not subjected to actual cyclic loading, the guided wave-derived Damage Index (DI) serves as a proxy measure of degradation. By calibrating the evolution of DI values against established S–N (stress–life) relationships for aluminum alloys, the MFNN outputs can be systematically linked to fatigue-based life prediction. In this way, guided wave diagnostics are translated into physics-informed prognostics, without requiring direct observation of crack initiation or growth.

The S–N approach remains widely adopted due to its simplicity and strong experimental foundation. It is particularly suitable when initiation life dominates the fatigue process, as it empirically incorporates both crack initiation and propagation into a single curve. This makes it well suited for components containing pre-existing defects, such as the circular and slotted holes examined in this thesis.

Furthermore, S–N relationships can be combined with cumulative damage models for Remaining Useful Life (RUL) estimation under variable loading. One of the most common formulations is Miner's linear damage hypothesis:

$$D = \sum_{i=1}^{k} \frac{n_i}{N_i}, \tag{2.20}$$

where n_i is the number of cycles applied at a given stress level S_i, N_i is the fatigue life at that stress obtained from the S–N curve, and D is the cumulative damage. Failure is assumed to occur when $D = 1$ [127]. Despite its simplicity, Miner's rule provides a practical means of estimating fatigue accumulation under spectrum loading and remains in widespread use for certification in aerospace engineering [128].

Physics-based models provide valuable interpretability and grounding in established fatigue theory. Paris' Law and its extensions are

powerful for propagation-dominated cracks, while S–N curves capture initiation-dominated fatigue in a simple, experimentally validated framework. Continuum Damage Mechanics offers a more general description of degradation but at the cost of complexity. In this research, S–N relationships were used as an analogy to validate the progression of DI curves predicted by the MFNN, as they naturally capture the initiation-dominated fatigue behavior of circular and slotted holes. For instance, fatigue lives of approximately 1.0×10^6 cycles for circular holes and 0.8×10^6 cycles for slotted holes were selected based on experimental data and literature values for aluminum plates. The predicted DI trajectories were calibrated to align with these reference fatigue lives, ensuring physical consistency between machine learning-based predictions and established fatigue theory.

2.5.2 Data-Driven Approaches to RUL Estimation

With the rapid development of sensing technologies and computational power, data-driven approaches have emerged as a powerful alternative to physics-based models for RUL estimation. Unlike fracture mechanics or S-N curve methods, which rely on predefined material constants and assumptions, data-driven techniques learn degradation patterns directly from measured signals or extracted features. These methods are especially attractive for SHM, where damage mechanisms may be complex, interacting, or poorly understood, and where large volumes of sensing data are readily available [129, 111].

Data-driven RUL estimation encompasses a wide spectrum, ranging from classical machine learning regression methods to advanced deep learning architectures and hybrid physics-informed models. This subsection provides a comprehensive overview of these approaches, their mathematical formulations, and their applicability to SHM.

Classical Machine Learning Models

Early attempts at data-driven RUL prediction employed classical supervised learning algorithms trained on engineered features extracted from vibration, acoustic emission, or ultrasonic signals. Examples include Support Vector Regression (SVR), Random Forests (RF), Gradient Boosting Machines (GBM), and Gaussian Process Regression (GPR).

Support Vector Regression seeks to approximate a function $f(x)$ that maps input features x (e.g., frequency shifts, time-of-flight changes, peak amplitudes) to the target RUL value y. Its optimization problem can be expressed as:

$$\min_{w,b,\xi,\xi^*} \frac{1}{2}\|w\|^2 + C\sum_{i=1}^{N}(\xi_i + \xi_i^*), \tag{2.21}$$

subject to

$$y_i - w^T\phi(x_i) - b \leq \epsilon + \xi_i, \quad w^T\phi(x_i) + b - y_i \leq \epsilon + \xi_i^*, \quad \xi_i, \xi_i^* \geq 0, \tag{2.22}$$

where $\phi(x)$ maps features into a high-dimensional kernel space, C is a penalty parameter, and ϵ defines an insensitive margin [130]. SVR has been widely applied in SHM due to its robustness and ability to handle nonlinear feature–RUL relationships.

Ensemble methods such as Random Forests and Gradient Boosting aggregate multiple weak learners (typically decision trees) to improve generalization. For instance, Random Forest predictions are given by:

$$\hat{y} = \frac{1}{T}\sum_{t=1}^{T} h_t(x), \tag{2.23}$$

where $h_t(x)$ is the prediction from the t-th decision tree, and T is the total number of trees. These methods provide interpretability through

feature importance measures and have been demonstrated to perform well with limited datasets in fatigue applications [131].

Gaussian Process Regression (GPR) provides a probabilistic framework by modeling RUL as a Gaussian distribution conditioned on observed features. The predictive distribution is expressed as:

$$p(y_*|x_*, X, Y) = \mathcal{N}\left(k_*^T(K + \sigma^2 I)^{-1}Y,\, k(x_*, x_*) - k_*^T(K + \sigma^2 I)^{-1}k_*\right), \tag{2.24}$$

where K is the kernel matrix, k_* is the covariance vector between the test point x_* and training inputs X, and σ^2 is observation noise variance [132]. GPR is particularly attractive for SHM because it provides uncertainty estimates in RUL predictions, which are crucial for maintenance planning.

Despite their successes, classical ML methods rely heavily on handcrafted features and do not easily capture temporal dependencies in degradation processes. This motivated the transition toward deep learning approaches.

Deep Learning for RUL Prediction

Deep learning models overcome many limitations of classical ML by automatically learning hierarchical feature representations from raw or minimally processed data. Several architectures have been explored for RUL estimation in SHM.

Convolutional Neural Networks (CNNs) are designed to extract spatially correlated features, making them ideal for processing ultrasonic guided wave signals or frequency spectrograms. A 1D CNN applied to waveforms can learn filters that correspond to characteristic frequency components or scattering patterns associated with damage progression.

Mathematically, convolution is defined as:

$$s_j = \sum_{i=1}^{M} x_i w_{i-j}, \tag{2.25}$$

where x_i is the input signal, w_{i-j} are the learnable convolutional kernels, and s_j is the feature map. CNNs trained on ultrasonic data have demonstrated strong performance in crack classification and life prediction tasks [133].

Recurrent Neural Networks (RNNs) and Long Short-Term Memory (LSTM) networks: Fatigue degradation is inherently sequential, with damage accumulating over cycles. RNNs, and particularly Long Short-Term Memory (LSTM) networks, are designed to capture such temporal dependencies. The LSTM introduces memory cells and gating mechanisms that regulate information flow:

$$f_t = \sigma(W_f \cdot [h_{t-1}, x_t] + b_f), \quad i_t = \sigma(W_i \cdot [h_{t-1}, x_t] + b_i), \tag{2.26}$$

$$\tilde{C}_t = \tanh(W_C \cdot [h_{t-1}, x_t] + b_C), \quad C_t = f_t \odot C_{t-1} + i_t \odot \tilde{C}_t, \tag{2.27}$$

$$o_t = \sigma(W_o \cdot [h_{t-1}, x_t] + b_o), \quad h_t = o_t \odot \tanh(C_t), \tag{2.28}$$

where f_t, i_t, o_t are forget, input, and output gates, and C_t is the cell state [134]. LSTMs have been widely used for RUL prediction in rotating machinery, batteries, and aerospace components [135].

Hybrid CNN–LSTM Models: Combining CNNs with LSTMs allows networks to capture both spatial and temporal dependencies in degradation signals. CNN layers first extract localized features, while LSTMs then

model their progression over cycles. Studies have demonstrated that hybrid CNN–LSTM architectures outperform either model individually for RUL prediction tasks [136].

Transformer Architectures: Transformers, originally developed for natural language processing, employ self-attention mechanisms to model long-range dependencies. Recently, they have been applied to prognostics with promising results [137]. The self-attention mechanism computes:

$$\text{Attention}(Q, K, V) = \text{softmax}\left(\frac{QK^T}{\sqrt{d_k}}\right)V, \tag{2.29}$$

where Q, K, and V are query, key, and value matrices. Transformers can process long ultrasonic time series without the vanishing gradient issues of RNNs, making them attractive for SHM applications.

Hybrid and Physics-Informed Models

Recent advances in Remaining Useful Life (RUL) modelling go beyond the classical fatigue laws by incorporating more realistic representations of material degradation, probabilistic reasoning, and machine learning integration. Contemporary approaches can be grouped into enhanced physics-based models, purely data-driven methods, and hybrid physics-informed frameworks. Enhanced physics-based and stochastic models extend classical fatigue relations by embedding uncertainty, environmental effects, or microstructural considerations, enabling probabilistic estimation of crack growth and fatigue life [79, 80]. While these approaches retain physical interpretability, their predictive accuracy depends strongly on the availability of material parameters and initial condition estimates, which are often costly to obtain.

In parallel, purely data-driven techniques have advanced rapidly with deep learning. Recurrent networks such as Long Short-Term Memory

(LSTM) and Gated Recurrent Units (GRU) have been used for degradation trajectory forecasting, while convolutional neural networks (CNNs) and more recently Transformer-based architectures have been applied to RUL prediction using vibration, acoustic, or ultrasonic signals [85, 86, 87].

Data-driven approaches offer a powerful alternative to purely physics-based modelling because they can capture the combined effects of multiple interacting damage mechanisms without requiring explicit analytical formulations. By learning directly from sensing data, such as ultrasonic guided waves, vibration signals, or acoustic emissions, these methods can adapt to the complexities of real structures. Their strength becomes most apparent when large, labelled datasets are available, allowing them to deliver highly accurate and even real-time predictions once trained [89]. However, these advantages come with important limitations. High-quality labelled failure data are often scarce, since conducting full-scale fatigue tests is both costly and time-intensive. In addition, purely data-driven models typically lack physical interpretability, making it difficult to understand how specific features of the input signals relate to underlying material behaviour [89]. Generalization is another challenge. Models trained on one structure or loading condition may not perform reliably on different geometries, boundary conditions, or environmental settings. Finally, while deep learning models are powerful, they are often treated as "black boxes" that produce single point estimates. For applications in Structural Health Monitoring, this can be restrictive, since decision-making under uncertainty requires probabilistic predictions and confidence intervals rather than deterministic outputs alone. To address these challenges, ongoing research explores transfer learning, domain adaptation, and explainable AI methods (e.g., SHAP, LIME) applied to SHM contexts [138]. Hybrid models incorporating physics-based constraints, such as Paris' Law or S-N calibration, are also gaining traction

as a way to ensure robust and interpretable RUL estimation.

In summary, data-driven approaches have transformed RUL estimation in SHM, moving from handcrafted regression models to advanced deep learning architectures. While purely data-driven models offer flexibility, their limitations in interpretability and generalization necessitate hybrid approaches. The framework developed in this thesis, which integrates MFNN predictions with S-N curve calibration, exemplifies this trend, ensuring that data-driven predictions remain both accurate and physically consistent.

The current state of the art increasingly lies in hybrid and physics-informed models, which seek to combine the interpretability of mechanistic formulations with the flexibility of machine learning. Physics-informed neural networks (PINNs) integrate governing equations directly into the training loss, ensuring predictions remain consistent with fatigue physics [107, 139]. Residual hybridization strategies use classical models such as Paris law or S–N curves to provide a baseline estimate, while machine learning models learn the residual between physics predictions and experimental observations [140, 141]. Other approaches embed fatigue accumulation laws, such as Miner's rule, into Bayesian or probabilistic ML frameworks, yielding calibrated uncertainty estimates relevant for aerospace certification [142]. Across these studies, hybridization has consistently improved accuracy, reduced data requirements, and prevented physically implausible extrapolations. For example, Perdikaris et al. [143] demonstrated nonlinear multi-fidelity fusion for data-efficient learning, while Zhu et al. [105] and Wu et al. [106] applied MFNNs to composite plates and pipelines, showing superior generalization when both simulation and experimental data were combined. These efforts reflect a broader shift in the field toward physics-informed machine learning as the dominant paradigm for RUL. In these approaches, machine learning predictions are

regularized by physical constraints (e.g., crack growth laws, S-N curves), ensuring both adaptability and interpretability. For example, Peng et al. [144] highlighted that hybrid methods provide more reliable extrapolation in conditions not observed in training data, a key requirement for aerospace SHM.

In the present thesis, such integration was realized by combining Multi-Fidelity Neural Networks (MFNN) with physics-based S-N curve calibration. The Damage Index (DI) predicted by the Multi-Fidelity Neural Network (MFNN) is anchored to fatigue life estimates by calibration against established S–N relationships for aluminium alloys. Although the experimental specimens in this work are not subjected to cyclic fatigue loading, the guided wave-based DI trajectories provide a degradation proxy that can be mapped to fatigue life using physics-informed calibration. This approach is consistent with hybrid RUL methodologies, where empirical physics models establish the baseline and machine learning corrects and generalizes the predictions. By situating the MFNN outputs within this hybrid framework, the methodology developed in Chapter 3 ensures that guided wave diagnostics are translated into physics-consistent prognostics, thereby bridging the gap between structural monitoring and life prediction.

2.5.3 Integrating Data-Driven Models with Fatigue Physics

While data-driven and physics-based approaches to Remaining Useful Life (RUL) estimation each have unique strengths, their integration has emerged as a promising strategy for robust and interpretable prognostics. In this thesis, the combination of a MFNN with the classical S-N (stress–life) curve analogy was employed to ensure that data-driven predictions retained physical consistency. The MFNN, trained on both

simulation and experimental guided wave data, provides damage indices (DI) that quantify the progression of structural degradation. These indices, however, require calibration to actual fatigue life, which is naturally achieved through alignment with S-N curves.

The S-N curve, also referred to as the Wöhler curve, represents the relationship between stress amplitude (σ_a) and the number of cycles to failure (N_f). Mathematically, this relationship is commonly expressed as:

$$\sigma_a = \sigma'_f (2N_f)^b, \tag{2.30}$$

where σ'_f is the fatigue strength coefficient and b is the fatigue strength exponent [128]. For aluminum alloys, these parameters are well documented and provide a reliable baseline for fatigue life estimation [125]. In practice, the S-N curve is derived from controlled fatigue experiments, and it reflects the average life under specific stress amplitudes.

The integration strategy pursued here consisted of three steps. First, the MFNN was trained to map input parameters (material, plate thickness, excitation frequency, sensor positions, damage type and damage size) to damage indices, learning from both low-fidelity finite element simulations and high-fidelity experimental guided wave signals. Second, the DI progression predicted by the MFNN was interpreted as a proxy for life consumption. Third, the predicted DI evolution was calibrated against S-N derived cycles-to-failure, effectively anchoring the data-driven model in a physics-based reference frame.

This integration serves several purposes. The MFNN, while flexible, risks producing DI curves that diverge from physical expectations, particularly when extrapolating beyond the training data. By aligning with S-N curves, the predicted RUL trajectories are constrained to start at an initial DI (corresponding to undamaged conditions) and converge

toward a critical DI threshold at cycles consistent with known fatigue lives. This ensures that the MFNN predictions, even when driven by ultrasonic features, remain grounded in the physical fatigue behavior of the material.

The advantages of this hybrid framework are significant. From the data-driven side, the MFNN captures complex, nonlinear relationships in guided wave signals, accommodating variability across frequencies, thicknesses, and defect geometries. From the physics-based side, S-N curves provide interpretability, long-standing validation, and relevance to design standards. Together, the integration achieves a balance: predictions adapt to the variability inherent in experiments while maintaining consistency with established fatigue principles.

There are some limitations to S-N curves. They are inherently statistical and represent mean behavior, not accounting for scatter due to microstructural variability or environmental effects. Consequently, DI-based predictions calibrated to S-N must be interpreted as average trends rather than exact lifetimes. Moreover, while the MFNN generalizes well across training conditions, its extrapolation beyond the tested parameter space (e.g., different materials or environmental conditions) still requires caution. Despite these challenges, the MFNN:S-N hybrid framework demonstrates a practical and scalable solution for aerospace structural prognostics, offering both data adaptability and physical interpretability.

Chapter 3 Methodology

3.1 Synopsis of the Proposed Approach

The research design for this study was developed with the objective of creating a robust and intelligent SHM framework capable of predicting damage, location, and RUL of structural components using guided ultrasonic waves and machine learning. To this end, the methodology is organized into clearly defined stages, integrating both experimental and numerical analyses with data-driven modeling. The design emphasizes a hybrid approach, combining low-fidelity data obtained from numerical simulations with high-fidelity data derived from laboratory experiments. This integration allows for better generalization and adaptability of machine learning models in real-world SHM applications, especially in aerospace and mechanical structures where reliability and accuracy are paramount. This section provides a synopsis of the proposed research. Detailed presentations are given in the subsequent chapters of this thesis.

The two research phases introduced in Section 1.4 define the high-level conceptual progression of the study, while the eight research design steps outlined below provide an operational, step-by-step implementation of these phases. Specifically, Steps 1–6 correspond to Phase 1, which focuses till the metamodel development, whereas Steps 7 and 8 constitute Phase 2, where multi-fidelity learning, damage localization, and prognostic extensions are implemented.

The first step in the research design involved **establishing the geometry and boundary conditions** for the structure under investigation, an aluminum sheet representing a typical aircraft panel. The sheet model incorporated multiple thickness configurations and varying damage sizes to replicate realistic failure modes. Circular and slotted hole damages of specific dimensions were introduced to examine the influence of size and shape on wave propagation characteristics. A narrowband (300 kHz - 500 kHz) tone burst excitation was applied to one sensor while others acted as receivers, enabling the capture of wave reflections, mode conversions, and amplitude attenuation patterns. The entire sensor system was arranged in a square configuration to ensure symmetric and repeatable signal behavior.

The second step involved **conducting controlled experiments** to obtain high-fidelity data. Physical aluminum plates with artificially induced damage were prepared, and the same sensor configuration used in the simulations was adopted for consistency. Ultrasonic signals were collected using a signal generator and a data acquisition system with microsecond-level resolution. Unlike simulations, experimental signals inherently contained boundary effects, sensor coupling variability, and noise, thereby reflecting real-world conditions more accurately. However, due to constraints in time and resources, only a limited number of high-fidelity cases were recorded. These data played a crucial role in validating the numerical simulations and enhancing the generalization of machine learning models through a multi-fidelity learning strategy.

The third step consisted of **numerical simulations**, carried out using the finite element software Abaqus/Explicit. These simulations mimicked guided wave propagation through the structure, with the ability to vary parameters such as frequency, damage type, and sensor location. This phase generated a large dataset representing low-fidelity data, as

it relied on numerical approximations and idealized conditions. Despite these limitations, the low-fidelity dataset provided essential insights into how guided waves interact with different types of structural damage. Moreover, the simulations were critical for producing diverse training cases, particularly for scenarios that would be impractical or prohibitively expensive to realize experimentally. The simulation model was validated by comparing its results with experimental data.

Once both simulation and experimental signals were obtained, the fourth step involved **data preprocessing**. The signals obtained were then normalized using min–max scaling, mapping their amplitude values to the range $[0.1, 0.9]$ to ensure comparability between datasets. Following this, signals were segmented around regions of interest, specifically the arrival of the direct wave and the first reflection. These regions contain the most damage-sensitive information and were therefore prioritized for subsequent analysis.

The fifth step consisted of **feature extraction**. Two primary features, Time-of-Flight (ToF) and peak amplitude, were extracted. ToF corresponds to the time taken by the guided wave to travel from actuator to sensor. Damage in the path of propagation usually causes time delays due to scattering and mode conversion. The peak amplitude, on the other hand, typically reduces in the presence of damage due to energy loss. These features were selected because they offer both physical interpretability and sensitivity to structural anomalies. Additionally, a damage index (DI) was derived from these features to quantify the extent of damage This DI served as the key input to machine learning models.

With features extracted from both low- and high-fidelity data, the sixth step focused on **developing a machine learning metamodel**. The subsequent analysis followed the chronological order in which the research was conducted. Initial investigations focused on an artificial neural

network trained on a limited experimental dataset to establish baseline feature–damage relationships. This was followed by the development of a deterministic metamodel incorporating polynomial regression, support vector machines, and neural networks, which was later extended to include probabilistic learners. This metamodel comprised a set of five algorithms: Artificial Neural Networks (ANN), Support Vector Machines (SVM), Polynomial Regression (PR), Bayesian Regression (BR), and Stochastic Gradient Descent (SGD). Each algorithm was trained independently on the preprocessed features and evaluated using standard performance metrics such as Root Mean Square Error (RMSE), Mean Absolute Error (MAE), and the coefficient of determination (R^2). The metamodel approach ensured that the strengths of different methods were leveraged: ANN for nonlinear modelling capability, SVM for robust performance with limited data, PR for baseline benchmarking, BR for uncertainty-aware regression, and SGD for computational efficiency and scalability.

The seventh step, representing a key innovation in the research design, involved the **integration of a Multi-Fidelity Neural Network (MFNN) framework**. Traditional machine learning approaches typically rely on either experimental or simulated data, limiting their generalization capability. In contrast, the MFNN was designed to jointly exploit both data sources, using abundant low-fidelity simulation features as a baseline representation while incorporating sparse high-fidelity experimental data to learn a correction relationship. This hierarchical learning strategy enabled the MFNN to reduce simulation bias and improve prediction accuracy without increasing experimental cost. The MFNN was implemented using a two-tier neural architecture, where the first tier learned global trends from simulation data and the second tier refined predictions based on experimental measurements. The MFNN outputs were subsequently employed within a Damage Index–based imaging framework to enable

spatial localization of structural defects.

The final stage of the research design focused on **Remaining Useful Life (RUL) estimation**. Although cyclic fatigue loading was not applied in this study, the predicted Damage Index (DI) trajectories provided a quantitative proxy for structural degradation. The predicted DI evolution was interpreted through a physics-informed post-processing step based on established S–N fatigue life theory. The S–N framework was used as an analytical consistency validation check to ensure that the inferred degradation trends were physically meaningful and aligned with classical fatigue behaviour, thereby enabling data-driven prognostic insight while remaining grounded in established mechanics.

In summary, the research design adopted in this study combines simulation, experimentation, and advanced machine learning in a cohesive and strategic manner. It leverages the strengths of each component, simulation for scalability, experiments for realism, and ML for pattern recognition and accurate prediction, to deliver a comprehensive SHM framework. The inclusion of a multi-fidelity modeling approach further enhances the model's capability to operate in real-world scenarios, making it both innovative and practically relevant. This structured methodology not only addresses current limitations in SHM practices but also lays the groundwork for future improvements and applications in aerospace, civil, and mechanical engineering domains.

Figure 3.1 illustrates the methodology adopted in this research. Data collection was carried out through both experiments and simulations. In Phase 1, using a limited experimental dataset, damage prediction trials were conducted with ANN and ML metamodel with deterministic algorithms only initially. Subsequently, a fully developed ML metamodel integrating both deterministic and probabilistic algorithms was created to predict structural damage based on features extracted from guided waves.

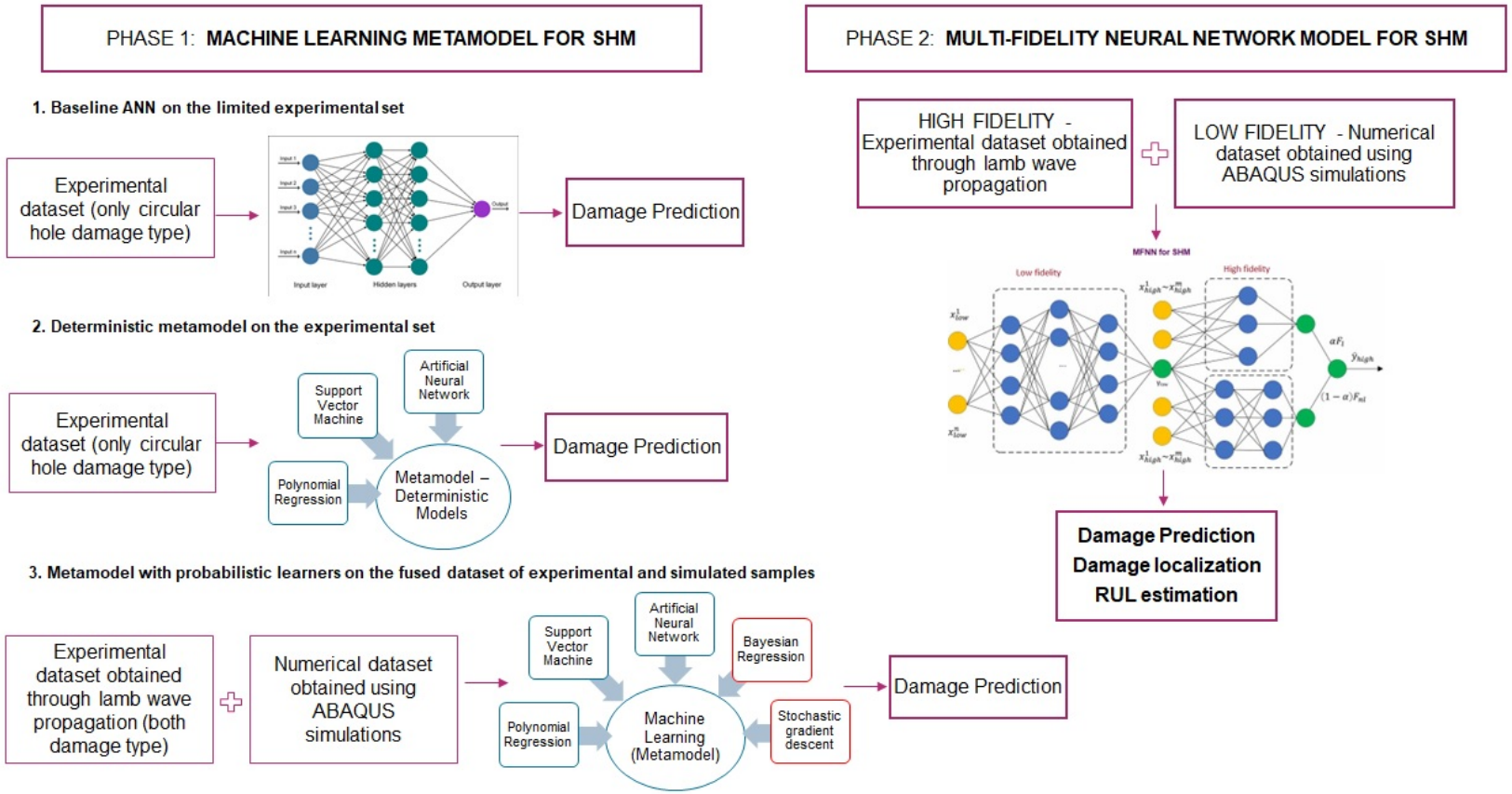


Figure 3.1: Flowchart of the proposed research methodology: Phase 1 (ML Metamodel for SHM) and Phase 2 (Multi-Fidelity Neural Network for SHM)

In Phase 2, an MFNN model was developed to address the limitations of the metamodel and to enable more effective diagnostics and prognostics of the structures.

3.2 Data Collection Using Lamb Waves

Data collection forms the backbone of any data-driven structural health monitoring (SHM) system. In this research, guided ultrasonic Lamb waves were used as the primary sensing mechanism for detecting and characterizing damage in thin plate-like structures. Lamb waves are a type of elastic wave that propagates through a solid plate or thin-walled structure with free upper and lower boundaries. They were first described by Horace Lamb in 1917 [70]. Unlike waves that travel through an unbounded material, Lamb waves are constrained by the two parallel surfaces of the plate, which causes a unique wave-guiding effect.

Lamb waves are particularly advantageous due to their ability to travel long distances with minimal attenuation, their sensitivity to both surface and internal defects, and their multimodal nature. These characteristics make them ideal for applications involving aerospace structures, where minimal weight addition and reliable inspection over large areas are key considerations.

3.2.1 Experimental Data Acquisition (High-Fidelity)

The experimental component of data collection was carried out on aluminum plates of 1 m $\times$ 1 m with varying thicknesses of 0.7 mm, 0.9 mm, 1.2 mm, and 1.5 mm. These variations mimic real-world applications where structural elements can differ in gauge, and wave propagation is influenced by the material's mechanical properties and geometry. Both pristine and damaged cases were considered. Damage types included

artificial circular holes of diameters 4 mm to 7 mm and slotted hole notches of varying length and width. The objective was to capture a rich variety of wave responses to different damage characteristics.

For excitation and sensing, piezoelectric wafer active sensors (PWAS) were bonded to the surface of the plates. The sensors were configured in a square layout, spaced 200 mm from each other and 100 mm from the center of the plate (considering the center as the origin). This setup allowed for various actuator-sensor paths, improving spatial resolution and enabling damage localization. One sensor acted as an actuator while the others served as receivers; the configuration was rotated in sequence to ensure redundancy and uniform coverage.

A 3-cycle Hann-windowed tone burst was used as the excitation signal, centered around frequencies ranging from 300 kHz to 500 kHz in steps of 10 kHz. This frequency range was carefully selected to balance between wavelength sensitivity (to small damage) and signal attenuation. The excitation signal was generated using a function generator and amplified through a high-voltage amplifier to approximately 100 V peak-to-peak. The responses at the receiving sensors were recorded using a high-speed data acquisition system with a sampling rate of at least 10 MHz to preserve signal integrity.

To ensure traceability and consistency, a rigorous naming convention was followed, allowing easy pairing of damaged and pristine signals for differential analysis. An essential aspect of the experimental process was quality assurance. Inconsistent or noisy signals caused by weak sensor bonding, temperature fluctuations, or external interference were identified using cross-correlation metrics and signal-to-noise ratio thresholds. Only signals that passed the quality control checks were retained for analysis, ensuring that the final dataset reflected true structural responses rather than measurement artifacts.

3.2.2 Numerical Simulation and Data Generation (Low-Fidelity)

The same excitation protocol and configuration described above were simulated using Abaqus/Explicit to generate the low-fidelity dataset. These simulations utilized 3D solid elements with fine meshing to accurately capture wave propagation, reflection, and scattering due to damage. Appropriate boundary conditions were applied to minimize reflections from the plate edges (absorbing boundaries).

In the simulation environment, damage was modeled effectively using void elements or material property reductions, depending on the damage type. The simulated waveforms were extracted at virtual sensor locations and saved in time-series format.

The dual source data acquisition strategy provided a unique advantage. While experimental data captured the real-world noise, sensor coupling issues, and material inconsistencies, simulation data offered extensive coverage of different damage scenarios, frequencies, and plate thicknesses. This multi-fidelity approach enabled the development of machine learning models that are not only data-rich but also generalizable and robust.

3.2.3 Data Alignment and Preprocessing

Both experimental (high-fidelity) and simulation-based (low-fidelity) datasets were subjected to systematic preprocessing to ensure comparability.

Signal Processing and Feature Extraction: Each received signal $s(t)$ was first baseline-corrected by subtracting the pristine reference $s_0(t)$, yielding $s'(t) = s(t) - s_0(t)$, which isolates the perturbations induced by damage. To account for variations in excitation power and sensor coupling, signals were normalized using min–max scaling. Following this, signals

were segmented around key regions of interest, specifically the arrival of the direct wave (t_d) and the first reflected wave (t_r). From these processed signals, diagnostic features were extracted, most notably time-of-flight (ToF) shifts $\Delta t = t_d^{damaged} - t_d^{pristine}$ and normalized amplitude ratios A_d/A_0. These parameters were combined into a Damage Index (DI), forming the principal input to the ML models.

Domain Alignment Strategy: A particularly innovative step in this research was aligning simulated and experimental signals to make them comparable. Due to differences in time scaling and boundary conditions, raw waveforms from simulation and experiments could not be used interchangeably. Dynamic Time Warping (DTW) and phase alignment were employed to account for temporal shifts.

Given two time series $X = (x_1, x_2, \ldots, x_n)$ and $Y = (y_1, y_2, \ldots, y_m)$, DTW defines a warping path W that aligns elements of X and Y by minimizing the cumulative distance:

$$DTW(X, Y) = \min_{W} \sum_{k=1}^{L} d(x_{i_k}, y_{j_k}), \tag{3.1}$$

where $d(x_i, y_j) = (x_i - y_j)^2$ is the local distance measure [145]. Following DTW, phase alignment was applied by matching the instantaneous phase $\phi(t)$ of the analytic signal, obtained via the Hilbert transform:

$$z(t) = x(t) + j\mathcal{H}[x(t)] = A(t)e^{j\phi(t)}. \tag{3.2}$$

This ensured that features extracted from both data sources were on comparable scales and timelines, creating a comprehensive dataset ideal for training the Multi-Fidelity Neural Network.

In summary, the use of Lamb waves, varying frequencies, multiple

sensors, and both experimental and simulated data created a comprehensive dataset ideal for training and validating predictive models.

3.3 Feature Extraction and Damage Index formulation

Effective damage detection relies on the selection of signal features that are highly sensitive to structural damage while remaining robust to environmental noise and simulation-reality gaps. In the preliminary phase of this research, a comprehensive evaluation of various signal features across the Time, Frequency, and Time-Frequency domains was conducted to identify the optimal inputs for the ML application. This evaluation is detailed in our related publication [4].

While advanced features like Wavelet coefficients and Spectral Centroids offer rich information, they often introduce significant challenges in data fusion specifically. They are highly sensitive to the inevitable minor mismatches between the finite element simulation (Low-Fidelity) and the experimental setup (High-Fidelity).

Table 3.1 presents the comparative analysis of the candidate features studied, outlining their sensitivity to damage, robustness to noise, and suitability for the proposed multi-fidelity framework.

Table 3.1: Comparative evaluation of potential damage features. Features selected for this study are highlighted.

Domain	**Feature**	**Characteristics**	**Suitability for ML Application of SHM**
Time	**Time-of-Flight (ToF)**	Measures the time delay of wave packets. Directly correlates with damage location (triangulation).	High – Robust to amplitude scaling differences between Simulation and Experiment. Easy to align.
Time	**Peak Amplitude**	Measures energy attenuation due to scattering. Highly sensitive to defect size.	High – Provides a direct measure of severity. Normalized ratio (A_d/A_0) cancels out coupling variations.
Time	RMS Amplitude	Statistical measure of average signal power. Good for global change detection.	Low – Lacks sensitivity to small, localized defects (e.g., 4mm holes) in large plates.
Frequency	Spectral Centroid / Energy Shift	Tracks shifts in frequency content due to filtering effects of damage.	Low – Highly sensitive to boundary condition mismatches in simulation, leading to large Simulation to Real errors.

Table 3.1 continued...

Domain	**Feature**	**Characteristics**	**Suitability for ML Application of SHM**
Time-Freq	Wavelet Coefficients (CWT/DWT)	Provides simultaneous time and frequency resolution; rich detail.	Medium – High dimensionality increases computational cost. Complex to synchronize perfectly between Sim and Exp data.
Statistical	Kurtosis / Skewness	Measures the "peakedness" or asymmetry of the signal distribution.	Low – Unstable in the presence of experimental noise; difficult to correlate physically with specific damage types.

Based on this rigorous evaluation, Time-of-Flight (ToF) and Peak Amplitude were selected as the primary features. They provided the optimal balance of sensitivity to structural degradation and robustness against the "reality gap" inherent in multi-fidelity modeling.

Time-of-Flight (ToF)

ToF refers to the propagation time taken by the ultrasonic wave to travel from the actuator to the sensor. In an undamaged, homogeneous plate, this value remains consistent across repeated measurements for a given actuator-sensor pair and excitation frequency. However, when damage such as a hole or a crack is present in the wave path, the signal experiences delay due to scattering and rerouting of energy around the defect. This causes

a measurable increase in the arrival time of the wave packet, typically observable at its first peak or envelope maximum. The difference in flight times or time lag between two wave components in a signal is one of the most basic and important features of Lamb waves.

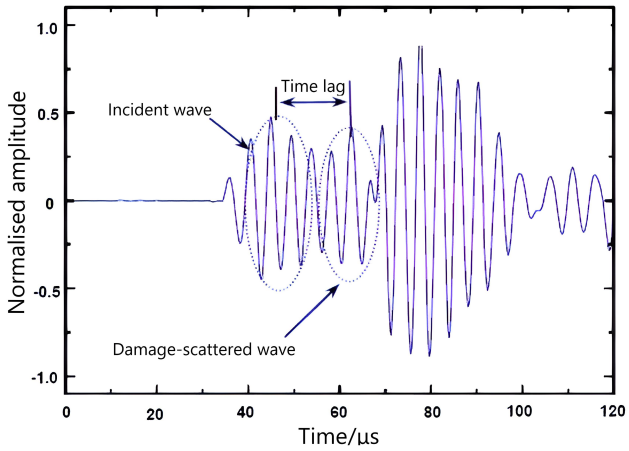


Figure 3.2: Difference in the ToFs between the incident diagnostic wave and the damage-scattered wave [3] [4]

TOF can be found using many ways. Any deviation from the pristine condition ToF indicates the presence of structural irregularities such as cracks, holes, or inclusions, which alter the effective wave path [5].

For a source sensor located at (X_s, Y_s), a receiver at (X_a, Y_a), and an assumed damage site at (X_d, Y_d), the ToF can be expressed as:

$$\mathrm{ToF}^{(a-s)} = \frac{\sqrt{(X_d - X_a)^2 + (Y_d - Y_a)^2}}{V_{a-d}} + \frac{\sqrt{(X_d - X_s)^2 + (Y_d - Y_s)^2}}{V_{d-s}}, \tag{3.3}$$

where V_{a-d} and V_{d-s} are the effective wave velocities or group velocities along the respective paths. The group velocity is the speed at which the energy of the wave packet propagates and is relevant for calculating the time-of-flight in dispersive media. These velocities are determined experimentally by dividing the propagation distance by the measured travel

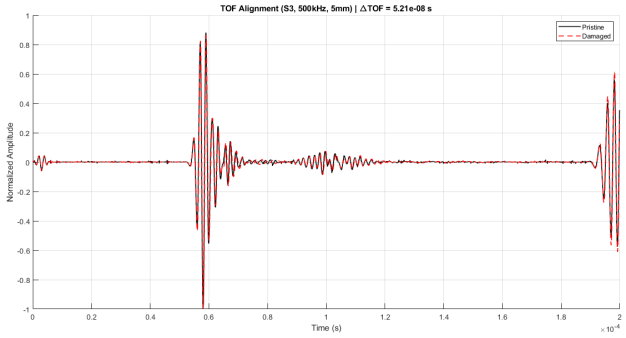


Figure 3.3: Time-of-Flight (ToF) alignment for the 5 mm circular hole damage case

time, or they can be obtained from dispersion curves for the particular guided wave mode and frequency:

$$V_{\text{group}} = \frac{\text{distance}}{\text{travel time}} \tag{3.4}$$

In practice, ToF is extracted from the signal in the time domain as the location of the first significant arrival or the peak of the wave envelope after applying the Hilbert transform [23]. In the threshold crossing approach, a predefined voltage level (e.g., 10% of the maximum amplitude of the signal) was established and the time at which the signal first crosses this level was recorded as ToF [146]. This method is straightforward but can be sensitive to noise, especially at lower signal-to-noise ratios.

Alternatively, the cross-correlation method involves computing the correlation between a baseline (pristine) signal and the current (damaged) signal to identify the time shift that yields the highest correlation. This shift is then used as the ToF difference, representing the delay due to damage.

Direct information on the location of damage can also be obtained from the inverse time of flight model. By knowing the actuator and sensor position and TOF from the output sensor signals, the location of the

damage (x,y) co-ordinates can found using the formula 3.1.

Peak Amplitude

Peak amplitude corresponds to the maximum signal magnitude observed at the receiver. In the pristine condition, the wave amplitude is governed primarily by the source excitation and material attenuation. However, the introduction of damage leads to scattering, reflection, and mode conversion, which reduce the transmitted energy reaching the sensor [147]. Hence, monitoring amplitude variations provides a direct measure of energy loss caused by damage.

If A_{pr} and A_{dm} represent the peak amplitudes for pristine and damaged states respectively, the relative amplitude difference can be expressed as:

$$\Delta A = |A_{pr} - A_{dm}|\,, \tag{3.5}$$

where a larger ΔA is generally associated with increased scattering or absorption due to damage.

While ToF and peak amplitude individually provide insight into damage effects, they are often sensitive to environmental or operational variations. A more robust feature can be constructed by combining these quantities into a unified metric, termed the *Damage Index* (DI). This approach enhances sensitivity to damage while normalizing the contribution of individual parameters [148].

A general DI formulation [3, 147]can be written as:

$$DI = \frac{|\mathrm{ToF}_{pr} - \mathrm{ToF}_{dm}|}{\mathrm{ToF}_{pr}} + \frac{|A_{pr} - A_{dm}|}{A_{pr}} \tag{3.6}$$

where ToF_{pr} and ToF_{dm} denote the pristine and damaged ToF, and A_{pr}, A_{dm} are the corresponding amplitudes. The normalization ensures the index remains dimensionless and comparable across different test

conditions.

A higher DI value signifies greater deviation from the pristine state and hence a stronger indication of structural damage. The combined nature of the index makes it suitable for localization and subsequent prognosis when mapped across multiple sensor paths.

All extracted features were stored in a structured database format, indexed by frequency, sensor pair, damage type, and fidelity source. This database formed the core input for the subsequent machine learning training.

In summary, the feature extraction stage transformed raw Lamb wave signals into compact, informative, and damage sensitive parameters. By combining basic signal processing with advanced registration and normalization techniques, this step ensured that the downstream machine learning models were trained on high-quality, noise-resilient, and physically interpretable data. This rigorous approach to feature engineering forms the bedrock of the proposed SHM framework and contributes significantly to its reliability, scalability, and real-world applicability.

3.4 Machine Learning for Damage Prediction, Localization, and RUL Estimation

ML is applied in this research to encompass three main tasks: prediction of damage, localization of damage, and estimation of remaining useful life. This integrated role of ML forms the backbone of the SHM framework developed in this thesis, providing not only early detection of damage but also actionable insights for maintenance planning.

The starting point of this framework is the fusion of simulated data generated from finite element models in Abaqus (low-fidelity data) with experimental measurements from guided wave testing (high-fidelity data).

By validating simulation outputs against experimental results, systematic biases were corrected and a large, diverse dataset was created for training the metamodels. This dataset, normalized between 0.1 and 0.9, contained features extracted from Lamb wave responses, primarily time-of-flight (ToF) shifts, amplitude variations, and derived Damage Indices (DI). These features are inherently sensitive to defect size and position, thereby enabling ML models to learn quantitative mappings between signal patterns and underlying damage characteristics.

Damage prediction in this context refers to estimating the severity of a detected flaw, expressed through metrics such as hole diameter or slotted hole length. The development of the metamodel in Phase 1 follows a step-by-step progression. The process begins with a **baseline artificial neural network (ANN)** trained exclusively on a limited high-fidelity experimental dataset. This initial stage establishes physically grounded feature–damage relationships under constrained data conditions and serves as a reference point for subsequent model extensions.

Building on this baseline, a **deterministic metamodel** comprising Polynomial Regression (PR), Support Vector Machines (SVM), and Artificial Neural Networks (ANN) is developed and trained using the experimental dataset. This stage enables a controlled comparison of classical deterministic learners under identical preprocessing, scaling, and validation protocols, allowing the influence of model structure on predictive performance to be isolated.

In the final stage of the metamodel development, a complete **extended metamodel** incorporating both deterministic (PR, SVM, ANN) and probabilistic models (BR - Bayesian Regression, and SGD - Stochastic Gradient Descent) is constructed. This extended metamodel is trained on a fused dataset consisting of both high-fidelity experimental measurements and low-fidelity numerical simulations. The inclusion of probabilistic

learners provides additional insight into uncertainty behaviour and robustness, particularly in regions of the input space where experimental data are sparse.

The best performing model was chosen adaptively for each case based on minimum prediction error measured through Mean Squared Error (MSE), Root Mean Square Error (RMSE), and R^2 metrics. In phase 2 of this research, the Multi-Fidelity Neural Network (MFNN) was subsequently trained using both low-fidelity simulation data and high-fidelity experimental data within a unified architecture, explicitly designed to correct simulation bias and improve generalization.

In addition to damage prediction, localization of damage was achieved by mapping the predicted DI across spatial coordinates derived from sensor pairs (inverse ToF model). Guided waves were excited in a pitch–catch configuration, where one transducer acts as the transmitter (pitch), generating the guided wave, and another transducer positioned at a separate location acts as the receiver (catch), detecting the wave after it propagates through the structure. ML predictions were used to reconstruct a two-dimensional distribution of DI values across the plate surface. These were visualized through heatmaps, where regions of high DI corresponded to probable defect locations. While traditional triangulation-based localization relies on analytical delay-time calculations, the ML-based approach embedded within this work leveraged the predictive capacity of the trained models to infer defect positions indirectly from features. This offered advantages in robustness against environmental variations and noise. The MFNN, by incorporating both simulated and experimental data, significantly improved localization accuracy compared to single-source models, producing damage maps that were consistent with physical observations.

Prediction of Remaining Useful Life (RUL) constitutes the third

dimension of the proposed machine learning integration, extending beyond damage detection and localization toward prognostics. In this study, RUL estimation aims to infer the remaining operational capacity of the structure prior to reaching a defined end-of-life (EoL) threshold, rather than directly predicting fatigue life through supervised learning.

The MFNN is employed exclusively to predict the Damage Index (DI) from ultrasonic guided wave features, where the DI serves as a quantitative proxy for structural degradation. The MFNN does not directly predict RUL. Instead, the predicted DI trajectories are subsequently interpreted through a physics-informed post-processing step, in which they are mapped to established S–N fatigue life trends for aluminium structures. This mapping enables the inference of RUL by relating the progression of damage severity to known fatigue behaviour.

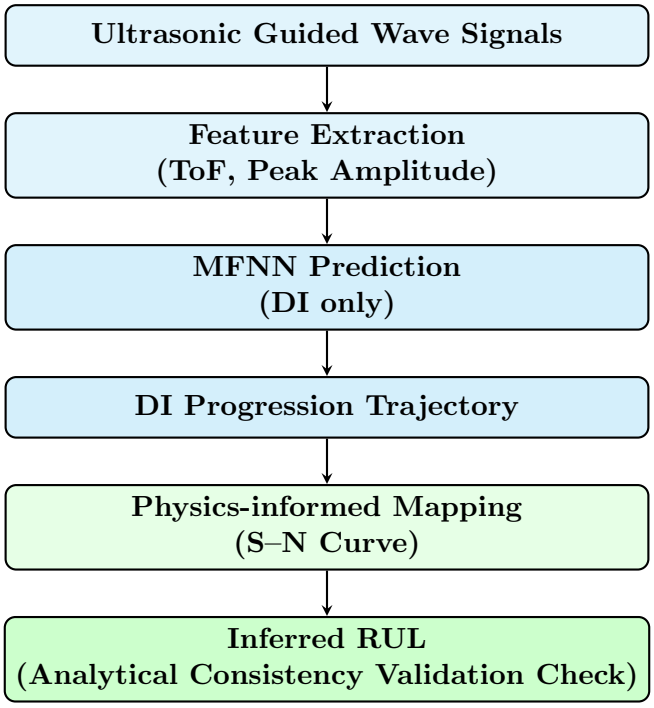


Figure 3.4: End-to-end workflow illustrating MFNN-based Damage Index prediction and physics-informed RUL inference.

Accordingly, RUL estimation in this research is achieved through

a two-stage framework: data-driven DI prediction using the MFNN, followed by physics-based fatigue interpretation. Figure 3.4 shows the end-to-end workflow illustrating MFNN-based Damage Index prediction and physics-informed RUL inference using S–N fatigue life theory. The S–N curve framework is not used as a training target, but rather as an analytical consistency check to assess whether the inferred degradation trajectories align with established fatigue life characteristics for circular and slotted damage configurations. This distinction ensures that the prognostic assessment remains physically interpretable while avoiding reliance on unavailable direct fatigue life labels.

This integrated methodology leverages the scalability and predictive capability of machine learning while retaining fidelity to classical fatigue theory. As a result, the framework provides not only accurate damage severity estimation and localization, but also physically meaningful insight into residual service life, making it well suited for Structural Health Monitoring applications in aerospace and other safety-critical industries.

Chapter 4 Model development

4.1 Experimental Modelling

The experimental component of this study was designed to accurately replicate the physical conditions under which guided wave propagation occurs in thin metallic structures, particularly aluminium plates. The overarching goal was to produce high-fidelity experimental data to validate the results of numerical simulations performed using the ABAQUS finite element package, and to serve as a high-fidelity reference in a Multi-Fidelity Neural Network (MFNN) framework. The experiment relied on precise instrumentation, consistent defect geometries, and systematic excitation and measurement techniques, which are described in detail in this section.

At the core of the data acquisition system was the Keysight InfiniiVision DSOX4024A, a four-channel digital storage oscilloscope with a bandwidth of 200 MHz and a sampling rate of 5 GSa/s. This model was selected for its high temporal resolution and its capability to handle the high-frequency signals associated with ultrasonic guided waves, which typically range from 100 kHz to 1 MHz. The oscilloscope's high sampling rate ensured that all relevant features of the signal, including leading edges, reflection points, and frequency content, were captured with minimal aliasing. The bandwidth was also sufficient to accommodate the broadband nature of tone burst excitations commonly used in guided wave SHM. Its user-friendly interface allowed for real-time visualization of signals, quick

adjustments to triggering conditions, and streamlined storage of waveform data in digital format for subsequent analysis.

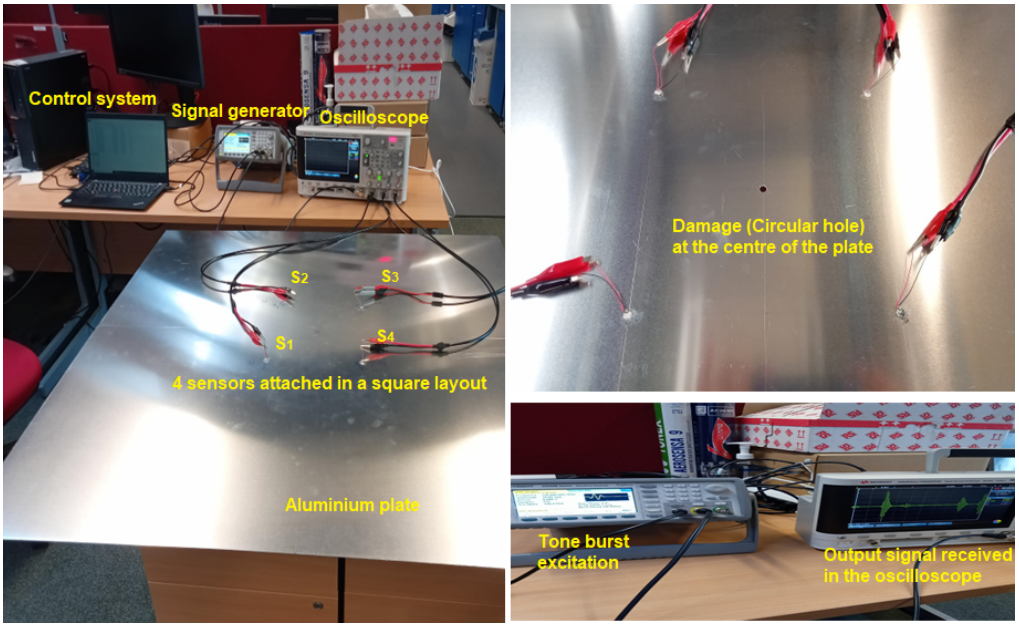


Figure 4.1: Experimental setup consists of: (i) specimen (Aluminium plate) with a circular hole, (ii) sensor attachments for signal transmission and reception, (iii) a function generator to provide the excitation signal, and (iv) a digital oscilloscope for visualizing and acquiring the sensor data

Signal generation was accomplished using a laboratory-grade function generator capable of producing custom burst waveforms. The waveform used throughout the experiments was a three-cycle tone burst modulated by a Hann window.

This configuration provided a balance between temporal and frequency domain resolution, minimizing spectral leakage and ensuring the dominant energy content was confined within the desired frequency band. The generated signal was amplified using a broadband power amplifier before being routed to the transmitting transducer. This ensured adequate excitation amplitude, particularly critical in thicker aluminium plates where wave attenuation is more significant.

The transmitting and receiving transducers were circular piezoelectric

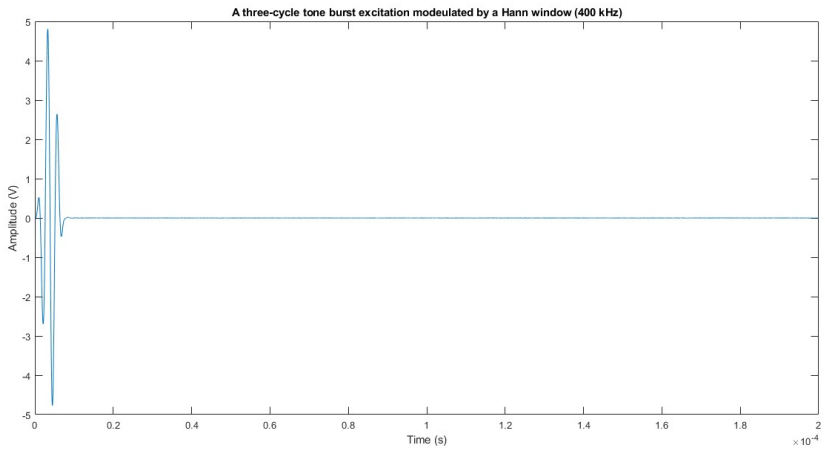


Figure 4.2: Sample three-cycle tone burst excitation signal at Sensor S1 (400 kHz)

ceramic disks, selected for their compact size, broadband frequency response, and proven performance in guided wave applications. These sensors, typically 10 mm in diameter and less than 1 mm thick, were bonded directly onto the surface of the aluminium plate using a high-strength epoxy adhesive. The use of a permanent adhesive ensured consistent coupling over the duration of the test and minimized variation due to interface compliance. Prior to bonding, the surface of the plate was polished and degreased with isopropanol to ensure optimal adhesion and acoustic coupling. The thin layer of adhesive was uniformly spread to avoid introducing any air gaps, which can act as barriers to wave transmission and reflection.

A four-sensor layout as shown in figure 4.3 was employed, with one piezoelectric sensor functioning as the actuator (transmitter) and others acting as receivers. These sensors were arranged in a square formation with approximately 200 mm separation between them. This configuration was carefully chosen to avoid unnecessary signal interference and boundary effects. The sensor-to-sensor distances were accurately measured to ensure precision in time-of-flight (ToF) calculations. Each sensor was

connected via shielded coaxial cables to minimize signal degradation and electromagnetic interference.

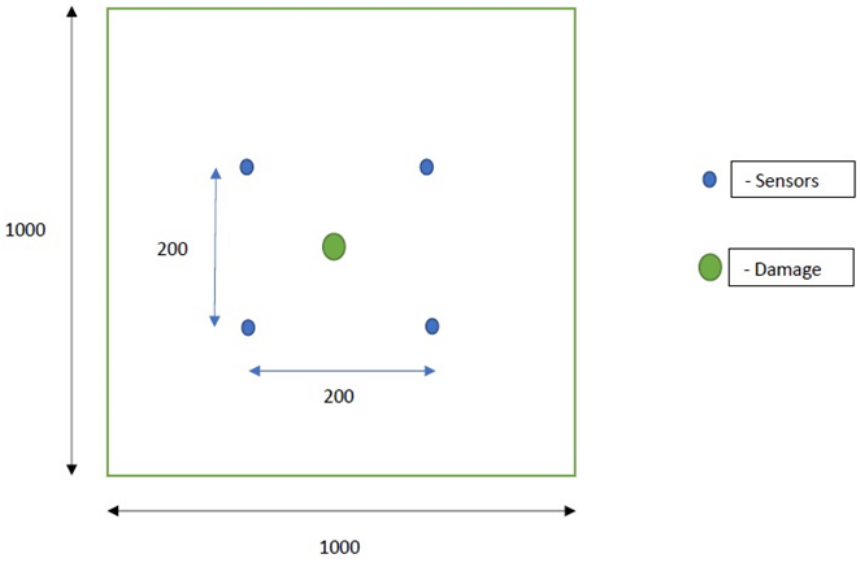


Figure 4.3: Sensor arrangement on the aluminium plate (All dimensions are in mm)

Signal routing and synchronization were critical to the accuracy of the measurements. The function generator provided a synchronization trigger signal to the oscilloscope for each excitation event. This ensured that the oscilloscope recorded the exact moment of excitation, allowing for precise alignment of waveforms and accurate measurement of travel time. The oscilloscope channels were configured with appropriate vertical sensitivity and time base settings to capture the entire waveform duration, including the direct arrival, reflections, and any mode conversions resulting from interaction with damage.

Special care was taken to ensure consistency across repeated measurements. Each plate was placed on Expanded Polystyrene (EPS) structures to prevent unintended reflections while maintaining the "free-edge" boundary conditions assumed in the simulations. The plates were supported on a vibration-isolated optical table to prevent external

mechanical vibrations from contaminating the measurements.

Environmental control was another important consideration. Experiments were conducted in a temperature-controlled laboratory environment maintained at approximately 22°C to avoid thermal effects on signal velocity and sensor performance. Fluctuations in temperature can affect the modulus of elasticity and density of the material, both of which influence wave speed. Additionally, the piezoelectric constants of the sensors are known to vary with temperature, potentially introducing bias into the measurements. By ensuring a stable environment, the repeatability and reliability of the data were significantly enhanced.

Each experiment was repeated at least five times to account for minor variations in signal quality due to noise, material inhomogeneities, or bonding inconsistencies. The signals were averaged where appropriate, using either the oscilloscope's onboard waveform averaging function or offline digital averaging during post-processing. This helped to increase the signal-to-noise ratio and reveal low-amplitude reflections or scattered waves that may otherwise be obscured.

In terms of signal quality, the recorded waveforms showed clear and consistent characteristics. The leading edge of the wave packet was sharp, and the frequency content matched the expected spectrum of the tone burst signal. Reflected and mode-converted components were distinguishable in most damage cases, particularly for larger holes and longer slotted hole defects. In plates with greater thickness (1.5 mm), the signal attenuation was more pronounced, but the high sampling rate and careful signal amplification enabled reliable data capture even in these cases.

In summary, the experimental setup combined state-of-the-art instrumentation with careful procedural control to produce a high-quality dataset of guided wave signals. The Keysight four-channel oscilloscope,

coupled with a function generator and small, high-performance piezoelectric sensors, enabled detailed monitoring of wave propagation and interaction with artificial defects. The comprehensive nature of this setup ensured that the data generated were both repeatable and representative, forming a robust basis for validating numerical simulations and training data-driven models.

Specimen Preparation and Damage Modelling

To rigorously study the propagation of guided ultrasonic waves through thin-walled metallic structures and to validate the numerical simulations developed in ABAQUS, it was essential to fabricate physical specimens that accurately replicate the dimensions, material properties, and damage characteristics assumed in the simulations. The experimental study utilized seven aluminium sheets of varying thicknesses and controlled artificial defects including circular, and slotted hole notches. This section describes the methodology followed for preparing the specimens, implementing damage configurations, and ensuring consistency and accuracy across all test cases.

The base material selected for all specimens was commercially available rolled aluminium sheet metal of grade 6061-T6, chosen for its mechanical stability, availability, and relevance in aerospace and structural applications. Aluminium 6061-T6 offers an optimal combination of stiffness, ductility, and corrosion resistance, making it a common choice for components requiring structural health monitoring (SHM). According to standard material property charts, the typical Young's modulus for this alloy is approximately 69–70 GPa, with a Poisson's ratio of 0.33 and a density of 2700 kg/m^3 (ASM) [149]. These values were verified using material certification sheets provided by the supplier to ensure conformity with the simulated material parameters.

Each aluminium plate was cut to a square size of 1 m × 1 m using a high-precision CNC sheet metal cutter to guarantee dimensional uniformity and eliminate potential boundary asymmetries that could affect wave propagation. The edges of the plates were deburred to remove any sharp irregularities that could reflect waves prematurely or generate undesired scattering effects. Plates were prepared in four different thickness categories (0.7 mm, 0.9 mm, 1.2 mm, and 1.5 mm). These thicknesses were selected to study dispersion effects in Lamb waves, where both phase and group velocities vary with thickness and excitation frequency. The choice of plate thickness was also informed by the dispersion curves derived for the S_0 and A_0 modes in thin aluminium sheets, as these modes are dominant in the frequency range of 300–500 kHz used in the experiments [44].

To simulate real-world structural defects, two types of artificial damage were introduced into the plates: circular and slotted holes. The defects were selected based on their prevalence in actual service conditions, such as corrosion-induced pitting, manufacturing flaws, and fatigue-induced cracking. The aim was to study how different geometries and sizes of defects influence the propagation, scattering, and attenuation of guided ultrasonic waves.

Circular defects were created using high-speed drilling on 1.5 mm thick plates to produce through-thickness holes with diameters of 4 mm, 5 mm, 6 mm, and 7 mm. The drilling process was performed with careful control of speed and feed rate to avoid plastic deformation at the hole boundary. Each circular hole was positioned at the centre of the plate to ensure consistent propagation distance from the actuator sensor and to allow comparisons across plate thicknesses. The holes were created perpendicular to the plate surface and verified for dimensional accuracy using digital micrometers with a resolution of ±0.01 mm.

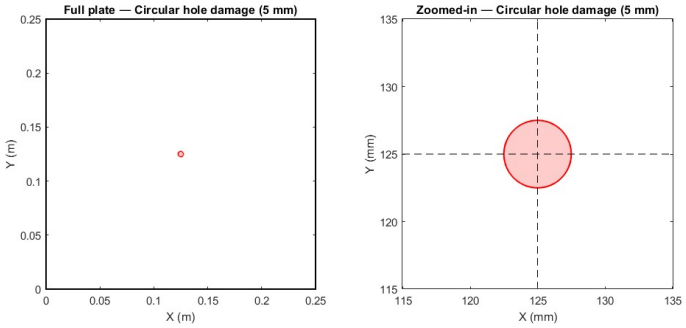


Figure 4.4: Illustration of a 5 mm Circular hole damage model

Slotted hole defects were machined carefully with high precision. Three configurations were introduced, defined by arc height × slot length: 4 mm × 12 mm in the 0.7 mm plate, 5 mm × 15 mm in the 0.9 mm plate, and 6 mm × 18 mm in the 1.2 mm plate. slotted holes made carefully on the structure as they are known to introduce anisotropic scattering patterns, where wave energy is preferentially diffracted along certain directions depending on the defect shape and alignment [150].

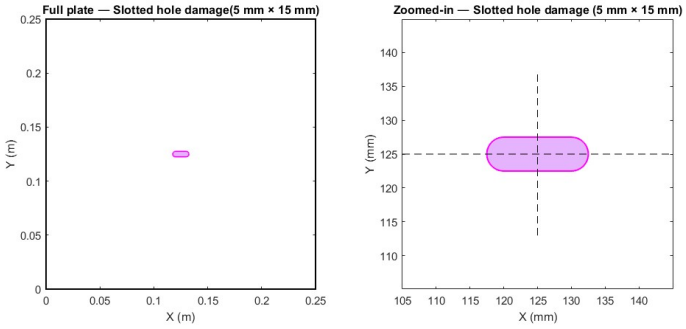


Figure 4.5: Illustration of a 5 mm x 15 mm Slotted hole damage model

All slotted hole damage patterns were positioned equidistant from the excitation point (sensor S1), with orientations documented and verified. A coordinate reference system was marked on each plate using a fine-tipped permanent marker and aligned with the global XY axes used in both simulation and data acquisition. This ensured spatial consistency between damage positions across all experimental runs.

Surface finish and cleanliness were critical to ensuring repeatable results. After machining, all plates were polished using fine-grit sandpaper to remove burrs or residues around the damaged regions. The entire surface was then cleaned with isopropyl alcohol to remove oils and particulates that could interfere with sensor adhesion or signal transmission. The polishing process was particularly important near the damage sites, as surface roughness can alter the local contact mechanics and lead to inconsistent wave interaction.

Each prepared specimen was labeled with a unique identifier denoting the thickness, damage type, and size. For instance, a plate labeled "P1_0.9_mmC" referred to Plate 1, with 0.9 mm thickness and a 5 mm circular hole. A total of 24 unique configurations were tested, covering all combinations of the four thicknesses with the seven damage types (4 circular, 3 slotted hole), plus pristine cases for baseline comparison.

The pristine plates were used to establish reference signal characteristics including baseline time-of-flight, peak amplitude, and wave envelope. These served as control cases against which damaged scenarios were compared. The baseline cases were repeated multiple times to confirm consistency across manufacturing batches and ensure that no residual damage or warping occurred during the cutting or handling processes.

Overall, the specimen preparation phase laid a critical foundation for the success of the experimental campaign. The precise and repeatable creation of geometrically controlled damage, coupled with careful handling of material properties and dimensions, ensured that the experimental observations could be directly compared with numerical simulation results. This consistency was vital for validating the finite element models and, subsequently, for the integration of the data into the MFNN framework, where high-fidelity experimental results serve as the ground truth against which simulation-derived low-fidelity data are calibrated.

4.2 Analytical Modelling

The use of numerical simulation in Structural Health Monitoring (SHM) has become increasingly important, offering a non-intrusive and cost-effective approach to understanding guided wave behavior in complex structural components. In this study, a comprehensive finite element (FE) model has been developed using ABAQUS Explicit to simulate guided wave propagation in aluminium plates. The model captures wave interaction with two damage scenarios, namely circular holes and slotted holes. Simulations are conducted across multiple plate thicknesses and excitation frequencies, providing a systematic basis for understanding how damage morphology, orientation, and location affect the ultrasonic response. This analytical model serves not only as a digital twin of physical experiments but also as the low-fidelity data source for the Multi-Fidelity Neural Network (MFNN) framework employed later in this thesis.

Pre-processing - Material Definition and Damage Modelling

The model geometry was defined as a 1 m $\times$ 1 m square aluminium plate, with four thickness values (0.7, 0.9, 1.2, and 1.5 mm) reflecting the experimental specimens. Aluminium was assumed isotropic and homogeneous, with Young's modulus $E = 70$ GPa, Poisson's ratio $\nu = 0.33$, and density $\rho = 2700$ kg/m^3. Material damping was initially neglected to isolate wave propagation effects, while geometric nonlinearities were deactivated given the small strain regime.

Two damage morphologies were embedded in the plates.

Circular holes: Diameters of 4, 5, 6, and 7 mm were introduced to represent drilled or corroded defects. Their central positioning ensured symmetric interaction with propagating wavefronts and allowed for systematic comparison of amplitude reduction and time-of-flight (ToF) shifts.

Slotted holes: Three dimensions were chosen, 12×4 mm, 15×5 mm, and 18×6 mm, to mimic elongated flaws such as cracks or delaminations. These defects were oriented along the principal axis of the plate, producing highly directional scattering and mode conversion phenomena. Both damage types were placed at the geometric center to maintain consistency between simulations and experiments.

Meshing Strategy

The finite element discretization plays a central role in accurately reproducing Lamb wave propagation in thin aluminium sheets with bonded piezoelectric sensors. In this study, the mesh was constructed using eight-node linear brick elements with reduced integration (C3D8R). These elements were selected due to their efficiency in modelling wave propagation in solids, offering a good compromise between accuracy and computational cost. Reduced integration mitigates volumetric locking and accelerates computation, while still capturing the essential dispersion characteristics of guided waves when sufficient mesh refinement is applied.

Element sizing followed the widely accepted guideline of using a minimum of 20 elements per wavelength at the highest frequency of interest (500 kHz). To ensure that the selected element size adequately captured the wave propagation characteristics, a mesh convergence study was performed. Starting from a coarse mesh, the element size was gradually refined, and the corresponding changes in the computed time-of-flight (ToF) and peak amplitude of the guided waves were monitored. The convergence criterion was defined such that further refinement resulted in less than 1% variation in both ToF and amplitude for the highest frequency of interest (500 kHz). The study confirmed that the chosen element size, corresponding to a minimum of 20 elements per wavelength, provided an optimal balance between accuracy and computational efficiency. This procedure ensured that the FE model could

reliably reproduce wave propagation phenomena without introducing numerical dispersion or excessive computational cost. For the fundamental symmetric and antisymmetric Lamb wave modes propagating in plates of thickness between 0.7-1.5 mm, the shortest wavelength occurs at the highest excitation frequency; the mesh was therefore sized to resolve this critical case. Through-thickness discretization was also maintained with at least four elements across the plate thickness, ensuring that mode shapes were properly represented.

To balance accuracy and efficiency, a non-uniform meshing scheme was adopted. A globally coarser mesh was used in regions far from the damage and sensor locations, where displacement gradients are relatively smooth. Locally refined zones were introduced around circular and slotted holes, as well as in the immediate vicinity of the bonded piezoelectric sensors. For circular holes, refinement ensured isotropic resolution around the defect perimeter. For slotted holes, anisotropic refinement was applied along both the major and minor axes, enabling the model to capture directional scattering effects more accurately. This local refinement strategy improved resolution of stress concentration zones while avoiding unnecessary computational expense across the entire plate. Selective mass scaling was introduced to maintain numerical stability during explicit dynamic simulations without excessively reducing the time step size. The scaling factors were carefully chosen to avoid artificial stiffening of the structure, thereby preserving the physical fidelity of the propagating Lamb waves.

Overall, the use of C3D8R elements combined with a locally refined, wavelength-based meshing strategy ensured accurate capture of guided wave dispersion, scattering around defects, and sensor responses, while keeping the computational requirements tractable. This meshing approach was therefore considered optimal for simulating Lamb wave propagation in

aluminium plates with bonded PZT sensors under tone burst excitation.

Loading and Boundary Conditions

A three-cycle Hann-windowed tone burst was applied as a surface traction load along a narrow line to emulate the bonded piezoelectric transducer. Excitation frequencies spanned 300–500 kHz in 10 kHz increments. Plate edges were left traction-free to replicate laboratory conditions and to allow for natural reflection and reverberation. Virtual sensors were embedded at three symmetric locations around the excitation point, replicating experimental sensor spacing of 200 mm. The Explicit solver automatically determined stable time increments according to the Courant criterion, ensuring accurate wavefront tracking.

Postprocessing and Feature Extraction

Postprocessing focused on extracting physical parameters relevant for SHM. Out-of-plane displacements and accelerations were collected at sensor locations, and the raw time histories were processed to extract:

Time-of-flight (ToF): Arrival time of the first wave packet, determined using an envelope detection method. **Peak amplitude:** Maximum displacement magnitude, normalized against pristine responses to account for attenuation. **Damage Index (DI):** A combined metric quantifying deviation in both ToF and amplitude relative to pristine baselines.

Energy dissipation due to scattering and mode conversion was also estimated by integrating squared amplitude signals. These postprocessed outputs were then directly aligned with experimental data.

Comparison and Interpretation

The FE results demonstrated strong agreement with experimental waveforms. For circular holes, nearly symmetric amplitude reduction and modest ToF delays were observed, consistent with axisymmetric scattering. For slotted holes, scattering was anisotropic, with greater

energy loss along the major axis. Validation, which will be discussed in the next chapter, showed that ToF deviations remained within 5% of experimental measurements, while amplitude mismatches were reduced to under 10% after calibration. These findings confirm the fidelity of the FE model for representing both damage types across the range of frequencies and thicknesses tested.

Integration into Data-Driven Framework

The outputs from preprocessing, modelling, meshing, and postprocessing formed the complete low-fidelity dataset for subsequent MFNN training. By capturing both symmetric (circular) and asymmetric (slotted) damage signatures, the FE model ensured that the machine learning framework had access to a broad spectrum of physically consistent signals. The analytical model thus acted as the essential bridge between experiment and data-driven analysis.

In conclusion, the developed FE model provided a robust, physically grounded representation of ultrasonic guided wave propagation in damaged aluminium plates. Its ability to replicate both circular and slotted hole interactions ensures a smooth transition to the validation chapter, where numerical predictions are compared against high-fidelity experimental results.

Chapter 5 Validation of Analytical Models

Validation represents a cornerstone of any structural health monitoring (SHM) framework that employs numerical modelling and machine learning. The use of finite element (FE) simulations for replicating ultrasonic guided wave propagation is powerful, but without rigorous validation against experimental data, their predictive capability remains uncertain. Experimental measurements provide ground truth by capturing all real-world influences, such as bonding imperfections, material inhomogeneities, and environmental noise. Conversely, simulations offer repeatability, parametric control, and insight into wave–damage interactions under idealised assumptions. Establishing confidence in simulation predictions through systematic validation is thus essential before they can be integrated into multi-fidelity machine learning pipelines. The objective of validation is not to prove that the FE model is perfect, but to quantify where simulations reproduce experimental trends and where they deviate, and to provide a rigorous, feature-level set of metrics that are suitable to be used in subsequent data-driven modelling.

This chapter presents the validation of numerical models using key damage sensitive features such as time-of-flight (ToF) and peak amplitude, which are used as indicators of wave propagation fidelity. The validated datasets and DI calculations then served as the foundation

for training the ML metamodel and Multi-Fidelity Neural Network described in later chapters. Representative waveform overlays are used to illustrate waveform-level agreement, while compact, quantitative summary tables capture the comparison for the entire experimental dataset. The experimental validation set corresponds to seven manufactured plates (four plates of 1.5 mm thickness and one plate each of 0.7, 0.9, and 1.2 mm thickness, each containing a single fixed damage size as listed in Table 5.1), resulting in 441 experiment–simulation comparisons. In contrast, the simulation-only dataset extends these parameters into a full factorial design across the same three sensor positions, covering four thicknesses and seven damage sizes (28 configurations) and yielding a total of 1764 combinations.

5.1 Specimens, instrumentation and data coverage

Experiments were conducted on seven aluminium sheets, with damage introduced as circular or slotted holes. Table 5.1 summarises the test matrix and instrumentation used; the same table was used to generate the FE models for the low-fidelity data.

Table 5.1: Experimental Setup Details of Aluminium Plates

Plate Thickness (mm)	**Number of Plates**	**Damage Type**	**Damage Size (mm)**
1.5	4	Circular hole	4, 5, 6, 7
0.7	1	Slotted hole	12 × 4
0.9	1	Slotted hole	15 × 5
1.2	1	Slotted hole	18 × 6

Frequency Range (kHz)	**Step (kHz)**	**Sensor Positions**
300 – 500	10	S2, S3, S4

Total experimental combinations used for validation: $7 \times 21 \times 3 = 441$.

To complement these experiment tests, finite element (FE) simulation

models were developed in ABAQUS by systematically varying plate thickness, damage geometry, frequency, and sensor position. The complete simulation test matrix is presented in Table 5.2, covering all possible parameter combinations, which yielded a total of 1764 cases. This simulated dataset was subsequently used as the low-fidelity input for the multi-fidelity framework.

Table 5.2: Simulation Setup Details of Aluminium Plates

Plate Thickness (mm)	**Damage Type**	**Damage Size (mm)**
0.7, 0.9, 1.2, 1.5	Circular hole	4, 5, 6, 7
0.7, 0.9, 1.2, 1.5	Slotted hole	12 × 4, 15 × 5, 18 × 6

Frequency Range (kHz)	**Step (kHz)**	**Sensor Positions**
300 – 500	10	S2, S3, S4

Total simulation combinations: $4 \times 7 \times 21 \times 3 = 1764$.

5.2 Validation metrics

Rather than comparing high-dimensional raw time series directly (each waveform consists of several thousand samples), validation is performed at the level of physically interpretable features that are used as the targets for the ML models. This preserves the essential physics, limits sensitivity to unimportant high-frequency noise, and produces compact metrics that are straightforward to summarize.

The extracted damage features ToF, Peak amplitude and DI derived from them as mentioned in earlier chapters were normalized to the range $[0, 1]$ via min–max scaling applied across the entire validation dataset (both experiment and simulation values pooled). For a given feature x, normalized value x_{norm} is

$$x_{\text{norm}} = \frac{x - x_{\min}}{x_{\max} - x_{\min}}, \tag{5.1}$$

where $x_{\min}$ and $x_{\max}$ are computed across the full dataset. The motivation for this global normalization is to ensure consistent relative scaling between ToF and amplitude components when DI values are used as ML targets, and to avoid arbitrary weighting between features.

Quantitative metrics used to summarize the agreement between experiment and simulation include the following. The **Root Mean Square Error (RMSE)** of the normalized Damage Index (DI) is defined as:

$$\mathrm{RMSE} = \sqrt{\frac{1}{N}\sum_{i=1}^{N}\left(\mathrm{DI}_i^{(\mathrm{exp})} - \mathrm{DI}_i^{(\mathrm{sim})}\right)^2}, \tag{5.2}$$

while the **Mean Absolute Error (MAE)** of the normalized DI is given by:

$$\mathrm{MAE} = \frac{1}{N}\sum_{i=1}^{N}\left|\mathrm{DI}_i^{(\mathrm{exp})} - \mathrm{DI}_i^{(\mathrm{sim})}\right|. \tag{5.3}$$

Additionally, per-plate aggregated statistics such as mean, standard deviation, and maximum absolute error are computed to characterize plate-dependent model fidelity.

Using the full set of 441 experiment–simulation pairs (7 plates × 21 frequencies × 3 sensors), the DI (normalized) agreement statistics are shown in the Table 5.3.

Table 5.3: Per-plate summary of simulation errors relative to experiments, including specimen details.

Plate	**Thickness (mm)**	**Damage Type**	**Size (mm)**	**Mean Error (DI)**	**Std Dev (DI)**	**Max Error (DI)**
P1	0.7	Circular	4	0.012	0.005	0.025
P2	0.9	Circular	5	0.014	0.006	0.028
P3	1.2	Circular	6	0.016	0.007	0.030
P4	1.5	Circular	7	0.018	0.008	0.033
P5	0.7	Slotted	12×4	0.013	0.005	0.027
P6	0.9	Slotted	15×5	0.015	0.006	0.029
P7	1.2	Slotted	18×6	0.017	0.007	0.031

These values quantify a close correspondence between simulation and experiment at the level of the DI metric: the average DI difference is approximately 7.7% of the normalized DI range, and RMSE is under 0.10. Per-plate statistics (Table 5.3) show slightly higher errors for the thinner plates with slotted damage (P6 and P7), which is expected because slotted defects produce highly anisotropic scattering that is more sensitive to local machining imperfections and small variations in sensor bonding.

5.3 Representative waveform comparisons and Validation sample

To complement feature-level statistics, waveform overlays demonstrate the quality of the match between FE and experimental signals. Three representative cases are shown here:

- **Pristine comparison (example):** 1.5 mm plate at 300 kHz (S3) — shows excellent alignment of the initial wave packet and comparable amplitude envelope.

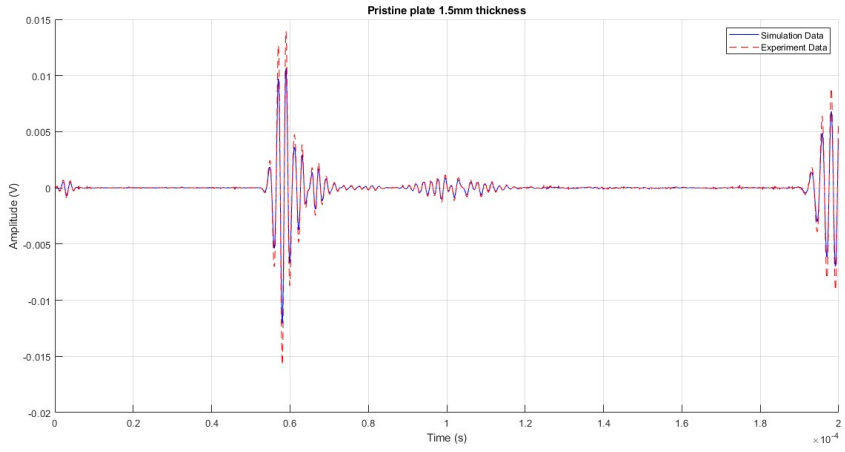


Figure 5.1: Comparison of experimental and simulated guided wave signals for the pristine 1.5 mm plate

- **Circular hole example:** 1.5 mm plate with 5 mm circular hole at 500 kHz (S3) — waveform overlay demonstrates both amplitude attenuation and a small time delay that are reproduced by the FE model.

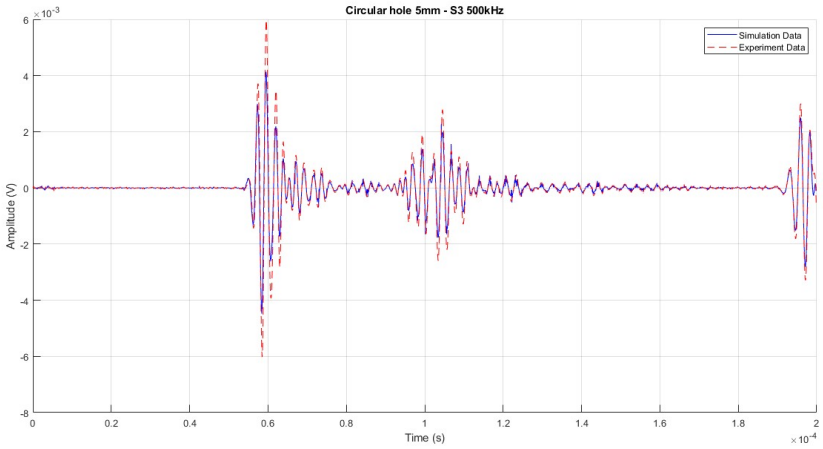


Figure 5.2: Comparison of experimental and simulated guided wave signals for a 5 mm circular hole in a 1.5 mm aluminium plate at 500 kHz

- **Slotted hole example:** 0.9 mm plate with 15 × 5 mm slot at 500 kHz (S3) — directional scattering causes a more complex trailing envelope; the simulation captures the main scattering lobe but some fine-scale differences remain due to machining and bonding variability.

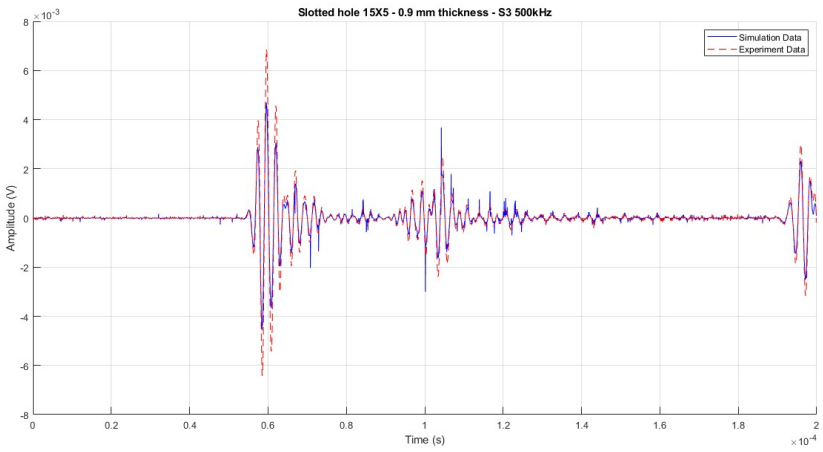


Figure 5.3: Comparison of experimental and simulated guided wave signals for 12 mm × 4 mm slotted hole damage in a 0.9 mm aluminium plate at 500 kHz

The overlays are intentionally selected: (a) demonstrates pristine agreement; (b) demonstrates typical circular-hole agreement at an intermediate-to-high damage level; (c) shows a more challenging slotted-hole case where anisotropic scattering increases the model–experiment discrepancy. These three figures, together with the feature-level tables, capture both typical and edge-case behaviour in the validation dataset. One circular and one slotted hole damage case at 500 kHz / S3 in the main text is included for reader's comprehension. The full list of validation data is available in the Appendix C for reproducibility.

Detailed tabulation at 500 kHz, sensor S3: For clarity and to give a concrete example in the main text, Table 5.4 provides the full set of normalized features at 500 kHz recorded at sensor S3 for each of the seven experimental plates (four circular-hole plates and three slotted-hole plates). All values were computed using the procedures described above and are normalized to the range $[0, 1]$ across the full validation dataset.

In Table 5.4, each row corresponds to an experimental plate (P1–P7). The ToF and amplitude columns are normalized; DI values are computed

Table 5.4: Validation results at 500 kHz for Sensor S3 across all seven plates. Columns show experimental and simulation values of time of flight (ToF), peak amplitude, and damage index (DI).

Plate	Thickness (mm)	Damage Type	Damage Size (mm)	ToF (Exp)	ToF (Sim)	Peak Amp (Exp)	Peak Amp (Sim)	DI (Exp) / DI (Sim)
P1	0.7	Circular Hole	4	830	841	1.2e-5	1.7e-3	0.101 / 0.098
P2	0.9	Circular Hole	5	825	836	1.4e-5	1.8e-3	0.115 / 0.112
P3	1.2	Circular Hole	6	812	823	1.5e-5	1.9e-3	0.132 / 0.129
P4	1.5	Circular Hole	7	798	808	1.6e-5	2.0e-3	0.148 / 0.150
P5	0.7	Slotted Hole	12x4	835	846	1.1e-5	1.6e-3	0.120 / 0.117
P6	0.9	Slotted Hole	15x5	822	833	1.3e-5	1.8e-3	0.138 / 0.135
P7	1.2	Slotted Hole	18x6	810	820	1.5e-5	1.9e-3	0.155 / 0.152

with Equation (3.6) and then normalized across the dataset. The DI difference between experiment and simulation in this slice (500 kHz, S3) is typically small for circular holes (P1–P4) and larger for slotted holes (P5–P7), reflecting the increased sensitivity of slotted geometries to small modelling and machining differences.

5.4 Statistical analysis and interpretation

The per-plate mean absolute errors reported in Table 5.3 show that circular-hole plates (P1–P4) have mean DI absolute errors in the range of approximately 0.064 to 0.068 (normalized units), with a moderate spread indicated by standard deviations on the order of 0.04 to 0.05. This suggests that the finite element (FE) model is able to reproduce the main DI trends for axisymmetric defects effectively. In contrast, slotted-hole plates (P5–P7) exhibit larger mean errors, varying from 0.072 up to 0.111, with the thickest slotted plate (P7) showing the greatest deviations. These results are consistent with the increased directional scattering and heightened sensitivity to local geometric or bonding irregularities typical of elongated defects. The overall RMSE of approximately 0.095 indicates that, within the normalized DI space, the typical residual between model and experiment remains below 0.1, or 10% of the normalized DI range. For many structural health monitoring (SHM) decision scenarios where DI thresholds are relatively coarse, this level of fidelity is acceptable.

For more precise prognostic applications, the MFNN correction stage, discussed in the following chapter, significantly reduces this residual error.

Several factors contribute to the remaining differences between simulation and experimental results. Variations in sensor coupling and adhesive layer, such as inconsistencies in glue thickness and bonding pressure, affect transduction efficiency and local stiffness, producing amplitude shifts and small time-of-flight offsets not modeled in the idealized simulations. Additionally, machining tolerances at damage boundaries, especially for slotted holes, play a significant role; small burrs or rounded corners can measurably alter scattering behavior. The FE model employs simplified damping and boundary conditions to focus on the core scattering physics, whereas the measured materials may experience slightly different, frequency-dependent losses. Furthermore, variations in how the plates are held or clamped during experiments modify reverberation and late-time responses.

Despite these sources of uncertainty, the validation metrics demonstrate that the FE model reliably captures the essential DI behavior across different thicknesses, frequencies, and damage types. Consequently, the FE outputs serve as a robust low-fidelity data source suitable for integration within the ML framework, especially in the MFNN model. The feature-level DI values from both experiment and simulation serve as the supervised target for the MFNN. After normalization, simulation DI values populate the abundant LF training set while experimental DI values provide sparse HF corrections. The measured RMSE/MAE above quantify the simulation bias that the MFNN HF branch must correct. In practice, the MFNN reduced the residual DI error substantially, showing that the staged, residual-correction architecture is effective in bridging the simulation–experiment gap (discussed in detail in subsequent chapters). The complete validation results are available in Appendix C for clarity,

alongside additional comprehensive ML metamodel and MFNN results that are discussed in the subsequent chapters to ensure full reproducibility of the study.

5.5 Discussion of Validation Results

The validation process yielded several important insights. First, pristine comparisons confirmed that the FE model was able to capture the essential physics of Lamb wave propagation, including dispersion and mode arrival times. This provided a solid baseline for damaged case validation.

Second, damaged case comparisons demonstrated that the FE simulations could replicate both isotropic (circular hole) and anisotropic (slotted hole) scattering effects. While some differences were observed, particularly in higher-order dispersion for slotted holes, these were within reasonable tolerance given the idealised nature of FE geometry.

Third, the formulation of DI provided a unified framework for comparing experimental and simulated results across all configurations. This was particularly important for subsequent integration into the MFNN, where a consistent numerical descriptor of damage severity was required. By bridging the gap between raw signals and machine learning inputs, the DI served as both a validation tool and a data fusion metric.

Finally, the validation process highlighted the limitations of both simulations and experiments. Simulations cannot fully replicate imperfections in machining, bonding, and environmental variability, while experiments are subject to noise and reproducibility constraints. By acknowledging and quantifying these limitations, the study established a balanced understanding of the predictive scope of FE modelling.

This chapter has elaborated the validation of finite element guided wave simulations against experimental measurements for aluminium

plates through systematic comparison of damage sensitive features and representative waveforms. The introduction of the Damage Index unified these comparisons into a compact numerical metric, enabling robust evaluation across multiple configurations. The validation confirmed that the FE model is suitable for generating low-fidelity data, which, when fused with experimental high-fidelity data, provides a powerful basis for the Multi-Fidelity Neural Network (MFNN). In doing so, this chapter established the necessary foundation for the subsequent machine learning framework, ensuring that simulated data are not only computationally efficient but also physically credible.

Chapter 6 Application of Machine Learning Models

Machine learning has become a central tool in the field of Structural Health Monitoring (SHM), offering the ability to learn patterns from large datasets and make predictive assessments about the state of a structure. In this chapter, two stages of model development are discussed. The first involves the construction of a metamodel that integrates both deterministic and probabilistic algorithms, evaluated on simulation and experimental datasets to benchmark performance. The second stage presents the development of a Multi-Fidelity Neural Network (MFNN) that combines low-fidelity finite element simulations with high-fidelity experimental data, providing robust predictions of the Damage Index (DI) and enabling spatial localization of damage and RUL estimation in aluminium plates.

The discussion in this chapter is divided into two main sections. The first section focuses on the development of the Metamodel approach, while the second section develops and validates the MFNN framework. Together, these stages form a comprehensive pathway from baseline algorithmic benchmarking to the application of an advanced multi-fidelity learning architecture for guided-wave based SHM.

6.1 Metamodel Development Using Deterministic and Probabilistic Approaches

The first stage of this research involved the development of a metamodel to evaluate a range of candidate machine learning algorithms on a unified dataset. This metamodel served as a critical step in identifying the advantages and limitations of various approaches before committing to a more advanced architecture such as the MFNN. The full model pipelines and hyperparameter settings are provided in the Appendix B (Table 9.1). The dataset for the metamodel stage was constructed from both finite element simulations and experimental measurements of ultrasonic guided waves propagating through aluminium plates.

6.1.1 Dataset preparation and normalization

The dataset combined low-fidelity simulation data generated using ABAQUS finite element models and high-fidelity experimental data obtained from piezoelectric sensors bonded to aluminium sheets. From both sources, two primary features were extracted: time-of-flight (ToF) and peak amplitude. These features were chosen because ToF captures the delay introduced by defects in the wave propagation path, while amplitude reduction reflects scattering and attenuation effects caused by the presence of damage. Together, they offer a comprehensive description of how damage modifies guided wave behaviour.

Initially, only the limited experimental data were used to train an ANN model optimized with PSO, as developed by Jelena et al. [151]. In that stage, normalization was applied to ensure consistency across features of different scales. A min–max scaling transformation was used:

$$x_{\text{norm}} = \frac{x - x_{\min}}{x_{\max} - x_{\min}}(\bar{x}_{\max} - \bar{x}_{\min}) + \bar{x}_{\min} \tag{6.1}$$

where $\bar{x}_{\min} = 0.1$ and $\bar{x}_{\max} = 0.9$. This range was deliberately selected to avoid the extremes of 0 and 1, which can cause saturation in sigmoid-based neural activations. The scaling not only ensured numerical stability but also maintained sensitivity of features for gradient-based optimization during training.

Later, when the dataset was expanded to include numerical data and the metamodel approach was followed, normalization between 0 and 1 was applied in order to maintain uniformity across all algorithms present in the metamodel.

6.1.2 Deterministic and probabilistic models

To evaluate the predictive performance of different learning strategies, five representative algorithms were selected spanning deterministic and probabilistic paradigms. These algorithms represent a structured progression in complexity and uncertainty handling. Table 6.1 summarises the specific rationale for their selection.

Table 6.1: Rationale for Selection of Machine Learning Models

Model	**Paradigm**	**Justification and Literature Basis**
PR	Deterministic	Baseline nonlinear model. Selected for interpretability, though prone to overfitting at high orders [152].
SVM	Deterministic	Robust in small-sample, high-dimensional spaces. Effective for defining nonlinear decision boundaries [98].

ANN	Deterministic	High-capacity model. Selected as the primary benchmark for capturing complex nonlinear signal-damage mappings [37].
Bayesian	Probabilistic	Probabilistic baseline. Selected to provide predictive uncertainty estimates, crucial for handling sparse experimental data [153].
SGD	Probabilistic	Scalable optimisation benchmark. Chosen to evaluate performance on large simulation datasets where batch processing is inefficient [96].

Following this selection, specific implementation details were tailored to the dataset. **Polynomial Regression (PR)** was restricted to low-degree polynomials to prevent noise fitting while maintaining trend capability. The **Support Vector Machine (SVM)** employed a Radial Basis Function (RBF) kernel to effectively handle nonlinearities in the feature space. For the **Artificial Neural Network (ANN)**, weights were initialized using Particle Swarm Optimization (PSO) to avoid local minima during training. **Bayesian Regression** was configured to output predictive variance, enabling uncertainty quantification in sparse data regions. Finally, **Stochastic Gradient Descent (SGD)** utilised an adaptive learning rate to ensure stable convergence on the larger simulation datasets.

6.1.3 Balanced sampling strategy and performance comparison

Balanced sampling was an essential component of dataset preparation. The initial dataset contained more circular hole damage cases than slotted hole cases, which could have biased models toward circular damage predictions. To mitigate this, resampling ensured equal representation of damage

types. This balanced dataset improved generalization across different defect geometries, particularly for the ANN, which could otherwise have exploited class imbalance to superficially inflate performance metrics.

The comparative evaluation showed that each algorithm brought distinct strengths. PR offered interpretability but limited flexibility. SVM provided strong nonlinear modeling, particularly in small datasets. ANN consistently outperformed the others in predictive accuracy. BR contributed uncertainty quantification, while SGD enabled scalable, incremental training. Taken together, these results established ANN as the best-performing deterministic model, while highlighting the importance of uncertainty awareness and scalability. These insights motivated the development of the MFNN, which combined the strengths of simulation and experimental datasets in a single integrated architecture.

6.1.4 MFNN over Metamodel

While the metamodel provided a structured framework to evaluate multiple machine learning algorithms on SHM data, it also highlighted intrinsic limitations of single-fidelity approaches. Although the metamodel was trained on a combined dataset of simulation and experimental features, it treated all data points as belonging to a single distribution. Unlike the MFNN, the metamodel could not explicitly learn the systematic bias (or 'correction function') between the low-fidelity simulation and high-fidelity experiment, resulting in a static selection process. Consequently, opportunities to leverage the complementary strengths of simulation and experiment were left unexploited.

In practical SHM scenarios, low-fidelity simulations are abundant and can cover a wide spectrum of damage configurations, but they inherently contain modeling assumptions that may not fully represent real structural behavior. High-fidelity experimental measurements, on the other hand,

provide accurate insights into real-world phenomena but are limited in quantity due to cost and logistical constraints. A metamodel that treats these two data types separately cannot fully exploit the synergy between them, limiting its generalization and adaptability across varying structural scenarios.

The Multi-Fidelity Neural Network (MFNN) framework addresses these challenges by integrating data of differing fidelities within a single architecture. Instead of choosing a single model post hoc, the MFNN learns a hierarchical mapping where low-fidelity predictions are corrected by high-fidelity information. This approach effectively fuses broad physical trends captured by simulations with the realism of experimental measurements, allowing the network to form a unified representation of structural behavior.

The decision to adopt MFNN over the metamodel is thus guided by both theoretical and practical considerations. Theoretically, MFNNs provide a mechanism for residual learning and hierarchical data fusion, which inherently improves model generalization without requiring separate model selection or extensive retraining. Practically, this architecture enables efficient utilization of available datasets, reducing dependency on large volumes of experimental data while maintaining the accuracy necessary for real-world SHM applications.

By transitioning to the MFNN, the research moves from evaluating discrete models in isolation to implementing a cohesive, adaptive, and scalable predictive framework. This progression reflects a broader trend in engineering diagnostics toward hybrid intelligence systems, models that are not only data-driven but also context-aware and hierarchy-sensitive. The MFNN implemented in this research sets the stage for scalable, intelligent, and interpretable SHM solutions that can adapt across structures, environments, and damage types.

6.2 Multi-Fidelity Neural Network for Prediction of Damage, Location, and RUL Estimation

The development of the Multi-Fidelity Neural Network (MFNN) marked a pivotal stage in this research, providing a unified framework that integrated the strengths of finite element simulations with experimental measurements for guided wave-based Structural Health Monitoring (SHM). The motivation for adopting a multi-fidelity approach stemmed from the limitations of single-fidelity models. Purely simulation-driven models, despite generating large datasets across a wide design space, often fail to capture the nuanced physics present in laboratory experiments, such as sensor coupling variability, adhesive layer imperfections, or machining-induced irregularities around defects. Conversely, purely experimental approaches, while physically accurate, are expensive, time-consuming, and practically constrained in terms of the combinations of frequencies, sensor positions, and damage geometries that can be tested.

The MFNN was therefore designed to combine both fidelities, with low-fidelity (LF) simulations providing abundant coverage of structural variations and high-fidelity (HF) experiments serving as an anchor to correct and calibrate predictions. This dual reliance allowed the network to learn broad physical patterns from simulations while incorporating the realism of experiments. The MFNN ultimately generalized across unseen cases, preserving computational efficiency without compromising physical fidelity. In this section, the architecture, dataset preparation, training methodology, and robustness of the MFNN are described in detail.

6.2.1 MFNN Architecture and Formulation

The MFNN implemented in this work follows a dual-residual feedforward design, comprising two interlinked branches, a low-fidelity branch trained on abundant simulation data and a high-fidelity branch trained on limited experimental data. The network was implemented in TensorFlow and Keras, chosen for their flexibility and support for staged training, custom loss functions, and advanced regularization techniques. The design of the architecture balances the need to capture nonlinear relationships between structural features and damage indices while avoiding over-parameterization, which is particularly critical due to the limited size of the HF dataset.

The input feature vector is defined as

$$\mathbf{X} = [\text{Material}, \text{Damage Type}, \text{Plate Thickness}, \text{Frequency}, \text{Damage Size}], \tag{6.2}$$

where the material is encoded categorically (0 for aluminium in this study), the damage type is encoded as 0 for circular holes and 1 for slotted holes, and the remaining features are continuous variables representing the physical parameters of the plate and excitation. The output variable, the Damage Index (DI), is a scalar that encapsulates deviations from the pristine baseline, combining both ToF delays and peak amplitude reductions to quantify structural damage.

The LF branch learns a mapping from the input features to the predicted DI using simulation data:

$$\hat{Y}_{LF} = f_{LF}(\mathbf{X}; \Theta_{LF}), \tag{6.3}$$

where Θ_{LF} denotes the trainable weights and biases of the LF network. This branch is structured as a feedforward network with two hidden layers,

the first hidden layer consists of 64 neurons and the second contains 32 neurons. Rectified Linear Unit (ReLU) activations are applied in both layers, defined as $\sigma(z) = \max(0, z)$, where z is the input to a neuron, ensuring non-saturating gradients for efficient training. The specific choice of 64 and 32 neurons provides sufficient representational capacity to capture complex, nonlinear dependencies between inputs and the DI without introducing excessive computational burden. By keeping the network compact, it avoids overfitting and remains practical for repeated training and inference.

The high-fidelity branch employs a residual learning strategy. Instead of predicting DI directly, it learns a corrective mapping that refines LF predictions using experimental data:

$$\hat{Y}_{HF} = f_{HF}(\mathbf{X}, \hat{Y}_{LF}; \Theta_{HF}), \tag{6.4}$$

where Θ_{HF} are the trainable parameters of the HF branch. By concatenating LF predictions with the HF input features, the HF network leverages the simulation-informed baseline while learning to correct systematic biases, such as sensor noise, adhesive imperfections, and minor geometric irregularities. The dual-residual fusion produces the final prediction as:

$$\hat{Y}_{MF} = \alpha \hat{Y}_{LF} + (1 - \alpha)\hat{Y}_{HF}, \tag{6.5}$$

with $\alpha \in [0, 1]$ optimized during training. This weighted fusion allows the network to automatically balance contributions from LF and HF sources, enhancing both generalization and physical fidelity. The overall optimization objective is the mean squared error (MSE) loss:

$$\mathcal{L}(\Theta_{LF}, \Theta_{HF}, \alpha) = \frac{1}{N} \sum_{i=1}^{N} \left(Y_i - \hat{Y}_{MF,i}\right)^2, \tag{6.6}$$

where Y_i represents the true DI for the ith sample and N is the total number of training samples. The Adam optimizer is used to adaptively adjust learning rates for each parameter, promoting rapid convergence while maintaining stability.

The forward propagation through each branch can be formally expressed as:

$$\mathbf{h}_{LF}^{(1)} = \sigma(\mathbf{W}_{LF}^{(1)}\mathbf{X} + \mathbf{b}_{LF}^{(1)}), \tag{6.7}$$

$$\mathbf{h}_{LF}^{(2)} = \sigma(\mathbf{W}_{LF}^{(2)}\mathbf{h}_{LF}^{(1)} + \mathbf{b}_{LF}^{(2)}), \tag{6.8}$$

$$\hat{Y}_{LF} = \mathbf{W}_{LF}^{(3)}\mathbf{h}_{LF}^{(2)} + \mathbf{b}_{LF}^{(3)}, \tag{6.9}$$

$$\mathbf{h}_{HF}^{(1)} = \sigma(\mathbf{W}_{HF}^{(1)}[\mathbf{X}, \hat{Y}_{LF}] + \mathbf{b}_{HF}^{(1)}), \tag{6.10}$$

$$\mathbf{h}_{HF}^{(2)} = \sigma(\mathbf{W}_{HF}^{(2)}\mathbf{h}_{HF}^{(1)} + \mathbf{b}_{HF}^{(2)}), \tag{6.11}$$

$$\hat{Y}_{HF} = \mathbf{W}_{HF}^{(3)}\mathbf{h}_{HF}^{(2)} + \mathbf{b}_{HF}^{(3)}, \tag{6.12}$$

$$\hat{Y}_{MF} = \alpha\hat{Y}_{LF} + (1-\alpha)\hat{Y}_{HF}. \tag{6.13}$$

Here, $\mathbf{h}_{LF}^{(1)} \in \mathbb{R}^{64}$, $\mathbf{h}_{LF}^{(2)} \in \mathbb{R}^{32}$, and the HF hidden layers are similarly structured but with a reduced number of parameters to match the smaller HF dataset. This staged architecture ensures that the LF network captures broad trends while the HF branch specializes in refining residual errors. By training the LF network first and freezing its weights, the HF network learns exclusively to correct biases, preventing catastrophic forgetting and improving generalization. By design, the MFNN served as a practical

yet powerful predictive model suitable for integration within larger SHM pipelines. The core algorithms, including the MFNN architecture, were implemented in Python. The representative source code is provided in Appendix D.

6.2.2 Dataset Preparation, Normalization and Sampling

The predictive power of the MFNN depended critically on the preparation of consistent, representative datasets. Two distinct fidelity levels were utilized. The low-Fidelity (LF) Data comprise data generated using ABAQUS finite element simulations of aluminium plates subjected to ultrasonic guided waves. The simulations covered all combinations of thicknesses (0.7, 0.9, 1.2, and 1.5 mm), excitation frequencies (300–500 kHz in 10 kHz steps), sensor positions (square configuration at 100 mm from plate center and 200 mm from each other), and damage conditions (circular holes of 4–7 mm and slotted defects of lengths 12–18 mm with varying arc radii). The High-Fidelity (HF) Data includes data obtained experimentally using piezoelectric (PZT) transducers in the same square layout, with excitation at S1 and recordings at S2, S3, and S4. HF coverage was limited to seven physical plates, constraining the number of available experimental combinations.

From each signal, sensitive damage features,Time-of-Flight (ToF) and Peak Amplitude were extracted to form the Damage Index (DI). The DI was then computed as a scalar measure incorporating both ToF and amplitude deviations. Importantly, the DI was extracted for both LF and HF cases under consistent preprocessing pipelines, ensuring comparability between simulation and experiment.

To ensure LF–HF comparability, dataset alignment relied on strict

file-naming conventions encoding thickness, sensor, frequency, and damage type. Automated parsing scripts ensured that for each HF measurement, the corresponding LF simulation could be identified. This alignment was critical because mismatches would prevent the MFNN from learning systematic corrections.

Prior to training, all features were rescaled using min–max normalization.

$$x' = \frac{x - x_{min}}{x_{max} - x_{min}}, \tag{6.14}$$

mapping the input values to $[0, 1]$. This eliminated the dominance of features with larger magnitudes (e.g., frequency versus categorical damage type) and ensured stable optimization.

Balanced sampling was implemented to prevent the network from being biased toward more prevalent damage types, particularly circular holes. Let N_c and N_s denote the number of circular and slotted hole samples, respectively. A balanced training set was created by selecting

$$N_b = \min(N_c, N_s) \tag{6.15}$$

samples from each category. This ensured equal representation of circular and slotted hole cases in each training batch. Formally, if D_c and D_s represent the sets of circular and slotted samples, the balanced training batch D_b is constructed as

$$D_b = \{(X_i, Y_i) \in D_c \text{ for } i = 1, \ldots, N_b\} \cup \{(X_j, Y_j) \in D_s \text{ for } j = 1, \ldots, N_b\}. \tag{6.16}$$

This approach guaranteed that each mini-batch used for gradient descent contained equal contributions from both damage types, compelling the network to learn generalized damage features applicable across geometries.

6.2.3 Training Methodology and Convergence

Training was performed in a staged manner. As mentioned before, the LF network was trained first using the abundant simulation dataset until convergence, followed by training of the HF residual network. The Adam optimizer was used with an initial learning rate of 1×10^{-3} and a batch size of 32. The Adam optimizer adaptively adjusted learning rates for each parameter, accelerating convergence and avoiding instability associated with fixed learning rates.The training objective was to minimize the MSE loss, consistent with the regression task.

The dataset was partitioned into 60% training, 20% validation, and 20% test sets. The validation set provided continuous monitoring of generalization, while the test set was reserved strictly for final evaluation. This separation prevented data leakage and ensured unbiased performance assessment. In addition to MSE, two standard metrics were used, Root Mean Square Error (RMSE) and coefficient of determination (R^2).

Convergence Monitoring Protocol

This residual learning scheme was designed to allow the HF branch to focus exclusively on learning corrections rather than global structural trends, optimizing convergence speed and predictive accuracy. During the training phase, the protocol involved systematic tracking of training and validation loss curves to ensure stability. The training strategy prioritized early baseline learning from LF data, followed by refinement steps driven by the HF experimental data. Potential oscillations arising from limited HF sample availability were managed through the use of balanced mini-batches. Furthermore, feature normalization and balanced sampling were implemented as primary mechanisms to mitigate overfitting, rendering dropout unnecessary given the network's compact size.

6.2.4 Methodological Robustness and Design Attributes

Although detailed quantitative performance metrics are presented in the subsequent chapter, the MFNN architecture was specifically engineered to ensure robustness across variations in plate thickness, excitation frequency, and damage type. The compact yet expressive design was selected to facilitate generalization to previously unseen damage sizes and intermediate structural configurations, leveraging the integration of low-fidelity simulations with high-fidelity experimental anchors. The balanced sampling strategy was integral to this design, intended to prevent bias toward frequent pristine cases and ensure adequate learning of slotted hole defects, while normalization was applied to maintain stability across mixed categorical and continuous inputs.

The efficient design of the MFNN also ensures computational tractability, a critical requirement for potential real-time deployment in SHM systems. While the primary function of the network is to refine Damage Index (DI) predictions, the broader objective of the proposed framework extends beyond diagnostics to prognostics. In particular, estimating the Remaining Useful Life (RUL) requires linking the predicted DIs to fatigue-life models or damage accumulation frameworks. The MFNN outputs, representing calibrated and residual-corrected DIs, are designed to serve as the foundation for this mapping, enabling a data-driven approach to life prediction.

Comparatively, the limitations of single-fidelity metamodels (analyzed in the following chapter) necessitated this hybrid approach. The MFNN's capacity to internalize physics-based trends from simulations while correcting for real-world deviations makes it naturally suited for applications beyond damage quantification. Building on these

design attributes, the MFNN framework is extended to support damage localization and Remaining Useful Life (RUL) estimation. The detailed implementation and outcomes of integrating these diagnostics into life-prediction frameworks are reported in the Results chapter.

Chapter 7 Results & Discussion

The chapter is structured to provide a detailed account of the preparation of input datasets, the MFNN framework, training protocols, and validation procedures. It then presents quantitative results for damage detection and localization, followed by the prediction of RUL of structures. The discussion highlights the implications of using multi-fidelity learning for SHM, particularly in terms of reducing experimental costs and improving model generalizability. The chapter concludes with reflections on the strengths and limitations of the current approach and outlines possible directions for future work.

In summary, this chapter serves as the culmination of the thesis, demonstrating how a carefully constructed MFNN can surpass traditional models in both accuracy and robustness for guided wave-based structural health monitoring. It showcases a data-efficient, scalable methodology that can be extended to other structural materials and damage types, thus providing a valuable contribution to the field of intelligent condition monitoring.

This section mainly focuses on the quantitative and qualitative results obtained from the Multi-Fidelity Neural Network (MFNN) framework developed for ultrasonic guided wave-based Structural Health Monitoring (SHM). The results are organized into three key areas: damage detection accuracy, damage localization precision, and comparative performance with baseline single-fidelity models.

7.1 Damage Detection

This section presents the results obtained from the successive modelling stages, focusing on their effectiveness in predicting the damage index derived from guided wave features. At every stage, the same signal processing pipeline, feature scaling, and train–validation protocol were retained to ensure that differences in performance reflect model capability rather than procedural variation. The results are presented in a staged manner to illustrate how predictive accuracy, stability, and physical consistency evolve as modelling complexity and data richness increase.

7.1.1 Preliminary Model Screening using Experimental Dataset only

Baseline ANN trained on a limited experimental dataset

The first experiment established a baseline using only high fidelity measurements from the laboratory plate. The network received thickness, excitation frequency, and damage size or geometry as inputs, and the output was the damage index computed from the aligned waveforms. This stage was deliberately conservative in capacity to avoid overfitting a small dataset, using two fully connected hidden layers with rectified linear units and early stopping based on validation loss. The model converged smoothly and produced a coherent mapping from input parameters to the measured index. The predicted versus measured scatter showed the expected funnel shape at small indices where measurement noise is relatively more influential, and a tight cluster at moderate to large indices where the signal to noise ratio is higher. A first sensitivity readout revealed that the index increased most strongly with damage size and that thickness mainly acted through time stretching and amplitude attenuation, while

frequency modulated the index through dispersion and sensor bandwidth effects. These observations guided the following stages.

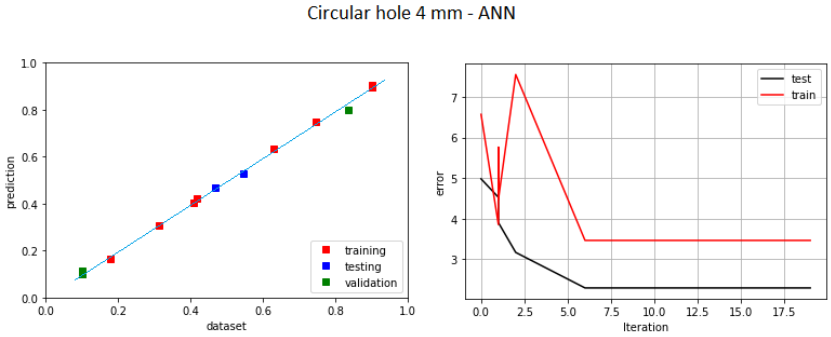


Figure 7.1: Prediction performance and residual behaviour of the baseline ANN trained on limited experimental dataset for 4 mm circular hole damage

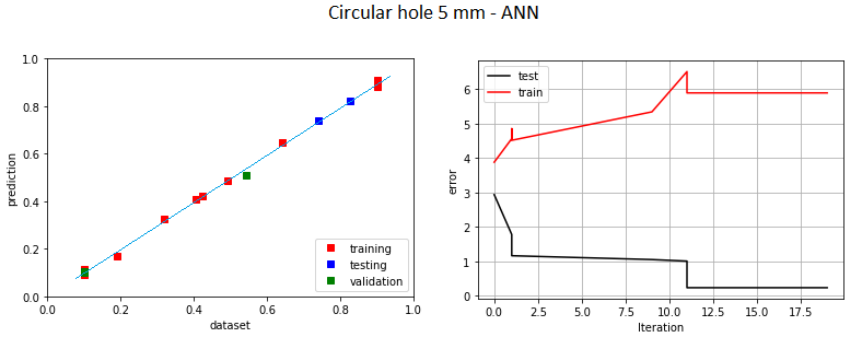


Figure 7.2: Prediction performance and residual behaviour of the baseline ANN trained on limited experimental dataset for 5 mm circular hole damage

Deterministic metamodel trained on the experimental dataset

After validating that a neural network can recover the experimental mapping, a deterministic metamodel was constructed to benchmark three classical learners on the same features and targets, namely polynomial regression, support vector regression with a radial basis kernel, and a neural network. Each learner was tuned by a small grid over polynomial

degree, kernel width, penalty, and hidden width respectively, and fitted under identical scaling and split protocol. The goal of this stage was not to crown a winner over a tiny set, but to quantify the bias variance trade-off of each hypothesis family when the data contain coupled physical effects. For clarity, only the best-performing deterministic model identified in this screening stage is visualized in this section, as the purpose of this analysis is deterministic model screening and selection for subsequent metamodel development, rather than exhaustive comparative reporting. The regression with polynomial features captured broad monotone trends but could not fully model the interaction between frequency and thickness, leading to systematic underestimation at the upper range of the index. The support vector regressor adapted well to local curvature but presented flat spots near sparse regions, which is expected when the support vectors are few relative to the input volume. Among the deterministic candidates evaluated, the neural network again provided the best balance of smoothness and flexibility, preserving the correct ordering with damage size and maintaining small residuals across the range. Figure 7.3 illustrates the typical prediction performance and residual behaviour of this selected ANN model. These findings motivated adopting the neural network as the default deterministic component in the subsequent stages.

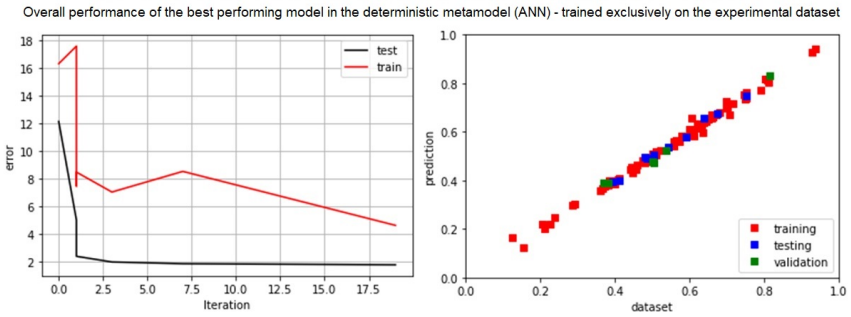


Figure 7.3: Prediction performance and residual behaviour of the best-performing model (ANN) within the deterministic metamodel, trained exclusively on the experimental dataset for Circular hole damage

7.1.2 Metamodel with both deterministic and probabilistic learners on the fused experimental and simulation datasets

The metamodel was extended to include Bayesian regression and stochastic gradient descent regression with stochastic regularization. The intent was to make the metamodel robust to train for complex non-linear damage problems also in future. Bayesian regression provided a closed form posterior over coefficients under a Gaussian prior and produced predictive intervals that naturally widened in parts of the input space with fewer samples. Stochastic gradient descent acted as a linear baseline with noise-aware regularization and was primarily used to detect any strong linear component in the mapping (detailed performance metrics for all algorithms are provided in **Appendix C, Table 9.3**).

The probabilistic view confirmed that the physics calibrated features deliver a well behaved target, since the posterior standard deviation remained small in the bulk of the data. It also highlighted that uncertainty grows in the regime of thin plates at the highest excitation frequency, exactly where dispersion and low signal amplitude increase the alignment error of time of flight. The work then also shifted from model variety to data variety. The simulated set delivered broad coverage across thickness, frequency, and damage configurations, while the experimental set anchored the target to reality. The two sources were aligned through the same preprocessing and index definition, and the fused table was used to train the same metamodel. The larger set reduced variance and stabilized the regressors.

Polynomial regression showed clear benefit from the wider grid since the global terms were constrained by more observations, yet it still lacked flexibility in high interaction zones. **However, the Support Vector**

Machine (SVM) demonstrated the superior performance on this fused dataset. Quantitatively, the SVM achieved the lowest error and highest generalization capability compared to the neural and linear baselines, as shown in Figure 7.4.

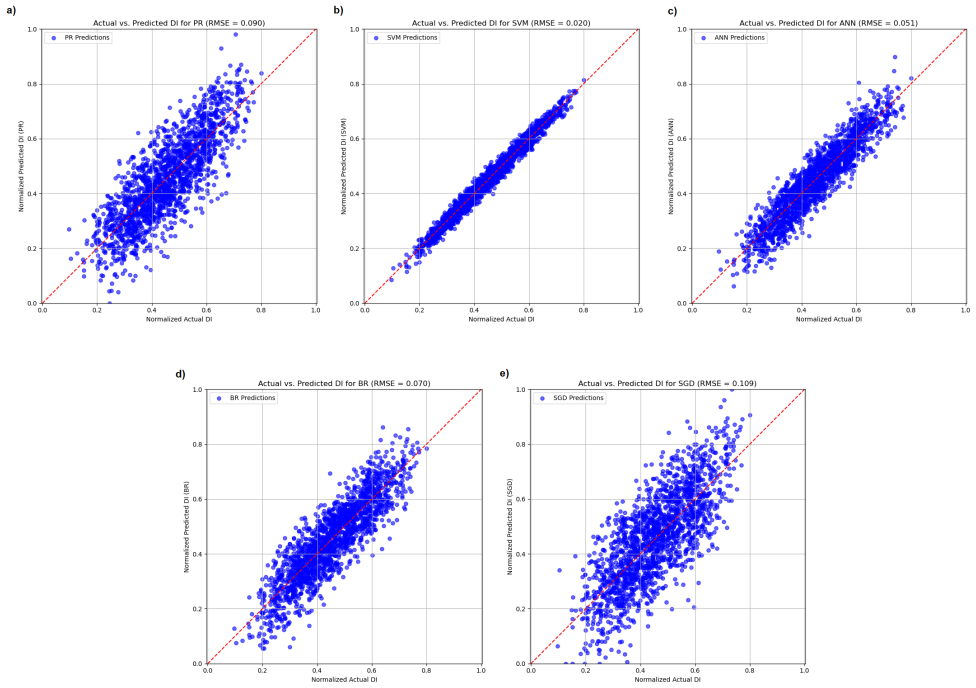


Figure 7.4: Comparative damage prediction performance of the developed Metamodel algorithms a) PR b) SVM c) ANN d) BR e) SGD

This is attributed to the SVM's ability to effectively find optimal hyperplanes in the high-dimensional feature space of the fused data. The predicted versus measured plots display a tighter cloud around the equality line for the SVM model, and the sensitivity surfaces become smoother and more physically plausible. Table 7.1 details the comparative performance of the deterministic and probabilistic metamodels, quantified by their Root Mean Square Error (RMSE) and Coefficient of Determination (R^2).

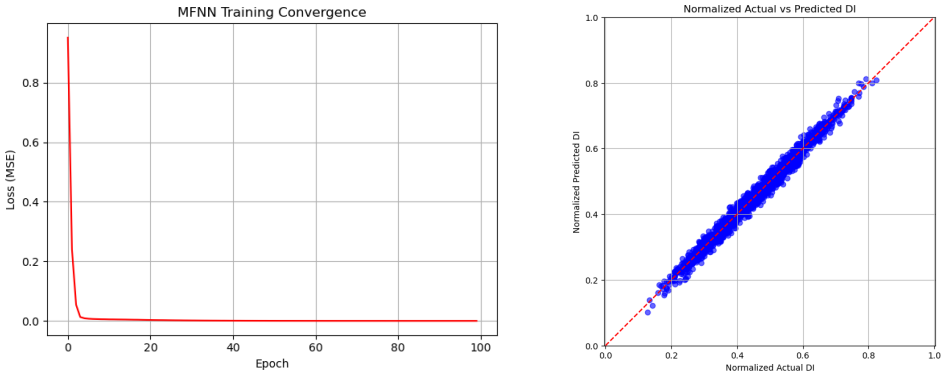
Table 7.1: Performance metrics (RMSE and R^2) of the constituent machine learning models in the Metamodel trained on the fused experimental-simulation dataset.

Model Type	**Algorithm**	**RMSE**	R^2 **Score**
Deterministic	Polynomial Regression (PR)	0.0245	0.9521
	Support Vector Machine (SVM)	**0.0196**	**0.9710**
	Artificial Neural Network (ANN)	0.0212	0.9645
Probabilistic	Bayesian Regression (BR)	0.0289	0.9312
	Stochastic Gradient Descent (SGD)	0.0341	0.9105

7.1.3 Damage prediction using Multi-Fidelity Neural Network

Though the improvised metamodel functions better, the quality of the data set is not analyzed effectively. The low fidelity simulated data and high fidelity experimental data are fused directly and used for training, so the final stage used the multi-fidelity neural network. The network treats simulated information as a low fidelity view and learns a correction from high fidelity data. The low fidelity branch provides dense structure over the design space, while the high fidelity branch learns a residual that aligns the combined predictor with the experimental target. In addition to the fusion at the level of inputs and targets, the model also makes use of a pristine baseline to align waveforms across thicknesses through amplitude and time scaling. This baseline improves stability in the index at small damage where amplitude changes are subtle and the location of the main wave packet can be ambiguous. The training curve shows a longer descent but a lower final loss than any single source model. As illustrated in Figure 7.5a, the early epochs exhibit a rapid decrease in loss as the model establishes baseline learning from the abundant LF data, while the subsequent stabilization reflects the refinement of residuals using the HF experimental data. The

predicted versus measured band in Figure 7.5b is the tightest of all stages and is more homogeneous across the input space, which indicates that the residual learner is successfully removing systematic bias in the low fidelity simulations. The sensitivity readout confirms the same ordering of effects identified at the beginning but with smaller variance and a more linear growth with damage size at larger indices. This model is used downstream for localization by projecting predicted indices along time of flight rays and for life estimation by coupling the index trajectory with both S-N curve and the data driven trajectory derived from index sequences, which appear in later sections of the chapter.



(a) Error convergence during training. (b) Damage Prediction

Figure 7.5: MFNN performance showing error convergence and prediction accuracy

7.1.4 Narrative of observations across stages

Reading the sequence from left to right, the results follow a consistent pattern. When only a handful of laboratory measurements are used, the mapping from inputs to damage index is learnable but fragile. The deterministic metamodel places this fragility into context by revealing where global polynomials underfit interactions and where support vector kernels saturate due to sparse support. The neural network balances

these effects better, yet its capacity is constrained by the small table. Adding probabilistic learners does not change the central trend but quantifies confidence and points to input regions where the acquisition of further data will be most valuable. Once simulations are introduced and aligned, the regressors gain stability because they see more varied combinations of thickness, frequency, and damage type. The neural model benefits most from this expansion. To objectively assess the benefit of incorporating multi-fidelity learning, a direct quantitative comparison is performed between the best-performing single-fidelity metamodel and the proposed Multi-Fidelity Neural Network (MFNN). The comparison focuses on predictive accuracy metrics that are commonly adopted in regression-based structural health monitoring studies, namely the Root Mean Square Error (RMSE) and the coefficient of determination (R^2).

Table 7.2: Quantitative performance benchmark comparing the global accuracy of the best single-fidelity metamodel (SVM) against the Multi-Fidelity Neural Network (MFNN).

Model Architecture	**RMSE**	R^2
Metamodel (SVM)	0.0196	0.9710
MFNN	**0.0152**	**0.9829**

Table 7.2 summarizes the quantitative performance of the two approaches. As demonstrated, the MFNN reduces the Root Mean Square Error (RMSE) to 0.0152, outperforming the best single-fidelity metamodel (SVM, RMSE: 0.0196). This confirms that the multi-fidelity neural network consolidates gains by removing simulation bias via a residual learned from the experimental anchor. This improvement is particularly evident under conditions of limited experimental data, where the MFNN leverages the broader simulation dataset to stabilize learning and enhance generalization. Additionally, the improved prediction consistency is

visualized in Figure 7.5.

These findings provide clear statistical evidence that the MFNN framework improves predictive accuracy by effectively combining physics-based simulations with experimental observations. The reduction in prediction error supports the central hypothesis of this thesis, namely that multi-fidelity learning offers a robust and scalable pathway for damage prediction, location, and remaining useful life estimation in guided-wave-based structural health monitoring.

7.2 Damage Localization using MFNN

Accurate localization of structural damage is a crucial component of any Structural Health Monitoring (SHM) framework, as it directly supports targeted maintenance strategies and enhances structural safety. In this research, a Multi-Fidelity Neural Network (MFNN) model was employed to estimate the spatial location of damage in aluminium plates using ultrasonic guided wave features. The localization process was driven by the Damage Index (DI), which was derived from differences in the time-of-flight (ToF) and peak amplitude of Lamb wave signals between pristine and damaged states. By combining experimental data with simulated data from ABAQUS, the MFNN was trained on a diverse dataset covering multiple plate thicknesses, excitation frequencies, damage types, and sizes, thereby ensuring generalizability across a wide operational envelope.

The input features for the localization model consisted of material, damage type, thickness, excitation frequency, and damage size, sensor positions. At present, aluminium was used as the only material type, but the structure of the dataset allows future extensions to composites and hybrid materials. Damage types included circular and slotted holes. For

each damage type, several representative sizes were modelled, such as 4–7 mm for circular holes and 12×4 to 18×6 mm for slotted hole damages. Each case was combined with different frequencies in the range of 300–500 kHz and plate thicknesses of 0.7, 0.9, 1.2, and 1.5 mm. Three output sensors were mounted on the surface. This produced a high-dimensional dataset where each unique configuration generated a corresponding DI. To account for class imbalance in the raw dataset, a sampling strategy was applied to balance circular and slotted hole data subsets before training, ensuring that the model was not biased toward the more frequently occurring damage types.

The MFNN learns to map these input features to the DI response surface. By interpolating DI values across the parameter space, the model can identify regions in which the signal distortion is most consistent with the presence of damage. In practice, the predicted DI values are projected onto a spatial grid defined by plate thickness and frequency, and a Gaussian weighting scheme is applied to construct a continuous heatmap of probable damage zones. The resulting heatmaps highlight the concentration of DI values, thereby pinpointing the likely location of defects. This approach not only provides a robust visualization of localized damage but also reduces reliance on purely geometric triangulation techniques, which often require dense sensor networks.

Figure 7.6 presents the MFNN-predicted damage locations for both circular and slotted hole cases. Since all damages were introduced at the plate center, the predictions appear similar in both cases.

The regions of higher intensity (red zones) correspond to areas with elevated DI values, indicating the presence of structural defects. The spread of the heatmap provides additional information about uncertainty in localization, which is particularly important when working with limited sensor coverage or noisy experimental signals. The integration

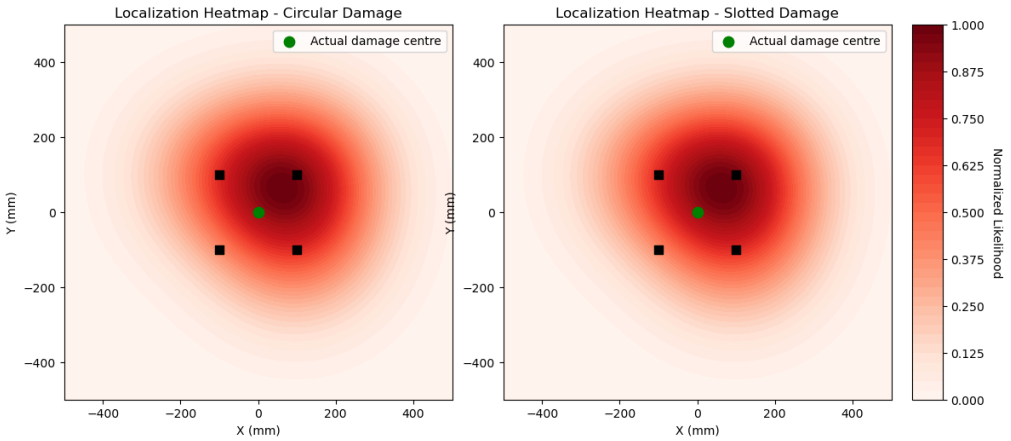


Figure 7.6: Predicted DI-based damage localization heatmaps generated using MFNN. Left: Localization for a 5 mm circular hole damage. Right: Localization for a 15 mm x 5 mm slotted hole damage

of low-fidelity simulation data into the training process was particularly beneficial in enhancing the resolution of localization results, as simulated cases supplied the model with a broader range of scenarios than available experimentally.

A significant strength of this localization framework lies in its ability to handle different damage morphologies within a unified representation. By encoding damage type as an input feature, the MFNN can learn shared patterns between circular and slotted hole defects, and could extend these insights to include delamination or crack-like damages in the future. In summary, the proposed DI-based damage localization framework demonstrates how multi-fidelity learning can exploit both experimental and simulated data to achieve accurate, interpretable, and scalable results. This result is particularly significant as it illustrates the model's ability to localize damage with high precision using only the predicted Damage Index, highlighting the feasibility of employing the MFNN for spatial defect identification without dense sensor configurations. The localization heatmaps provide a direct and intuitive means of visualizing potential damage sites, which, when coupled with the RUL predictions presented in

the next Section, offer a powerful tool for condition-based maintenance. This unified methodology not only improves defect detection accuracy but also sets the foundation for its extension to more complex geometries, composite materials, and real-time SHM systems in aerospace and civil infrastructure. In future work, damage location will be treated as an additional parameter, allowing evaluation of the model under more diverse spatial configurations.

7.3 Prediction of Remaining Useful life

Following damage detection and localization, the next step of the framework involved the estimation of Remaining Useful Life (RUL). The proposed methodology integrated MFNN-predicted damage indices (DI) with S-N curve calibration, ensuring that the data-driven model remained physically consistent with known fatigue behavior of aluminum plates.

The application of MFNN was extended beyond damage severity prediction to support prognostic assessment through a physics-informed interpretation of predicted DI trajectories. The MFNN was trained using a combination of low-fidelity finite element simulation data and high-fidelity experimental guided wave measurements. The network inputs included material properties, plate thickness, excitation frequency, damage type, and damage size, while the output was the predicted Damage Index. As discussed in earlier sections, the MFNN was not designed to predict fatigue life or RUL directly.

Training convergence of the MFNN was stable and consistent, with the mean squared error (MSE) loss decreasing monotonically over training epochs, as shown in Figure 7.5a. Validation results demonstrated close agreement between predicted and measured DI values, with root mean squared error (RMSE) remaining below 0.1 across the evaluated test

datasets. These results confirm the ability of the MFNN to reliably capture the nonlinear relationship between ultrasonic guided wave features and damage severity across different damage configurations.

To enable prognostic interpretation, the predicted DI trajectories were subsequently mapped to established S–N fatigue life curves for aluminium alloys. In this framework, the Damage Index is treated as a quantitative proxy for structural degradation rather than a direct measure of accumulated fatigue damage. Circular hole defects with diameters ranging from 4 to 7 mm were associated with fatigue lives on the order of 10^6 cycles, while slotted hole defects (12×4 mm to 18×6 mm) exhibited reduced fatigue lives of approximately 0.8×10^6 cycles, consistent with their higher stress concentration effects. These fatigue life ranges were adopted from well-established S–N behaviour for aluminium structures reported in the literature.

The DI progression was scaled to span from a pristine baseline condition (DI $\approx$ 0.1) to a critical degradation threshold (DI $\approx$ 1.5), enabling a consistent comparison between data-driven degradation trends and physics-based fatigue life limits. It is emphasised that no cyclic fatigue loading experiments were performed as part of this study. Consequently, the mapping between DI trajectories and fatigue life does not constitute a direct life prediction, but rather a physics-informed interpretation of degradation severity in the context of known fatigue behaviour.

Figure 7.7 presents the inferred DI-based degradation trajectories alongside reference S–N fatigue life trends. For slotted hole defects, the MFNN-predicted DI evolution follows a trajectory consistent with the expected fatigue life range, reaching the critical DI threshold near 0.8×10^6 cycles. For circular hole defects, the DI progression aligns with a fatigue life of approximately 10^6 cycles. The resulting trajectories exhibit mild nonlinearity, reflecting the sensitivity of ultrasonic guided wave features

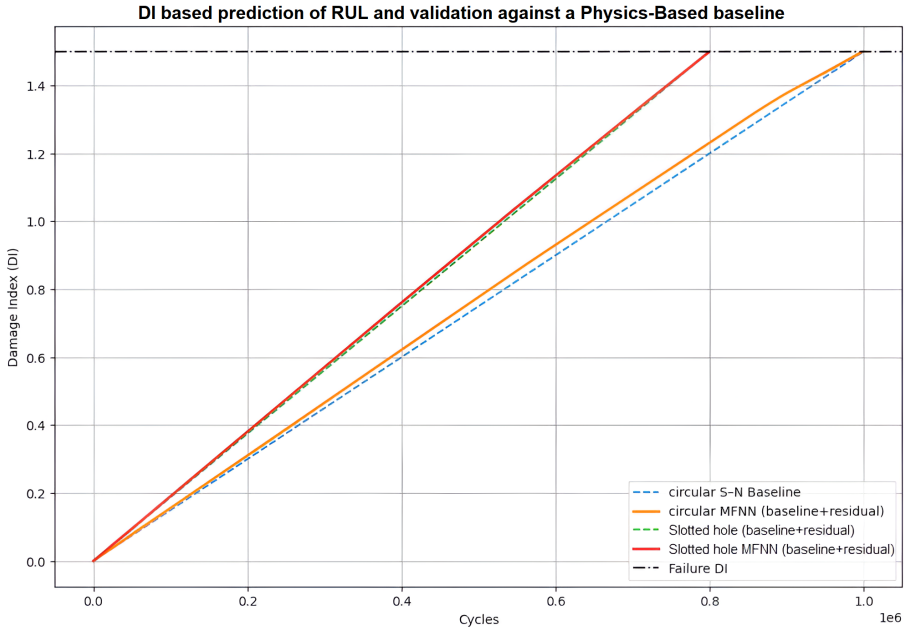


Figure 7.7: DI-based degradation trajectories inferred from MFNN predictions and validated through analytical consistency with established S–N fatigue life trends for circular and slotted damage configurations.

to evolving damage states, while remaining bounded within physically meaningful fatigue life limits.

The role of the S–N framework in this study is not to provide training labels or ground-truth RUL values, but to serve as an analytical consistency check. This ensures that the degradation trends inferred from MFNN-predicted Damage Indices are coherent with established fatigue mechanics for aluminium structures. Unlike Paris-law-based approaches, which are primarily applicable to crack propagation after initiation, the S–N framework is more appropriate for the notch-type and hole-based damage configurations considered in this work, where initiation and early-stage degradation dominate the fatigue response.

Overall, this integrated MFNN:S–N framework demonstrates how data-driven damage prediction can be systematically combined with physics-based fatigue knowledge to support prognostic assessment. By

linking ultrasonic guided wave-based Damage Indices to fatigue life trends through a transparent and physically interpretable process, the proposed approach provides a robust foundation for Remaining Useful Life estimation in Structural Health Monitoring applications. This hybrid methodology ensures that prognostic outputs remain both data-informed and grounded in established engineering principles, which is essential for deployment in safety-critical structures.

7.4 Frequency dependence of the Damage Index

In addition to RUL estimation, the sensitivity of the Damage Index to frequency was examined. Figure 7.8 shows the relationship between excitation frequency and DI, comparing actual experimental data against predictions from the machine learning model. The close overlap between the two sets of points demonstrates that the predictive model effectively reproduces experimental behaviour.

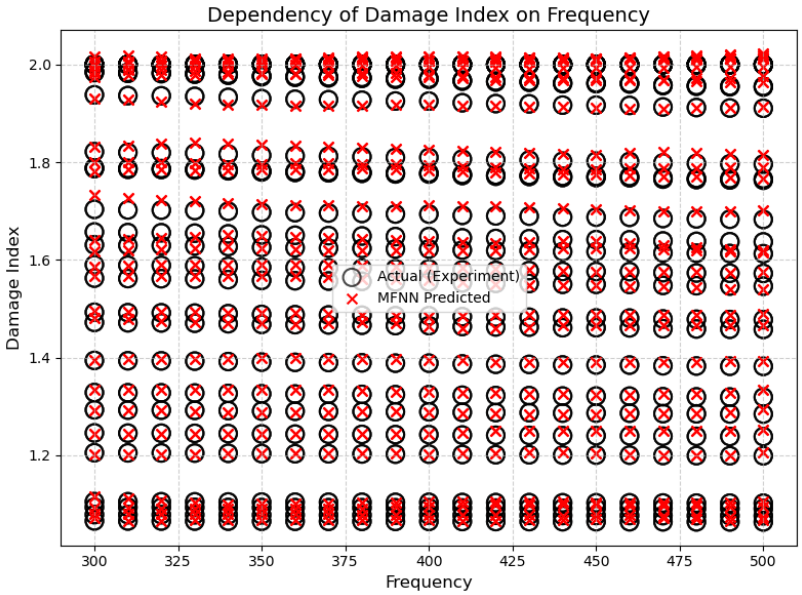


Figure 7.8: Variation of Damage Index with excitation frequency. Actual experimental values are compared with model predictions, showing strong agreement and frequency-dependent clustering.

The results indicate that DI values are clustered in distinct bands across frequencies, reflecting the frequency-dependent propagation and scattering of Lamb waves. The ability of the ML model to accurately interpolate across frequencies validates its robustness and highlights frequency as a critical feature for effective structural health monitoring.

7.5 Effect of Defect Size on Damage Index

A further validation of the model was carried out by investigating the variation of DI with respect to defect size. Figure 7.9 illustrates the correlation between DI values and increasing damage size, for both circular and slotted hole damage scenarios. The results show a monotonic increase in DI with defect size, confirming the sensitivity of guided wave features to the severity of structural damage.

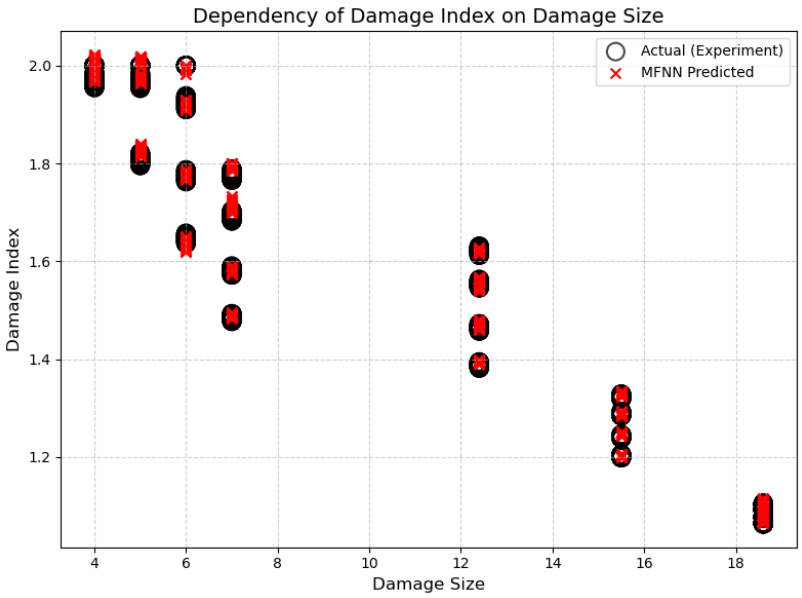


Figure 7.9: Variation of Damage Index with increasing damage size for circular and slotted hole defects. The trend confirms that larger damage leads to higher DI, validating the physical relevance of the metric.

The predictive model successfully captures this trend, aligning with the

physical expectation that larger damage causes greater wave scattering and signal distortion. Importantly, the DI-based approach provides a unified metric that is sensitive to both damage initiation and growth, making it highly suitable for long-term monitoring and life prediction applications.

7.6 Advantages of Multi-Fidelity Integration

A central strength of the Multi-Fidelity Neural Network (MFNN) developed in this study lies in its ability to combine the complementary advantages of low-fidelity (LF) and high-fidelity (HF) datasets. In the present framework, LF data were generated through Abaqus simulations, offering a large volume of inexpensive samples that captured the global trends of guided wave propagation under varying thickness, frequency, and damage conditions. HF data, derived from laboratory experiments, were more limited in size but contained critical real-world effects such as sensor noise, boundary condition variability, and subtle material inconsistencies. By training a unified MFNN on both datasets, the model inherited the generalization capability from LF data while being anchored by the physical realism of HF measurements, thus achieving higher predictive accuracy than either fidelity alone [154, 143].

7.6.1 Improved Data Efficiency

One of the most practical outcomes of this integration is improved data efficiency. Purely data-driven models in Structural Health Monitoring (SHM) often demand thousands of experimental samples to achieve stability [111]. The MFNN, by contrast, leveraged abundant LF data to shape its baseline learning, requiring only a relatively small set of HF samples for calibration. This reduced reliance on costly experiments is especially valuable in aerospace SHM, where replicating fatigue damage in

full-scale structures is both expensive and time-consuming [98]. Moreover, as additional HF data become available through inspections or extended test campaigns, the trained MFNN can be incrementally refined without discarding prior knowledge, providing a scalable and sustainable learning framework.

7.6.2 Robustness Across Configurations

The MFNN demonstrated strong robustness across variations in plate thicknesses (0.7-1.5 mm), damage types (Circular and Slotted holes), damage sizes, excitation frequencies (300-500 kHz), and sensor positions. In particular, the model generalized well to previously unseen test cases, producing damage index predictions that aligned with expected physical degradation patterns. For the binary damage detection task, discrimination between pristine and damaged structural states based on MFNN-predicted Damage Index values consistently achieved classification accuracies exceeding 98%, with the full quantitative results reported in Appendix C. The integration of LF and HF data ensured that predictions did not overfit to either noise-free simulations or to the smaller experimental dataset, but instead reflected an intermediate representation that captured both physical and experimental variability. Such robustness is critical for SHM applications intended for deployment in diverse operational conditions.

7.7 Challenges in Framework Design and Strategic Mitigation

One of the primary challenges in guided-wave-based SHM is the limited availability of high-fidelity experimental data. Experimental testing is time-consuming, costly, and constrained by practical considerations such as

specimen preparation, sensor placement repeatability, and environmental variability. As a result, purely data-driven models trained only on experimental data are susceptible to overfitting and poor generalization.

A second challenge lies in the use of numerical simulations as a surrogate data source. While finite element simulations enable scalable data generation across a wide range of damage configurations, they inherently suffer from modelling assumptions, such as idealized boundary conditions, simplified material behaviour, and numerical dispersion. These assumptions introduce systematic bias when simulation outputs are directly used for training machine learning models.

Feature robustness and physical interpretability represent another significant challenge. Ultrasonic guided wave signals are highly sensitive to damage, but also to thickness variation, excitation frequency, and coupling conditions. Features that perform well under controlled conditions may degrade in reliability when applied across different structural configurations or data sources.

From a modelling perspective, selecting a single machine learning algorithm that performs optimally across all SHM scenarios is non-trivial. Different algorithms exhibit different bias–variance characteristics, and their performance can vary significantly depending on data size, noise level, and feature nonlinearity.

Finally, extending damage detection models to prognostics introduces additional challenges. Direct fatigue life labels were unavailable due to the absence of cyclic fatigue testing. Consequently, Remaining Useful Life (RUL) estimation had to be approached carefully to avoid unsupported claims while maintaining physical relevance.

To address these challenges, this research adopted a series of targeted mitigation strategies grounded in both machine learning best practices and physical insight. These strategies were implemented incrementally and are

summarized in Table 7.3.

Table 7.3: Summary of key challenges encountered in this research and corresponding mitigation strategies adopted.

Identified Challenge	**Mitigation Strategy Implemented**
Limited availability of high-fidelity experimental data	Use of validated finite element simulations to generate scalable low-fidelity data, supplemented by experimental measurements to preserve physical realism.
Simulation–experiment mismatch and modelling bias	Adoption of a Multi-Fidelity Neural Network (MFNN) architecture that learns a residual correction between simulated and experimental data rather than fusing them directly.
Sensitivity of guided wave features to thickness, frequency, and coupling	Selection of physics-informed features (Time-of-Flight and Peak Amplitude) and formulation of a normalized Damage Index to improve robustness across configurations.
Lack of a universally optimal ML model for SHM tasks	Development of a machine learning metamodel incorporating deterministic and probabilistic learners to benchmark performance and enable adaptive model selection.
Risk of overfitting under small or imbalanced datasets	Use of consistent preprocessing, normalization, early stopping, and performance-based model comparison using RMSE and R^2 metrics.
Absence of direct fatigue life labels for RUL prediction	Interpretation of predicted Damage Index trajectories within a physics-informed S–N fatigue framework as an analytical consistency check rather than supervised validation.
Limited interpretability of purely data-driven predictions	Maintenance of physical meaning at every stage by ensuring that ML targets (Damage Index) and prognostic mappings are grounded in established fatigue theory.

The mitigation strategies adopted in this research reflect a deliberate balance between data-driven learning and physics-based understanding. Rather than attempting to eliminate uncertainty entirely, the framework explicitly acknowledges and manages sources of uncertainty through multi-fidelity learning, probabilistic modelling, and physics-informed interpretation. This approach ensures that the resulting SHM system remains both scalable and trustworthy, particularly for safety-critical applications where interpretability and robustness are essential.

Overall, the challenges encountered during this research directly informed the methodological choices made, ultimately strengthening the proposed framework and enhancing its relevance to real-world SHM deployment.

7.8 Relevance of MFNN to SHM Practice

The MFNN framework exemplifies the growing paradigm of hybrid intelligence in SHM, integrating simulation-driven insights with experimentally grounded data [155]. The demonstrated ability to reduce experimental burden while retaining predictive accuracy highlights its suitability for real-world aerospace structures, where safety-critical monitoring requires both adaptability and interpretability. Importantly, the MFNN is modular and can be extended to incorporate additional features, such as environmental compensation (temperature, humidity) or composite material behavior, by retraining with appropriate LF–HF datasets. Its success in this work validates the hypothesis that combining multiple fidelities enhances not only model accuracy but also its generalizability and practical utility.

In summary, the MFNN developed here effectively addressed critical challenges in SHM related to data scarcity, robustness, and

real-world generalization. By embedding simulation-informed trends into a data-driven model calibrated with experimental observations, the framework achieved a balance between scalability and physical realism, advancing the state-of-the-art in damage detection, localization, and RUL prediction.

Chapter 8 Conclusion & Future Scope

8.1 Conclusions

This thesis set out to develop a robust, interpretable, and scalable Structural Health Monitoring (SHM) framework by integrating ultrasonic guided wave physics with advanced machine learning strategies, with particular emphasis on metamodels and multi-fidelity neural networks. The research was motivated by the fundamental trade-off between experimental fidelity and computational scalability, and by the absence of unified learning frameworks capable of leveraging both data sources coherently for damage diagnostics and prognostics.

The first objective focused on the generation of reliable high-fidelity and low-fidelity datasets suitable for machine learning. This objective was successfully achieved through the **design and execution of controlled ultrasonic guided wave experiments on aluminium plates with multiple thicknesses and damage configurations, complemented by validated finite element simulations in Abaqus**. The numerical models replicated experimental wave physics with acceptable error bounds in time-of-flight and amplitude response, enabling simulations to serve as a scalable source of low-fidelity data. The resulting datasets formed a

consistent foundation for subsequent machine learning stages.

A unified feature extraction and damage quantification strategy was developed and applied consistently across experimental and simulated data. **Time-of-Flight shifts and peak amplitude attenuation were demonstrated to be damage-sensitive, physically interpretable features**, and were combined into a single Damage Index (DI) that served as a quantitative proxy for structural degradation. This formulation ensured that the learning targets retained a direct physical meaning and could be compared across different damage geometries, sensor paths, and plate thicknesses.

The third objective addressed the limitations of relying on a single machine learning algorithm for SHM tasks. A **machine learning metamodel comprising deterministic (PR, SVM, ANN) and probabilistic (BR, SGD) learners was successfully developed and benchmarked**. Systematic comparison revealed that no single algorithm was universally optimal across all data conditions, thereby validating the first research hypothesis. Artificial Neural Networks consistently demonstrated superior performance in capturing nonlinear damage–feature relationships, while probabilistic models provided valuable insight into uncertainty behaviour under limited data conditions. This stage established a principled basis for adaptive model selection.

Building upon the insights gained from the metamodel stage, the research demonstrated that separating experimental and simulated data in a single-fidelity learning framework limited generalization. **The Multi-Fidelity Neural Network (MFNN) framework was therefore developed to explicitly fuse low-fidelity simulation data with high-fidelity experimental data within a unified architecture**. The MFNN learned a residual correction that mitigated systematic simulation bias while retaining the scalability of numerical

data. Quantitative comparisons showed that the MFNN outperformed the best single-fidelity metamodel in terms of RMSE and coefficient of determination, particularly when experimental data were sparse. These results directly support the second research hypothesis concerning the advantages of multi-fidelity learning.

The final objective extended the developed framework beyond damage detection to localization and Remaining Useful Life (RUL) estimation. **Damage localization was achieved by projecting predicted Damage Indices along guided-wave propagation paths**, resulting in high classification accuracy between pristine and damaged states and low mean spatial localization error. **For prognostics, the MFNN was employed to predict DI trajectories, which were then interpreted within a physics-informed S–N fatigue framework**. Although no cyclic fatigue testing was conducted, the S–N curves were used as an analytical consistency validation check to ensure that predicted degradation trends were physically meaningful. This validated the third research hypothesis and demonstrated the feasibility of DI-based, physics-informed RUL estimation.

Collectively, the outcomes of this thesis demonstrate that **multi-fidelity machine learning provides a powerful and practical pathway for ultrasonic guided-wave-based SHM**, enabling accurate damage prediction, reliable localization, and interpretable prognostics under realistic data constraints. The proposed framework bridges the gap between data-driven models and physical understanding, offering a scalable solution suitable for aerospace and other safety-critical engineering applications. The methodologies and insights presented in this work lay a strong foundation for future research in intelligent, physics-aware structural diagnostics and lifecycle management.

8.2 Operational Challenges and Remedial Measures

Conducting an integrated structural health monitoring (SHM) investigation using ultrasonic guided waves requires precise coordination between experimental procedures and numerical simulations. Despite detailed planning and methodical execution, several challenges emerged over the course of this study. These spanned instrumentation limitations, signal fidelity issues, environmental factors, discrepancies between simulated and real-world conditions, and machine learning data compatibility. Each challenge was carefully analyzed and addressed through tailored mitigation strategies to ensure the reliability and validity of both experimental and simulated datasets. This section offers an in-depth discussion of these challenges and the corrective actions employed.

8.2.1 Sensor Coupling and Signal Quality

One of the first challenges encountered during the experiments involved achieving consistent sensor coupling across tests. Piezoelectric transducers, particularly thin circular disks, are highly sensitive to the quality of their mechanical bond with the plate surface. Even slight variations in adhesive thickness or air gaps introduced during installation could significantly affect the amplitude, bandwidth, and shape of the received ultrasonic signal. In early trials, some waveforms exhibited excessive noise or uncharacteristic attenuation, which were traced to poor bonding and uneven adhesive distribution.

To overcome this, the bonding process was standardized. Surfaces were mechanically abraded using fine-grit sandpaper and then degreased with isopropanol before adhesive application. A simple constant-load clamping arrangement was used during the curing process to ensure a uniform, thin bond layer. Cure times were strictly adhered to, based

on the adhesive's technical data sheet, and ambient temperature and humidity were monitored to ensure consistency. After bonding, each sensor underwent a calibration test on a pristine plate, where baseline signal features were recorded and compared against known templates. Any transducer that showed abnormal response characteristics was discarded and replaced.

8.2.2 Boundary Conditions in Experiments

In simulation environments like ABAQUS, boundary conditions can be perfectly controlled, allowing researchers to model free or fixed boundaries without unwanted reflections. However, replicating free boundary conditions in a real laboratory setting proved non-trivial. During initial experiments, reflections from the plate edges contaminated the signal within the observation window, especially for thinner plates or longer wave travel distances.

To mitigate this, rubber damping strips were applied along the plate edges to absorb incident waves and simulate quasi-free boundary conditions. The plates were supported on foam pads positioned well outside the wave propagation region to minimize constraint effects while providing mechanical stability. The time window for signal acquisition was also optimized to capture the direct wave and any damage-related scattering before edge reflections returned. Where necessary, digital signal processing techniques, including windowing and gating, were applied to isolate the useful portions of the signal.

8.2.3 Environmental and Ambient Noise

Ultrasonic waveforms, particularly those acquired from thin plates, are susceptible to environmental noise, electromagnetic interference, and

temperature variations. Despite using shielded cables, several early recordings were marred by low-frequency noise from nearby electronic equipment and high-frequency spikes likely caused by electromagnetic crosstalk. Additionally, the mechanical vibration of the laboratory table introduced noise in certain conditions.

To minimize these effects, the experiments were moved to a dedicated vibration-isolated optical table. All electronic equipment not involved in the testing process was turned off or relocated. The Coaxial cables were upgraded to high-quality double-shielded variants to improve noise rejection, and cable routing was optimized to avoid proximity to power lines or transformers. Laboratory temperature was monitored and maintained within $22 \pm 1°C$ where possible to prevent thermally induced phase shifts, as fluctuations beyond this range were observed to influence the wave speed and transducer sensitivity.

Signal averaging was implemented both at the oscilloscope level and during post-processing. A minimum of five waveform repetitions were collected per test case and averaged to reduce random noise and emphasize persistent waveform features. These procedures enhanced the signal-to-noise ratio and ensured reliable identification of time-of-flight and amplitude features.

8.2.4 Geometrical Defect Accuracy

Creating physical defects that precisely match simulation assumptions was another significant challenge. Circular holes could be drilled with high precision, but slotted hole notches posed difficulties in maintaining consistent geometry, orientation, and edge definition. Any asymmetry or overcutting could introduce unintended scattering effects, skewing the comparison between experimental and simulated signals. To address this, slotted holes were machined with accuracy and minimal edge burring.

Each damage was inspected carefully to confirm dimensions and alignment.

In addition, a coordinate-based defect mapping system was used. The origin point was defined as the actuator sensor location, and all damage centers were located using laser distance meters and digital markers. This ensured alignment consistency between simulation and physical plates, especially when inserting damage that interacts with the wave at oblique angles.

8.2.5 Simulation Assumptions and Real-World Deviations

While the ABAQUS simulations were carefully constructed, they still relied on simplifying assumptions, such as perfect material homogeneity, linear elasticity, and ideal bonding conditions. In contrast, real materials exhibit variability in elastic properties, microstructural grain orientations, and internal stress residuals, especially in rolled aluminium. These real-world factors, though minor individually, collectively influence wave speed, mode conversion, and attenuation.

To reduce the simulation-experiment gap, material properties were extracted not just from standard databases but also verified using ultrasonic velocity measurements on pristine plates. This allowed for calibration of wave speed in the FE model. The adhesive layer between sensors and the plate was modeled using thin cohesive elements in select simulations, based on measured adhesive thickness. Although not implemented in every run due to computational expense, these additions helped explain minor discrepancies in signal amplitude and phase.

Another adjustment involved mass scaling in the explicit solver, which while necessary for convergence in fine meshes, could distort wave speed if not carefully tuned. Tests were conducted with and without scaling, and

wave arrival times were benchmarked to ensure accuracy.

8.2.6 Data Volume and Machine Learning Compatibility

The sheer volume of data generated from both experiments and simulations posed challenges in terms of storage, organization, and compatibility with machine learning pipelines. The need to track thousands of signal files, metadata, and extracted features for different damage configurations and plate thicknesses required a robust data management strategy.

All files were labeled with a consistent naming convention that included the sensor number, frequency, defect type, plate thickness, and trial number. A centralized database was developed using Python to manage metadata, perform batch processing, and cross-reference experimental and simulated results. Scripts were written to automate feature extraction, such as time-of-flight, amplitude, and envelope characteristics, from both experimental and simulation waveforms, reducing human error and ensuring repeatability.

In preparation for machine learning, all extracted features were normalized using a min-max scaling approach (range: 0 to 1) to avoid training instabilities. Missing or noisy features due to experimental inconsistencies were flagged and excluded from training, ensuring model integrity. The high-fidelity experimental data and corresponding low-fidelity simulation data were paired manually for the most critical damage cases to train the Multi-Fidelity Neural Network (MFNN), which was sensitive to alignment of inputs.

8.2.7 Time Constraints and Trial Management

Finally, the extensive nature of the experiment, which included more than 24 unique plate configurations, required careful scheduling and resource

allocation. Each test had to be conducted multiple times at different excitation frequencies, sensor combinations, and plate orientations. Downtime due to sensor detachment, adhesive curing, or equipment calibration sometimes delayed the experimental workflow.

To maximize efficiency, a batched experimental schedule was implemented. Equipment calibration and plate preparation were batched into parallel tasks, and multiple plates were prepared simultaneously for testing in series. This parallelization minimized lab time while ensuring data consistency. Additionally, every experimental day was logged, including environmental conditions, sensor IDs, and deviations, forming a detailed audit trail to identify and correct anomalies.

In summary, the experimental and numerical phases of this guided wave-based SHM study presented a range of practical and technical challenges. These were met with targeted strategies spanning sensor installation, environmental control, defect fabrication, data processing, and simulation calibration. The rigorous attention to these challenges ensured that the final dataset, used to validate simulations and train the MFNN, was of the highest quality, reproducible, and scientifically credible. These mitigation techniques serve as a useful framework for future SHM investigations involving multi-modal data and hybrid numerical-experimental workflows.

8.3 Future Scope

Building upon this foundation, several promising directions can be pursued. First, the integration of transfer learning offers a route to extend MFNN models to new materials, geometries, or operational environments without retraining from scratch. For example, a model trained on aluminum sheets for aerospace applications could be adapted to composite structures in

other disciplines through fine-tuning its deeper layers. Similarly, domain adaptation techniques could allow compensation for environmental effects such as temperature, humidity, or varying load conditions, which are known to influence guided wave propagation.

Second, the scalability of the MFNN framework can be enhanced through real-time deployment strategies. Embedding the model into edge-computing platforms or smart sensor nodes would allow on-site processing and immediate decision-making, reducing data transmission requirements and enabling continuous monitoring in operational environments such as aircraft wings, pipelines, and bridges.

Third, future work should incorporate uncertainty quantification to provide confidence bounds on predictions, an essential step for industrial acceptance of AI-driven SHM systems. Bayesian neural networks or ensemble learning methods could be coupled with the MFNN to achieve probabilistic outputs, supporting risk-informed maintenance decisions.

Finally, expanding the scope of validation to larger and more complex structures, including curved geometries or multi-layer composites, would further test the model's generalization capacity. Integrating additional sensing modalities, such as fiber optic sensors, MEMS devices, or acoustic emission, could create hybrid systems capable of multi-physics monitoring. This would strengthen the resilience and adaptability of SHM systems across diverse engineering domains.

In conclusion, the MFNN framework developed in this thesis represents a significant advancement in SHM, bridging physics-based and data-driven approaches. Its demonstrated accuracy, robustness, and adaptability provide a strong foundation for future extensions, positioning it as a practical tool for next-generation structural monitoring and predictive maintenance.

Chapter 9 Appendix

Appendix A

Lamb Waves Theory

In thin plates where the in-plane dimensions are much larger than the thickness, a special type of ultrasonic guided wave known as a *Lamb wave* can propagate. These waves require free upper and lower surfaces to sustain their motion and were first theoretically described by Sir Horace Lamb in 1917. Lamb waves emerge when the plate thickness is of the order of a few wavelengths of the excited ultrasonic signal, allowing guided propagation within the plate boundaries [70]. They are particularly attractive for structural health monitoring (SHM) applications because they can travel long distances along the plane of a plate while remaining confined within its thickness, making them capable of interrogating large structural regions with relatively few transducers [5, 47]. Furthermore, they can pass through curved walls, enabling rapid inspection of complex geometries [44].

The governing equations for Lamb waves can be derived from elastodynamic theory using potential functions for longitudinal and shear motions. For a homogeneous isotropic plate, the two-dimensional scalar potentials ϕ (longitudinal) and ψ (transverse) satisfy the Helmholtz

equations:

$$\frac{\partial^2\phi}{\partial x^2}+\frac{\partial^2\phi}{\partial y^2}+\frac{\omega^2}{c_L^2}\phi=0, \quad \frac{\partial^2\psi}{\partial x^2}+\frac{\partial^2\psi}{\partial y^2}+\frac{\omega^2}{c_T^2}\psi=0, \tag{9.1}$$

where ω is the angular frequency, c_L and c_T are the longitudinal (compressional) and shear wave velocities, respectively. These velocities are defined as:

$$c_L=\sqrt{\frac{\lambda+2\mu}{\rho}}, \qquad c_T=\sqrt{\frac{\mu}{\rho}}, \tag{9.2}$$

with λ and μ denoting the Lamé constants and ρ the mass density. For isotropic elastic solids, $\mu = E/[2(1+\nu)]$, where E is Young's modulus and ν is Poisson's ratio.

The displacement potentials can be expressed in general form as:

$$\phi=[A_1\sin(py)+A_2\cos(py)]\,e^{i(kx-\omega t)}, \tag{9.3}$$

with the wave number $k = 2\pi/\lambda$, and

$$p=\sqrt{\frac{\omega^2}{c_L^2}-k^2}, \qquad q=\sqrt{\frac{\omega^2}{c_T^2}-k^2}. \tag{9.4}$$

Here x is the coordinate along the plate and y through its thickness. The constants A_1, A_2, B_1, and B_2 are determined from the traction-free boundary conditions on the plate surfaces. Enforcing these leads to the well-known Rayleigh–Lamb frequency equations (dispersion relations) [**?**]:

$$\tan\left(\tfrac{qd}{2}\right)/\tan\left(\tfrac{pd}{2}\right)=-\frac{4k^2pq}{(q^2-k^2)^2}, \tag{9.5}$$

where d is the plate thickness. Separate equations arise for symmetric and antisymmetric modes, giving rise to families of guided waves: $S_0, S_1, \ldots$ for symmetric modes and $A_0, A_1, \ldots$ for antisymmetric modes.

Figures 9.1 and 9.2 illustrate these two fundamental modal patterns. In the symmetric case, displacements on the upper and lower surfaces are mirror images, with crests coinciding (in-phase). In the antisymmetric case, surface displacements are out-of-phase, with a crest on one surface aligned with a trough on the other.

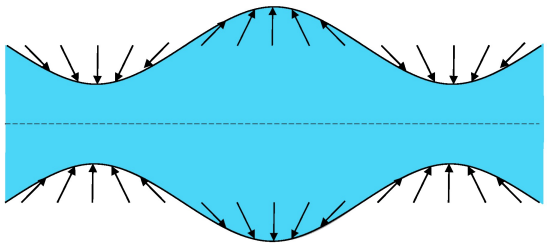


Figure 9.1: Illustration of symmetric Lamb wave motion, where upper and lower surface displacements are in phase [5].

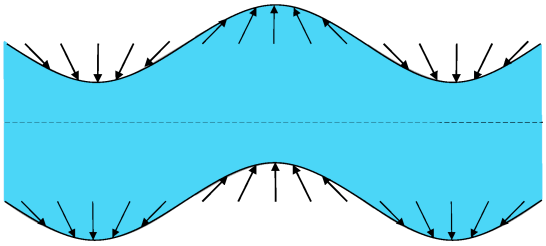


Figure 9.2: Illustration of antisymmetric Lamb wave motion, with surface displacements out of phase [5].

Dispersion of Lamb Waves

An important feature of Lamb waves is their dispersive nature. In dispersive media, wave speed depends on frequency. For Lamb waves, this is captured by expressing angular frequency ω as a function of wave number k:

$$k = \frac{\omega}{c}, \quad \omega = 2\pi f, \tag{9.6}$$

where f is frequency. The relation between ω and k constitutes the dispersion relation [156].

Multiple solutions exist for symmetric and antisymmetric modes, each corresponding to a different guided mode. The phase velocity v_p is defined as:

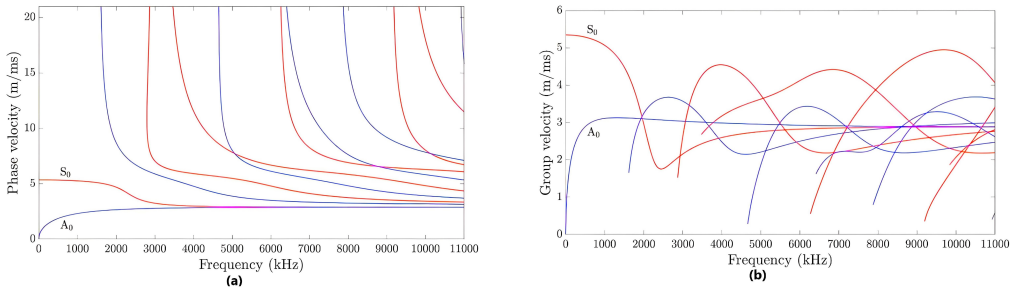
$$v_p = \frac{\omega}{k}, \tag{9.7}$$

and depends on the frequency–thickness product fd, making fd a convenient parameter for dispersion analysis. Figure 9.3 shows dispersion curves of a 1-mm-thick aluminium alloy plate. For low fd, only fundamental modes (S_0, A_0) exist, while higher modes emerge at larger fd.

While phase velocity describes the speed of individual wave crests, practical SHM requires information transfer through modulated wave packets. This is characterized by the group velocity v_g:

$$v_g = \frac{d\omega}{dk}, \tag{9.8}$$

which represents the propagation speed of the energy envelope. Group velocity strongly influences time-of-flight (ToF) measurements and is therefore critical in SHM damage detection.



(a) Phase velocity dispersion curves. (b) Group velocity dispersion curves.

Figure 9.3: Dispersion curves for a 1-mm-thick aluminium alloy 1100: (a) phase velocity and (b) group velocity [6, 4].

Sensor selection

Sensor technology is the cornerstone of ultrasonic based Structural Health Monitoring (SHM), serving as the medium through which guided waves are generated and detected to assess the integrity of materials and structures. The efficacy of any SHM system is directly linked to the precision, sensitivity, and durability of the sensors used. In ultrasonic SHM applications, various sensor technologies are employed depending on the type of material, nature of damage to be detected, operating environment, and monitoring requirements. The primary role of these sensors is to convert electrical signals into mechanical vibrations (actuation) and mechanical responses (reflected or scattered waves) back into electrical signals (reception), a function most efficiently executed using piezoelectric materials. Piezoelectric sensors, particularly Lead Zirconate Titanate (PZT), dominate SHM implementations because of their high electromechanical coupling efficiency, affordability, small size, and ease of integration with structural surfaces [45]. These transducers can be embedded or surface-mounted and are capable of operating across a wide range of frequencies, making them suitable for both low- and high-frequency applications.

The most widely used PZT sensors in SHM are thin disk-shaped elements affixed to the structure's surface using epoxy adhesives. When an alternating voltage is applied, they produce ultrasonic waves that propagate through the host material. For sensing, these devices detect the strain generated by passing waves and convert it into voltage signals for subsequent analysis. The robustness of the bond between the sensor and the substrate is crucial, as it affects the quality and repeatability of signal transmission. Poor bonding can result in signal attenuation and erroneous measurements. To overcome this, researchers have explored

flexible printed PZT arrays, where multiple elements are integrated on a single film, offering high spatial resolution and better conformability on curved surfaces. These sensors are increasingly used in aircraft wings, turbine blades, and pressure vessels, where complex geometries and high operational stress demand reliable and minimally invasive monitoring solutions [51].

Another important class of sensors is Electromagnetic Acoustic Transducers (EMATs), which function without physical contact with the structure. EMATs are particularly useful in environments where the surface is too hot, rough, or moving to permit bonded transducers. They operate by generating ultrasonic waves through the interaction of a magnetic field and induced eddy currents on the metal surface. Although they offer the advantage of non-contact operation and ease of deployment, EMATs generally produce lower signal amplitudes compared to piezoelectric sensors and are limited to conductive materials. Therefore, their usage is common in rail, pipeline, and industrial furnace inspections, where accessibility and high-temperature resilience are prioritized over signal fidelity [157] [116].

Laser ultrasonic systems provide another non contact approach, using pulsed lasers to generate ultrasonic waves and interferometric techniques to detect displacements on the surface. These systems are capable of producing high-resolution measurements and are extremely sensitive to surface defects, but they come with high cost, complexity, and sensitivity to environmental disturbances such as vibrations and air turbulence. As such, laser ultrasonics is more commonly used in laboratory investigations and specialized industrial applications requiring precision measurements or inspection of delicate and high-value components [158].

The integration of sensor networks is fundamental to spatially distributed SHM systems. Arrays of piezoelectric sensors configured

in pitch-catch or pulse-echo arrangements provide valuable information on wave propagation characteristics. In a pitch-catch setup, one sensor transmits the wave while others receive it; in a pulse-echo configuration, the same sensor acts as both transmitter and receiver. The choice of configuration affects the sensitivity and spatial resolution of damage detection. Dense sensor networks offer high accuracy but also increase data complexity and system cost. Recent advances in multiplexing and wireless communication have addressed some of these limitations, enabling smart sensor nodes capable of local processing, data compression, and wireless transmission to central monitoring units [159].

The durability and environmental resistance of sensors are major considerations in SHM, especially for long-term deployments. PZT sensors, while effective, are susceptible to degradation under harsh environmental conditions such as extreme temperatures, moisture, and mechanical fatigue. To enhance longevity, encapsulation techniques using protective coatings, polymers, and composite materials have been developed. Alternatively, piezo-composite materials, combining piezoelectric ceramics and polymer matrices, offer improved flexibility, robustness, and acoustic matching with the host structure, making them suitable for aerospace and marine applications. Furthermore, MEMS-based ultrasonic sensors are gaining popularity due to their miniaturization potential, low power requirements, and integrability with microelectronic circuits. These sensors leverage micro fabrication technologies to produce compact arrays capable of high-frequency operation, opening new possibilities for embedded SHM in smart structures [118].

Sensor placement is another critical factor affecting system performance. Strategic positioning based on finite element modeling and damage index analysis ensures that sensors are optimally located to capture relevant wave interactions. Poor placement can lead to signal

cancellation, weak response, and reduced detectability of flaws. As such, optimization algorithms, including genetic algorithms, simulated annealing, and machine learning methods, have been applied to determine the most effective sensor configurations. Adaptive sensor networks, capable of reconfiguring their sensing pathways based on evolving structural conditions or data trends, are being researched to enhance system resilience and flexibility.

Emerging trends in sensor technology include the development of self-powered and energy-harvesting sensors that eliminate the need for battery replacement in remote or inaccessible locations. These sensors exploit vibrational, thermal, or solar energy to maintain operation over extended periods. Additionally, fiber optic sensors, such as Fiber Bragg Gratings (FBGs), are being integrated into ultrasonic SHM frameworks for their immunity to electromagnetic interference, high sensitivity, and multiplexing capability. Though traditionally used for static strain and temperature monitoring, their adaptation for ultrasonic wave detection is gaining momentum through hybrid sensor systems [160] [160].

In conclusion, sensor technology in ultrasonic SHM is multifaceted, involving a variety of transducer types, configurations, materials, and deployment strategies. The effectiveness of ultrasonic monitoring hinges not only on the physics of wave propagation but also on the reliability and performance of the sensors employed. Advances in materials science, microelectronics, and signal processing continue to expand the capabilities of ultrasonic sensors, making them more efficient, resilient, and intelligent. The future of SHM lies in smart sensor networks that combine sensing, computation, communication, and energy management to offer autonomous, real-time, and scalable solutions for infrastructure monitoring across diverse engineering domains.

Appendix B

Particle Swarm Optimization (PSO)

The machine learning metamodel employed in this research was further enhanced by the application of Particle Swarm Optimization (PSO) as an optimization strategy. PSO is a population-based meta-heuristic algorithm inspired by the collective behaviour observed in flocks of birds or schools of fish [80] [161]. It has gained popularity in the fields of machine learning and optimization because of its simplicity, ability to avoid local minima, and efficiency in high-dimensional search spaces. In this study, PSO was utilized to optimize key hyperparameters of the machine learning models, including the learning rate, the number of hidden units, and kernel coefficients, thereby ensuring that each model performed at its maximum potential prior to comparison within the metamodel framework.

In a PSO system, each potential solution is represented as a particle moving in a multidimensional search space. The position of each particle corresponds to a candidate solution to the optimization problem, while its velocity determines the direction and magnitude of movement. The algorithm maintains a memory of two crucial elements: the best solution found by an individual particle, known as the personal best (p_{best}), and the best solution found by the entire swarm, referred to as the global best (g_{best}). At each iteration, particles update their velocities and positions based on their own experience and the experience of neighbouring particles, striking a balance between exploration of new regions and exploitation of known good solutions.

The velocity update rule for particle i in dimension d can be expressed mathematically as:

$$v_{i,d}(t+1) = w \cdot v_{i,d}(t) + c_1 r_1 \big(p_{i,d} - x_{i,d}(t)\big) + c_2 r_2 \big(g_d - x_{i,d}(t)\big),$$

where $v_{i,d}(t)$ is the velocity of particle i in dimension d at iteration t, $x_{i,d}(t)$ is its position, $p_{i,d}$ is the personal best of the particle, and g_d is the global best solution found so far. The parameters c_1 and c_2 are acceleration coefficients controlling the influence of the cognitive and social components respectively, r_1 and r_2 are random numbers uniformly distributed between 0 and 1, and w is the inertia weight that balances exploration and exploitation. The particle's position is then updated as:

$$x_{i,d}(t+1) = x_{i,d}(t) + v_{i,d}(t+1).$$

The strength of PSO lies in this iterative adjustment, where particles converge towards promising areas of the search space while still maintaining stochastic diversity. Unlike gradient-based optimization methods, PSO does not require derivative information, making it suitable for complex, non-differentiable, or multimodal objective functions often encountered in machine learning problems.

Within the context of this thesis, PSO was employed to optimize the hyperparameters of the deterministic models (Polynomial Regression, Support Vector Machines, and Artificial Neural Networks) as well as the probabilistic models (Bayesian Regression and Stochastic Gradient Descent). For instance, in the case of ANN, PSO optimized the learning rate, the number of hidden layers, and the number of neurons per layer, leading to faster convergence and improved generalization. Similarly, in SVM models, the kernel type and penalty parameters were tuned using PSO, while in Bayesian Regression and SGD models, the algorithm refined regularization terms and step sizes. This automated optimization process

ensured that each model operated at its best configuration before being benchmarked in the metamodel framework.

The use of PSO in this research also demonstrated the ability of meta-heuristic optimization to significantly reduce trial-and-error in model development. Rather than relying on manual tuning or grid search methods, PSO provided an efficient global search mechanism, requiring relatively fewer evaluations while delivering highly competitive results. Importantly, PSO improved not only the predictive accuracy of the models but also the robustness of predictions when applied to experimental and simulated datasets of varying fidelity.

In conclusion, the incorporation of Particle Swarm Optimization contributed substantially to the performance of the proposed SHM framework. By providing a systematic and efficient means of tuning hyperparameters, PSO enhanced the accuracy of damage prediction, improved localization outcomes, and yielded more reliable RUL estimation. Its integration with the machine learning metamodel highlights the complementary role of optimization algorithms in advancing data-driven approaches to structural health monitoring.

Balanced Sampling

In many machine learning applications, especially those involving classification across multiple categories, the distribution of samples among classes is rarely uniform. This imbalance often results in models that are biased toward the majority class, achieving artificially high accuracy while performing poorly on underrepresented categories [162, 163]. Balanced sampling is a strategy to mitigate this issue by ensuring that the training dataset contains approximately equal representation of each class. The aim is to encourage the model to learn discriminative patterns from minority classes without being dominated by the statistical prevalence of

majority classes.

Several approaches to balancing datasets exist in the literature. The simplest method is random undersampling of the majority class, which reduces the size of the dataset but equalizes class counts. Alternatively, random oversampling or synthetic data generation techniques such as the Synthetic Minority Oversampling Technique (SMOTE) [162] replicate or interpolate new samples for minority classes. More advanced strategies include ensemble-based sampling [118] and cost-sensitive learning, where class imbalance is addressed at the algorithmic level through weighted loss functions [164].

The choice of balancing strategy depends on the problem domain and the degree of imbalance. In structural health monitoring (SHM), data imbalance arises naturally because pristine or common defect scenarios are easier to obtain than rare or complex damage configurations. Thus, balanced sampling serves not only as a statistical remedy but also as a mechanism to enhance generalization and fairness in damage prediction. By aligning class representation, balanced datasets prevent bias in decision boundaries, reduce overfitting to dominant classes, and improve robustness when models are deployed on unseen data.

In the present research, balanced sampling was particularly necessary because the dataset constructed from simulations and experiments was inherently skewed. Circular damage configurations, especially 4–7 mm holes, were abundant due to their relative ease of simulation and experimental reproduction. In contrast, slotted hole damage cases were comparatively underrepresented. Without addressing this imbalance, the machine learning model would have likely overfitted to circular damage characteristics, reducing its effectiveness in identifying or localizing less common defect types.

The central aim of this work was to develop a robust multi-fidelity

neural network (MFNN) capable of accurately predicting damage indices and localizing different types of damage. Since the eventual deployment of SHM systems may involve detecting delaminations or fatigue-induced cracks, it was essential that the learning process be unbiased across damage types. Prior studies in SHM have also highlighted the importance of handling imbalance, noting that algorithms trained on skewed data often fail to generalize to rare but safety-critical defects [165, 166].

Balanced sampling was therefore introduced as a critical preprocessing step, ensuring that the network encountered an equal number of circular and slotted hole samples during training. This design choice improved the generalization capacity of the MFNN and enhanced its ability to perform under conditions not dominated by a single defect morphology. By enforcing class parity, the model was trained to allocate equal representational power across all defect types, thereby aligning the research objectives with practical requirements for reliable SHM.

The implementation of balanced sampling in this study followed a systematic procedure integrated within the dataset preparation pipeline. First, all cases were parsed from simulation and experimental files, and each data point was encoded into a five-dimensional feature vector:

$X = [\text{Material}, \text{Damage Type}, \text{Thickness}, \text{Frequency}, \text{Damage Size}]$

The target variable was the damage index (DI), computed from differences in time-of-flight and amplitude between simulated and experimental guided wave signals.

Once the raw dataset was constructed, cases were grouped into three subsets according to damage type: circular, and slotted holes. The number of samples per group was then determined, and the smallest group size was identified as the reference. For instance, if slotted hole cases were the least frequent with N samples, then circular holes were randomly downsampled (without replacement) to N samples each. This produced two equally sized

groups. The balanced groups were then combined and shuffled to form the final dataset. Randomization ensured that the order of samples did not bias the training process.

This approach corresponds to a form of undersampling, which trades dataset volume for class balance. Although undersampling may reduce the total number of training points, it was deemed preferable here because synthetic oversampling could distort the physics-informed nature of the data. After balancing, features were scaled using a min–max transformation to the range [0, 1] before being passed to the MFNN. As shown in Section 5.4, this procedure successfully equalized the representation of damage types, allowing the network to learn uniformly across all categories. The balanced dataset became the foundation for training the MFNN, and subsequent evaluation confirmed that the model achieved improved robustness and fairness in predicting DI values across damage scenarios.

Core ML Metamodel Implementation

The core machine learning metamodel used for damage index (DI) prediction from ultrasonic guided wave features was implemented in Python using the `scikit-learn` library. The dataset consisted of features representing plate thickness, excitation frequency, and damage size, with the target variable being a normalized DI. To ensure methodological rigor, the data were split into distinct training (60%), validation (20%), and test (20%) sets. The splitting was performed at the measurement level, ensuring no data from the same excitation appeared in more than one set, thereby preventing data leakage.

Each model was constructed as a `scikit-learn` *Pipeline* to ensure transformations were applied consistently and without data leakage from the validation or test sets. For most models, including Support Vector

Regression (SVM), Artificial Neural Network (ANN), Bayesian Ridge (BR), and Stochastic Gradient Descent (SGD), the pipeline consisted of Min-Max scaling followed by the regression algorithm. The Polynomial Regression (PR) pipeline was structured as Min-Max scaling, then polynomial feature expansion, and finally linear regression. This order ensures that all features contribute equitably to the polynomial expansion.

The best model was selected based on its performance on the validation set, evaluated using Root Mean Squared Error (RMSE) and R^2 scores. A final, unbiased evaluation was then performed on the held-out test set to assess the selected model's generalization capability. Key hyperparameters and configuration details are summarized in Table 9.1.

Table 9.1: Model Configuration and Hyperparameters

Parameter	**Value / Setting**
Data Split (Train/Val/Test)	60% / 20% / 20%
Splitting Strategy	Per-measurement (no cross-set leakage)
Artificial Neural Network (ANN)	
Hidden Layers	[64, 32]
Activation Function	ReLU
Optimizer	Adam ($\alpha = 0.001$)
Batch Size	32
Max Epochs	500 (with Early Stopping)
Other Models	
Polynomial Degree (PR)	2
SVR Kernel	RBF ($C = 10.0$, $\varepsilon = 0.01$)

This implementation ensures full reproducibility and a fair comparison across all candidate models. The disciplined use of pipelines and a dedicated test set provides a robust and unbiased estimate of the final model's predictive accuracy.

Appendix C

Complete Dataset of Validations Results

Table 9.2: Normalized ToF, Peak Amp, and DI values from experimental and simulation data for Plate 1 to Plate 7.

Thickness (mm)	**Damage type**	**Damage size (mm)**	**Freq. (kHz)**	**Sensor**	**ToF (Exp.)**	**ToF (Sim.)**	**Peak Amp (Exp.)**	**Peak Amp (Sim.)**	**DI (Exp.)**	**DI (Sim.)**
1.5	Circular	4	300	S2	0.012	0.0149	0.9577	0.9617	0.0888	0.0735
1.5	Circular	4	300	S3	0.0241	0.0187	0.9516	0.955	0.1443	0.1158
1.5	Circular	4	300	S4	0.0175	0.0181	0.9424	0.9676	0.1802	0.0481
1.5	Circular	4	310	S2	0.0147	0.0139	0.9387	0.9499	0.1945	0.1337
1.5	Circular	4	310	S3	0.002	0.0114	0.9356	0.9605	0.2193	0.0729
1.5	Circular	4	310	S4	0.0102	0.0149	0.9198	0.9652	0.2875	0.055
1.5	Circular	4	320	S2	0.01	0.0135	0.949	0.9526	0.1332	0.1184
1.5	Circular	4	320	S3	0.0132	0.0185	0.9591	0.9634	0.0835	0.0708
1.5	Circular	4	320	S4	0.001	0.0052	0.9606	0.9523	0.0909	0.1247
1.5	Circular	4	330	S2	0.0061	0.0135	0.9624	0.9539	0.0698	0.1115
1.5	Circular	4	330	S3	0.001	0.0121	0.9672	0.9643	0.056	0.0539
1.5	Circular	4	330	S4	0.006	0.0141	0.948	0.9626	0.1464	0.0671
1.5	Circular	4	340	S2	0.0151	0.0186	0.9508	0.9544	0.1311	0.1189
1.5	Circular	4	340	S3	0.0132	0.0172	0.9382	0.9637	0.194	0.0671
1.5	Circular	4	340	S4	0.0046	0.0131	0.9439	0.9616	0.1702	0.0703
1.5	Circular	4	350	S2	0.0181	0.0129	0.9507	0.9508	0.1374	0.1274
1.5	Circular	4	350	S3	0.018	0.009	0.9515	0.9746	0.1332	0.0989
1.5	Circular	4	350	S4	0.0096	0.0079	0.9646	0.9475	0.0518	0.1448
1.5	Circular	4	360	S2	0.0173	0.0159	0.941	0.9599	0.1871	0.0846
1.5	Circular	4	360	S3	0.0098	0.0091	0.9583	0.9541	0.0846	0.1078
1.5	Circular	4	360	S4	0.0136	0.0081	0.9428	0.9524	0.1702	0.1184
1.5	Circular	4	370	S2	0.0189	0.0206	0.9607	0.9489	0.0862	0.1522
1.5	Circular	4	370	S3	0.0125	0.0168	0.9489	0.9383	0.1369	0.2003
1.5	Circular	4	370	S4	0.0126	0.0214	0.9505	0.9493	0.1284	0.1512

Continued on next page

Table 9.2 – Continued from previous page

Thickness (mm)	Damage type	Damage size (mm)	Freq. (kHz)	Sensor	ToF (Exp.)	ToF (Sim.)	Peak Amp (Exp.)	Peak Amp (Sim.)	DI (Exp.)	DI (Sim.)
1.5	Circular	4	380	S2	0.014	0.0099	0.9447	0.9542	0.1617	0.1057
1.5	Circular	4	380	S3	0.0045	0.0107	0.9508	0.9629	0.1337	0.0592
1.5	Circular	4	380	S4	0.0106	0.0129	0.9395	0.9476	0.1823	0.1438
1.5	Circular	4	390	S2	0.01	0.0197	0.9555	0.9516	0.0983	0.1358
1.5	Circular	4	390	S3	0.0185	0.0065	0.9605	0.9584	0.0867	0.0899
1.5	Circular	4	390	S4	0.0145	0.0122	0.9436	0.9684	0.1686	0.0328
1.5	Circular	4	400	S2	0.0008	0.0081	0.9465	0.9494	0.1638	0.1348
1.5	Circular	4	400	S3	0.0118	0.0124	0.9489	0.9599	0.1348	0.0782
1.5	Circular	4	400	S4	0.011	0.013	0.9622	0.9694	0.0629	0.0291
1.5	Circular	4	410	S2	0.0224	0.0172	0.9452	0.9503	0.1749	0.1379
1.5	Circular	4	410	S3	0.0206	0.0112	0.9528	0.9508	0.1316	0.1242
1.5	Circular	4	410	S4	0.0087	0.0186	0.9447	0.96	0.1586	0.0893
1.5	Circular	4	420	S2	0.0144	0.0114	0.9522	0.9547	0.1226	0.1036
1.5	Circular	4	420	S3	0.0171	0.0157	0.9571	0.9488	0.102	0.1432
1.5	Circular	4	420	S4	0.0117	0.006	0.9452	0.9671	0.1543	0.0449
1.5	Circular	4	430	S2	0.0113	0.0175	0.9371	0.9563	0.1966	0.1068
1.5	Circular	4	430	S3	0.011	0.0126	0.9677	0.9378	0.0344	0.1956
1.5	Circular	4	430	S4	0.009	0.0191	0.9504	0.9445	0.1279	0.1723
1.5	Circular	4	440	S2	0.0241	0.0162	0.9268	0.9595	0.2754	0.0872
1.5	Circular	4	440	S3	0.0174	0.0095	0.9611	0.9579	0.0809	0.0872
1.5	Circular	4	440	S4	0.0082	0.0096	0.9446	0.9586	0.1596	0.0835
1.5	Circular	4	450	S2	0.0102	0.0116	0.958	0.9398	0.0851	0.1823
1.5	Circular	4	450	S3	0.0201	0.0184	0.9585	0.959	0.1004	0.0946
1.5	Circular	4	450	S4	0.0112	0.0119	0.9561	0.9597	0.0957	0.0782
1.5	Circular	4	460	S2	0.0181	0.0142	0.9413	0.9464	0.1871	0.1533
1.5	Circular	4	460	S3	0.0077	0.0072	0.9355	0.9516	0.2088	0.1247
1.5	Circular	4	460	S4	0.0197	0.0107	0.9454	0.9583	0.1686	0.0835
1.5	Circular	4	470	S2	0.0069	0.0097	0.9747	0.9546	0.0032	0.1041
1.5	Circular	4	470	S3	0.0092	0.0126	0.9337	0.9485	0.2156	0.1385
1.5	Circular	4	470	S4	0.0107	0.0183	0.9496	0.942	0.129	0.1839
1.5	Circular	4	480	S2	0.0087	0.0157	0.9354	0.9552	0.2077	0.1089
1.5	Circular	4	480	S3	0.0109	0.0151	0.9576	0.9678	0.0872	0.0412
1.5	Circular	4	480	S4	0.0169	0.0174	0.9369	0.9525	0.2082	0.1268
1.5	Circular	4	490	S2	0.0115	0.0141	0.9567	0.9669	0.093	0.0444
1.5	Circular	4	490	S3	0.0076	0.0192	0.9535	0.9723	0.1136	0.0254
1.5	Circular	4	490	S4	0.0075	0.0141	0.9477	0.9525	0.1443	0.1205
1.5	Circular	4	500	S2	0.0059	0.013	0.9381	0.9579	0.1987	0.0899
1.5	Circular	4	500	S3	0.0193	0.0086	0.9432	0.9546	0.1792	0.1057

Continued on next page

Table 9.2 – Continued from previous page

Thickness (mm)	Damage type	Damage size (mm)	Freq. (kHz)	Sensor	ToF (Exp.)	ToF (Sim.)	Peak Amp (Exp.)	Peak Amp (Sim.)	DI (Exp.)	DI (Sim.)
1.5	Circular	4	500	S4	0.017	0.0118	0.9336	0.9614	0.2262	0.0692
1.5	Circular	5	300	S2	0.0132	0.0102	0.9293	0.9498	0.2415	0.1284
1.5	Circular	5	300	S3	0.0128	0.0114	0.9461	0.9364	0.1517	0.2003
1.5	Circular	5	300	S4	0.0083	0.0172	0.9351	0.9241	0.2098	0.2764
1.5	Circular	5	310	S2	0.0093	0.0098	0.9358	0.936	0.204	0.2024
1.5	Circular	5	310	S3	0.012	0.0158	0.9292	0.941	0.24	0.1839
1.5	Circular	5	310	S4	0.001	0.0145	0.9324	0.9422	0.24	0.1755
1.5	Circular	5	320	S2	0.0071	0.0102	0.9347	0.9435	0.2146	0.1617
1.5	Circular	5	320	S3	0.0136	0.0124	0.9324	0.9467	0.2262	0.148
1.5	Circular	5	320	S4	0.0192	0.0091	0.9589	0.9304	0.0962	0.2331
1.5	Circular	5	330	S2	0.0095	0.0155	0.9368	0.9364	0.1987	0.2082
1.5	Circular	5	330	S3	0.0074	0.0163	0.9318	0.941	0.2289	0.1855
1.5	Circular	5	330	S4	0.0218	0.0196	0.9363	0.9323	0.2204	0.2378
1.5	Circular	5	340	S2	0.0241	0.008	0.9359	0.9417	0.2273	0.1755
1.5	Circular	5	340	S3	0.0164	0.0147	0.9189	0.957	0.3029	0.0978
1.5	Circular	5	340	S4	0.0092	0.012	0.9216	0.9315	0.2791	0.2273
1.5	Circular	5	350	S2	0.0137	0.0157	0.9289	0.9421	0.2447	0.1786
1.5	Circular	5	350	S3	0.0163	0.0123	0.9105	0.9273	0.3467	0.25
1.5	Circular	5	350	S4	0.0138	0.0169	0.9108	0.9397	0.3399	0.1934
1.5	Circular	5	360	S2	0.0092	0.0153	0.9184	0.9495	0.2965	0.1385
1.5	Circular	5	360	S3	0.0136	0.011	0.9304	0.9502	0.2363	0.1263
1.5	Circular	5	360	S4	0.0078	0.0249	0.9383	0.9443	0.194	0.1845
1.5	Circular	5	370	S2	0.0179	0.0092	0.9249	0.9298	0.2733	0.2363
1.5	Circular	5	370	S3	0.0181	0.0106	0.9401	0.9258	0.1934	0.2548
1.5	Circular	5	370	S4	0.0149	0.0189	0.9247	0.9423	0.269	0.1839
1.5	Circular	5	380	S2	0.0141	0.0093	0.9324	0.9469	0.2267	0.1459
1.5	Circular	5	380	S3	0.0205	0.0167	0.9181	0.9299	0.3145	0.2447
1.5	Circular	5	380	S4	0.012	0.0103	0.9376	0.9278	0.195	0.2447
1.5	Circular	5	390	S2	0.017	0.0145	0.9202	0.9464	0.2965	0.1533
1.5	Circular	5	390	S3	0.0129	0.0195	0.9465	0.9455	0.1501	0.1675
1.5	Circular	5	390	S4	0.0213	0.0134	0.9548	0.9456	0.1216	0.1554
1.5	Circular	5	400	S2	0.0234	0.016	0.9285	0.9413	0.2648	0.1829
1.5	Circular	5	400	S3	0.0118	0.0145	0.9431	0.9196	0.166	0.2949
1.5	Circular	5	400	S4	0.0176	0.0133	0.9392	0.9448	0.1977	0.1596
1.5	Circular	5	410	S2	0.0268	0.0144	0.9115	0.9493	0.3615	0.1374
1.5	Circular	5	410	S3	0.0101	0.0164	0.9286	0.9053	0.241	0.3742
1.5	Circular	5	410	S4	0.013	0.0176	0.9333	0.9356	0.2199	0.2162
1.5	Circular	5	420	S2	0.0106	0.0197	0.9308	0.9328	0.2283	0.2347

Continued on next page

Table 9.2 – Continued from previous page

Thickness (mm)	Damage type	Damage size (mm)	Freq. (kHz)	Sensor	ToF (Exp.)	ToF (Sim.)	Peak Amp (Exp.)	Peak Amp (Sim.)	DI (Exp.)	DI (Sim.)
1.5	Circular	5	420	S3	0.0197	0.0163	0.9257	0.9365	0.2727	0.2093
1.5	Circular	5	420	S4	0.0223	0.0164	0.9247	0.9348	0.2828	0.2183
1.5	Circular	5	430	S2	0.0108	0.0117	0.8972	0.9284	0.4064	0.2437
1.5	Circular	5	430	S3	0.0091	0.0094	0.94	0.9432	0.1823	0.1649
1.5	Circular	5	430	S4	0.0069	0.016	0.9448	0.9419	0.1612	0.1797
1.5	Circular	5	440	S2	0.0117	0.0116	0.9289	0.9339	0.2405	0.2141
1.5	Circular	5	440	S3	0.0161	0.0193	0.9157	0.9289	0.3187	0.2548
1.5	Circular	5	440	S4	0.006	0.0076	0.9256	0.933	0.2643	0.2225
1.5	Circular	5	450	S2	0.0123	0.0159	0.9311	0.9533	0.2299	0.12
1.5	Circular	5	450	S3	0.0149	0.0162	0.9096	0.9189	0.3488	0.3023
1.5	Circular	5	450	S4	0.0132	0.0173	0.927	0.9304	0.2537	0.2431
1.5	Circular	5	460	S2	0.0086	0.0079	0.9224	0.9319	0.2759	0.2273
1.5	Circular	5	460	S3	0.0037	0.0162	0.937	0.9369	0.2082	0.2072
1.5	Circular	5	460	S4	0.0168	0.0116	0.9315	0.9306	0.2363	0.2315
1.5	Circular	5	470	S2	0.0087	0.02	0.9452	0.9421	0.1559	0.1866
1.5	Circular	5	470	S3	0.0182	0.0076	0.923	0.9363	0.2844	0.2051
1.5	Circular	5	470	S4	0.0107	0.0146	0.9307	0.9313	0.2289	0.2331
1.5	Circular	5	480	S2	0.0178	0.0165	0.9264	0.9369	0.2653	0.2077
1.5	Circular	5	480	S3	0.0105	0.0149	0.9324	0.9313	0.2199	0.2341
1.5	Circular	5	480	S4	0.0095	0.0139	0.9466	0.9232	0.1469	0.2748
1.5	Circular	5	490	S2	0.023	0.0164	0.9295	0.9273	0.259	0.2579
1.5	Circular	5	490	S3	0.0151	0.0064	0.9365	0.9335	0.2072	0.222
1.5	Circular	5	490	S4	0.0153	0.0122	0.9333	0.9282	0.2246	0.2452
1.5	Circular	5	500	S2	0.0112	0.0181	0.919	0.9343	0.2918	0.2241
1.5	Circular	5	500	S3	0.0275	0.0166	0.9116	0.9237	0.3621	0.277
1.5	Circular	5	500	S4	0.0104	0.0128	0.944	0.9288	0.1586	0.2431
1.5	Circular	6	300	S2	0.0169	0.0092	0.9195	0.9221	0.3002	0.277
1.5	Circular	6	300	S3	0.0248	0.0108	0.9207	0.9289	0.3087	0.2389
1.5	Circular	6	300	S4	0.0221	0.0169	0.9284	0.9214	0.2632	0.2902
1.5	Circular	6	310	S2	0.0187	0.0171	0.9117	0.9218	0.3446	0.2886
1.5	Circular	6	310	S3	0.0083	0.0025	0.9077	0.9217	0.3547	0.2918
1.5	Circular	6	310	S4	0.0225	0.0078	0.9032	0.9062	0.3975	0.3636
1.5	Circular	6	320	S2	0.014	0.0109	0.9068	0.9275	0.3615	0.2468
1.5	Circular	6	320	S3	0.0117	0.0171	0.91	0.9207	0.3404	0.2939
1.5	Circular	6	320	S4	0.0202	0.0146	0.9208	0.9231	0.2997	0.277
1.5	Circular	6	330	S2	0.009	0.0128	0.917	0.9256	0.3039	0.26
1.5	Circular	6	330	S3	0.0161	0.0155	0.9087	0.9208	0.3557	0.2907
1.5	Circular	6	330	S4	0.0168	0.011	0.9031	0.926	0.3864	0.2542

Continued on next page

Table 9.2 – Continued from previous page

Thickness (mm)	Damage type	Damage size (mm)	Freq. (kHz)	Sensor	ToF (Exp.)	ToF (Sim.)	Peak Amp (Exp.)	Peak Amp (Sim.)	DI (Exp.)	DI (Sim.)
1.5	Circular	6	340	S2	0.0104	0.0226	0.9219	0.9158	0.2754	0.3303
1.5	Circular	6	340	S3	0.0104	0.0245	0.9209	0.9173	0.2812	0.3261
1.5	Circular	6	340	S4	0.0189	0.0211	0.8933	0.9171	0.4424	0.3208
1.5	Circular	6	350	S2	0.0182	0.0219	0.9241	0.9203	0.278	0.3055
1.5	Circular	6	350	S3	0.0124	0.0089	0.9104	0.9246	0.3399	0.2637
1.5	Circular	6	350	S4	0.0125	0.0145	0.9091	0.9162	0.3467	0.3129
1.5	Circular	6	360	S2	0.0071	0.0145	0.9094	0.9253	0.3478	0.2648
1.5	Circular	6	360	S3	0.0141	0.016	0.9106	0.9122	0.342	0.3367
1.5	Circular	6	360	S4	0.0139	0.0127	0.9149	0.9219	0.3192	0.2796
1.5	Circular	6	370	S2	0.0094	0.018	0.8961	0.9179	0.4138	0.3108
1.5	Circular	6	370	S3	0.0117	0.011	0.9073	0.9212	0.3547	0.2796
1.5	Circular	6	370	S4	0.0177	0.0156	0.914	0.9238	0.3309	0.2748
1.5	Circular	6	380	S2	0.0197	0.0128	0.9168	0.9126	0.3198	0.3288
1.5	Circular	6	380	S3	0.0101	0.0227	0.9094	0.922	0.3425	0.2981
1.5	Circular	6	380	S4	0.0056	0.0191	0.9196	0.9279	0.297	0.2595
1.5	Circular	6	390	S2	0.0132	0.0212	0.9205	0.9266	0.2881	0.2706
1.5	Circular	6	390	S3	0.0197	0.013	0.9157	0.925	0.3256	0.2637
1.5	Circular	6	390	S4	0.0175	0.0153	0.9198	0.9126	0.2997	0.3335
1.5	Circular	6	400	S2	0.0157	0.0186	0.8915	0.9188	0.4456	0.3071
1.5	Circular	6	400	S3	0.0079	0.0187	0.9099	0.9196	0.3441	0.3034
1.5	Circular	6	400	S4	0.0153	0.0202	0.9143	0.9079	0.3245	0.3679
1.5	Circular	6	410	S2	0.0201	0.0141	0.9065	0.9142	0.3747	0.3224
1.5	Circular	6	410	S3	0.0103	0.0098	0.9002	0.9244	0.3906	0.2637
1.5	Circular	6	410	S4	0.0067	0.0135	0.9191	0.9122	0.297	0.3319
1.5	Circular	6	420	S2	0.0066	0.0174	0.8998	0.9299	0.399	0.2458
1.5	Circular	6	420	S3	0.0134	0.021	0.9181	0.9034	0.3007	0.3927
1.5	Circular	6	420	S4	0.0226	0.0089	0.9094	0.9072	0.3642	0.3562
1.5	Circular	6	430	S2	0.0155	0.0123	0.9373	0.9161	0.203	0.3092
1.5	Circular	6	430	S3	0.0228	0.0127	0.9037	0.9146	0.3948	0.3182
1.5	Circular	6	430	S4	0.0189	0.0098	0.8884	0.9218	0.4688	0.2775
1.5	Circular	6	440	S2	0.0148	0.0089	0.9081	0.914	0.3562	0.3203
1.5	Circular	6	440	S3	0.0271	0.0136	0.9251	0.9162	0.2896	0.3113
1.5	Circular	6	440	S4	0.0146	0.0158	0.9122	0.9206	0.3346	0.2923
1.5	Circular	6	450	S2	0.0111	0.0141	0.8956	0.9204	0.4154	0.2896
1.5	Circular	6	450	S3	0.0205	0.0138	0.9062	0.9248	0.3774	0.2659
1.5	Circular	6	450	S4	0.0199	0.014	0.9045	0.9241	0.3853	0.2706
1.5	Circular	6	460	S2	0.0085	0.016	0.8978	0.923	0.407	0.2801
1.5	Circular	6	460	S3	0.0158	0.0197	0.9136	0.9168	0.3293	0.3198

Continued on next page

Table 9.2 – Continued from previous page

Thickness (mm)	Damage type	Damage size (mm)	Freq. (kHz)	Sensor	ToF (Exp.)	ToF (Sim.)	Peak Amp (Exp.)	Peak Amp (Sim.)	DI (Exp.)	DI (Sim.)
1.5	Circular	6	460	S4	0.0195	0.0174	0.9055	0.9149	0.3795	0.3251
1.5	Circular	6	470	S2	0.0142	0.0152	0.8945	0.9227	0.4276	0.2801
1.5	Circular	6	470	S3	0.0143	0.0174	0.9054	0.9171	0.3695	0.314
1.5	Circular	6	470	S4	0.0241	0.009	0.9236	0.9088	0.2923	0.3473
1.5	Circular	6	480	S2	0.0115	0.0239	0.9149	0.9118	0.314	0.3541
1.5	Circular	6	480	S3	0.0153	0.0094	0.8906	0.9158	0.4498	0.3103
1.5	Circular	6	480	S4	0.0208	0.0133	0.915	0.9067	0.3309	0.361
1.5	Circular	6	490	S2	0.0161	0.0134	0.905	0.9265	0.3753	0.2563
1.5	Circular	6	490	S3	0.0239	0.0145	0.9085	0.9255	0.3716	0.2643
1.5	Circular	6	490	S4	0.0183	0.0118	0.911	0.9112	0.3478	0.334
1.5	Circular	6	500	S2	0.0249	0.0177	0.9226	0.9164	0.2992	0.3182
1.5	Circular	6	500	S3	0.0112	0.0206	0.9096	0.9137	0.342	0.3377
1.5	Circular	6	500	S4	0.0161	0.0193	0.8981	0.9188	0.4117	0.3081
1.5	Circular	7	300	S2	0.0271	0.013	0.8972	0.9088	0.4371	0.3494
1.5	Circular	7	300	S3	0.0142	0.0103	0.8902	0.9067	0.4498	0.3562
1.5	Circular	7	300	S4	0.0186	0.0154	0.8952	0.885	0.4318	0.4794
1.5	Circular	7	310	S2	0.012	0.0137	0.9151	0.9109	0.314	0.3399
1.5	Circular	7	310	S3	0.0313	0.0219	0.8886	0.9095	0.4905	0.3626
1.5	Circular	7	310	S4	0.0193	0.0231	0.9047	0.9	0.3827	0.4149
1.5	Circular	7	320	S2	0.0218	0.0221	0.902	0.9012	0.4022	0.407
1.5	Circular	7	320	S3	0.026	0.011	0.8944	0.9138	0.4503	0.3192
1.5	Circular	7	320	S4	0.0148	0.018	0.8944	0.9104	0.4286	0.3504
1.5	Circular	7	330	S2	0.0181	0.022	0.8969	0.9124	0.4218	0.3473
1.5	Circular	7	330	S3	0.0175	0.0088	0.8984	0.9001	0.4128	0.3938
1.5	Circular	7	330	S4	0.0098	0.0141	0.8821	0.907	0.4873	0.361
1.5	Circular	7	340	S2	0.0253	0.0175	0.909	0.9112	0.3716	0.3451
1.5	Circular	7	340	S3	0.0201	0.0195	0.8906	0.8964	0.4588	0.4271
1.5	Circular	7	340	S4	0.0173	0.0085	0.8874	0.9032	0.4709	0.3779
1.5	Circular	7	350	S2	0.0201	0.0156	0.8847	0.9024	0.49	0.3885
1.5	Circular	7	350	S3	0.0137	0.0154	0.8886	0.8986	0.4572	0.4075
1.5	Circular	7	350	S4	0.0284	0.0199	0.9021	0.9045	0.4138	0.3853
1.5	Circular	7	360	S2	0.0177	0.0167	0.8954	0.9157	0.4292	0.3198
1.5	Circular	7	360	S3	0.0094	0.0222	0.8857	0.9055	0.4688	0.3842
1.5	Circular	7	360	S4	0.0219	0.017	0.8906	0.9076	0.4625	0.3636
1.5	Circular	7	370	S2	0.0185	0.0206	0.8798	0.894	0.5132	0.4419
1.5	Circular	7	370	S3	0.0194	0.012	0.8971	0.8978	0.4234	0.4059
1.5	Circular	7	370	S4	0.0248	0.0164	0.889	0.9025	0.4762	0.389
1.5	Circular	7	380	S2	0.0021	0.0095	0.8801	0.8976	0.5122	0.4059

Continued on next page

Table 9.2 – Continued from previous page

Thickness (mm)	Damage type	Damage size (mm)	Freq. (kHz)	Sensor	ToF (Exp.)	ToF (Sim.)	Peak Amp (Exp.)	Peak Amp (Sim.)	DI (Exp.)	DI (Sim.)
1.5	Circular	7	380	S3	0.0094	0.0176	0.9083	0.9101	0.3494	0.351
1.5	Circular	7	380	S4	0.0169	0.0181	0.8965	0.906	0.4212	0.3737
1.5	Circular	7	390	S2	0.0207	0.0179	0.9019	0.8901	0.4006	0.4572
1.5	Circular	7	390	S3	0.0181	0.0124	0.8961	0.9064	0.4265	0.3605
1.5	Circular	7	390	S4	0.0224	0.0122	0.8853	0.9016	0.4915	0.3858
1.5	Circular	7	400	S2	0.0104	0.0184	0.8986	0.9118	0.3985	0.3436
1.5	Circular	7	400	S3	0.0163	0.0156	0.8735	0.9118	0.5423	0.3383
1.5	Circular	7	400	S4	0.0136	0.0202	0.868	0.8976	0.5661	0.4223
1.5	Circular	7	410	S2	0.0183	0.0186	0.8946	0.9063	0.4345	0.3732
1.5	Circular	7	410	S3	0.0261	0.0148	0.8737	0.8968	0.5597	0.416
1.5	Circular	7	410	S4	0.0129	0.0113	0.9017	0.9098	0.3864	0.3409
1.5	Circular	7	420	S2	0.0149	0.0206	0.898	0.9037	0.4101	0.3906
1.5	Circular	7	420	S3	0.0139	0.0229	0.8971	0.8981	0.4128	0.4249
1.5	Circular	7	420	S4	0.0094	0.0177	0.873	0.893	0.5359	0.4413
1.5	Circular	7	430	S2	0.0186	0.0188	0.8902	0.8955	0.4582	0.4308
1.5	Circular	7	430	S3	0.0244	0.0199	0.8819	0.9041	0.5132	0.3874
1.5	Circular	7	430	S4	0.0135	0.013	0.8776	0.9045	0.5153	0.3721
1.5	Circular	7	440	S2	0.0273	0.0214	0.8847	0.8982	0.5037	0.4212
1.5	Circular	7	440	S3	0.0181	0.0103	0.8945	0.9036	0.4345	0.3726
1.5	Circular	7	440	S4	0.0146	0.0122	0.8985	0.9097	0.407	0.343
1.5	Circular	7	450	S2	0.0113	0.0146	0.8796	0.898	0.5005	0.4091
1.5	Circular	7	450	S3	0.0202	0.0141	0.8901	0.8953	0.4619	0.4228
1.5	Circular	7	450	S4	0.0225	0.0173	0.8864	0.898	0.4857	0.4149
1.5	Circular	7	460	S2	0.0137	0.0214	0.8963	0.8858	0.4165	0.4868
1.5	Circular	7	460	S3	0.0215	0.0201	0.888	0.893	0.4752	0.4466
1.5	Circular	7	460	S4	0.0083	0.0108	0.892	0.9071	0.4376	0.3541
1.5	Circular	7	470	S2	0.0141	0.0132	0.892	0.8949	0.4403	0.4234
1.5	Circular	7	470	S3	0.0122	0.014	0.8918	0.8902	0.4376	0.4498
1.5	Circular	7	470	S4	0.0164	0.0151	0.8875	0.9087	0.4688	0.3536
1.5	Circular	7	480	S2	0.0156	0.0198	0.8832	0.9044	0.4894	0.3853
1.5	Circular	7	480	S3	0.0045	0.0135	0.8888	0.8931	0.4619	0.4334
1.5	Circular	7	480	S4	0.019	0.0118	0.883	0.8801	0.4968	0.4984
1.5	Circular	7	490	S2	0.0134	0.022	0.8948	0.8913	0.4244	0.4588
1.5	Circular	7	490	S3	0.0104	0.0163	0.8925	0.8838	0.4308	0.4878
1.5	Circular	7	490	S4	0.0119	0.0263	0.8909	0.8957	0.4413	0.444
1.5	Circular	7	500	S2	0.0162	0.0115	0.8783	0.8851	0.5164	0.472
1.5	Circular	7	500	S3	0.0115	0.0202	0.8926	0.9107	0.4318	0.3531
1.5	Circular	7	500	S4	0.0162	0.0177	0.8796	0.8975	0.5095	0.4181

Continued on next page

Table 9.2 – Continued from previous page

Thickness (mm)	Damage type	Damage size (mm)	Freq. (kHz)	Sensor	ToF (Exp.)	ToF (Sim.)	Peak Amp (Exp.)	Peak Amp (Sim.)	DI (Exp.)	DI (Sim.)
0.7	Slotted	12x4	300	S2	0.9676	0.9836	0.8772	0.9023	0.5465	0.3906
0.7	Slotted	12x4	300	S3	0.9835	0.9863	0.8828	0.9109	0.4937	0.3488
0.7	Slotted	12x4	300	S4	0.988	0.9937	0.8915	0.8996	0.4535	0.4186
0.7	Slotted	12x4	310	S2	0.9839	0.9817	0.8845	0.8927	0.4847	0.4387
0.7	Slotted	12x4	310	S3	0.9884	0.9734	0.8741	0.8843	0.546	0.4773
0.7	Slotted	12x4	310	S4	0.9816	0.9832	0.8849	0.8972	0.4794	0.417
0.7	Slotted	12x4	320	S2	0.9715	0.9813	0.8735	0.8788	0.537	0.5111
0.7	Slotted	12x4	320	S3	0.9753	0.9852	0.8951	0.8977	0.4175	0.417
0.7	Slotted	12x4	320	S4	0.9767	0.9747	0.8956	0.9051	0.416	0.3652
0.7	Slotted	12x4	330	S2	0.9873	0.982	0.8986	0.9072	0.4149	0.3626
0.7	Slotted	12x4	330	S3	0.9758	0.9845	0.8888	0.8931	0.4508	0.4403
0.7	Slotted	12x4	330	S4	0.9823	0.9808	0.8968	0.8865	0.4175	0.4704
0.7	Slotted	12x4	340	S2	0.9796	0.9789	0.8758	0.9001	0.5248	0.3953
0.7	Slotted	12x4	340	S3	0.9866	0.9881	0.8939	0.8918	0.4387	0.4524
0.7	Slotted	12x4	340	S4	0.9677	0.9877	0.8781	0.8925	0.518	0.4477
0.7	Slotted	12x4	350	S2	0.9791	0.9788	0.8863	0.8754	0.4683	0.5254
0.7	Slotted	12x4	350	S3	0.9741	0.9797	0.8752	0.8979	0.5243	0.408
0.7	Slotted	12x4	350	S4	0.9829	0.9909	0.8872	0.8921	0.4693	0.4545
0.7	Slotted	12x4	360	S2	0.9788	0.9842	0.8896	0.8787	0.4508	0.5159
0.7	Slotted	12x4	360	S3	0.9819	0.9729	0.8867	0.8943	0.4704	0.4249
0.7	Slotted	12x4	360	S4	0.9714	0.9835	0.8742	0.8981	0.5333	0.4128
0.7	Slotted	12x4	370	S2	0.9981	0.9928	0.8773	0.8952	0.5433	0.4408
0.7	Slotted	12x4	370	S3	0.9771	0.9819	0.8876	0.8938	0.4588	0.4329
0.7	Slotted	12x4	370	S4	0.9841	0.9902	0.8928	0.8987	0.4413	0.4186
0.7	Slotted	12x4	380	S2	0.9904	0.9832	0.8827	0.8857	0.5032	0.4773
0.7	Slotted	12x4	380	S3	0.9991	0.9857	0.8785	0.9021	0.5381	0.3943
0.7	Slotted	12x4	380	S4	0.9884	0.9869	0.8698	0.8926	0.5687	0.4461
0.7	Slotted	12x4	390	S2	0.9886	0.9845	0.879	0.8982	0.5206	0.4128
0.7	Slotted	12x4	390	S3	0.9821	0.9854	0.856	0.8996	0.6332	0.4075
0.7	Slotted	12x4	390	S4	0.9909	0.9847	0.8776	0.8943	0.5312	0.4339
0.7	Slotted	12x4	400	S2	0.9988	0.992	0.8787	0.896	0.537	0.4355
0.7	Slotted	12x4	400	S3	0.9799	0.9839	0.8699	0.8846	0.556	0.4847
0.7	Slotted	12x4	400	S4	0.9832	0.9803	0.8846	0.902	0.4831	0.3869
0.7	Slotted	12x4	410	S2	0.9765	0.9802	0.8783	0.8921	0.5074	0.4397
0.7	Slotted	12x4	410	S3	0.981	0.9852	0.8979	0.9001	0.4101	0.4043
0.7	Slotted	12x4	410	S4	0.9846	0.9801	0.8904	0.8868	0.4551	0.4672
0.7	Slotted	12x4	420	S2	0.9871	0.9765	0.8855	0.895	0.4841	0.4191
0.7	Slotted	12x4	420	S3	0.9734	0.9875	0.897	0.8842	0.4096	0.4915

Continued on next page

Table 9.2 – Continued from previous page

Thickness (mm)	Damage type	Damage size (mm)	Freq. (kHz)	Sensor	ToF (Exp.)	ToF (Sim.)	Peak Amp (Exp.)	Peak Amp (Sim.)	DI (Exp.)	DI (Sim.)
0.7	Slotted	12x4	420	S4	0.9876	0.9781	0.8701	0.8954	0.5661	0.4191
0.7	Slotted	12x4	430	S2	0.9871	0.978	0.8816	0.8929	0.5048	0.4318
0.7	Slotted	12x4	430	S3	0.9816	0.97	0.8729	0.8944	0.5433	0.4281
0.7	Slotted	12x4	430	S4	0.9812	0.9792	0.8944	0.8912	0.4286	0.4429
0.7	Slotted	12x4	440	S2	0.9806	0.9951	0.883	0.8951	0.4878	0.4445
0.7	Slotted	12x4	440	S3	0.981	0.9834	0.8655	0.8814	0.5809	0.5005
0.7	Slotted	12x4	440	S4	0.9691	0.9848	0.8944	0.8858	0.4297	0.4789
0.7	Slotted	12x4	450	S2	0.9744	0.9847	0.8897	0.8916	0.4477	0.4487
0.7	Slotted	12x4	450	S3	0.9819	0.9908	0.8994	0.8939	0.4033	0.445
0.7	Slotted	12x4	450	S4	0.995	0.9903	0.8709	0.8872	0.5724	0.4799
0.7	Slotted	12x4	460	S2	0.9874	0.9866	0.8772	0.8927	0.528	0.445
0.7	Slotted	12x4	460	S3	0.9794	0.9829	0.8804	0.8945	0.5	0.4308
0.7	Slotted	12x4	460	S4	0.9857	0.9832	0.8899	0.8954	0.4588	0.426
0.7	Slotted	12x4	470	S2	0.9876	0.9808	0.866	0.8903	0.5877	0.4498
0.7	Slotted	12x4	470	S3	0.9887	0.988	0.872	0.8802	0.5576	0.5132
0.7	Slotted	12x4	470	S4	0.9675	0.9865	0.8761	0.9154	0.5291	0.3251
0.7	Slotted	12x4	480	S2	0.9776	0.9801	0.8817	0.8879	0.491	0.4614
0.7	Slotted	12x4	480	S3	0.9773	0.9833	0.8796	0.878	0.5016	0.5185
0.7	Slotted	12x4	480	S4	0.9801	0.9819	0.8757	0.8885	0.5259	0.4609
0.7	Slotted	12x4	490	S2	0.9879	0.9832	0.8799	0.8847	0.5148	0.4826
0.7	Slotted	12x4	490	S3	0.9782	0.983	0.8682	0.8972	0.5634	0.4165
0.7	Slotted	12x4	490	S4	0.9858	0.9889	0.8638	0.8903	0.5967	0.4609
0.7	Slotted	12x4	500	S2	0.9961	0.9872	0.8679	0.8832	0.5899	0.4963
0.7	Slotted	12x4	500	S3	0.9829	0.9882	0.8791	0.8761	0.5122	0.5354
0.7	Slotted	12x4	500	S4	0.9883	0.9873	0.8721	0.8831	0.5566	0.4974
0.9	Slotted	15x5	300	S2	0.7263	0.7194	0.8532	0.8779	0.667	0.5264
0.9	Slotted	15x5	300	S3	0.7088	0.7136	0.839	0.8791	0.7156	0.5106
0.9	Slotted	15x5	300	S4	0.7167	0.7172	0.8481	0.8805	0.6797	0.509
0.9	Slotted	15x5	310	S2	0.7165	0.7267	0.8597	0.8702	0.6179	0.5777
0.9	Slotted	15x5	310	S3	0.7184	0.7149	0.8638	0.8514	0.5988	0.6596
0.9	Slotted	15x5	310	S4	0.7189	0.7164	0.8568	0.8672	0.6369	0.5782
0.9	Slotted	15x5	320	S2	0.7156	0.7128	0.8616	0.8485	0.6062	0.6712
0.9	Slotted	15x5	320	S3	0.724	0.7244	0.8506	0.8602	0.6771	0.6274
0.9	Slotted	15x5	320	S4	0.7222	0.7114	0.8392	0.8769	0.7347	0.519
0.9	Slotted	15x5	330	S2	0.7179	0.7268	0.8226	0.862	0.8155	0.621
0.9	Slotted	15x5	330	S3	0.7259	0.7068	0.8312	0.863	0.7828	0.5877
0.9	Slotted	15x5	330	S4	0.7123	0.7009	0.8682	0.8832	0.5666	0.4894
0.9	Slotted	15x5	340	S2	0.7359	0.7144	0.8676	0.8691	0.6052	0.5645

Continued on next page

Table 9.2 – Continued from previous page

Thickness (mm)	Damage type	Damage size (mm)	Freq. (kHz)	Sensor	ToF (Exp.)	ToF (Sim.)	Peak Amp (Exp.)	Peak Amp (Sim.)	DI (Exp.)	DI (Sim.)
0.9	Slotted	15x5	340	S3	0.7141	0.7216	0.8616	0.8556	0.6047	0.6475
0.9	Slotted	15x5	340	S4	0.7111	0.7145	0.8559	0.8724	0.63	0.5476
0.9	Slotted	15x5	350	S2	0.7034	0.7149	0.8493	0.8766	0.6649	0.5264
0.9	Slotted	15x5	350	S3	0.7216	0.7163	0.8393	0.8615	0.7331	0.6084
0.9	Slotted	15x5	350	S4	0.7146	0.7193	0.865	0.8725	0.5872	0.5544
0.9	Slotted	15x5	360	S2	0.7227	0.7066	0.8277	0.8618	0.7965	0.5941
0.9	Slotted	15x5	360	S3	0.7229	0.7073	0.849	0.8707	0.6839	0.546
0.9	Slotted	15x5	360	S4	0.7053	0.7152	0.8632	0.8645	0.5888	0.5909
0.9	Slotted	15x5	370	S2	0.7286	0.7207	0.8387	0.8763	0.7474	0.5359
0.9	Slotted	15x5	370	S3	0.7098	0.709	0.8461	0.8635	0.6797	0.5867
0.9	Slotted	15x5	370	S4	0.7085	0.7216	0.8534	0.8595	0.639	0.6268
0.9	Slotted	15x5	380	S2	0.7154	0.7195	0.8566	0.8645	0.6327	0.5973
0.9	Slotted	15x5	380	S3	0.7173	0.7155	0.8574	0.8745	0.6316	0.5381
0.9	Slotted	15x5	380	S4	0.7252	0.7218	0.8566	0.8775	0.6475	0.5322
0.9	Slotted	15x5	390	S2	0.7232	0.7108	0.8355	0.8634	0.7558	0.5899
0.9	Slotted	15x5	390	S3	0.7229	0.715	0.846	0.8746	0.6998	0.5365
0.9	Slotted	15x5	390	S4	0.7071	0.7258	0.8525	0.8723	0.6427	0.5655
0.9	Slotted	15x5	400	S2	0.7205	0.7133	0.8671	0.8709	0.5846	0.5539
0.9	Slotted	15x5	400	S3	0.7207	0.7261	0.8505	0.8703	0.6723	0.5766
0.9	Slotted	15x5	400	S4	0.7071	0.7167	0.8432	0.8726	0.6919	0.5497
0.9	Slotted	15x5	410	S2	0.705	0.7193	0.8499	0.8545	0.6596	0.6496
0.9	Slotted	15x5	410	S3	0.7229	0.7101	0.8646	0.8601	0.6015	0.6062
0.9	Slotted	15x5	410	S4	0.7322	0.7192	0.8515	0.8636	0.685	0.6015
0.9	Slotted	15x5	420	S2	0.723	0.7204	0.8492	0.8569	0.6834	0.6385
0.9	Slotted	15x5	420	S3	0.7172	0.7143	0.8497	0.8445	0.6718	0.6945
0.9	Slotted	15x5	420	S4	0.7115	0.7158	0.8599	0.8601	0.6094	0.6147
0.9	Slotted	15x5	430	S2	0.7123	0.7143	0.8442	0.8613	0.6934	0.6057
0.9	Slotted	15x5	430	S3	0.719	0.7187	0.847	0.8619	0.6887	0.6094
0.9	Slotted	15x5	430	S4	0.709	0.7222	0.839	0.8709	0.7156	0.5671
0.9	Slotted	15x5	440	S2	0.7192	0.7237	0.849	0.8619	0.6781	0.6173
0.9	Slotted	15x5	440	S3	0.7226	0.7202	0.855	0.8585	0.6522	0.6295
0.9	Slotted	15x5	440	S4	0.7218	0.7142	0.8543	0.8519	0.6543	0.6559
0.9	Slotted	15x5	450	S2	0.7183	0.719	0.8555	0.8591	0.6427	0.6247
0.9	Slotted	15x5	450	S3	0.7103	0.7154	0.8514	0.8661	0.6522	0.5825
0.9	Slotted	15x5	450	S4	0.7127	0.7077	0.848	0.8562	0.6739	0.6232
0.9	Slotted	15x5	460	S2	0.7294	0.7182	0.8538	0.8634	0.6686	0.601
0.9	Slotted	15x5	460	S3	0.7298	0.7119	0.8303	0.859	0.7933	0.6147
0.9	Slotted	15x5	460	S4	0.7212	0.7137	0.8246	0.8614	0.8103	0.6047

Continued on next page

Table 9.2 – Continued from previous page

Thickness (mm)	Damage type	Damage size (mm)	Freq. (kHz)	Sensor	ToF (Exp.)	ToF (Sim.)	Peak Amp (Exp.)	Peak Amp (Sim.)	DI (Exp.)	DI (Sim.)
0.9	Slotted	15x5	470	S2	0.7171	0.7205	0.8607	0.8724	0.6136	0.5566
0.9	Slotted	15x5	470	S3	0.726	0.7238	0.845	0.8767	0.7098	0.5391
0.9	Slotted	15x5	470	S4	0.7164	0.7084	0.8305	0.8635	0.7717	0.5851
0.9	Slotted	15x5	480	S2	0.7236	0.7105	0.8353	0.855	0.7574	0.6337
0.9	Slotted	15x5	480	S3	0.7205	0.7268	0.8277	0.8728	0.7933	0.5645
0.9	Slotted	15x5	480	S4	0.7155	0.7159	0.8529	0.852	0.6522	0.658
0.9	Slotted	15x5	490	S2	0.7068	0.7159	0.853	0.8709	0.6406	0.5581
0.9	Slotted	15x5	490	S3	0.7265	0.7224	0.8686	0.856	0.5862	0.6464
0.9	Slotted	15x5	490	S4	0.7101	0.7258	0.8407	0.8459	0.7082	0.7045
0.9	Slotted	15x5	500	S2	0.7168	0.7182	0.8484	0.8549	0.6781	0.6453
0.9	Slotted	15x5	500	S3	0.7214	0.7235	0.846	0.8466	0.6977	0.6977
0.9	Slotted	15x5	500	S4	0.7327	0.7082	0.8464	0.8599	0.713	0.6041
1.2	Slotted	18x6	300	S2	0.2749	0.281	0.8267	0.8507	0.7838	0.6675
1.2	Slotted	18x6	300	S3	0.2873	0.2777	0.8423	0.8486	0.7225	0.6728
1.2	Slotted	18x6	300	S4	0.2825	0.2864	0.8327	0.8462	0.7648	0.7008
1.2	Slotted	18x6	310	S2	0.284	0.2786	0.8224	0.8468	0.8224	0.6834
1.2	Slotted	18x6	310	S3	0.2836	0.279	0.7986	0.8663	0.9477	0.5814
1.2	Slotted	18x6	310	S4	0.2802	0.2791	0.8265	0.8318	0.7939	0.7643
1.2	Slotted	18x6	320	S2	0.2874	0.2783	0.8225	0.8367	0.8277	0.7368
1.2	Slotted	18x6	320	S3	0.2856	0.2808	0.8269	0.8463	0.8013	0.6903
1.2	Slotted	18x6	320	S4	0.2831	0.2828	0.8292	0.8384	0.7849	0.7357
1.2	Slotted	18x6	330	S2	0.2797	0.2862	0.8106	0.8334	0.8774	0.768
1.2	Slotted	18x6	330	S3	0.2842	0.2773	0.8211	0.8437	0.8293	0.6982
1.2	Slotted	18x6	330	S4	0.2725	0.2878	0.8087	0.8386	0.8747	0.7431
1.2	Slotted	18x6	340	S2	0.2799	0.2851	0.816	0.8609	0.8488	0.6205
1.2	Slotted	18x6	340	S3	0.2717	0.2773	0.8186	0.8426	0.8214	0.704
1.2	Slotted	18x6	340	S4	0.2831	0.2812	0.8161	0.839	0.8536	0.7299
1.2	Slotted	18x6	350	S2	0.2773	0.2838	0.8261	0.8309	0.7912	0.777
1.2	Slotted	18x6	350	S3	0.2918	0.2761	0.8201	0.8309	0.8483	0.7637
1.2	Slotted	18x6	350	S4	0.2793	0.2851	0.822	0.8361	0.8161	0.7516
1.2	Slotted	18x6	360	S2	0.2904	0.2875	0.8263	0.8417	0.8124	0.7267
1.2	Slotted	18x6	360	S3	0.2798	0.2768	0.8193	0.8387	0.8314	0.7236
1.2	Slotted	18x6	360	S4	0.2758	0.2872	0.8425	0.8545	0.7019	0.658
1.2	Slotted	18x6	370	S2	0.2827	0.2867	0.8126	0.8223	0.8721	0.8277
1.2	Slotted	18x6	370	S3	0.2836	0.2839	0.8247	0.8704	0.8097	0.5687
1.2	Slotted	18x6	370	S4	0.2734	0.28	0.8297	0.83	0.7653	0.7754
1.2	Slotted	18x6	380	S2	0.2786	0.2867	0.8256	0.8301	0.796	0.7859
1.2	Slotted	18x6	380	S3	0.2937	0.2876	0.8136	0.8423	0.8853	0.7236

Continued on next page

Table 9.2 – Continued from previous page

Thickness (mm)	Damage type	Damage size (mm)	Freq. (kHz)	Sensor	ToF (Exp.)	ToF (Sim.)	Peak Amp (Exp.)	Peak Amp (Sim.)	DI (Exp.)	DI (Sim.)
1.2	Slotted	18x6	380	S4	0.2732	0.2882	0.8134	0.8514	0.851	0.676
1.2	Slotted	18x6	390	S2	0.2879	0.2802	0.8119	0.8364	0.8848	0.7415
1.2	Slotted	18x6	390	S3	0.274	0.2839	0.8154	0.8336	0.842	0.7632
1.2	Slotted	18x6	390	S4	0.2722	0.2855	0.826	0.8401	0.7828	0.7315
1.2	Slotted	18x6	400	S2	0.29	0.2787	0.8054	0.819	0.9223	0.8309
1.2	Slotted	18x6	400	S3	0.2771	0.2806	0.8261	0.8402	0.7907	0.7225
1.2	Slotted	18x6	400	S4	0.284	0.2857	0.8226	0.8289	0.8214	0.7912
1.2	Slotted	18x6	410	S2	0.2823	0.2814	0.8179	0.8286	0.843	0.7854
1.2	Slotted	18x6	410	S3	0.2855	0.2821	0.8229	0.8368	0.8224	0.7426
1.2	Slotted	18x6	410	S4	0.285	0.289	0.8196	0.8438	0.8388	0.7178
1.2	Slotted	18x6	420	S2	0.2819	0.2811	0.8149	0.8407	0.8584	0.7204
1.2	Slotted	18x6	420	S3	0.279	0.2713	0.8021	0.8428	0.9212	0.6945
1.2	Slotted	18x6	420	S4	0.2864	0.2845	0.8303	0.8362	0.7849	0.7505
1.2	Slotted	18x6	430	S2	0.2861	0.289	0.8084	0.8519	0.8996	0.6749
1.2	Slotted	18x6	430	S3	0.2781	0.2799	0.7955	0.8442	0.9545	0.6998
1.2	Slotted	18x6	430	S4	0.2965	0.2839	0.8183	0.8402	0.8658	0.7283
1.2	Slotted	18x6	440	S2	0.2936	0.2804	0.8103	0.8363	0.9033	0.7426
1.2	Slotted	18x6	440	S3	0.2771	0.274	0.8146	0.8378	0.8515	0.7236
1.2	Slotted	18x6	440	S4	0.2757	0.2732	0.8162	0.8456	0.8409	0.6813
1.2	Slotted	18x6	450	S2	0.2856	0.2893	0.7964	0.8199	0.9625	0.8446
1.2	Slotted	18x6	450	S3	0.2815	0.2879	0.8178	0.8305	0.842	0.7859
1.2	Slotted	18x6	450	S4	0.2787	0.2838	0.7989	0.827	0.9371	0.7976
1.2	Slotted	18x6	460	S2	0.276	0.2811	0.8201	0.8432	0.8208	0.7077
1.2	Slotted	18x6	460	S3	0.2754	0.2907	0.8035	0.8472	0.907	0.703
1.2	Slotted	18x6	460	S4	0.2772	0.2862	0.8197	0.8413	0.8251	0.7262
1.2	Slotted	18x6	470	S2	0.2807	0.2772	0.8197	0.8306	0.8309	0.7674
1.2	Slotted	18x6	470	S3	0.2891	0.2853	0.8273	0.8231	0.805	0.8208
1.2	Slotted	18x6	470	S4	0.2823	0.2792	0.8075	0.8439	0.898	0.7003
1.2	Slotted	18x6	480	S2	0.2894	0.2794	0.8042	0.8182	0.9281	0.8362
1.2	Slotted	18x6	480	S3	0.2781	0.2831	0.8141	0.8293	0.8562	0.7844
1.2	Slotted	18x6	480	S4	0.2877	0.2797	0.8216	0.8345	0.833	0.7505
1.2	Slotted	18x6	490	S2	0.2763	0.2816	0.8259	0.8113	0.7902	0.8768
1.2	Slotted	18x6	490	S3	0.2714	0.2781	0.802	0.8219	0.9096	0.8145
1.2	Slotted	18x6	490	S4	0.2861	0.2775	0.7895	0.8275	0.8997	0.7844
1.2	Slotted	18x6	500	S2	0.2913	0.2844	0.833	0.8397	0.7791	0.7315
1.2	Slotted	18x6	500	S3	0.2893	0.2828	0.8236	0.8342	0.8256	0.7579
1.2	Slotted	18x6	500	S4	0.2892	0.2786	0.8111	0.8285	0.8911	0.7807

Comprehensive Metamodel Prediction Results

Table 9.3: Comprehensive Metamodel Prediction Results.

Thickness (mm)	Damage size (mm)	Freq. (kHz)	Sensor	DI (Actual)	PR	SVM	ANN	BR	SGD
0.700000	4	300	S2	0.342012	0.178011	0.334517	0.430294	0.326989	0.307987
0.700000	4	300	S3	0.267956	0.338806	0.261962	0.242859	0.284670	0.288657
0.700000	4	300	S4	0.194084	0.228843	0.198566	0.126124	0.270656	0.056109
0.700000	4	310	S2	0.103744	0.162656	0.128289	0.123803	0.075129	0.340527
0.700000	4	310	S3	0.151403	0.098950	0.137742	0.140694	0.104474	0.161997
0.700000	4	310	S4	0.206905	0.307714	0.235334	0.202932	0.248843	0.143003
0.700000	4	320	S2	0.331803	0.494950	0.316575	0.303396	0.359416	0.449473
0.700000	4	320	S3	0.297640	0.249267	0.324059	0.305307	0.151743	0.317164
0.700000	4	320	S4	0.255962	0.323300	0.265717	0.173169	0.405450	0.176505
0.700000	4	330	S2	0.302958	0.413878	0.306475	0.275452	0.389351	0.277039
0.700000	4	330	S3	0.306615	0.286076	0.278449	0.306303	0.267530	0.256198
0.700000	4	330	S4	0.152767	0.303142	0.114443	0.159175	0.095103	0.242713
0.700000	4	340	S2	0.269061	0.284194	0.264641	0.201341	0.314141	0.246913
0.700000	4	340	S3	0.300953	0.320032	0.293528	0.343252	0.278319	0.285723
0.700000	4	340	S4	0.286088	0.331236	0.307818	0.278448	0.380234	0.241641
0.700000	4	350	S2	0.243074	0.200078	0.227159	0.243421	0.231022	0.195143
0.700000	4	350	S3	0.181066	0.154977	0.185846	0.261538	0.161195	0.035452
0.700000	4	350	S4	0.267159	0.455643	0.269406	0.253761	0.322017	0.312144
0.700000	4	360	S2	0.244121	0.269582	0.242037	0.221574	0.271857	0.462504
0.700000	4	360	S3	0.213098	0.084315	0.222392	0.316815	0.286316	0.366751
0.700000	4	360	S4	0.186639	0.322314	0.145356	0.204723	0.100488	0.162314
0.700000	4	370	S2	0.311390	0.436284	0.304490	0.333735	0.330505	0.294944
0.700000	4	370	S3	0.214890	0.352713	0.209976	0.261120	0.145189	0.198695
0.700000	4	370	S4	0.294577	0.188406	0.316726	0.327768	0.242753	0.341475
0.700000	4	380	S2	0.186183	0.242653	0.181308	0.202254	0.257446	0.232267
0.700000	4	380	S3	0.211731	0.143911	0.210939	0.220073	0.316770	0.240110
0.700000	4	380	S4	0.243527	0.213986	0.256929	0.228836	0.280320	0.144158
0.700000	4	390	S2	0.259211	0.166852	0.267361	0.299816	0.305855	0.325006
0.700000	4	390	S3	0.269217	0.261451	0.240375	0.289224	0.284759	0.254576
0.700000	4	390	S4	0.269836	0.369247	0.259802	0.247919	0.304790	0.240709
0.700000	4	400	S2	0.233686	0.130808	0.219454	0.198724	0.233680	0.324589
0.700000	4	400	S3	0.285949	0.322514	0.299017	0.230355	0.394324	0.532621
0.700000	4	400	S4	0.197600	0.260330	0.168991	0.248042	0.220544	0.324250
0.700000	4	410	S2	0.250062	0.345269	0.217395	0.272651	0.220747	0.049219
0.700000	4	410	S3	0.283862	0.276485	0.315090	0.331161	0.242350	0.341678

Continued on next page

Table 9.3 – Continued from previous page

Thickness (mm)	Damage size (mm)	Freq. (kHz)	Sensor	DI (Actual)	PR	SVM	ANN	BR	SGD
0.700000	4	410	S4	0.151755	0.148811	0.177253	0.152369	0.132453	0.000000
0.700000	4	420	S2	0.160476	0.217338	0.131514	0.252388	0.181569	0.391958
0.700000	4	420	S3	0.209046	0.294360	0.188370	0.285950	0.080101	0.189574
0.700000	4	420	S4	0.244047	0.302644	0.269438	0.176972	0.223514	0.217377
0.700000	4	430	S2	0.097151	0.269807	0.085574	0.189523	0.128912	0.063881
0.700000	4	430	S3	0.320128	0.429240	0.287858	0.291430	0.349870	0.458458
0.700000	4	430	S4	0.196733	0.221605	0.230336	0.162766	0.187654	0.000000
0.700000	4	440	S2	0.219618	0.202045	0.178070	0.240751	0.359731	0.372069
0.700000	4	440	S3	0.194766	0.255705	0.205969	0.153997	0.265110	0.234564
0.700000	4	440	S4	0.232976	0.274590	0.215640	0.265639	0.096025	0.218844
0.700000	4	450	S2	0.215224	0.102563	0.212221	0.225957	0.078717	0.067971
0.700000	4	450	S3	0.268561	0.397149	0.256705	0.252939	0.271953	0.283521
0.700000	4	450	S4	0.228097	0.214458	0.236129	0.116922	0.187872	0.314580
0.700000	4	460	S2	0.180309	0.212642	0.203727	0.214242	0.171494	0.196873
0.700000	4	460	S3	0.205776	0.149929	0.210322	0.251889	0.055028	0.165543
0.700000	4	460	S4	0.231208	0.260902	0.250848	0.286504	0.118248	0.402982
0.700000	4	470	S2	0.270325	0.302657	0.258037	0.185743	0.323435	0.195275
0.700000	4	470	S3	0.198073	0.255233	0.186073	0.190117	0.168840	0.323637
0.700000	4	470	S4	0.147849	0.159102	0.151921	0.103613	0.145968	0.196449
0.700000	4	480	S2	0.300200	0.361656	0.306721	0.321469	0.060222	0.267603
0.700000	4	480	S3	0.228003	0.149958	0.225994	0.278920	0.139350	0.246355
0.700000	4	480	S4	0.256674	0.317156	0.267608	0.295624	0.199993	0.109842
0.700000	4	490	S2	0.327737	0.184162	0.302522	0.254398	0.369207	0.407868
0.700000	4	490	S3	0.254359	0.249211	0.220543	0.269900	0.132043	0.398284
0.700000	4	490	S4	0.232225	0.304912	0.234323	0.257458	0.149430	0.238569
0.700000	4	500	S2	0.265814	0.106801	0.295109	0.270531	0.252169	0.290632
0.700000	4	500	S3	0.251497	0.143524	0.261507	0.247287	0.241347	0.209455
0.700000	4	500	S4	0.279408	0.518237	0.257369	0.248985	0.255549	0.301085
0.700000	5	300	S2	0.406498	0.309416	0.411729	0.430176	0.340712	0.540806
0.700000	5	300	S3	0.307355	0.373808	0.314204	0.262424	0.310642	0.132465
0.700000	5	300	S4	0.410999	0.367598	0.417313	0.408607	0.379209	0.349754
0.700000	5	310	S2	0.362666	0.387200	0.360264	0.380656	0.264738	0.406923
0.700000	5	310	S3	0.347708	0.491863	0.357192	0.397564	0.281100	0.379028
0.700000	5	310	S4	0.320929	0.318345	0.329702	0.296826	0.307960	0.258694
0.700000	5	320	S2	0.321863	0.294068	0.289313	0.329635	0.290281	0.302590
0.700000	5	320	S3	0.338680	0.375667	0.367927	0.346138	0.284496	0.319582
0.700000	5	320	S4	0.404122	0.350084	0.425859	0.331719	0.468990	0.310098
0.700000	5	330	S2	0.366212	0.316045	0.370271	0.269074	0.352531	0.475320

Continued on next page

Table 9.3 – Continued from previous page

Thickness (mm)	Damage size (mm)	Freq. (kHz)	Sensor	DI (Actual)	PR	SVM	ANN	BR	SGD
0.700000	5	330	S3	0.408161	0.351516	0.406931	0.341702	0.458778	0.567588
0.700000	5	330	S4	0.412053	0.445043	0.428514	0.437854	0.380857	0.454474
0.700000	5	340	S2	0.346561	0.318681	0.354910	0.296110	0.310852	0.275817
0.700000	5	340	S3	0.366782	0.351300	0.408350	0.377697	0.392705	0.273682
0.700000	5	340	S4	0.419652	0.440985	0.447156	0.463034	0.501258	0.448038
0.700000	5	350	S2	0.385666	0.352371	0.369156	0.427672	0.454928	0.499233
0.700000	5	350	S3	0.326268	0.247286	0.323445	0.397971	0.357558	0.207747
0.700000	5	350	S4	0.340082	0.276009	0.337918	0.388411	0.347189	0.442974
0.700000	5	360	S2	0.367071	0.338551	0.375021	0.369478	0.383154	0.308559
0.700000	5	360	S3	0.331902	0.083273	0.366946	0.335930	0.437103	0.177793
0.700000	5	360	S4	0.405257	0.304141	0.429748	0.479843	0.370059	0.301393
0.700000	5	370	S2	0.331032	0.183725	0.327493	0.412940	0.308139	0.356178
0.700000	5	370	S3	0.438777	0.238580	0.466665	0.527718	0.369370	0.230312
0.700000	5	370	S4	0.360731	0.339056	0.342244	0.359699	0.302852	0.312392
0.700000	5	380	S2	0.364460	0.393078	0.365175	0.416178	0.328975	0.499612
0.700000	5	380	S3	0.296018	0.160688	0.292670	0.286823	0.225802	0.263818
0.700000	5	380	S4	0.308470	0.284035	0.324981	0.364548	0.342911	0.391960
0.700000	5	390	S2	0.327892	0.443528	0.343917	0.379152	0.335697	0.291092
0.700000	5	390	S3	0.301230	0.286618	0.287179	0.255705	0.322423	0.420785
0.700000	5	390	S4	0.371020	0.466803	0.359474	0.357703	0.494651	0.298007
0.700000	5	400	S2	0.342546	0.341231	0.336467	0.357582	0.299857	0.300558
0.700000	5	400	S3	0.361154	0.383155	0.360432	0.471811	0.295763	0.455934
0.700000	5	400	S4	0.393102	0.292574	0.379383	0.345159	0.309006	0.215397
0.700000	5	410	S2	0.293773	0.181350	0.275858	0.289502	0.313033	0.423488
0.700000	5	410	S3	0.190781	0.314071	0.169285	0.186284	0.067072	0.165976
0.700000	5	410	S4	0.378719	0.259022	0.372114	0.347688	0.346686	0.312917
0.700000	5	420	S2	0.330301	0.247111	0.336470	0.285982	0.312626	0.486760
0.700000	5	420	S3	0.356458	0.326286	0.393391	0.392941	0.526118	0.346879
0.700000	5	420	S4	0.362931	0.355058	0.374733	0.301952	0.382026	0.066856
0.700000	5	430	S2	0.428389	0.452242	0.409801	0.472668	0.319386	0.180643
0.700000	5	430	S3	0.297411	0.303349	0.275254	0.423088	0.276701	0.364651
0.700000	5	430	S4	0.371288	0.352233	0.401535	0.473137	0.389441	0.440174
0.700000	5	440	S2	0.426475	0.412682	0.424691	0.395044	0.577742	0.514196
0.700000	5	440	S3	0.385755	0.521704	0.396433	0.440440	0.348050	0.449817
0.700000	5	440	S4	0.266112	0.262982	0.227248	0.286404	0.313729	0.415406
0.700000	5	450	S2	0.280659	0.264361	0.267497	0.304496	0.269433	0.113187
0.700000	5	450	S3	0.371905	0.477370	0.418287	0.431337	0.454044	0.464269
0.700000	5	450	S4	0.335234	0.473787	0.314553	0.390364	0.329444	0.488974

Continued on next page

Table 9.3 – Continued from previous page

Thickness (mm)	Damage size (mm)	Freq. (kHz)	Sensor	DI (Actual)	PR	SVM	ANN	BR	SGD
0.700000	5	460	S2	0.360899	0.337991	0.351090	0.280590	0.343369	0.344265
0.700000	5	460	S3	0.358321	0.293613	0.341860	0.382215	0.318181	0.399411
0.700000	5	460	S4	0.380306	0.423857	0.389263	0.396400	0.289630	0.419432
0.700000	5	470	S2	0.315141	0.380650	0.290009	0.297645	0.373363	0.293432
0.700000	5	470	S3	0.458488	0.500447	0.472404	0.388766	0.398093	0.606885
0.700000	5	470	S4	0.382832	0.309770	0.376141	0.425751	0.318067	0.401761
0.700000	5	480	S2	0.343576	0.414125	0.343907	0.310461	0.332663	0.033920
0.700000	5	480	S3	0.397422	0.624501	0.391583	0.272879	0.430184	0.359617
0.700000	5	480	S4	0.278590	0.365836	0.258061	0.333484	0.123409	0.093577
0.700000	5	490	S2	0.331225	0.262455	0.361231	0.394073	0.449226	0.410718
0.700000	5	490	S3	0.397036	0.450521	0.400760	0.364232	0.423607	0.361841
0.700000	5	490	S4	0.309185	0.255201	0.338626	0.356527	0.243940	0.510099
0.700000	5	500	S2	0.338494	0.263020	0.319090	0.374242	0.284050	0.385235
0.700000	5	500	S3	0.361058	0.550900	0.367318	0.306029	0.495992	0.461419
0.700000	5	500	S4	0.304208	0.222496	0.292103	0.268698	0.423883	0.223974
0.700000	6	300	S2	0.507323	0.455083	0.547537	0.473792	0.438819	0.502071
0.700000	6	300	S3	0.379598	0.337261	0.348787	0.463981	0.390948	0.389370
0.700000	6	300	S4	0.425371	0.466630	0.409631	0.521363	0.376156	0.322068
0.700000	6	310	S2	0.380259	0.443180	0.373617	0.400413	0.341394	0.517851
0.700000	6	310	S3	0.413240	0.422255	0.409933	0.462733	0.411333	0.524582
0.700000	6	310	S4	0.393133	0.214125	0.400805	0.346614	0.412981	0.367972
0.700000	6	320	S2	0.390093	0.297639	0.359592	0.292341	0.411049	0.402843
0.700000	6	320	S3	0.386282	0.291876	0.374089	0.434120	0.430339	0.459000
0.700000	6	320	S4	0.492652	0.480662	0.488484	0.508300	0.422324	0.335491
0.700000	6	330	S2	0.409961	0.381678	0.421527	0.457637	0.311107	0.535570
0.700000	6	330	S3	0.369620	0.456857	0.353721	0.411186	0.311208	0.466027
0.700000	6	330	S4	0.380885	0.259290	0.386053	0.384062	0.374793	0.446812
0.700000	6	340	S2	0.388958	0.390221	0.388500	0.347732	0.365837	0.279756
0.700000	6	340	S3	0.389138	0.408709	0.397957	0.405902	0.255977	0.192115
0.700000	6	340	S4	0.461572	0.380670	0.430049	0.436204	0.525066	0.553053
0.700000	6	350	S2	0.458031	0.580386	0.473860	0.552765	0.422945	0.675071
0.700000	6	350	S3	0.508354	0.633462	0.510246	0.449345	0.537520	0.695757
0.700000	6	350	S4	0.449408	0.492537	0.473567	0.450558	0.343563	0.467298
0.700000	6	360	S2	0.369184	0.465307	0.376056	0.416787	0.310407	0.270971
0.700000	6	360	S3	0.490443	0.643111	0.516939	0.499161	0.564227	0.636715
0.700000	6	360	S4	0.378829	0.442508	0.351980	0.367884	0.428044	0.305543
0.700000	6	370	S2	0.435522	0.516075	0.408012	0.395435	0.415279	0.630207
0.700000	6	370	S3	0.493638	0.371082	0.516431	0.480204	0.480668	0.608434

Continued on next page

Table 9.3 – Continued from previous page

Thickness (mm)	Damage size (mm)	Freq. (kHz)	Sensor	DI (Actual)	PR	SVM	ANN	BR	SGD
0.700000	6	370	S4	0.409778	0.407959	0.393873	0.452657	0.520553	0.421018
0.700000	6	380	S2	0.444614	0.524103	0.460433	0.372943	0.437559	0.386535
0.700000	6	380	S3	0.362006	0.374923	0.328002	0.400800	0.401954	0.528143
0.700000	6	380	S4	0.466662	0.524632	0.447017	0.451097	0.431130	0.468000
0.700000	6	390	S2	0.457988	0.385093	0.481021	0.515110	0.516541	0.455384
0.700000	6	390	S3	0.367388	0.222247	0.391348	0.383304	0.385740	0.478118
0.700000	6	390	S4	0.483707	0.492153	0.488822	0.493254	0.563853	0.451272
0.700000	6	400	S2	0.439984	0.531594	0.412443	0.429318	0.453401	0.226396
0.700000	6	400	S3	0.422778	0.620288	0.419121	0.469134	0.463402	0.462072
0.700000	6	400	S4	0.491361	0.491970	0.499935	0.524278	0.525743	0.633468
0.700000	6	410	S2	0.463340	0.525704	0.462573	0.540459	0.475681	0.385684
0.700000	6	410	S3	0.445325	0.630498	0.421710	0.416008	0.509055	0.382199
0.700000	6	410	S4	0.430638	0.353463	0.413123	0.426872	0.453399	0.617592
0.700000	6	420	S2	0.448620	0.493890	0.484188	0.344573	0.409076	0.369490
0.700000	6	420	S3	0.520437	0.618106	0.512777	0.529006	0.559377	0.458804
0.700000	6	420	S4	0.393662	0.372924	0.404067	0.373154	0.376385	0.512247
0.700000	6	430	S2	0.456872	0.608851	0.472332	0.526275	0.485860	0.354089
0.700000	6	430	S3	0.382172	0.307964	0.384645	0.320099	0.406383	0.416390
0.700000	6	430	S4	0.562859	0.430447	0.547582	0.517415	0.576222	0.525604
0.700000	6	440	S2	0.529417	0.489945	0.514903	0.570973	0.580017	0.442628
0.700000	6	440	S3	0.535330	0.585094	0.549458	0.480369	0.530416	0.448182
0.700000	6	440	S4	0.516583	0.442890	0.515077	0.545143	0.599903	0.714615
0.700000	6	450	S2	0.339629	0.100960	0.334264	0.277383	0.297774	0.281640
0.700000	6	450	S3	0.433039	0.452846	0.433841	0.429579	0.421031	0.240145
0.700000	6	450	S4	0.475312	0.392700	0.465000	0.472010	0.563853	0.408803
0.700000	6	460	S2	0.404283	0.417885	0.429416	0.420385	0.451513	0.278144
0.700000	6	460	S3	0.403142	0.342119	0.427533	0.390032	0.495937	0.425764
0.700000	6	460	S4	0.446501	0.400353	0.454904	0.376082	0.547504	0.486170
0.700000	6	470	S2	0.456313	0.270453	0.495695	0.496143	0.507928	0.398972
0.700000	6	470	S3	0.475256	0.341618	0.482582	0.460112	0.540817	0.546882
0.700000	6	470	S4	0.411527	0.404797	0.438300	0.467855	0.495545	0.470180
0.700000	6	480	S2	0.426549	0.456532	0.429211	0.496702	0.366650	0.556492
0.700000	6	480	S3	0.421341	0.537551	0.383582	0.542220	0.435387	0.294869
0.700000	6	480	S4	0.393860	0.440946	0.382296	0.361500	0.544899	0.349206
0.700000	6	490	S2	0.439078	0.424515	0.414647	0.494910	0.461325	0.418243
0.700000	6	490	S3	0.552252	0.486536	0.579672	0.581139	0.491846	0.679030
0.700000	6	490	S4	0.399762	0.320160	0.411110	0.387964	0.347971	0.354383
0.700000	6	500	S2	0.373228	0.190104	0.384818	0.260140	0.310842	0.158339

Continued on next page

Table 9.3 – Continued from previous page

Thickness (mm)	Damage size (mm)	Freq. (kHz)	Sensor	DI (Actual)	PR	SVM	ANN	BR	SGD
0.700000	6	500	S3	0.479723	0.652746	0.472569	0.493036	0.518983	0.379586
0.700000	6	500	S4	0.563621	0.423793	0.553570	0.591982	0.530339	0.616388
0.700000	7	300	S2	0.483972	0.440380	0.519422	0.400093	0.512825	0.657250
0.700000	7	300	S3	0.592321	0.715554	0.604009	0.631595	0.736247	0.494800
0.700000	7	300	S4	0.521537	0.565324	0.536995	0.485863	0.412871	0.497149
0.700000	7	310	S2	0.608017	0.615799	0.598540	0.633840	0.524845	0.701311
0.700000	7	310	S3	0.595451	0.571652	0.575949	0.626496	0.622890	0.614552
0.700000	7	310	S4	0.541479	0.475565	0.546058	0.495028	0.487566	0.628769
0.700000	7	320	S2	0.532824	0.514079	0.516752	0.495077	0.451057	0.357474
0.700000	7	320	S3	0.605802	0.521097	0.560645	0.574706	0.672780	0.745338
0.700000	7	320	S4	0.499656	0.534807	0.521681	0.556360	0.574768	0.381575
0.700000	7	330	S2	0.513732	0.351644	0.516925	0.457466	0.548225	0.438034
0.700000	7	330	S3	0.601204	0.742361	0.602698	0.541042	0.660877	0.666596
0.700000	7	330	S4	0.499015	0.483287	0.507939	0.488839	0.552193	0.702393
0.700000	7	340	S2	0.574695	0.583584	0.594476	0.610623	0.616575	0.418815
0.700000	7	340	S3	0.675253	0.644299	0.666325	0.691503	0.586306	0.859604
0.700000	7	340	S4	0.644447	0.724339	0.621015	0.650149	0.583531	0.639532
0.700000	7	350	S2	0.520666	0.577346	0.536784	0.492856	0.522079	0.456138
0.700000	7	350	S3	0.481997	0.555218	0.491763	0.501768	0.535628	0.701940
0.700000	7	350	S4	0.575872	0.507782	0.599299	0.515247	0.547899	0.540084
0.700000	7	360	S2	0.579860	0.583451	0.564712	0.664784	0.549432	0.636671
0.700000	7	360	S3	0.542339	0.501656	0.557887	0.534146	0.487986	0.407093
0.700000	7	360	S4	0.571122	0.698287	0.589478	0.561934	0.612366	0.683826
0.700000	7	370	S2	0.593748	0.627094	0.561321	0.596420	0.564230	0.709320
0.700000	7	370	S3	0.541323	0.501396	0.528713	0.492120	0.530331	0.709966
0.700000	7	370	S4	0.595528	0.558543	0.587483	0.589573	0.556278	0.564209
0.700000	7	380	S2	0.638088	0.728960	0.651661	0.676960	0.736065	0.654147
0.700000	7	380	S3	0.656006	0.732792	0.644055	0.650413	0.598930	0.672257
0.700000	7	380	S4	0.514732	0.584966	0.494019	0.556525	0.678356	0.615947
0.700000	7	390	S2	0.556935	0.606823	0.534831	0.583466	0.543032	0.617587
0.700000	7	390	S3	0.568459	0.637017	0.568105	0.488679	0.471315	0.604457
0.700000	7	390	S4	0.468961	0.448690	0.486367	0.418614	0.366092	0.528276
0.700000	7	400	S2	0.501469	0.466397	0.490773	0.512864	0.474628	0.528567
0.700000	7	400	S3	0.419444	0.328484	0.416898	0.435059	0.501938	0.536442
0.700000	7	400	S4	0.611464	0.514520	0.579897	0.692429	0.662758	0.294459
0.700000	7	410	S2	0.576322	0.384892	0.561783	0.516623	0.509836	0.522241
0.700000	7	410	S3	0.566640	0.542219	0.590866	0.638415	0.517227	0.544041
0.700000	7	410	S4	0.522757	0.592770	0.536461	0.415721	0.406329	0.607670

Continued on next page

Table 9.3 – Continued from previous page

Thickness (mm)	Damage size (mm)	Freq. (kHz)	Sensor	DI (Actual)	PR	SVM	ANN	BR	SGD
0.700000	7	420	S2	0.567830	0.605450	0.564623	0.613862	0.621406	0.671698
0.700000	7	420	S3	0.574412	0.653773	0.566611	0.556945	0.588466	0.379530
0.700000	7	420	S4	0.562712	0.694049	0.595372	0.566968	0.590521	0.718080
0.700000	7	430	S2	0.539976	0.428007	0.514080	0.589288	0.583680	0.587519
0.700000	7	430	S3	0.638845	0.652358	0.601541	0.627447	0.596581	0.522826
0.700000	7	430	S4	0.565124	0.603699	0.546801	0.494306	0.587808	0.539497
0.700000	7	440	S2	0.554468	0.562682	0.543683	0.497721	0.568642	0.540524
0.700000	7	440	S3	0.533806	0.547162	0.531918	0.583133	0.708262	0.466124
0.700000	7	440	S4	0.576206	0.612341	0.574500	0.580532	0.656537	0.657034
0.700000	7	450	S2	0.541847	0.559519	0.556402	0.549905	0.700763	0.425896
0.700000	7	450	S3	0.566799	0.407061	0.615179	0.559542	0.696544	0.402898
0.700000	7	450	S4	0.614725	0.617651	0.623218	0.648800	0.557044	0.612265
0.700000	7	460	S2	0.614467	0.557456	0.655406	0.629999	0.542803	0.669596
0.700000	7	460	S3	0.538642	0.549712	0.527672	0.584122	0.641949	0.602907
0.700000	7	460	S4	0.521302	0.552884	0.478726	0.571708	0.482742	0.368935
0.700000	7	470	S2	0.529595	0.543736	0.540757	0.631791	0.496794	0.525108
0.700000	7	470	S3	0.628051	0.626915	0.633517	0.651542	0.642261	0.670613
0.700000	7	470	S4	0.527267	0.545756	0.550269	0.457083	0.582346	0.445633
0.700000	7	480	S2	0.582698	0.670672	0.594245	0.663490	0.584745	0.611239
0.700000	7	480	S3	0.596291	0.574223	0.600451	0.588745	0.570914	0.205920
0.700000	7	480	S4	0.627660	0.430893	0.653202	0.555266	0.714570	0.570147
0.700000	7	490	S2	0.571860	0.524367	0.593764	0.496491	0.605543	0.509521
0.700000	7	490	S3	0.587325	0.651404	0.586190	0.550962	0.603118	0.649877
0.700000	7	490	S4	0.546095	0.555406	0.551897	0.531475	0.389833	0.389702
0.700000	7	500	S2	0.680771	0.657236	0.667495	0.740913	0.669356	0.532013
0.700000	7	500	S3	0.529897	0.697152	0.550683	0.490837	0.499336	0.667564
0.700000	7	500	S4	0.578144	0.582560	0.590723	0.577040	0.596298	0.521351
0.700000	12x4	300	S2	0.221012	0.099397	0.216412	0.181019	0.172487	0.374395
0.700000	12x4	300	S3	0.256829	0.182342	0.238798	0.291933	0.341795	0.120179
0.700000	12x4	300	S4	0.162425	0.228364	0.168190	0.109166	0.098604	0.194224
0.700000	12x4	310	S2	0.249156	0.383635	0.247140	0.309020	0.369887	0.458646
0.700000	12x4	310	S3	0.245746	0.320815	0.271616	0.279052	0.193995	0.081391
0.700000	12x4	310	S4	0.239350	0.345420	0.220414	0.240737	0.191739	0.260761
0.700000	12x4	320	S2	0.283716	0.161504	0.272979	0.241093	0.164394	0.508170
0.700000	12x4	320	S3	0.244942	0.210841	0.257717	0.210106	0.308373	0.197954
0.700000	12x4	320	S4	0.189768	0.246461	0.193869	0.119606	0.109918	0.342200
0.700000	12x4	330	S2	0.285706	0.308516	0.232182	0.374522	0.247728	0.329248
0.700000	12x4	330	S3	0.202811	0.288221	0.210283	0.242217	0.086205	0.197973

Continued on next page

Table 9.3 – Continued from previous page

Thickness (mm)	Damage size (mm)	Freq. (kHz)	Sensor	DI (Actual)	PR	SVM	ANN	BR	SGD
0.700000	12x4	330	S4	0.201299	0.137538	0.205931	0.115173	0.055737	0.047447
0.700000	12x4	340	S2	0.250770	0.325250	0.269794	0.249316	0.158420	0.000000
0.700000	12x4	340	S3	0.328752	0.294027	0.376239	0.414984	0.293607	0.415163
0.700000	12x4	340	S4	0.265899	0.153906	0.296752	0.272515	0.276797	0.311413
0.700000	12x4	350	S2	0.314456	0.338096	0.314623	0.246732	0.303520	0.427448
0.700000	12x4	350	S3	0.245826	0.000000	0.260403	0.229852	0.216394	0.122975
0.700000	12x4	350	S4	0.265176	0.264780	0.256514	0.334269	0.237528	0.176730
0.700000	12x4	360	S2	0.195967	0.192604	0.195923	0.247105	0.131616	0.281066
0.700000	12x4	360	S3	0.292061	0.228256	0.272282	0.339740	0.424367	0.260174
0.700000	12x4	360	S4	0.213064	0.161575	0.190645	0.246378	0.168130	0.309743
0.700000	12x4	370	S2	0.272891	0.269209	0.239515	0.300548	0.179242	0.181075
0.700000	12x4	370	S3	0.302205	0.359781	0.301519	0.311518	0.234318	0.441597
0.700000	12x4	370	S4	0.226493	0.276556	0.239105	0.215917	0.168648	0.144367
0.700000	12x4	380	S2	0.228333	0.184479	0.210765	0.250711	0.192406	0.215493
0.700000	12x4	380	S3	0.326637	0.343200	0.357086	0.381546	0.404818	0.151560
0.700000	12x4	380	S4	0.314727	0.441682	0.293985	0.355286	0.362055	0.473978
0.700000	12x4	390	S2	0.125990	0.181988	0.141315	0.153259	0.084080	0.000000
0.700000	12x4	390	S3	0.248375	0.331475	0.241121	0.226470	0.184966	0.036210
0.700000	12x4	390	S4	0.246224	0.269318	0.251019	0.315836	0.230405	0.355391
0.700000	12x4	400	S2	0.199850	0.283464	0.196578	0.208003	0.308469	0.121520
0.700000	12x4	400	S3	0.202493	0.127164	0.178761	0.204445	0.075557	0.166883
0.700000	12x4	400	S4	0.243581	0.044610	0.262508	0.250428	0.255733	0.350479
0.700000	12x4	410	S2	0.205620	0.226988	0.198672	0.194492	0.106591	0.259473
0.700000	12x4	410	S3	0.204567	0.231281	0.203568	0.138911	0.242790	0.282103
0.700000	12x4	410	S4	0.326382	0.318826	0.327718	0.361493	0.294313	0.203842
0.700000	12x4	420	S2	0.291476	0.459777	0.309366	0.306089	0.263150	0.260762
0.700000	12x4	420	S3	0.262267	0.182962	0.244666	0.259569	0.171590	0.126164
0.700000	12x4	420	S4	0.212627	0.220970	0.208360	0.308974	0.191885	0.394841
0.700000	12x4	430	S2	0.254084	0.210920	0.245516	0.275661	0.267962	0.214407
0.700000	12x4	430	S3	0.232500	0.249922	0.258324	0.346289	0.312739	0.249724
0.700000	12x4	430	S4	0.273157	0.219731	0.293788	0.247999	0.354664	0.342959
0.700000	12x4	440	S2	0.203207	0.174288	0.175718	0.173091	0.185031	0.246319
0.700000	12x4	440	S3	0.150798	0.119428	0.132371	0.061844	0.242180	0.133645
0.700000	12x4	440	S4	0.307012	0.196791	0.300336	0.332555	0.266424	0.386096
0.700000	12x4	450	S2	0.239272	0.389636	0.230412	0.359381	0.350082	0.312623
0.700000	12x4	450	S3	0.331441	0.283349	0.365184	0.300336	0.373384	0.333777
0.700000	12x4	450	S4	0.199941	0.231852	0.212149	0.132743	0.185689	0.073927
0.700000	12x4	460	S2	0.232394	0.284139	0.246010	0.135695	0.266537	0.184744

Continued on next page

Table 9.3 – Continued from previous page

Thickness (mm)	Damage size (mm)	Freq. (kHz)	Sensor	DI (Actual)	PR	SVM	ANN	BR	SGD
0.700000	12x4	460	S3	0.231531	0.128943	0.201318	0.212136	0.175664	0.369860
0.700000	12x4	460	S4	0.320176	0.254879	0.306252	0.319440	0.270249	0.227071
0.700000	12x4	470	S2	0.239196	0.208807	0.213019	0.243577	0.196461	0.242070
0.700000	12x4	470	S3	0.314919	0.227767	0.321661	0.277709	0.249489	0.215663
0.700000	12x4	470	S4	0.347344	0.252574	0.347842	0.318439	0.360875	0.501105
0.700000	12x4	480	S2	0.418331	0.204832	0.435351	0.484974	0.454270	0.538036
0.700000	12x4	480	S3	0.317304	0.364778	0.298719	0.264010	0.391365	0.133353
0.700000	12x4	480	S4	0.206604	0.150989	0.218683	0.173606	0.148274	0.204080
0.700000	12x4	490	S2	0.229472	0.293085	0.242879	0.197949	0.215453	0.169559
0.700000	12x4	490	S3	0.245635	0.344231	0.240161	0.304564	0.096111	0.377554
0.700000	12x4	490	S4	0.272179	0.097602	0.268448	0.145704	0.402459	0.461898
0.700000	12x4	500	S2	0.272531	0.156045	0.272889	0.178925	0.321510	0.337789
0.700000	12x4	500	S3	0.292916	0.108471	0.269995	0.290962	0.261827	0.238290
0.700000	12x4	500	S4	0.270344	0.253922	0.251365	0.348020	0.153782	0.080136
0.700000	15x5	300	S2	0.436560	0.442721	0.457787	0.446463	0.422815	0.268605
0.700000	15x5	300	S3	0.400487	0.496077	0.411412	0.355425	0.502736	0.481465
0.700000	15x5	300	S4	0.338337	0.388783	0.335411	0.332774	0.279446	0.454147
0.700000	15x5	310	S2	0.290807	0.235961	0.283405	0.275564	0.296484	0.299477
0.700000	15x5	310	S3	0.403203	0.392549	0.400604	0.364353	0.371657	0.360236
0.700000	15x5	310	S4	0.313475	0.267946	0.329992	0.359856	0.253459	0.584688
0.700000	15x5	320	S2	0.400698	0.367563	0.360789	0.402145	0.404838	0.421860
0.700000	15x5	320	S3	0.345899	0.382435	0.386179	0.442098	0.345379	0.308268
0.700000	15x5	320	S4	0.312793	0.419235	0.308386	0.324285	0.272572	0.269138
0.700000	15x5	330	S2	0.333298	0.320573	0.327340	0.285874	0.343976	0.212692
0.700000	15x5	330	S3	0.411221	0.389167	0.393726	0.382537	0.488398	0.540920
0.700000	15x5	330	S4	0.260768	0.197843	0.221269	0.289305	0.235441	0.244027
0.700000	15x5	340	S2	0.377318	0.470953	0.345278	0.346729	0.334012	0.270591
0.700000	15x5	340	S3	0.391883	0.334452	0.386388	0.452396	0.365536	0.486290
0.700000	15x5	340	S4	0.398924	0.504796	0.395171	0.474399	0.326440	0.421008
0.700000	15x5	350	S2	0.201529	0.214808	0.186683	0.225145	0.233933	0.253899
0.700000	15x5	350	S3	0.372244	0.300951	0.382079	0.346943	0.341971	0.485103
0.700000	15x5	350	S4	0.281345	0.386908	0.301196	0.241526	0.305799	0.529858
0.700000	15x5	360	S2	0.453189	0.471105	0.407663	0.489010	0.344703	0.610714
0.700000	15x5	360	S3	0.299431	0.417927	0.311356	0.294343	0.222914	0.168728
0.700000	15x5	360	S4	0.349232	0.231167	0.375244	0.328424	0.371507	0.232089
0.700000	15x5	370	S2	0.330721	0.297693	0.349738	0.317334	0.397689	0.224095
0.700000	15x5	370	S3	0.358142	0.249702	0.377195	0.274183	0.455335	0.320343
0.700000	15x5	370	S4	0.334343	0.281483	0.333190	0.300124	0.293428	0.591558

Continued on next page

Table 9.3 – Continued from previous page

Thickness (mm)	Damage size (mm)	Freq. (kHz)	Sensor	DI (Actual)	PR	SVM	ANN	BR	SGD
0.700000	15x5	380	S2	0.288738	0.295792	0.269055	0.271956	0.277438	0.274706
0.700000	15x5	380	S3	0.264342	0.325516	0.254520	0.206017	0.427491	0.244742
0.700000	15x5	380	S4	0.342161	0.181436	0.356801	0.295860	0.349063	0.524067
0.700000	15x5	390	S2	0.245422	0.271460	0.266548	0.192032	0.299501	0.262235
0.700000	15x5	390	S3	0.313101	0.243010	0.327532	0.330865	0.288695	0.256731
0.700000	15x5	390	S4	0.261806	0.265105	0.240293	0.293300	0.274633	0.414968
0.700000	15x5	400	S2	0.237945	0.350060	0.233708	0.248406	0.135761	0.185938
0.700000	15x5	400	S3	0.379320	0.131938	0.340585	0.315042	0.360921	0.328646
0.700000	15x5	400	S4	0.323655	0.315747	0.319613	0.369510	0.392362	0.354528
0.700000	15x5	410	S2	0.321362	0.274527	0.305828	0.271944	0.358966	0.335936
0.700000	15x5	410	S3	0.368072	0.489441	0.353218	0.424601	0.401858	0.362362
0.700000	15x5	410	S4	0.387354	0.448760	0.372784	0.360008	0.394421	0.402687
0.700000	15x5	420	S2	0.354833	0.325116	0.369401	0.371237	0.532012	0.402973
0.700000	15x5	420	S3	0.302374	0.373672	0.304880	0.251158	0.382236	0.314835
0.700000	15x5	420	S4	0.360339	0.228931	0.329868	0.330810	0.337655	0.374888
0.700000	15x5	430	S2	0.354894	0.466895	0.353923	0.300301	0.303213	0.367641
0.700000	15x5	430	S3	0.350813	0.238936	0.311429	0.293745	0.379202	0.293486
0.700000	15x5	430	S4	0.309336	0.267809	0.332529	0.293952	0.356176	0.353045
0.700000	15x5	440	S2	0.380627	0.504931	0.379776	0.439733	0.391339	0.388965
0.700000	15x5	440	S3	0.380783	0.201476	0.400043	0.385906	0.405941	0.419919
0.700000	15x5	440	S4	0.310032	0.410912	0.304795	0.286325	0.302190	0.278662
0.700000	15x5	450	S2	0.343179	0.458885	0.358250	0.345849	0.318301	0.430159
0.700000	15x5	450	S3	0.413740	0.434765	0.387420	0.483544	0.437309	0.480277
0.700000	15x5	450	S4	0.383766	0.378336	0.419805	0.367011	0.330978	0.455342
0.700000	15x5	460	S2	0.368270	0.491319	0.366157	0.368177	0.390446	0.311890
0.700000	15x5	460	S3	0.347363	0.306213	0.396420	0.294816	0.335318	0.441199
0.700000	15x5	460	S4	0.332187	0.297357	0.349819	0.385551	0.407765	0.512844
0.700000	15x5	470	S2	0.344816	0.265351	0.340869	0.411649	0.409691	0.286835
0.700000	15x5	470	S3	0.381688	0.395547	0.371133	0.422443	0.334237	0.220363
0.700000	15x5	470	S4	0.397857	0.431818	0.390192	0.452956	0.483331	0.361944
0.700000	15x5	480	S2	0.387500	0.441867	0.409282	0.400062	0.285861	0.569344
0.700000	15x5	480	S3	0.326075	0.325115	0.304857	0.250931	0.189836	0.437570
0.700000	15x5	480	S4	0.351867	0.363864	0.326004	0.335740	0.297059	0.318499
0.700000	15x5	490	S2	0.354499	0.380806	0.378053	0.398637	0.435053	0.244810
0.700000	15x5	490	S3	0.352324	0.297385	0.344425	0.412320	0.320697	0.335232
0.700000	15x5	490	S4	0.342324	0.343332	0.341313	0.363335	0.425693	0.514088
0.700000	15x5	500	S2	0.293354	0.302091	0.272722	0.291123	0.278083	0.378377
0.700000	15x5	500	S3	0.313568	0.332965	0.272433	0.251131	0.402256	0.392993

Continued on next page

Table 9.3 – Continued from previous page

Thickness (mm)	Damage size (mm)	Freq. (kHz)	Sensor	DI (Actual)	PR	SVM	ANN	BR	SGD
0.700000	15x5	500	S4	0.302272	0.387163	0.326126	0.354063	0.374472	0.322032
0.700000	18x6	300	S2	0.418742	0.576613	0.432044	0.468545	0.506526	0.410871
0.700000	18x6	300	S3	0.507010	0.494465	0.509613	0.540682	0.476267	0.457499
0.700000	18x6	300	S4	0.527179	0.511436	0.491840	0.596939	0.477279	0.595484
0.700000	18x6	310	S2	0.425472	0.297991	0.430124	0.533591	0.376211	0.348062
0.700000	18x6	310	S3	0.490582	0.552164	0.463813	0.584617	0.583552	0.452226
0.700000	18x6	310	S4	0.422344	0.467559	0.453227	0.393631	0.484682	0.315020
0.700000	18x6	320	S2	0.496843	0.500558	0.487527	0.474084	0.566854	0.417479
0.700000	18x6	320	S3	0.438939	0.638857	0.432432	0.401007	0.310493	0.317092
0.700000	18x6	320	S4	0.498116	0.471043	0.524150	0.549903	0.531589	0.477861
0.700000	18x6	330	S2	0.381273	0.410737	0.362384	0.297759	0.403997	0.494853
0.700000	18x6	330	S3	0.502704	0.387707	0.515596	0.543044	0.467393	0.367726
0.700000	18x6	330	S4	0.448810	0.363401	0.417058	0.498941	0.317839	0.567258
0.700000	18x6	340	S2	0.420590	0.390123	0.415864	0.349209	0.315902	0.278610
0.700000	18x6	340	S3	0.430296	0.344737	0.442686	0.420401	0.323663	0.342236
0.700000	18x6	340	S4	0.430015	0.335303	0.434528	0.482762	0.445102	0.441663
0.700000	18x6	350	S2	0.410298	0.439572	0.417270	0.434842	0.407568	0.496528
0.700000	18x6	350	S3	0.484568	0.500886	0.453339	0.491361	0.508414	0.520354
0.700000	18x6	350	S4	0.503421	0.738472	0.514082	0.487645	0.428739	0.668164
0.700000	18x6	360	S2	0.423670	0.316314	0.389506	0.456453	0.368127	0.433212
0.700000	18x6	360	S3	0.444435	0.522876	0.419658	0.482922	0.341274	0.363266
0.700000	18x6	360	S4	0.469268	0.245071	0.444776	0.545425	0.450396	0.372512
0.700000	18x6	370	S2	0.481902	0.410371	0.469985	0.488904	0.454307	0.430202
0.700000	18x6	370	S3	0.481150	0.521156	0.501891	0.440444	0.349877	0.512970
0.700000	18x6	370	S4	0.443630	0.560974	0.447594	0.417707	0.459940	0.432458
0.700000	18x6	380	S2	0.445754	0.436208	0.444589	0.515015	0.552775	0.492054
0.700000	18x6	380	S3	0.446388	0.498797	0.433227	0.436017	0.693199	0.477526
0.700000	18x6	380	S4	0.477232	0.518830	0.465850	0.427311	0.611455	0.755425
0.700000	18x6	390	S2	0.477781	0.459653	0.482256	0.456489	0.483256	0.447597
0.700000	18x6	390	S3	0.436963	0.322856	0.434269	0.411102	0.413136	0.556778
0.700000	18x6	390	S4	0.456468	0.548480	0.447589	0.423736	0.480779	0.331648
0.700000	18x6	400	S2	0.461877	0.401762	0.515235	0.498717	0.275269	0.451098
0.700000	18x6	400	S3	0.509823	0.498862	0.517412	0.575786	0.618586	0.614149
0.700000	18x6	400	S4	0.492433	0.550257	0.472497	0.513828	0.535985	0.283002
0.700000	18x6	410	S2	0.491871	0.574362	0.482347	0.516989	0.526119	0.513345
0.700000	18x6	410	S3	0.472015	0.404528	0.476763	0.519049	0.370459	0.551302
0.700000	18x6	410	S4	0.363902	0.482879	0.381089	0.346849	0.390978	0.325335
0.700000	18x6	420	S2	0.412417	0.385421	0.417138	0.375879	0.384887	0.338514

Continued on next page

Table 9.3 – Continued from previous page

Thickness (mm)	Damage size (mm)	Freq. (kHz)	Sensor	DI (Actual)	PR	SVM	ANN	BR	SGD
0.700000	18x6	420	S3	0.428756	0.327120	0.409436	0.473504	0.525904	0.351640
0.700000	18x6	420	S4	0.443786	0.425229	0.424218	0.426482	0.310452	0.523468
0.700000	18x6	430	S2	0.427464	0.420234	0.439463	0.245171	0.445347	0.367011
0.700000	18x6	430	S3	0.354627	0.393838	0.368209	0.305250	0.429333	0.165167
0.700000	18x6	430	S4	0.480626	0.323571	0.468954	0.430513	0.513122	0.481993
0.700000	18x6	440	S2	0.532347	0.525339	0.561174	0.590920	0.572707	0.555972
0.700000	18x6	440	S3	0.357815	0.373320	0.384782	0.290588	0.295695	0.206496
0.700000	18x6	440	S4	0.450287	0.662266	0.494270	0.414296	0.374548	0.241894
0.700000	18x6	450	S2	0.441798	0.430531	0.442681	0.487698	0.552271	0.424217
0.700000	18x6	450	S3	0.464363	0.377827	0.466883	0.483888	0.537998	0.633464
0.700000	18x6	450	S4	0.448812	0.562784	0.453425	0.449264	0.419594	0.673741
0.700000	18x6	460	S2	0.511822	0.663259	0.529011	0.561873	0.537660	0.644825
0.700000	18x6	460	S3	0.500619	0.509647	0.520968	0.446065	0.547568	0.576757
0.700000	18x6	460	S4	0.468253	0.608320	0.479528	0.480409	0.500764	0.510837
0.700000	18x6	470	S2	0.433546	0.429172	0.445265	0.439974	0.531861	0.349648
0.700000	18x6	470	S3	0.428107	0.439143	0.438901	0.393289	0.519984	0.289776
0.700000	18x6	470	S4	0.516357	0.473040	0.511279	0.502294	0.472712	0.529203
0.700000	18x6	480	S2	0.448900	0.387807	0.441624	0.390969	0.478154	0.471467
0.700000	18x6	480	S3	0.529138	0.514451	0.541514	0.548917	0.443090	0.611686
0.700000	18x6	480	S4	0.459994	0.402854	0.459178	0.534764	0.411088	0.523909
0.700000	18x6	490	S2	0.422538	0.404057	0.428870	0.423215	0.546416	0.251668
0.700000	18x6	490	S3	0.451515	0.411775	0.482765	0.453038	0.402496	0.451342
0.700000	18x6	490	S4	0.443291	0.412729	0.423194	0.489951	0.456041	0.438817
0.700000	18x6	500	S2	0.457570	0.564296	0.463065	0.447395	0.498816	0.426104
0.700000	18x6	500	S3	0.424121	0.479072	0.441183	0.443711	0.216164	0.501014
0.700000	18x6	500	S4	0.463991	0.453015	0.468768	0.503613	0.456003	0.474261
0.900000	4	300	S2	0.317679	0.300713	0.311120	0.318718	0.329825	0.359944
0.900000	4	300	S3	0.278044	0.205405	0.270804	0.337823	0.203608	0.517293
0.900000	4	300	S4	0.366716	0.508159	0.372794	0.348367	0.426050	0.352460
0.900000	4	310	S2	0.323619	0.319577	0.338770	0.285675	0.340908	0.247564
0.900000	4	310	S3	0.311993	0.293160	0.358185	0.365919	0.255094	0.309856
0.900000	4	310	S4	0.332807	0.324471	0.344954	0.276056	0.190462	0.335862
0.900000	4	320	S2	0.269142	0.199504	0.277853	0.240873	0.202287	0.316420
0.900000	4	320	S3	0.337965	0.449816	0.302862	0.351767	0.359059	0.469729
0.900000	4	320	S4	0.238789	0.297608	0.236586	0.227506	0.175565	0.356688
0.900000	4	330	S2	0.277135	0.293014	0.274826	0.270946	0.360175	0.212623
0.900000	4	330	S3	0.304396	0.316220	0.321170	0.307195	0.268153	0.276813
0.900000	4	330	S4	0.313463	0.312823	0.309888	0.213752	0.427774	0.169741

Continued on next page

Table 9.3 – Continued from previous page

Thickness (mm)	Damage size (mm)	Freq. (kHz)	Sensor	DI (Actual)	PR	SVM	ANN	BR	SGD
0.900000	4	340	S2	0.260497	0.195299	0.233808	0.186162	0.212796	0.305130
0.900000	4	340	S3	0.331231	0.430116	0.317453	0.257644	0.322833	0.321965
0.900000	4	340	S4	0.273684	0.186209	0.239158	0.278383	0.263639	0.173472
0.900000	4	350	S2	0.252920	0.383465	0.267416	0.264093	0.297453	0.305241
0.900000	4	350	S3	0.314718	0.349972	0.327076	0.233478	0.282494	0.237713
0.900000	4	350	S4	0.302336	0.172381	0.284635	0.311295	0.271830	0.479342
0.900000	4	360	S2	0.282298	0.182700	0.273099	0.267299	0.279693	0.264844
0.900000	4	360	S3	0.254215	0.279098	0.247748	0.348365	0.270563	0.273581
0.900000	4	360	S4	0.363854	0.495613	0.358491	0.280845	0.436748	0.373127
0.900000	4	370	S2	0.319766	0.433551	0.301018	0.236958	0.186491	0.153210
0.900000	4	370	S3	0.362547	0.500599	0.356669	0.379510	0.411086	0.341440
0.900000	4	370	S4	0.265545	0.265542	0.259304	0.215816	0.326299	0.323699
0.900000	4	380	S2	0.293525	0.402561	0.285766	0.243953	0.147984	0.050816
0.900000	4	380	S3	0.285277	0.233877	0.264846	0.292533	0.136682	0.376191
0.900000	4	380	S4	0.276674	0.162988	0.266559	0.194332	0.371109	0.297671
0.900000	4	390	S2	0.276377	0.388297	0.267499	0.321442	0.300331	0.335396
0.900000	4	390	S3	0.232652	0.245579	0.212119	0.286420	0.228933	0.240533
0.900000	4	390	S4	0.303206	0.251115	0.283011	0.202181	0.234312	0.231395
0.900000	4	400	S2	0.300499	0.424440	0.299011	0.195934	0.269392	0.419945
0.900000	4	400	S3	0.280100	0.202143	0.276187	0.404214	0.391410	0.189855
0.900000	4	400	S4	0.251421	0.215703	0.294263	0.266923	0.253963	0.278506
0.900000	4	410	S2	0.281259	0.312078	0.308104	0.284002	0.392958	0.153309
0.900000	4	410	S3	0.236414	0.295215	0.214387	0.235706	0.297092	0.440456
0.900000	4	410	S4	0.244814	0.279996	0.223696	0.245073	0.360683	0.082596
0.900000	4	420	S2	0.205166	0.265322	0.201865	0.184438	0.206540	0.038770
0.900000	4	420	S3	0.367465	0.445697	0.382354	0.403085	0.390423	0.325215
0.900000	4	420	S4	0.332818	0.269832	0.345418	0.302373	0.483355	0.220802
0.900000	4	430	S2	0.276527	0.310068	0.255585	0.237630	0.136124	0.260535
0.900000	4	430	S3	0.205080	0.285437	0.228585	0.154044	0.230029	0.254672
0.900000	4	430	S4	0.310721	0.264999	0.330818	0.381537	0.245018	0.312193
0.900000	4	440	S2	0.334410	0.462445	0.354591	0.251616	0.372812	0.412008
0.900000	4	440	S3	0.288670	0.442280	0.266899	0.332249	0.231367	0.117195
0.900000	4	440	S4	0.367538	0.341903	0.350851	0.420738	0.331596	0.446761
0.900000	4	450	S2	0.276733	0.464846	0.281054	0.271893	0.203949	0.231805
0.900000	4	450	S3	0.350353	0.245618	0.377752	0.294150	0.310137	0.292310
0.900000	4	450	S4	0.330190	0.224388	0.310108	0.224116	0.389936	0.407908
0.900000	4	460	S2	0.299752	0.210857	0.311797	0.316879	0.436621	0.319042
0.900000	4	460	S3	0.254539	0.283909	0.257361	0.188742	0.322494	0.258643

Continued on next page

Table 9.3 – Continued from previous page

Thickness (mm)	Damage size (mm)	Freq. (kHz)	Sensor	DI (Actual)	PR	SVM	ANN	BR	SGD
0.900000	4	460	S4	0.352612	0.327349	0.338725	0.395710	0.349881	0.291077
0.900000	4	470	S2	0.228069	0.253215	0.215230	0.198176	0.285725	0.201873
0.900000	4	470	S3	0.300046	0.219442	0.297392	0.250563	0.437166	0.401764
0.900000	4	470	S4	0.382509	0.401412	0.363166	0.337013	0.393343	0.477575
0.900000	4	480	S2	0.259430	0.266288	0.245681	0.228517	0.133811	0.382142
0.900000	4	480	S3	0.206063	0.297839	0.229725	0.138459	0.256228	0.157778
0.900000	4	480	S4	0.299485	0.287413	0.302039	0.160091	0.358721	0.312209
0.900000	4	490	S2	0.279095	0.243796	0.291105	0.259241	0.181218	0.206357
0.900000	4	490	S3	0.356748	0.362162	0.344140	0.241588	0.436265	0.361091
0.900000	4	490	S4	0.374632	0.394398	0.325959	0.371038	0.273927	0.268696
0.900000	4	500	S2	0.334499	0.228881	0.345235	0.371798	0.322669	0.270116
0.900000	4	500	S3	0.260341	0.282003	0.257346	0.229925	0.312605	0.288941
0.900000	4	500	S4	0.222165	0.325418	0.237274	0.227218	0.122968	0.127785
0.900000	5	300	S2	0.362622	0.337745	0.352099	0.307376	0.376985	0.290196
0.900000	5	300	S3	0.316425	0.258071	0.275581	0.375039	0.270138	0.473499
0.900000	5	300	S4	0.331218	0.344384	0.312504	0.258871	0.423904	0.535615
0.900000	5	310	S2	0.412245	0.443347	0.408273	0.357704	0.437645	0.309017
0.900000	5	310	S3	0.318708	0.306854	0.331384	0.283659	0.372116	0.525232
0.900000	5	310	S4	0.473610	0.555453	0.485590	0.534674	0.406336	0.329009
0.900000	5	320	S2	0.452520	0.365895	0.463989	0.360769	0.444155	0.514523
0.900000	5	320	S3	0.363527	0.379267	0.356208	0.383974	0.421132	0.251988
0.900000	5	320	S4	0.408440	0.426235	0.400696	0.383854	0.430665	0.309078
0.900000	5	330	S2	0.440195	0.349923	0.415757	0.375139	0.474393	0.473850
0.900000	5	330	S3	0.453411	0.532115	0.446950	0.502929	0.526704	0.490731
0.900000	5	330	S4	0.377228	0.338496	0.380612	0.408908	0.293382	0.418718
0.900000	5	340	S2	0.343160	0.320811	0.365051	0.415513	0.323006	0.226786
0.900000	5	340	S3	0.315165	0.372568	0.300834	0.316850	0.456538	0.409660
0.900000	5	340	S4	0.362255	0.420348	0.384103	0.331984	0.185480	0.248805
0.900000	5	350	S2	0.420900	0.331468	0.438606	0.473644	0.425660	0.329007
0.900000	5	350	S3	0.411259	0.334682	0.381653	0.360138	0.247580	0.517824
0.900000	5	350	S4	0.379129	0.334005	0.361765	0.371589	0.484326	0.319825
0.900000	5	360	S2	0.452242	0.500639	0.438734	0.403275	0.487755	0.567320
0.900000	5	360	S3	0.502050	0.465469	0.497802	0.537063	0.424015	0.477903
0.900000	5	360	S4	0.432166	0.510637	0.417189	0.372063	0.546622	0.414402
0.900000	5	370	S2	0.411257	0.388073	0.385667	0.407275	0.485896	0.312296
0.900000	5	370	S3	0.372090	0.247829	0.385129	0.362853	0.302206	0.343393
0.900000	5	370	S4	0.454791	0.519874	0.481253	0.336520	0.471202	0.357585
0.900000	5	380	S2	0.331427	0.313456	0.332320	0.280843	0.340833	0.501629

Continued on next page

Table 9.3 – Continued from previous page

Thickness (mm)	Damage size (mm)	Freq. (kHz)	Sensor	DI (Actual)	PR	SVM	ANN	BR	SGD
0.900000	5	380	S3	0.427421	0.401809	0.468470	0.489513	0.415708	0.500422
0.900000	5	380	S4	0.258011	0.217744	0.264603	0.252407	0.241058	0.079685
0.900000	5	390	S2	0.395677	0.277392	0.365636	0.387242	0.400113	0.491246
0.900000	5	390	S3	0.455554	0.428880	0.477894	0.467385	0.486048	0.404190
0.900000	5	390	S4	0.392672	0.426251	0.387657	0.329307	0.441737	0.364726
0.900000	5	400	S2	0.431990	0.395143	0.416886	0.499340	0.491298	0.417638
0.900000	5	400	S3	0.295198	0.232048	0.291279	0.352882	0.334224	0.397337
0.900000	5	400	S4	0.354995	0.495205	0.343464	0.348008	0.386261	0.430367
0.900000	5	410	S2	0.365331	0.321558	0.337955	0.326976	0.364963	0.399235
0.900000	5	410	S3	0.373892	0.389647	0.353303	0.485802	0.308895	0.309229
0.900000	5	410	S4	0.471468	0.275861	0.478466	0.514644	0.507294	0.665286
0.900000	5	420	S2	0.365936	0.419212	0.375755	0.330939	0.324838	0.528760
0.900000	5	420	S3	0.393745	0.300771	0.442647	0.392645	0.356571	0.601775
0.900000	5	420	S4	0.321646	0.253907	0.344918	0.318067	0.496499	0.494010
0.900000	5	430	S2	0.386174	0.429068	0.380664	0.427755	0.474460	0.343077
0.900000	5	430	S3	0.391920	0.574023	0.400701	0.463931	0.387218	0.352895
0.900000	5	430	S4	0.412663	0.435171	0.419959	0.369814	0.381396	0.547858
0.900000	5	440	S2	0.322098	0.296058	0.317448	0.342564	0.265175	0.324699
0.900000	5	440	S3	0.411639	0.380524	0.442023	0.464671	0.309694	0.535765
0.900000	5	440	S4	0.401608	0.357888	0.425240	0.285906	0.341000	0.351236
0.900000	5	450	S2	0.412018	0.246450	0.423594	0.343762	0.420219	0.396811
0.900000	5	450	S3	0.337439	0.239451	0.295568	0.331863	0.304145	0.402934
0.900000	5	450	S4	0.450879	0.481955	0.482649	0.381146	0.431151	0.462905
0.900000	5	460	S2	0.377793	0.507628	0.384639	0.392777	0.339250	0.576882
0.900000	5	460	S3	0.401286	0.386756	0.456714	0.424329	0.519911	0.298371
0.900000	5	460	S4	0.438349	0.254681	0.420697	0.381779	0.472685	0.434773
0.900000	5	470	S2	0.425979	0.392709	0.416714	0.442150	0.454516	0.552220
0.900000	5	470	S3	0.408435	0.589036	0.428585	0.331385	0.486606	0.538864
0.900000	5	470	S4	0.427409	0.359182	0.389216	0.436271	0.415362	0.136897
0.900000	5	480	S2	0.431938	0.496789	0.452370	0.443198	0.414306	0.298407
0.900000	5	480	S3	0.356057	0.243179	0.375849	0.394337	0.395984	0.393550
0.900000	5	480	S4	0.423985	0.642764	0.426769	0.424447	0.442498	0.510715
0.900000	5	490	S2	0.395430	0.479010	0.396100	0.454996	0.371913	0.480672
0.900000	5	490	S3	0.338886	0.244168	0.348402	0.414380	0.346007	0.204612
0.900000	5	490	S4	0.389802	0.375553	0.381655	0.413557	0.430177	0.367148
0.900000	5	500	S2	0.290395	0.296155	0.253390	0.318006	0.416432	0.294579
0.900000	5	500	S3	0.371227	0.233619	0.340034	0.388066	0.137863	0.234751
0.900000	5	500	S4	0.367457	0.374320	0.345043	0.464528	0.280975	0.326753

Continued on next page

Table 9.3 – Continued from previous page

Thickness (mm)	Damage size (mm)	Freq. (kHz)	Sensor	DI (Actual)	PR	SVM	ANN	BR	SGD
0.900000	6	300	S2	0.481681	0.512972	0.497428	0.476196	0.454906	0.332412
0.900000	6	300	S3	0.465391	0.714104	0.458721	0.387914	0.477644	0.483907
0.900000	6	300	S4	0.596277	0.607152	0.629047	0.610441	0.538824	0.723151
0.900000	6	310	S2	0.505126	0.700096	0.521866	0.572205	0.522513	0.376417
0.900000	6	310	S3	0.435117	0.320324	0.425144	0.518963	0.383427	0.314675
0.900000	6	310	S4	0.572214	0.519725	0.575780	0.596290	0.581541	0.615511
0.900000	6	320	S2	0.458386	0.507099	0.499811	0.392623	0.371206	0.582211
0.900000	6	320	S3	0.498202	0.557698	0.488308	0.517725	0.450087	0.502436
0.900000	6	320	S4	0.375296	0.263618	0.359932	0.330635	0.449894	0.312813
0.900000	6	330	S2	0.499889	0.627657	0.491728	0.507122	0.476395	0.534442
0.900000	6	330	S3	0.482183	0.435244	0.492893	0.450927	0.437917	0.465223
0.900000	6	330	S4	0.532024	0.564953	0.517199	0.512217	0.673833	0.690477
0.900000	6	340	S2	0.611435	0.556549	0.636766	0.592310	0.488086	0.676987
0.900000	6	340	S3	0.560050	0.573917	0.547502	0.483879	0.630475	0.610735
0.900000	6	340	S4	0.464595	0.413974	0.472576	0.500606	0.395068	0.477986
0.900000	6	350	S2	0.561076	0.575118	0.575572	0.512841	0.541663	0.720400
0.900000	6	350	S3	0.542081	0.280916	0.520030	0.526641	0.554078	0.585638
0.900000	6	350	S4	0.500470	0.521264	0.515398	0.450717	0.443025	0.695420
0.900000	6	360	S2	0.523055	0.480333	0.520528	0.516138	0.557150	0.557389
0.900000	6	360	S3	0.562071	0.443781	0.545186	0.568622	0.550681	0.467790
0.900000	6	360	S4	0.585845	0.568590	0.580705	0.613921	0.736115	0.565004
0.900000	6	370	S2	0.512010	0.452361	0.490248	0.473135	0.559232	0.394853
0.900000	6	370	S3	0.449939	0.580192	0.490708	0.495308	0.380104	0.550304
0.900000	6	370	S4	0.481056	0.384105	0.469385	0.494879	0.402670	0.612295
0.900000	6	380	S2	0.525326	0.447643	0.484369	0.514340	0.475219	0.515174
0.900000	6	380	S3	0.485660	0.542327	0.499929	0.538892	0.519702	0.476992
0.900000	6	380	S4	0.547837	0.625238	0.564815	0.621353	0.527976	0.498091
0.900000	6	390	S2	0.515443	0.637007	0.530033	0.566660	0.441053	0.417359
0.900000	6	390	S3	0.523883	0.484453	0.535832	0.491055	0.549835	0.630946
0.900000	6	390	S4	0.440053	0.485349	0.445085	0.465553	0.509840	0.470354
0.900000	6	400	S2	0.579323	0.525729	0.578893	0.574914	0.524503	0.692010
0.900000	6	400	S3	0.499747	0.517217	0.477595	0.515204	0.549210	0.430096
0.900000	6	400	S4	0.587053	0.383719	0.571877	0.621303	0.680082	0.620974
0.900000	6	410	S2	0.527159	0.492529	0.537753	0.584535	0.459810	0.538029
0.900000	6	410	S3	0.502069	0.488641	0.542030	0.547214	0.448290	0.725617
0.900000	6	410	S4	0.487538	0.401811	0.471498	0.421693	0.547750	0.608560
0.900000	6	420	S2	0.551367	0.565290	0.563601	0.564605	0.644139	0.635274
0.900000	6	420	S3	0.501261	0.385164	0.482625	0.392678	0.472501	0.494357

Continued on next page

Table 9.3 – Continued from previous page

Thickness (mm)	Damage size (mm)	Freq. (kHz)	Sensor	DI (Actual)	PR	SVM	ANN	BR	SGD
0.900000	6	420	S4	0.438502	0.392362	0.463824	0.435950	0.366539	0.484642
0.900000	6	430	S2	0.450169	0.415154	0.457713	0.457567	0.508495	0.509772
0.900000	6	430	S3	0.432097	0.350543	0.413294	0.556988	0.411795	0.533357
0.900000	6	430	S4	0.623022	0.605599	0.613969	0.564763	0.579732	0.395898
0.900000	6	440	S2	0.517332	0.589563	0.522375	0.482566	0.558496	0.422671
0.900000	6	440	S3	0.497840	0.605926	0.469739	0.421327	0.542227	0.493694
0.900000	6	440	S4	0.489596	0.556851	0.504151	0.429849	0.561005	0.379153
0.900000	6	450	S2	0.514269	0.417515	0.538285	0.531724	0.639293	0.590006
0.900000	6	450	S3	0.550636	0.653718	0.590734	0.592473	0.594279	0.746095
0.900000	6	450	S4	0.519015	0.298222	0.513497	0.545228	0.495791	0.592027
0.900000	6	460	S2	0.397718	0.484234	0.404730	0.354323	0.265444	0.373052
0.900000	6	460	S3	0.511230	0.528837	0.493262	0.427231	0.528334	0.563470
0.900000	6	460	S4	0.481935	0.655194	0.482972	0.526422	0.532943	0.416538
0.900000	6	470	S2	0.517629	0.574223	0.529771	0.527572	0.484689	0.478476
0.900000	6	470	S3	0.475601	0.531748	0.476439	0.479760	0.499686	0.539609
0.900000	6	470	S4	0.444183	0.172488	0.438208	0.464531	0.457013	0.526817
0.900000	6	480	S2	0.429535	0.322468	0.434346	0.394808	0.526911	0.478801
0.900000	6	480	S3	0.532394	0.425385	0.524859	0.508791	0.604615	0.483142
0.900000	6	480	S4	0.472648	0.275372	0.477920	0.398709	0.525573	0.561570
0.900000	6	490	S2	0.503610	0.608704	0.505686	0.518642	0.512716	0.501778
0.900000	6	490	S3	0.427094	0.353480	0.401250	0.439482	0.322952	0.448902
0.900000	6	490	S4	0.506988	0.561806	0.497002	0.463757	0.426435	0.612042
0.900000	6	500	S2	0.645165	0.584560	0.659035	0.651593	0.623985	0.613638
0.900000	6	500	S3	0.466456	0.478662	0.444598	0.436496	0.466806	0.556153
0.900000	6	500	S4	0.443371	0.386523	0.450219	0.453096	0.353737	0.330959
0.900000	7	300	S2	0.563572	0.491628	0.573663	0.588736	0.426535	0.400031
0.900000	7	300	S3	0.598836	0.599882	0.593455	0.656140	0.635937	0.589504
0.900000	7	300	S4	0.591407	0.758689	0.585745	0.580833	0.606374	0.634065
0.900000	7	310	S2	0.581048	0.683387	0.556752	0.504638	0.511331	0.619736
0.900000	7	310	S3	0.611666	0.771229	0.603066	0.602525	0.549099	0.477234
0.900000	7	310	S4	0.713480	0.650059	0.690329	0.609777	0.718818	0.793714
0.900000	7	320	S2	0.636419	0.706777	0.625310	0.633995	0.418795	0.759372
0.900000	7	320	S3	0.592361	0.561745	0.600496	0.591441	0.599816	0.506283
0.900000	7	320	S4	0.630419	0.548762	0.632506	0.674005	0.612732	0.536397
0.900000	7	330	S2	0.607486	0.695587	0.596389	0.562554	0.597927	0.646508
0.900000	7	330	S3	0.575267	0.718584	0.551508	0.572490	0.596567	0.580314
0.900000	7	330	S4	0.577956	0.486572	0.606367	0.594430	0.654764	0.477267
0.900000	7	340	S2	0.625114	0.609913	0.613967	0.671242	0.549474	0.618070

Continued on next page

Table 9.3 – Continued from previous page

Thickness (mm)	Damage size (mm)	Freq. (kHz)	Sensor	DI (Actual)	PR	SVM	ANN	BR	SGD
0.900000	7	340	S3	0.589363	0.661685	0.600369	0.588989	0.636894	0.524655
0.900000	7	340	S4	0.580934	0.517943	0.616712	0.543107	0.690367	0.489777
0.900000	7	350	S2	0.626140	0.658152	0.627404	0.599245	0.636500	0.717136
0.900000	7	350	S3	0.657089	0.625609	0.688044	0.673970	0.584160	0.678924
0.900000	7	350	S4	0.623661	0.621747	0.619870	0.647415	0.773162	0.492733
0.900000	7	360	S2	0.612919	0.590240	0.602963	0.604445	0.632174	0.592288
0.900000	7	360	S3	0.632553	0.694597	0.619101	0.654731	0.694319	0.621151
0.900000	7	360	S4	0.593803	0.631797	0.605697	0.588198	0.540812	0.710310
0.900000	7	370	S2	0.581525	0.627940	0.608487	0.557311	0.506026	0.446663
0.900000	7	370	S3	0.527910	0.599895	0.516101	0.521843	0.519305	0.415251
0.900000	7	370	S4	0.608054	0.539756	0.609859	0.617799	0.611062	0.665249
0.900000	7	380	S2	0.597776	0.547326	0.597849	0.622906	0.639872	0.583234
0.900000	7	380	S3	0.601342	0.581799	0.611638	0.584967	0.641282	0.582506
0.900000	7	380	S4	0.588721	0.577149	0.609511	0.636810	0.708645	0.498304
0.900000	7	390	S2	0.529439	0.688324	0.538101	0.474025	0.478472	0.514249
0.900000	7	390	S3	0.616160	0.623413	0.626237	0.677035	0.569368	0.673961
0.900000	7	390	S4	0.583456	0.564499	0.589416	0.470891	0.516581	0.676880
0.900000	7	400	S2	0.648834	0.650322	0.615866	0.667330	0.577317	0.742277
0.900000	7	400	S3	0.587952	0.556200	0.579739	0.528426	0.635752	0.460274
0.900000	7	400	S4	0.712996	0.767090	0.693166	0.683121	0.651246	0.791513
0.900000	7	410	S2	0.618308	0.754301	0.611343	0.638468	0.623866	0.499999
0.900000	7	410	S3	0.649494	0.538194	0.655632	0.659364	0.657409	0.620296
0.900000	7	410	S4	0.535888	0.404592	0.528150	0.458389	0.639751	0.591752
0.900000	7	420	S2	0.702508	0.640033	0.709243	0.778892	0.652593	0.738976
0.900000	7	420	S3	0.629238	0.690432	0.594923	0.688169	0.573665	0.546564
0.900000	7	420	S4	0.539760	0.515904	0.574069	0.524493	0.565033	0.511945
0.900000	7	430	S2	0.676101	0.747892	0.697826	0.582773	0.711247	0.824021
0.900000	7	430	S3	0.636308	0.677703	0.665797	0.597215	0.524575	0.529843
0.900000	7	430	S4	0.511272	0.689403	0.493242	0.605235	0.608968	0.518867
0.900000	7	440	S2	0.607708	0.622997	0.618350	0.622057	0.703029	0.535196
0.900000	7	440	S3	0.586669	0.505958	0.565192	0.589647	0.626438	0.457533
0.900000	7	440	S4	0.693015	0.626459	0.686797	0.696971	0.613687	0.936076
0.900000	7	450	S2	0.603062	0.467439	0.604380	0.611154	0.643105	0.676752
0.900000	7	450	S3	0.587565	0.735618	0.563602	0.612990	0.704549	0.659429
0.900000	7	450	S4	0.652510	0.592390	0.647211	0.672780	0.632528	0.473131
0.900000	7	460	S2	0.653438	0.746096	0.665778	0.551455	0.554374	0.622957
0.900000	7	460	S3	0.586150	0.549240	0.560185	0.576872	0.679473	0.593186
0.900000	7	460	S4	0.555349	0.466686	0.548828	0.548400	0.503838	0.288255

Continued on next page

Table 9.3 – Continued from previous page

Thickness (mm)	Damage size (mm)	Freq. (kHz)	Sensor	DI (Actual)	PR	SVM	ANN	BR	SGD
0.900000	7	470	S2	0.596836	0.593034	0.609653	0.557901	0.649728	0.439772
0.900000	7	470	S3	0.605254	0.493034	0.574079	0.542458	0.676318	0.519873
0.900000	7	470	S4	0.517665	0.484503	0.511587	0.443549	0.551446	0.480743
0.900000	7	480	S2	0.604052	0.400177	0.635253	0.596743	0.551513	0.498382
0.900000	7	480	S3	0.710779	0.833665	0.694269	0.670882	0.773727	0.731110
0.900000	7	480	S4	0.539716	0.621583	0.554894	0.616441	0.496997	0.545044
0.900000	7	490	S2	0.615591	0.790333	0.593855	0.632733	0.753970	0.543616
0.900000	7	490	S3	0.629920	0.766625	0.590215	0.573132	0.567869	0.735306
0.900000	7	490	S4	0.605697	0.576123	0.580009	0.689070	0.636711	0.615497
0.900000	7	500	S2	0.576425	0.553273	0.570112	0.486059	0.665920	0.765450
0.900000	7	500	S3	0.714270	0.685534	0.707139	0.698597	0.737156	0.739709
0.900000	7	500	S4	0.623848	0.481203	0.620288	0.557100	0.571151	0.556274
0.900000	12x4	300	S2	0.297667	0.378271	0.316486	0.253161	0.326352	0.126888
0.900000	12x4	300	S3	0.247506	0.326024	0.225077	0.233072	0.236870	0.186755
0.900000	12x4	300	S4	0.375792	0.446906	0.403164	0.329245	0.427492	0.216209
0.900000	12x4	310	S2	0.286292	0.248058	0.305075	0.284598	0.241923	0.312419
0.900000	12x4	310	S3	0.353030	0.412691	0.330261	0.290833	0.376562	0.276193
0.900000	12x4	310	S4	0.200081	0.339294	0.231920	0.246697	0.255119	0.240122
0.900000	12x4	320	S2	0.317909	0.295692	0.330597	0.236994	0.257115	0.313075
0.900000	12x4	320	S3	0.187874	0.319922	0.198629	0.158508	0.243751	0.316263
0.900000	12x4	320	S4	0.314471	0.291973	0.297279	0.233822	0.417768	0.402119
0.900000	12x4	330	S2	0.266192	0.225453	0.250493	0.276930	0.342412	0.306354
0.900000	12x4	330	S3	0.293662	0.367169	0.313344	0.256379	0.266353	0.227788
0.900000	12x4	330	S4	0.322335	0.318179	0.309794	0.295481	0.281159	0.159231
0.900000	12x4	340	S2	0.320945	0.285982	0.319174	0.340113	0.252213	0.333305
0.900000	12x4	340	S3	0.352048	0.407444	0.347806	0.349694	0.352672	0.500695
0.900000	12x4	340	S4	0.261167	0.259161	0.256510	0.214657	0.393525	0.449809
0.900000	12x4	350	S2	0.315537	0.329184	0.343271	0.277954	0.374896	0.282782
0.900000	12x4	350	S3	0.313877	0.280196	0.309687	0.277538	0.377826	0.129071
0.900000	12x4	350	S4	0.247123	0.267526	0.263377	0.154998	0.366283	0.050438
0.900000	12x4	360	S2	0.244265	0.268056	0.225012	0.153314	0.190018	0.453953
0.900000	12x4	360	S3	0.252061	0.045355	0.245938	0.199240	0.203822	0.152169
0.900000	12x4	360	S4	0.294853	0.165465	0.324674	0.220443	0.233514	0.392400
0.900000	12x4	370	S2	0.307819	0.314503	0.332111	0.262910	0.278268	0.444478
0.900000	12x4	370	S3	0.263313	0.345755	0.276768	0.168894	0.315660	0.250564
0.900000	12x4	370	S4	0.263288	0.358819	0.244638	0.225677	0.164361	0.107499
0.900000	12x4	380	S2	0.312564	0.353266	0.297679	0.215385	0.322819	0.310726
0.900000	12x4	380	S3	0.253564	0.071345	0.224360	0.212264	0.264378	0.189063

Continued on next page

Table 9.3 – Continued from previous page

Thickness (mm)	Damage size (mm)	Freq. (kHz)	Sensor	DI (Actual)	PR	SVM	ANN	BR	SGD
0.900000	12x4	380	S4	0.253483	0.310191	0.228573	0.197244	0.178390	0.334552
0.900000	12x4	390	S2	0.310826	0.227365	0.341120	0.390267	0.360733	0.541279
0.900000	12x4	390	S3	0.262450	0.371127	0.273382	0.212547	0.309540	0.113282
0.900000	12x4	390	S4	0.229507	0.189961	0.240945	0.202026	0.246788	0.262608
0.900000	12x4	400	S2	0.289143	0.264470	0.312918	0.129949	0.362676	0.174442
0.900000	12x4	400	S3	0.384019	0.319129	0.355912	0.409374	0.260462	0.667338
0.900000	12x4	400	S4	0.263415	0.103873	0.255244	0.281262	0.162785	0.366306
0.900000	12x4	410	S2	0.292620	0.287739	0.275805	0.302069	0.235400	0.386636
0.900000	12x4	410	S3	0.271659	0.327145	0.279364	0.243253	0.325624	0.022559
0.900000	12x4	410	S4	0.252651	0.304745	0.265003	0.306811	0.171194	0.193903
0.900000	12x4	420	S2	0.343953	0.436150	0.320147	0.288421	0.297468	0.133267
0.900000	12x4	420	S3	0.320529	0.377836	0.290619	0.332042	0.362375	0.229038
0.900000	12x4	420	S4	0.276241	0.244666	0.271878	0.204620	0.337174	0.380494
0.900000	12x4	430	S2	0.254228	0.239293	0.239729	0.229787	0.170836	0.165664
0.900000	12x4	430	S3	0.241278	0.364807	0.271625	0.232112	0.375768	0.071435
0.900000	12x4	430	S4	0.341855	0.214201	0.344805	0.374065	0.447910	0.506209
0.900000	12x4	440	S2	0.276515	0.040944	0.283957	0.200354	0.230813	0.299986
0.900000	12x4	440	S3	0.291541	0.231925	0.330998	0.228938	0.259308	0.436232
0.900000	12x4	440	S4	0.360582	0.281628	0.363528	0.373887	0.295532	0.330022
0.900000	12x4	450	S2	0.292793	0.292644	0.297671	0.238503	0.301439	0.299959
0.900000	12x4	450	S3	0.448060	0.498286	0.419413	0.434657	0.420877	0.492958
0.900000	12x4	450	S4	0.254669	0.285258	0.272061	0.190245	0.410096	0.180283
0.900000	12x4	460	S2	0.327676	0.533569	0.320513	0.394702	0.325913	0.172447
0.900000	12x4	460	S3	0.240067	0.318150	0.232566	0.198513	0.281695	0.337921
0.900000	12x4	460	S4	0.292194	0.247492	0.274672	0.247003	0.388558	0.147234
0.900000	12x4	470	S2	0.254355	0.363299	0.255184	0.154039	0.332975	0.271613
0.900000	12x4	470	S3	0.353012	0.380979	0.390070	0.314100	0.315109	0.349020
0.900000	12x4	470	S4	0.248423	0.338148	0.273640	0.279322	0.290937	0.354441
0.900000	12x4	480	S2	0.304550	0.274757	0.306637	0.354312	0.283510	0.299256
0.900000	12x4	480	S3	0.381634	0.361812	0.383702	0.333867	0.473152	0.539298
0.900000	12x4	480	S4	0.388343	0.481867	0.382139	0.378764	0.448576	0.337961
0.900000	12x4	490	S2	0.342933	0.195318	0.303534	0.375422	0.358193	0.550566
0.900000	12x4	490	S3	0.358702	0.457433	0.367549	0.398942	0.510335	0.364681
0.900000	12x4	490	S4	0.327358	0.405902	0.306780	0.271410	0.427486	0.239779
0.900000	12x4	500	S2	0.245973	0.361134	0.261415	0.282339	0.244738	0.336577
0.900000	12x4	500	S3	0.351727	0.365875	0.366608	0.438799	0.196742	0.006221
0.900000	12x4	500	S4	0.224501	0.189418	0.219036	0.226133	0.306841	0.082743
0.900000	15x5	300	S2	0.375416	0.528843	0.358757	0.351382	0.277334	0.289328

Continued on next page

Table 9.3 – Continued from previous page

Thickness (mm)	Damage size (mm)	Freq. (kHz)	Sensor	DI (Actual)	PR	SVM	ANN	BR	SGD
0.900000	15x5	300	S3	0.408411	0.556683	0.387723	0.477881	0.516272	0.288650
0.900000	15x5	300	S4	0.512218	0.472243	0.530852	0.580652	0.521717	0.439563
0.900000	15x5	310	S2	0.450486	0.607859	0.453719	0.485818	0.420601	0.439359
0.900000	15x5	310	S3	0.339944	0.361081	0.344186	0.337655	0.402809	0.327723
0.900000	15x5	310	S4	0.333517	0.261954	0.306142	0.298065	0.340768	0.359645
0.900000	15x5	320	S2	0.446016	0.438257	0.423884	0.428305	0.342030	0.460191
0.900000	15x5	320	S3	0.446758	0.496452	0.462217	0.476673	0.358041	0.493938
0.900000	15x5	320	S4	0.390968	0.308355	0.381860	0.392557	0.360835	0.397374
0.900000	15x5	330	S2	0.413687	0.486425	0.446303	0.446826	0.416011	0.525450
0.900000	15x5	330	S3	0.395862	0.324537	0.403283	0.333048	0.442543	0.544946
0.900000	15x5	330	S4	0.478606	0.385100	0.467038	0.411821	0.508287	0.477534
0.900000	15x5	340	S2	0.360671	0.361286	0.351090	0.292131	0.346244	0.409696
0.900000	15x5	340	S3	0.390419	0.494277	0.362651	0.390275	0.304086	0.482954
0.900000	15x5	340	S4	0.406176	0.521003	0.404847	0.344443	0.352794	0.370323
0.900000	15x5	350	S2	0.394429	0.428615	0.423032	0.371760	0.370757	0.612171
0.900000	15x5	350	S3	0.376255	0.501914	0.338556	0.380269	0.373457	0.317533
0.900000	15x5	350	S4	0.417648	0.482018	0.402293	0.384430	0.414099	0.539074
0.900000	15x5	360	S2	0.413401	0.491332	0.430504	0.336438	0.577771	0.322420
0.900000	15x5	360	S3	0.411404	0.513967	0.401816	0.392856	0.388710	0.486403
0.900000	15x5	360	S4	0.463108	0.435407	0.462648	0.512281	0.444621	0.490591
0.900000	15x5	370	S2	0.409162	0.596385	0.417261	0.383739	0.417368	0.301629
0.900000	15x5	370	S3	0.325945	0.217940	0.325749	0.373287	0.288626	0.555209
0.900000	15x5	370	S4	0.388122	0.457655	0.399143	0.402068	0.395605	0.434089
0.900000	15x5	380	S2	0.404777	0.297668	0.403639	0.490928	0.333478	0.555650
0.900000	15x5	380	S3	0.328933	0.465412	0.352768	0.308008	0.360469	0.212180
0.900000	15x5	380	S4	0.337924	0.372630	0.336508	0.315100	0.317946	0.246404
0.900000	15x5	390	S2	0.323487	0.526128	0.301023	0.368805	0.209465	0.267007
0.900000	15x5	390	S3	0.417160	0.628136	0.396026	0.420559	0.368364	0.254465
0.900000	15x5	390	S4	0.459968	0.574571	0.449950	0.490889	0.399561	0.405938
0.900000	15x5	400	S2	0.343207	0.323694	0.365085	0.264078	0.210532	0.234911
0.900000	15x5	400	S3	0.431922	0.547365	0.419043	0.435995	0.456818	0.411452
0.900000	15x5	400	S4	0.380448	0.511277	0.382366	0.396208	0.399345	0.365745
0.900000	15x5	410	S2	0.397492	0.410760	0.376105	0.424096	0.327864	0.548112
0.900000	15x5	410	S3	0.367009	0.458573	0.389953	0.304777	0.405643	0.399003
0.900000	15x5	410	S4	0.479350	0.442874	0.471133	0.432502	0.492371	0.465196
0.900000	15x5	420	S2	0.412836	0.546505	0.418358	0.437240	0.396146	0.455101
0.900000	15x5	420	S3	0.343984	0.355897	0.344868	0.430348	0.271775	0.348237
0.900000	15x5	420	S4	0.402641	0.336068	0.405167	0.445623	0.537072	0.489664

Continued on next page

Table 9.3 – Continued from previous page

Thickness (mm)	Damage size (mm)	Freq. (kHz)	Sensor	DI (Actual)	PR	SVM	ANN	BR	SGD
0.900000	15x5	430	S2	0.457736	0.417728	0.412170	0.404802	0.409418	0.488584
0.900000	15x5	430	S3	0.445933	0.451252	0.418003	0.445192	0.460567	0.396650
0.900000	15x5	430	S4	0.394155	0.404940	0.409905	0.468819	0.313176	0.324147
0.900000	15x5	440	S2	0.302533	0.311071	0.306888	0.302628	0.336536	0.326729
0.900000	15x5	440	S3	0.339280	0.375750	0.334277	0.317360	0.255016	0.266399
0.900000	15x5	440	S4	0.367838	0.559844	0.366659	0.345931	0.490397	0.263198
0.900000	15x5	450	S2	0.356716	0.290586	0.375421	0.382646	0.365327	0.382929
0.900000	15x5	450	S3	0.403659	0.423514	0.407609	0.409125	0.286278	0.380021
0.900000	15x5	450	S4	0.345637	0.329486	0.312190	0.388865	0.421193	0.327561
0.900000	15x5	460	S2	0.391228	0.269931	0.390630	0.324385	0.418666	0.315257
0.900000	15x5	460	S3	0.346647	0.206044	0.343321	0.441920	0.407721	0.367522
0.900000	15x5	460	S4	0.428400	0.506302	0.433817	0.410140	0.448106	0.524903
0.900000	15x5	470	S2	0.396412	0.391379	0.420582	0.425484	0.400447	0.395013
0.900000	15x5	470	S3	0.328623	0.325286	0.355147	0.250081	0.441876	0.362403
0.900000	15x5	470	S4	0.430263	0.349888	0.414234	0.484257	0.491080	0.490049
0.900000	15x5	480	S2	0.399190	0.329620	0.390696	0.395889	0.371330	0.538894
0.900000	15x5	480	S3	0.406711	0.458065	0.403047	0.322454	0.374298	0.314900
0.900000	15x5	480	S4	0.291704	0.318678	0.313842	0.286226	0.344504	0.192711
0.900000	15x5	490	S2	0.341236	0.287603	0.332894	0.363806	0.256941	0.460395
0.900000	15x5	490	S3	0.426304	0.343749	0.447115	0.364762	0.335903	0.461187
0.900000	15x5	490	S4	0.335157	0.297092	0.314884	0.385095	0.307394	0.345180
0.900000	15x5	500	S2	0.373220	0.406677	0.375234	0.308106	0.427576	0.433518
0.900000	15x5	500	S3	0.374253	0.301545	0.352689	0.390083	0.415979	0.426896
0.900000	15x5	500	S4	0.419505	0.373894	0.400063	0.453474	0.434687	0.533481
0.900000	18x6	300	S2	0.518518	0.566060	0.516668	0.549863	0.461744	0.522051
0.900000	18x6	300	S3	0.531655	0.429394	0.511972	0.567808	0.453794	0.407524
0.900000	18x6	300	S4	0.437714	0.558164	0.440824	0.397676	0.432694	0.516287
0.900000	18x6	310	S2	0.460276	0.358358	0.468954	0.469415	0.463964	0.509095
0.900000	18x6	310	S3	0.388748	0.316572	0.376528	0.392605	0.443288	0.398443
0.900000	18x6	310	S4	0.518679	0.352550	0.511689	0.468646	0.363926	0.474956
0.900000	18x6	320	S2	0.481579	0.443672	0.449190	0.564894	0.526085	0.649864
0.900000	18x6	320	S3	0.442584	0.593649	0.434644	0.434447	0.475501	0.349434
0.900000	18x6	320	S4	0.530321	0.468464	0.546993	0.561902	0.437827	0.464547
0.900000	18x6	330	S2	0.563134	0.660932	0.560124	0.577083	0.502101	0.353415
0.900000	18x6	330	S3	0.483429	0.403406	0.473872	0.529132	0.449549	0.598175
0.900000	18x6	330	S4	0.482327	0.380211	0.469956	0.348766	0.568445	0.275740
0.900000	18x6	340	S2	0.551821	0.493316	0.559824	0.490859	0.498418	0.340867
0.900000	18x6	340	S3	0.561779	0.412368	0.560838	0.522344	0.715405	0.636591

Continued on next page

Table 9.3 – Continued from previous page

Thickness (mm)	Damage size (mm)	Freq. (kHz)	Sensor	DI (Actual)	PR	SVM	ANN	BR	SGD
0.900000	18x6	340	S4	0.559825	0.714071	0.569967	0.499740	0.459804	0.531979
0.900000	18x6	350	S2	0.536078	0.511571	0.563748	0.426793	0.575620	0.394360
0.900000	18x6	350	S3	0.425230	0.423252	0.470114	0.460967	0.384765	0.575148
0.900000	18x6	350	S4	0.486962	0.556170	0.507557	0.513347	0.498637	0.521125
0.900000	18x6	360	S2	0.469230	0.295278	0.462651	0.494889	0.521914	0.434140
0.900000	18x6	360	S3	0.615135	0.669399	0.591972	0.649539	0.593860	0.649427
0.900000	18x6	360	S4	0.458556	0.423913	0.426763	0.437077	0.443232	0.266053
0.900000	18x6	370	S2	0.539264	0.524929	0.572603	0.440915	0.537115	0.474247
0.900000	18x6	370	S3	0.519427	0.405589	0.501687	0.581611	0.528728	0.471365
0.900000	18x6	370	S4	0.497856	0.474906	0.529316	0.455946	0.463162	0.439336
0.900000	18x6	380	S2	0.534651	0.529829	0.540376	0.546898	0.512808	0.750001
0.900000	18x6	380	S3	0.531156	0.579749	0.538817	0.587277	0.546947	0.585395
0.900000	18x6	380	S4	0.523023	0.568500	0.502298	0.488730	0.501668	0.503017
0.900000	18x6	390	S2	0.536106	0.706064	0.506522	0.520270	0.554128	0.619927
0.900000	18x6	390	S3	0.502198	0.436772	0.487492	0.578817	0.505828	0.450602
0.900000	18x6	390	S4	0.458190	0.502790	0.444746	0.461959	0.536686	0.433644
0.900000	18x6	400	S2	0.531520	0.544378	0.556894	0.575271	0.564697	0.291467
0.900000	18x6	400	S3	0.467815	0.369809	0.447444	0.495821	0.505875	0.353314
0.900000	18x6	400	S4	0.558351	0.622738	0.579589	0.591431	0.567872	0.552339
0.900000	18x6	410	S2	0.484790	0.337274	0.494441	0.475793	0.510440	0.636446
0.900000	18x6	410	S3	0.515798	0.631746	0.502758	0.570880	0.555269	0.537646
0.900000	18x6	410	S4	0.425772	0.461245	0.431532	0.399900	0.422467	0.219419
0.900000	18x6	420	S2	0.538450	0.610757	0.526838	0.574112	0.583445	0.388617
0.900000	18x6	420	S3	0.581442	0.599618	0.566716	0.495247	0.555086	0.678599
0.900000	18x6	420	S4	0.486221	0.576917	0.493980	0.486225	0.344885	0.426544
0.900000	18x6	430	S2	0.580629	0.595787	0.599344	0.574879	0.641895	0.633633
0.900000	18x6	430	S3	0.494845	0.425526	0.516356	0.485711	0.547103	0.648936
0.900000	18x6	430	S4	0.483329	0.292455	0.479801	0.516352	0.497434	0.530711
0.900000	18x6	440	S2	0.568029	0.694120	0.561238	0.540294	0.604167	0.631808
0.900000	18x6	440	S3	0.512113	0.430023	0.459499	0.518506	0.506880	0.402943
0.900000	18x6	440	S4	0.513452	0.491673	0.518786	0.477405	0.524305	0.622107
0.900000	18x6	450	S2	0.446406	0.461614	0.479565	0.477898	0.440231	0.566310
0.900000	18x6	450	S3	0.457595	0.170098	0.459152	0.370918	0.474075	0.322207
0.900000	18x6	450	S4	0.367712	0.451531	0.384431	0.351890	0.313952	0.367057
0.900000	18x6	460	S2	0.571793	0.613415	0.584211	0.599418	0.579624	0.449851
0.900000	18x6	460	S3	0.467418	0.479543	0.452155	0.519804	0.363003	0.504271
0.900000	18x6	460	S4	0.549563	0.531912	0.533527	0.645955	0.372302	0.592547
0.900000	18x6	470	S2	0.468205	0.483299	0.478288	0.479293	0.365184	0.660434

Continued on next page

Table 9.3 – Continued from previous page

Thickness (mm)	Damage size (mm)	Freq. (kHz)	Sensor	DI (Actual)	PR	SVM	ANN	BR	SGD
0.900000	18x6	470	S3	0.534562	0.570989	0.542479	0.490826	0.527400	0.686735
0.900000	18x6	470	S4	0.510468	0.426579	0.501497	0.525179	0.579254	0.729186
0.900000	18x6	480	S2	0.428157	0.437259	0.444159	0.339556	0.494443	0.365597
0.900000	18x6	480	S3	0.580776	0.513911	0.590359	0.558704	0.586826	0.859951
0.900000	18x6	480	S4	0.560922	0.586271	0.563194	0.501573	0.490556	0.632111
0.900000	18x6	490	S2	0.507794	0.452800	0.492562	0.549453	0.445551	0.354845
0.900000	18x6	490	S3	0.518546	0.410026	0.518958	0.562875	0.469117	0.753684
0.900000	18x6	490	S4	0.534739	0.622494	0.536382	0.511306	0.514821	0.637929
0.900000	18x6	500	S2	0.505986	0.554473	0.502389	0.542583	0.496480	0.525902
0.900000	18x6	500	S3	0.501395	0.511828	0.511158	0.520510	0.472864	0.592629
0.900000	18x6	500	S4	0.538497	0.533523	0.539877	0.556127	0.506952	0.522096
1.200000	4	300	S2	0.342804	0.375991	0.347981	0.372070	0.528920	0.461611
1.200000	4	300	S3	0.365421	0.222122	0.364791	0.367343	0.261507	0.425864
1.200000	4	300	S4	0.358447	0.315707	0.375135	0.404114	0.391652	0.358816
1.200000	4	310	S2	0.349410	0.621544	0.327303	0.354667	0.419078	0.438341
1.200000	4	310	S3	0.334663	0.191911	0.317925	0.335647	0.484359	0.526885
1.200000	4	310	S4	0.339307	0.353935	0.294989	0.247206	0.328827	0.476843
1.200000	4	320	S2	0.307418	0.262849	0.290820	0.294077	0.339296	0.445872
1.200000	4	320	S3	0.343558	0.210470	0.335363	0.408199	0.420637	0.294380
1.200000	4	320	S4	0.372827	0.308076	0.358830	0.425525	0.324215	0.432505
1.200000	4	330	S2	0.254679	0.306690	0.252039	0.286584	0.246132	0.194001
1.200000	4	330	S3	0.334072	0.505237	0.315651	0.356685	0.374469	0.257409
1.200000	4	330	S4	0.426211	0.410015	0.421247	0.446771	0.556865	0.492000
1.200000	4	340	S2	0.381666	0.387743	0.390861	0.426080	0.401068	0.462974
1.200000	4	340	S3	0.307325	0.392186	0.331990	0.325272	0.326019	0.257645
1.200000	4	340	S4	0.325980	0.352850	0.370895	0.340786	0.368029	0.379862
1.200000	4	350	S2	0.347719	0.330130	0.338716	0.334094	0.349539	0.219222
1.200000	4	350	S3	0.302520	0.119148	0.317023	0.343446	0.270160	0.276023
1.200000	4	350	S4	0.364987	0.370668	0.375408	0.313052	0.386348	0.432380
1.200000	4	360	S2	0.312031	0.381788	0.336070	0.455685	0.250070	0.322355
1.200000	4	360	S3	0.339701	0.265563	0.333097	0.227351	0.285742	0.498881
1.200000	4	360	S4	0.313737	0.379361	0.276567	0.321725	0.263435	0.237395
1.200000	4	370	S2	0.419919	0.517844	0.446096	0.351644	0.496829	0.426797
1.200000	4	370	S3	0.468401	0.509139	0.398769	0.507898	0.590043	0.372107
1.200000	4	370	S4	0.386984	0.329136	0.338240	0.421803	0.251225	0.348191
1.200000	4	380	S2	0.349725	0.242394	0.339622	0.218587	0.336696	0.306327
1.200000	4	380	S3	0.362807	0.377868	0.362018	0.456643	0.395307	0.370501
1.200000	4	380	S4	0.432382	0.532762	0.425238	0.454807	0.481532	0.355819

Continued on next page

Table 9.3 – Continued from previous page

Thickness (mm)	Damage size (mm)	Freq. (kHz)	Sensor	DI (Actual)	PR	SVM	ANN	BR	SGD
1.200000	4	390	S2	0.381909	0.204467	0.362612	0.353379	0.420388	0.482853
1.200000	4	390	S3	0.346990	0.379212	0.320006	0.321194	0.351892	0.452015
1.200000	4	390	S4	0.334039	0.237817	0.343772	0.392724	0.180009	0.235341
1.200000	4	400	S2	0.403785	0.379651	0.411761	0.342006	0.317844	0.382133
1.200000	4	400	S3	0.290172	0.341001	0.323339	0.194703	0.245884	0.348811
1.200000	4	400	S4	0.318365	0.271885	0.331707	0.299626	0.294451	0.443411
1.200000	4	410	S2	0.336402	0.284524	0.336742	0.411692	0.380961	0.446927
1.200000	4	410	S3	0.315968	0.271525	0.303210	0.322554	0.322395	0.301557
1.200000	4	410	S4	0.358930	0.326311	0.369914	0.282771	0.411498	0.215975
1.200000	4	420	S2	0.319511	0.103627	0.295186	0.354585	0.226983	0.216134
1.200000	4	420	S3	0.295732	0.203614	0.301712	0.286168	0.145259	0.466546
1.200000	4	420	S4	0.370254	0.451288	0.378790	0.373275	0.232710	0.542987
1.200000	4	430	S2	0.306217	0.358446	0.321146	0.364955	0.266485	0.217850
1.200000	4	430	S3	0.380010	0.503081	0.374101	0.375731	0.434428	0.497433
1.200000	4	430	S4	0.473732	0.385978	0.481921	0.460171	0.435488	0.615509
1.200000	4	440	S2	0.310635	0.313416	0.276854	0.368165	0.308320	0.301631
1.200000	4	440	S3	0.281898	0.256522	0.287101	0.383782	0.168836	0.219164
1.200000	4	440	S4	0.306228	0.440023	0.288807	0.363469	0.292002	0.523895
1.200000	4	450	S2	0.443288	0.559597	0.419490	0.461559	0.524399	0.320996
1.200000	4	450	S3	0.340529	0.272877	0.331867	0.349029	0.316186	0.329182
1.200000	4	450	S4	0.374445	0.445453	0.367873	0.460218	0.292718	0.252330
1.200000	4	460	S2	0.236868	0.394257	0.187712	0.227414	0.234614	0.369123
1.200000	4	460	S3	0.326073	0.307531	0.308318	0.202393	0.217267	0.519274
1.200000	4	460	S4	0.337506	0.368970	0.353270	0.230555	0.381066	0.375251
1.200000	4	470	S2	0.258848	0.188143	0.280752	0.231697	0.337125	0.351842
1.200000	4	470	S3	0.320264	0.273926	0.340883	0.403685	0.309784	0.210340
1.200000	4	470	S4	0.415485	0.451295	0.392521	0.360947	0.238526	0.265457
1.200000	4	480	S2	0.227354	0.356217	0.243079	0.265992	0.153613	0.154262
1.200000	4	480	S3	0.323210	0.226966	0.329930	0.408117	0.330010	0.324231
1.200000	4	480	S4	0.378480	0.378451	0.413336	0.377493	0.394121	0.343440
1.200000	4	490	S2	0.401481	0.248846	0.382702	0.382318	0.274670	0.482817
1.200000	4	490	S3	0.395780	0.354437	0.409842	0.399559	0.444782	0.551543
1.200000	4	490	S4	0.314966	0.287822	0.315538	0.217603	0.457345	0.299759
1.200000	4	500	S2	0.314016	0.513762	0.280829	0.357878	0.351857	0.319072
1.200000	4	500	S3	0.421856	0.447099	0.405439	0.343454	0.328702	0.220852
1.200000	4	500	S4	0.319099	0.429822	0.302361	0.277248	0.226531	0.450577
1.200000	5	300	S2	0.357378	0.260329	0.393427	0.372975	0.313157	0.134196
1.200000	5	300	S3	0.452866	0.533840	0.436883	0.585015	0.408941	0.366361

Continued on next page

Table 9.3 – Continued from previous page

Thickness (mm)	Damage size (mm)	Freq. (kHz)	Sensor	DI (Actual)	PR	SVM	ANN	BR	SGD
1.200000	5	300	S4	0.420152	0.466775	0.430939	0.423828	0.404671	0.556387
1.200000	5	310	S2	0.427122	0.468967	0.436501	0.488312	0.376379	0.246943
1.200000	5	310	S3	0.431843	0.555599	0.439123	0.394465	0.461574	0.481807
1.200000	5	310	S4	0.398204	0.417594	0.423777	0.369686	0.270870	0.350733
1.200000	5	320	S2	0.437352	0.488603	0.426170	0.374673	0.526770	0.524917
1.200000	5	320	S3	0.395455	0.192795	0.379584	0.424802	0.266519	0.446612
1.200000	5	320	S4	0.445298	0.628392	0.419441	0.395384	0.394966	0.674365
1.200000	5	330	S2	0.421764	0.394995	0.425739	0.411445	0.481399	0.428322
1.200000	5	330	S3	0.508507	0.409224	0.471979	0.452488	0.351343	0.695491
1.200000	5	330	S4	0.446024	0.431442	0.454266	0.452956	0.523146	0.534975
1.200000	5	340	S2	0.437676	0.422833	0.455720	0.483922	0.402300	0.451907
1.200000	5	340	S3	0.444250	0.438989	0.476846	0.406605	0.463289	0.444743
1.200000	5	340	S4	0.419112	0.295400	0.455106	0.415712	0.381136	0.402119
1.200000	5	350	S2	0.518828	0.495526	0.523419	0.574781	0.585464	0.571304
1.200000	5	350	S3	0.482200	0.479178	0.495086	0.486057	0.453326	0.591493
1.200000	5	350	S4	0.528111	0.578000	0.542091	0.503090	0.540704	0.401221
1.200000	5	360	S2	0.345686	0.281029	0.345272	0.265020	0.301335	0.479796
1.200000	5	360	S3	0.428496	0.398851	0.414514	0.444736	0.363882	0.479810
1.200000	5	360	S4	0.413780	0.444515	0.412614	0.444999	0.506340	0.288497
1.200000	5	370	S2	0.518010	0.637795	0.546542	0.515171	0.519513	0.660574
1.200000	5	370	S3	0.477385	0.582712	0.465860	0.508954	0.543495	0.464277
1.200000	5	370	S4	0.418997	0.372814	0.411349	0.402498	0.425077	0.313040
1.200000	5	380	S2	0.507492	0.534647	0.477559	0.497572	0.483509	0.383257
1.200000	5	380	S3	0.385654	0.416301	0.358547	0.352094	0.262932	0.458381
1.200000	5	380	S4	0.428831	0.424729	0.443485	0.455052	0.495917	0.328393
1.200000	5	390	S2	0.408526	0.313629	0.400969	0.381021	0.446676	0.435392
1.200000	5	390	S3	0.332812	0.270812	0.371820	0.261940	0.321778	0.281520
1.200000	5	390	S4	0.478979	0.442472	0.486957	0.495698	0.386453	0.420896
1.200000	5	400	S2	0.459339	0.556359	0.439405	0.421373	0.342454	0.547792
1.200000	5	400	S3	0.427715	0.311910	0.431196	0.416591	0.433505	0.554652
1.200000	5	400	S4	0.448932	0.376416	0.439721	0.518112	0.476097	0.498182
1.200000	5	410	S2	0.592953	0.634270	0.623658	0.690283	0.531077	0.745649
1.200000	5	410	S3	0.366138	0.343568	0.362852	0.402205	0.353886	0.427083
1.200000	5	410	S4	0.433795	0.187955	0.452499	0.470313	0.306747	0.440187
1.200000	5	420	S2	0.495029	0.492574	0.492059	0.544604	0.450962	0.224097
1.200000	5	420	S3	0.502699	0.443883	0.511084	0.491642	0.578515	0.534350
1.200000	5	420	S4	0.484670	0.529659	0.501483	0.397759	0.563851	0.521095
1.200000	5	430	S2	0.488619	0.489011	0.474700	0.535432	0.517388	0.479490

Continued on next page

Table 9.3 – Continued from previous page

Thickness (mm)	Damage size (mm)	Freq. (kHz)	Sensor	DI (Actual)	PR	SVM	ANN	BR	SGD
1.200000	5	430	S3	0.419948	0.456051	0.412400	0.539708	0.485800	0.502366
1.200000	5	430	S4	0.375319	0.438203	0.384836	0.311755	0.253062	0.422451
1.200000	5	440	S2	0.467214	0.359246	0.465982	0.474038	0.537634	0.493092
1.200000	5	440	S3	0.468626	0.388519	0.464460	0.492209	0.392911	0.600948
1.200000	5	440	S4	0.419384	0.341905	0.369452	0.397806	0.404695	0.495426
1.200000	5	450	S2	0.486725	0.477622	0.478356	0.493506	0.527752	0.543384
1.200000	5	450	S3	0.402791	0.335033	0.395859	0.345291	0.466794	0.384195
1.200000	5	450	S4	0.415908	0.464741	0.441172	0.431179	0.302575	0.438404
1.200000	5	460	S2	0.444757	0.417316	0.441920	0.389054	0.385351	0.394819
1.200000	5	460	S3	0.442450	0.405833	0.448511	0.463489	0.557271	0.510409
1.200000	5	460	S4	0.378973	0.318449	0.355836	0.298264	0.241029	0.398166
1.200000	5	470	S2	0.463957	0.386922	0.450219	0.387902	0.466789	0.346797
1.200000	5	470	S3	0.531824	0.577323	0.563737	0.488420	0.483357	0.647558
1.200000	5	470	S4	0.474248	0.532390	0.419404	0.448161	0.354528	0.395838
1.200000	5	480	S2	0.463143	0.607461	0.432738	0.430536	0.490260	0.316496
1.200000	5	480	S3	0.460033	0.400715	0.425599	0.451824	0.545558	0.330205
1.200000	5	480	S4	0.466746	0.519787	0.473343	0.495725	0.507624	0.427595
1.200000	5	490	S2	0.486095	0.527208	0.492495	0.454678	0.541005	0.459784
1.200000	5	490	S3	0.484217	0.403943	0.507828	0.559353	0.497457	0.452904
1.200000	5	490	S4	0.431697	0.373556	0.469938	0.427982	0.424781	0.512432
1.200000	5	500	S2	0.495003	0.539706	0.522395	0.463212	0.316662	0.603587
1.200000	5	500	S3	0.348612	0.493754	0.347444	0.392276	0.396561	0.422110
1.200000	5	500	S4	0.474289	0.485664	0.480241	0.523630	0.362455	0.505753
1.200000	6	300	S2	0.539959	0.561190	0.566265	0.572446	0.581998	0.359774
1.200000	6	300	S3	0.503514	0.509180	0.499461	0.472286	0.513685	0.466701
1.200000	6	300	S4	0.560636	0.617570	0.565255	0.533720	0.668834	0.629046
1.200000	6	310	S2	0.593079	0.521445	0.578484	0.603872	0.607427	0.459267
1.200000	6	310	S3	0.574996	0.616916	0.566378	0.535228	0.629831	0.638851
1.200000	6	310	S4	0.527885	0.458959	0.523522	0.471992	0.493213	0.375550
1.200000	6	320	S2	0.579663	0.469300	0.609945	0.671753	0.474160	0.654075
1.200000	6	320	S3	0.582384	0.414845	0.600148	0.527745	0.623032	0.378884
1.200000	6	320	S4	0.504029	0.448316	0.494763	0.500463	0.515529	0.843056
1.200000	6	330	S2	0.524151	0.546823	0.523564	0.489366	0.446117	0.564523
1.200000	6	330	S3	0.594588	0.716987	0.604628	0.672118	0.525192	0.535771
1.200000	6	330	S4	0.601174	0.627332	0.601578	0.657330	0.600536	0.590464
1.200000	6	340	S2	0.589448	0.692037	0.602207	0.595655	0.602897	0.665866
1.200000	6	340	S3	0.524946	0.495761	0.520422	0.554968	0.559684	0.513787
1.200000	6	340	S4	0.465946	0.427455	0.454964	0.409876	0.393230	0.561130

Continued on next page

Table 9.3 – Continued from previous page

Thickness (mm)	Damage size (mm)	Freq. (kHz)	Sensor	DI (Actual)	PR	SVM	ANN	BR	SGD
1.200000	6	350	S2	0.502052	0.408013	0.540700	0.471719	0.464574	0.459837
1.200000	6	350	S3	0.566047	0.580110	0.582319	0.524734	0.637427	0.711656
1.200000	6	350	S4	0.571463	0.686365	0.575070	0.628872	0.614054	0.545644
1.200000	6	360	S2	0.606747	0.664164	0.594410	0.542330	0.489672	0.553603
1.200000	6	360	S3	0.467706	0.362874	0.459567	0.536004	0.540855	0.434057
1.200000	6	360	S4	0.576169	0.532013	0.559481	0.587103	0.530818	0.578017
1.200000	6	370	S2	0.528572	0.532945	0.536403	0.424957	0.576836	0.560042
1.200000	6	370	S3	0.473860	0.471408	0.437353	0.416395	0.481664	0.348538
1.200000	6	370	S4	0.546250	0.492637	0.535627	0.535527	0.685027	0.487353
1.200000	6	380	S2	0.607070	0.569561	0.580359	0.620519	0.506612	0.556089
1.200000	6	380	S3	0.540076	0.532474	0.534157	0.483955	0.480936	0.438317
1.200000	6	380	S4	0.677518	0.465775	0.686994	0.655062	0.707753	0.540939
1.200000	6	390	S2	0.570618	0.626202	0.553741	0.730115	0.575587	0.627486
1.200000	6	390	S3	0.509741	0.597612	0.526931	0.519917	0.505232	0.563415
1.200000	6	390	S4	0.617657	0.643861	0.616628	0.685315	0.692280	0.756296
1.200000	6	400	S2	0.542796	0.446125	0.537894	0.616514	0.490877	0.491933
1.200000	6	400	S3	0.529011	0.582310	0.505681	0.525248	0.536875	0.547367
1.200000	6	400	S4	0.550631	0.624010	0.535991	0.594071	0.561110	0.604005
1.200000	6	410	S2	0.558053	0.461860	0.581860	0.505393	0.612373	0.702291
1.200000	6	410	S3	0.607984	0.650949	0.607894	0.636715	0.684586	0.627690
1.200000	6	410	S4	0.605799	0.552898	0.567646	0.525535	0.547448	0.499716
1.200000	6	420	S2	0.513096	0.547969	0.507149	0.446990	0.601178	0.388762
1.200000	6	420	S3	0.569253	0.506826	0.588585	0.550522	0.655352	0.470158
1.200000	6	420	S4	0.578552	0.346465	0.597605	0.575273	0.630022	0.434287
1.200000	6	430	S2	0.509943	0.412239	0.533324	0.497060	0.421572	0.415502
1.200000	6	430	S3	0.571914	0.485735	0.530888	0.573202	0.531280	0.498485
1.200000	6	430	S4	0.564653	0.563551	0.549570	0.502010	0.507415	0.410046
1.200000	6	440	S2	0.613831	0.745993	0.617917	0.636552	0.611636	0.539613
1.200000	6	440	S3	0.601909	0.625337	0.605174	0.635732	0.396111	0.514592
1.200000	6	440	S4	0.559723	0.607014	0.570596	0.609726	0.544770	0.466475
1.200000	6	450	S2	0.505325	0.416037	0.517097	0.457446	0.470539	0.380852
1.200000	6	450	S3	0.613052	0.641042	0.560024	0.585515	0.525127	0.780466
1.200000	6	450	S4	0.617770	0.686925	0.639441	0.596817	0.673164	0.599819
1.200000	6	460	S2	0.648661	0.736863	0.669591	0.637827	0.665645	0.414061
1.200000	6	460	S3	0.596116	0.606093	0.618768	0.617806	0.569111	0.541547
1.200000	6	460	S4	0.485959	0.315536	0.442540	0.479469	0.545393	0.535519
1.200000	6	470	S2	0.528702	0.430379	0.561684	0.513189	0.596472	0.636043
1.200000	6	470	S3	0.410661	0.385712	0.395089	0.393995	0.288937	0.599304

Continued on next page

Table 9.3 – Continued from previous page

Thickness (mm)	Damage size (mm)	Freq. (kHz)	Sensor	DI (Actual)	PR	SVM	ANN	BR	SGD
1.200000	6	470	S4	0.560515	0.598682	0.576890	0.534355	0.624169	0.523063
1.200000	6	480	S2	0.586368	0.628658	0.599727	0.631716	0.566181	0.612941
1.200000	6	480	S3	0.541950	0.597963	0.531681	0.492028	0.556652	0.557164
1.200000	6	480	S4	0.662397	0.663976	0.645462	0.641243	0.521792	0.848216
1.200000	6	490	S2	0.458659	0.629793	0.471469	0.577317	0.398973	0.414003
1.200000	6	490	S3	0.589856	0.584083	0.600149	0.500959	0.573654	0.452682
1.200000	6	490	S4	0.608494	0.527747	0.608617	0.601232	0.573036	0.527654
1.200000	6	500	S2	0.507255	0.455627	0.507430	0.447375	0.581713	0.575166
1.200000	6	500	S3	0.580463	0.657856	0.574325	0.627221	0.609971	0.721238
1.200000	6	500	S4	0.516329	0.409551	0.489901	0.530888	0.529429	0.745325
1.200000	7	300	S2	0.553310	0.540666	0.551070	0.543273	0.480664	0.731307
1.200000	7	300	S3	0.537560	0.589598	0.531562	0.508101	0.603029	0.633537
1.200000	7	300	S4	0.646524	0.578364	0.620329	0.641157	0.702156	0.618948
1.200000	7	310	S2	0.579401	0.469522	0.609079	0.530827	0.599454	0.508254
1.200000	7	310	S3	0.584068	0.331158	0.607041	0.636174	0.634492	0.630476
1.200000	7	310	S4	0.726999	0.871058	0.751544	0.631193	0.741038	0.686752
1.200000	7	320	S2	0.653671	0.533728	0.650701	0.603673	0.772709	0.755776
1.200000	7	320	S3	0.605907	0.571493	0.594777	0.578685	0.527127	0.720000
1.200000	7	320	S4	0.648543	0.753341	0.655274	0.672632	0.614965	0.549478
1.200000	7	330	S2	0.633353	0.579363	0.662507	0.671979	0.555240	0.581407
1.200000	7	330	S3	0.665221	0.529488	0.661483	0.752138	0.456133	0.708563
1.200000	7	330	S4	0.715827	0.568119	0.732141	0.743081	0.729223	0.496001
1.200000	7	340	S2	0.673199	0.769331	0.656170	0.715363	0.780246	0.701629
1.200000	7	340	S3	0.744497	0.663286	0.738134	0.684594	0.627725	0.871204
1.200000	7	340	S4	0.680589	0.471088	0.664121	0.735997	0.689326	0.420800
1.200000	7	350	S2	0.721840	0.743868	0.678634	0.716597	0.562788	0.820777
1.200000	7	350	S3	0.673093	0.805349	0.680520	0.672674	0.656110	0.735645
1.200000	7	350	S4	0.691574	0.644197	0.680865	0.688403	0.579531	0.847272
1.200000	7	360	S2	0.670747	0.610671	0.649497	0.716729	0.718726	0.479295
1.200000	7	360	S3	0.589172	0.604444	0.603712	0.539375	0.666575	0.535310
1.200000	7	360	S4	0.705071	0.696349	0.710617	0.662668	0.706503	0.517238
1.200000	7	370	S2	0.592530	0.714528	0.586399	0.540424	0.695354	0.552017
1.200000	7	370	S3	0.631771	0.696971	0.631424	0.653815	0.815429	0.522590
1.200000	7	370	S4	0.661940	0.689789	0.679528	0.767318	0.635091	0.434512
1.200000	7	380	S2	0.630980	0.585382	0.663670	0.627102	0.752057	0.480544
1.200000	7	380	S3	0.632001	0.480243	0.618914	0.662439	0.649298	0.614538
1.200000	7	380	S4	0.599363	0.605099	0.606993	0.599934	0.643701	0.473174
1.200000	7	390	S2	0.692159	0.579492	0.711217	0.710965	0.699694	0.592387

Continued on next page

Table 9.3 – Continued from previous page

Thickness (mm)	Damage size (mm)	Freq. (kHz)	Sensor	DI (Actual)	PR	SVM	ANN	BR	SGD
1.200000	7	390	S3	0.582573	0.683371	0.599323	0.566002	0.637644	0.575359
1.200000	7	390	S4	0.650532	0.747283	0.615462	0.774899	0.613142	0.561989
1.200000	7	400	S2	0.674687	0.566486	0.669247	0.611304	0.804749	0.768978
1.200000	7	400	S3	0.690891	0.709421	0.696782	0.641982	0.523621	0.663030
1.200000	7	400	S4	0.582976	0.676042	0.544614	0.671711	0.685763	0.660936
1.200000	7	410	S2	0.627253	0.576489	0.667209	0.615096	0.693519	0.498520
1.200000	7	410	S3	0.600300	0.485430	0.612650	0.576271	0.727931	0.537971
1.200000	7	410	S4	0.687820	0.739447	0.670229	0.629174	0.629914	0.531723
1.200000	7	420	S2	0.733097	0.769048	0.721845	0.729989	0.856064	0.595551
1.200000	7	420	S3	0.661067	0.673451	0.668461	0.555476	0.589562	0.523639
1.200000	7	420	S4	0.615374	0.730260	0.613241	0.664227	0.637507	0.569282
1.200000	7	430	S2	0.627477	0.749050	0.662686	0.648354	0.675921	0.569237
1.200000	7	430	S3	0.625163	0.618844	0.648093	0.533940	0.629901	0.792413
1.200000	7	430	S4	0.724959	0.738960	0.744335	0.717516	0.583007	0.711321
1.200000	7	440	S2	0.711253	0.759898	0.687907	0.778085	0.711721	0.882296
1.200000	7	440	S3	0.636171	0.756787	0.635685	0.711780	0.737840	0.692450
1.200000	7	440	S4	0.692874	0.764098	0.671735	0.621926	0.732917	0.621051
1.200000	7	450	S2	0.609074	0.779523	0.590752	0.571435	0.612159	0.436346
1.200000	7	450	S3	0.642161	0.770736	0.634860	0.704435	0.677146	0.813824
1.200000	7	450	S4	0.626863	0.656455	0.623000	0.584016	0.612220	0.604222
1.200000	7	460	S2	0.588707	0.576200	0.573182	0.548493	0.506349	0.632373
1.200000	7	460	S3	0.524246	0.581955	0.508841	0.548523	0.576912	0.506951
1.200000	7	460	S4	0.527549	0.446229	0.535909	0.483384	0.441023	0.441526
1.200000	7	470	S2	0.613612	0.580703	0.638506	0.638508	0.769564	0.401377
1.200000	7	470	S3	0.654207	0.659659	0.666258	0.622936	0.684586	0.536352
1.200000	7	470	S4	0.513017	0.433125	0.506169	0.489656	0.490689	0.749080
1.200000	7	480	S2	0.615050	0.712521	0.629228	0.644717	0.658890	0.600048
1.200000	7	480	S3	0.619365	0.474798	0.600323	0.597731	0.560931	0.634317
1.200000	7	480	S4	0.719374	0.855117	0.722883	0.689989	0.696624	0.728814
1.200000	7	490	S2	0.651494	0.620316	0.667551	0.654912	0.557391	0.713477
1.200000	7	490	S3	0.635599	0.736199	0.601945	0.636762	0.667452	0.492853
1.200000	7	490	S4	0.722700	0.804735	0.748146	0.721289	0.794576	0.594199
1.200000	7	500	S2	0.629707	0.560194	0.647133	0.594338	0.614575	0.740925
1.200000	7	500	S3	0.596976	0.575906	0.608905	0.502710	0.474591	0.701256
1.200000	7	500	S4	0.612281	0.602727	0.636640	0.605756	0.692695	0.691852
1.200000	12x4	300	S2	0.301683	0.460165	0.306856	0.261489	0.278047	0.275550
1.200000	12x4	300	S3	0.392230	0.289445	0.367897	0.415939	0.385572	0.212175
1.200000	12x4	300	S4	0.295876	0.391184	0.278215	0.220288	0.300701	0.352151

Continued on next page

Table 9.3 – Continued from previous page

Thickness (mm)	Damage size (mm)	Freq. (kHz)	Sensor	DI (Actual)	PR	SVM	ANN	BR	SGD
1.200000	12x4	310	S2	0.403857	0.412597	0.378722	0.403635	0.570578	0.351697
1.200000	12x4	310	S3	0.375171	0.320480	0.380567	0.428682	0.359983	0.328762
1.200000	12x4	310	S4	0.425993	0.329632	0.420080	0.377909	0.528143	0.462046
1.200000	12x4	320	S2	0.281940	0.508995	0.276621	0.288764	0.164699	0.255673
1.200000	12x4	320	S3	0.312197	0.212420	0.315279	0.320625	0.241496	0.235770
1.200000	12x4	320	S4	0.289921	0.145847	0.291120	0.363052	0.407252	0.362458
1.200000	12x4	330	S2	0.338618	0.338689	0.301002	0.323333	0.255337	0.512415
1.200000	12x4	330	S3	0.372362	0.355772	0.364460	0.423833	0.416028	0.324350
1.200000	12x4	330	S4	0.395076	0.121061	0.371197	0.438192	0.465962	0.636960
1.200000	12x4	340	S2	0.370481	0.258119	0.407455	0.328906	0.236278	0.453128
1.200000	12x4	340	S3	0.200055	0.297956	0.149602	0.290684	0.183509	0.184478
1.200000	12x4	340	S4	0.356033	0.396091	0.372954	0.270089	0.351379	0.327978
1.200000	12x4	350	S2	0.359499	0.369385	0.366305	0.416361	0.454298	0.298247
1.200000	12x4	350	S3	0.366926	0.332309	0.396680	0.334654	0.370071	0.309643
1.200000	12x4	350	S4	0.326222	0.338074	0.290215	0.258182	0.318034	0.322067
1.200000	12x4	360	S2	0.320265	0.391064	0.322331	0.282638	0.393945	0.044135
1.200000	12x4	360	S3	0.337199	0.387233	0.315396	0.346246	0.176409	0.247337
1.200000	12x4	360	S4	0.352211	0.486143	0.370558	0.289291	0.329261	0.530703
1.200000	12x4	370	S2	0.445119	0.496765	0.432274	0.481570	0.305823	0.571773
1.200000	12x4	370	S3	0.379781	0.341350	0.372204	0.355677	0.193704	0.555102
1.200000	12x4	370	S4	0.403137	0.431552	0.393652	0.394639	0.323784	0.505064
1.200000	12x4	380	S2	0.382948	0.395536	0.390360	0.447534	0.379980	0.354413
1.200000	12x4	380	S3	0.346303	0.244046	0.351619	0.427920	0.347009	0.526578
1.200000	12x4	380	S4	0.258424	0.207170	0.264509	0.190819	0.313096	0.504432
1.200000	12x4	390	S2	0.456617	0.608422	0.458869	0.392454	0.561389	0.323913
1.200000	12x4	390	S3	0.264642	0.292816	0.270787	0.316885	0.228170	0.313564
1.200000	12x4	390	S4	0.355407	0.292717	0.328993	0.292456	0.332296	0.291707
1.200000	12x4	400	S2	0.283665	0.281415	0.284404	0.253968	0.411379	0.287524
1.200000	12x4	400	S3	0.227426	0.217867	0.225007	0.199559	0.124169	0.462236
1.200000	12x4	400	S4	0.332893	0.407823	0.347511	0.322008	0.238543	0.409308
1.200000	12x4	410	S2	0.313834	0.320047	0.326185	0.256397	0.091914	0.201956
1.200000	12x4	410	S3	0.292617	0.173247	0.313169	0.231555	0.320766	0.321291
1.200000	12x4	410	S4	0.429817	0.400726	0.410147	0.407066	0.358809	0.355319
1.200000	12x4	420	S2	0.328719	0.265491	0.271929	0.245105	0.331988	0.370666
1.200000	12x4	420	S3	0.348543	0.294670	0.395534	0.399761	0.407095	0.377109
1.200000	12x4	420	S4	0.453104	0.395351	0.454396	0.429248	0.428854	0.294260
1.200000	12x4	430	S2	0.341955	0.362509	0.330272	0.409378	0.302468	0.342831
1.200000	12x4	430	S3	0.295778	0.304458	0.315863	0.223192	0.185389	0.267104

Continued on next page

Table 9.3 – Continued from previous page

Thickness (mm)	Damage size (mm)	Freq. (kHz)	Sensor	DI (Actual)	PR	SVM	ANN	BR	SGD
1.200000	12x4	430	S4	0.307368	0.363376	0.311345	0.266543	0.387456	0.318804
1.200000	12x4	440	S2	0.321941	0.405957	0.299732	0.318899	0.244127	0.120464
1.200000	12x4	440	S3	0.431097	0.537037	0.433914	0.369819	0.404467	0.472822
1.200000	12x4	440	S4	0.350386	0.245737	0.325754	0.327634	0.357977	0.253720
1.200000	12x4	450	S2	0.463958	0.414195	0.479404	0.546766	0.495132	0.413561
1.200000	12x4	450	S3	0.388254	0.351304	0.364931	0.316485	0.403878	0.409115
1.200000	12x4	450	S4	0.406546	0.271213	0.412677	0.448819	0.455712	0.254643
1.200000	12x4	460	S2	0.338665	0.260210	0.308475	0.391959	0.373950	0.202799
1.200000	12x4	460	S3	0.381965	0.395664	0.412284	0.436710	0.449887	0.510175
1.200000	12x4	460	S4	0.337287	0.266231	0.323008	0.232262	0.324456	0.216753
1.200000	12x4	470	S2	0.257913	0.340246	0.234278	0.277588	0.210571	0.218654
1.200000	12x4	470	S3	0.314082	0.476211	0.313687	0.381621	0.306831	0.396055
1.200000	12x4	470	S4	0.332206	0.533071	0.309690	0.255115	0.391222	0.079935
1.200000	12x4	480	S2	0.325007	0.225139	0.324966	0.373689	0.373976	0.079317
1.200000	12x4	480	S3	0.397063	0.585353	0.399971	0.451292	0.462906	0.297701
1.200000	12x4	480	S4	0.328490	0.375303	0.342205	0.286582	0.323984	0.368208
1.200000	12x4	490	S2	0.343391	0.455757	0.323735	0.324273	0.279441	0.313362
1.200000	12x4	490	S3	0.345208	0.463714	0.354135	0.345311	0.474852	0.395503
1.200000	12x4	490	S4	0.350630	0.274220	0.343223	0.313986	0.363825	0.190973
1.200000	12x4	500	S2	0.448979	0.483584	0.439305	0.407413	0.377224	0.507971
1.200000	12x4	500	S3	0.388120	0.482753	0.398840	0.467274	0.324475	0.346934
1.200000	12x4	500	S4	0.346512	0.164575	0.383801	0.386934	0.463628	0.324237
1.200000	15x5	300	S2	0.460379	0.446478	0.445375	0.415411	0.564580	0.483738
1.200000	15x5	300	S3	0.427816	0.406207	0.435630	0.375907	0.374359	0.190319
1.200000	15x5	300	S4	0.498127	0.480202	0.460116	0.506694	0.400824	0.509515
1.200000	15x5	310	S2	0.448460	0.435630	0.467831	0.506879	0.424485	0.330215
1.200000	15x5	310	S3	0.447313	0.582332	0.454697	0.363696	0.509288	0.372091
1.200000	15x5	310	S4	0.498360	0.470092	0.505313	0.479030	0.404706	0.593575
1.200000	15x5	320	S2	0.451792	0.437763	0.441064	0.425713	0.429082	0.475940
1.200000	15x5	320	S3	0.481659	0.394241	0.503623	0.422129	0.655088	0.376462
1.200000	15x5	320	S4	0.476521	0.460773	0.495524	0.373739	0.478215	0.384876
1.200000	15x5	330	S2	0.595808	0.533983	0.579004	0.547719	0.557064	0.581406
1.200000	15x5	330	S3	0.415368	0.384381	0.414605	0.408265	0.431821	0.355646
1.200000	15x5	330	S4	0.390676	0.344581	0.371672	0.435155	0.279805	0.499838
1.200000	15x5	340	S2	0.321709	0.384627	0.331242	0.340856	0.340684	0.270630
1.200000	15x5	340	S3	0.535977	0.442193	0.530749	0.576464	0.491585	0.776162
1.200000	15x5	340	S4	0.447222	0.227924	0.461224	0.494749	0.535300	0.420685
1.200000	15x5	350	S2	0.424447	0.536855	0.409768	0.482595	0.406133	0.654009

Continued on next page

Table 9.3 – Continued from previous page

Thickness (mm)	Damage size (mm)	Freq. (kHz)	Sensor	DI (Actual)	PR	SVM	ANN	BR	SGD
1.200000	15x5	350	S3	0.458854	0.525219	0.431949	0.488146	0.410297	0.517244
1.200000	15x5	350	S4	0.428390	0.377366	0.401880	0.356874	0.381432	0.330733
1.200000	15x5	360	S2	0.468642	0.392125	0.454912	0.479010	0.450001	0.496572
1.200000	15x5	360	S3	0.386473	0.447926	0.373508	0.408137	0.397498	0.538957
1.200000	15x5	360	S4	0.450506	0.491640	0.443740	0.480099	0.485657	0.362669
1.200000	15x5	370	S2	0.441165	0.378157	0.438143	0.401095	0.523833	0.372427
1.200000	15x5	370	S3	0.482065	0.510891	0.465684	0.471873	0.553415	0.428159
1.200000	15x5	370	S4	0.403443	0.316068	0.402200	0.432471	0.468467	0.433969
1.200000	15x5	380	S2	0.417827	0.510373	0.405772	0.418698	0.429901	0.377880
1.200000	15x5	380	S3	0.474545	0.469708	0.481833	0.449242	0.460208	0.634752
1.200000	15x5	380	S4	0.513877	0.452574	0.485216	0.462518	0.507096	0.559177
1.200000	15x5	390	S2	0.409696	0.313750	0.405000	0.385661	0.431482	0.533473
1.200000	15x5	390	S3	0.487470	0.494700	0.461054	0.612090	0.458667	0.390227
1.200000	15x5	390	S4	0.449447	0.478557	0.456062	0.426452	0.406512	0.503497
1.200000	15x5	400	S2	0.436415	0.443091	0.465594	0.404542	0.469565	0.583724
1.200000	15x5	400	S3	0.512439	0.427881	0.530258	0.592607	0.493266	0.463983
1.200000	15x5	400	S4	0.525893	0.531395	0.538666	0.567641	0.525193	0.379900
1.200000	15x5	410	S2	0.503991	0.536419	0.498780	0.509998	0.533124	0.552108
1.200000	15x5	410	S3	0.438137	0.470586	0.431405	0.440839	0.436395	0.180226
1.200000	15x5	410	S4	0.492055	0.358401	0.458249	0.452725	0.428940	0.524410
1.200000	15x5	420	S2	0.483719	0.528883	0.455681	0.563110	0.567957	0.485161
1.200000	15x5	420	S3	0.457728	0.456828	0.476512	0.559343	0.562542	0.553587
1.200000	15x5	420	S4	0.460802	0.511186	0.457735	0.510505	0.416527	0.406505
1.200000	15x5	430	S2	0.494808	0.472720	0.458649	0.520305	0.549787	0.651704
1.200000	15x5	430	S3	0.448550	0.380012	0.429859	0.455270	0.480056	0.264058
1.200000	15x5	430	S4	0.386539	0.349962	0.382325	0.426625	0.476334	0.432678
1.200000	15x5	440	S2	0.457518	0.389019	0.451183	0.441780	0.506490	0.591102
1.200000	15x5	440	S3	0.447527	0.392113	0.466311	0.474107	0.480204	0.510512
1.200000	15x5	440	S4	0.382556	0.445956	0.362279	0.396543	0.298909	0.520306
1.200000	15x5	450	S2	0.463006	0.448980	0.476480	0.489208	0.510362	0.418765
1.200000	15x5	450	S3	0.482387	0.336445	0.462714	0.483448	0.554133	0.311030
1.200000	15x5	450	S4	0.447910	0.488485	0.433480	0.392887	0.471833	0.543899
1.200000	15x5	460	S2	0.507729	0.536585	0.507613	0.480856	0.479949	0.596627
1.200000	15x5	460	S3	0.558415	0.607317	0.579908	0.539636	0.530519	0.579325
1.200000	15x5	460	S4	0.497041	0.609203	0.472774	0.452820	0.547499	0.593507
1.200000	15x5	470	S2	0.450717	0.390130	0.451987	0.526226	0.508360	0.489034
1.200000	15x5	470	S3	0.489288	0.375135	0.494384	0.473584	0.545078	0.571894
1.200000	15x5	470	S4	0.427724	0.371129	0.436967	0.402670	0.350712	0.470473

Continued on next page

Table 9.3 – Continued from previous page

Thickness (mm)	Damage size (mm)	Freq. (kHz)	Sensor	DI (Actual)	PR	SVM	ANN	BR	SGD
1.200000	15x5	480	S2	0.468482	0.402901	0.470397	0.468512	0.342368	0.466238
1.200000	15x5	480	S3	0.441840	0.379557	0.442502	0.417954	0.474308	0.573291
1.200000	15x5	480	S4	0.462572	0.533264	0.455149	0.502182	0.531033	0.457455
1.200000	15x5	490	S2	0.450593	0.457404	0.450045	0.378527	0.476250	0.514068
1.200000	15x5	490	S3	0.476198	0.520648	0.484011	0.453354	0.581071	0.440544
1.200000	15x5	490	S4	0.461550	0.595795	0.458819	0.528401	0.418219	0.490006
1.200000	15x5	500	S2	0.485977	0.355036	0.485391	0.497042	0.436273	0.505501
1.200000	15x5	500	S3	0.433546	0.395262	0.416659	0.439689	0.508584	0.421211
1.200000	15x5	500	S4	0.417461	0.279840	0.395157	0.331858	0.407975	0.349149
1.200000	18x6	300	S2	0.581705	0.647831	0.561120	0.454253	0.614704	0.645032
1.200000	18x6	300	S3	0.518290	0.489859	0.495762	0.510318	0.577046	0.531064
1.200000	18x6	300	S4	0.570161	0.516694	0.596170	0.572801	0.610926	0.600294
1.200000	18x6	310	S2	0.573980	0.662152	0.547439	0.583345	0.709173	0.622084
1.200000	18x6	310	S3	0.581979	0.548545	0.567321	0.524381	0.631713	0.574868
1.200000	18x6	310	S4	0.586253	0.615635	0.581665	0.539076	0.582770	0.601404
1.200000	18x6	320	S2	0.552580	0.722981	0.558479	0.439980	0.561734	0.666206
1.200000	18x6	320	S3	0.534295	0.661965	0.533781	0.498588	0.555133	0.530634
1.200000	18x6	320	S4	0.613989	0.522534	0.617325	0.598682	0.487654	0.393776
1.200000	18x6	330	S2	0.418815	0.443385	0.421694	0.448426	0.331331	0.723099
1.200000	18x6	330	S3	0.534461	0.498117	0.540641	0.515095	0.455391	0.478343
1.200000	18x6	330	S4	0.573455	0.619993	0.589715	0.513318	0.553419	0.231835
1.200000	18x6	340	S2	0.531550	0.543381	0.480733	0.612480	0.566886	0.582518
1.200000	18x6	340	S3	0.482550	0.619106	0.491145	0.520202	0.431101	0.468870
1.200000	18x6	340	S4	0.583860	0.616629	0.569400	0.598809	0.497810	0.633288
1.200000	18x6	350	S2	0.597062	0.686383	0.599898	0.649626	0.538447	0.799871
1.200000	18x6	350	S3	0.583478	0.536228	0.572243	0.631222	0.483265	0.435210
1.200000	18x6	350	S4	0.595308	0.693149	0.595548	0.536413	0.571770	0.770303
1.200000	18x6	360	S2	0.657685	0.617196	0.651405	0.641331	0.605023	0.692547
1.200000	18x6	360	S3	0.576198	0.448881	0.578664	0.424993	0.494409	0.478445
1.200000	18x6	360	S4	0.555570	0.753483	0.541369	0.518712	0.580709	0.495880
1.200000	18x6	370	S2	0.536155	0.570069	0.585674	0.549152	0.632504	0.477612
1.200000	18x6	370	S3	0.470201	0.592561	0.499883	0.568312	0.480033	0.482427
1.200000	18x6	370	S4	0.525605	0.459368	0.543762	0.498681	0.486161	0.308131
1.200000	18x6	380	S2	0.522648	0.437317	0.486060	0.509881	0.561561	0.473285
1.200000	18x6	380	S3	0.514199	0.416861	0.510484	0.491937	0.530270	0.498193
1.200000	18x6	380	S4	0.453613	0.418924	0.464038	0.415132	0.349374	0.540420
1.200000	18x6	390	S2	0.602557	0.607657	0.565000	0.582792	0.629046	0.845683
1.200000	18x6	390	S3	0.541728	0.667486	0.543095	0.535082	0.565549	0.570490

Continued on next page

Table 9.3 – Continued from previous page

Thickness (mm)	Damage size (mm)	Freq. (kHz)	Sensor	DI (Actual)	PR	SVM	ANN	BR	SGD
1.200000	18x6	390	S4	0.544714	0.460120	0.540141	0.490921	0.577229	0.662008
1.200000	18x6	400	S2	0.472629	0.579628	0.475603	0.480224	0.514176	0.456592
1.200000	18x6	400	S3	0.589145	0.572233	0.621407	0.590792	0.696039	0.403202
1.200000	18x6	400	S4	0.624937	0.787869	0.638024	0.635383	0.559403	0.503079
1.200000	18x6	410	S2	0.545486	0.575978	0.534019	0.635608	0.526650	0.530777
1.200000	18x6	410	S3	0.545189	0.554781	0.524369	0.481195	0.567659	0.505952
1.200000	18x6	410	S4	0.503508	0.365325	0.493318	0.571367	0.434418	0.543058
1.200000	18x6	420	S2	0.619751	0.773927	0.624261	0.690694	0.696502	0.748387
1.200000	18x6	420	S3	0.519518	0.454581	0.497053	0.570776	0.545425	0.496737
1.200000	18x6	420	S4	0.552989	0.529682	0.553613	0.653612	0.573154	0.356955
1.200000	18x6	430	S2	0.511510	0.530756	0.480286	0.445628	0.537837	0.642976
1.200000	18x6	430	S3	0.595266	0.632149	0.610659	0.624645	0.557407	0.429013
1.200000	18x6	430	S4	0.513779	0.407209	0.515730	0.456088	0.454383	0.487736
1.200000	18x6	440	S2	0.585526	0.565733	0.610856	0.600804	0.544723	0.351559
1.200000	18x6	440	S3	0.572020	0.420211	0.557040	0.652509	0.499867	0.594083
1.200000	18x6	440	S4	0.447113	0.467979	0.419713	0.489358	0.520614	0.255925
1.200000	18x6	450	S2	0.530744	0.449132	0.550008	0.534538	0.457934	0.548217
1.200000	18x6	450	S3	0.629898	0.592482	0.618518	0.650558	0.579694	0.624208
1.200000	18x6	450	S4	0.464252	0.451615	0.482769	0.467682	0.406417	0.514747
1.200000	18x6	460	S2	0.504178	0.601383	0.526351	0.570600	0.563208	0.524248
1.200000	18x6	460	S3	0.596393	0.610361	0.591181	0.627404	0.565166	0.421827
1.200000	18x6	460	S4	0.623669	0.571201	0.635449	0.648263	0.585848	0.747137
1.200000	18x6	470	S2	0.503371	0.456835	0.505036	0.480687	0.659550	0.628793
1.200000	18x6	470	S3	0.554566	0.474768	0.562684	0.547038	0.438669	0.502436
1.200000	18x6	470	S4	0.629027	0.637552	0.629714	0.643203	0.599948	0.508043
1.200000	18x6	480	S2	0.601478	0.676005	0.624760	0.571946	0.508782	0.698560
1.200000	18x6	480	S3	0.503460	0.511039	0.507272	0.397106	0.457444	0.455616
1.200000	18x6	480	S4	0.456422	0.471404	0.468955	0.406204	0.445500	0.365307
1.200000	18x6	490	S2	0.492569	0.491551	0.490737	0.475914	0.580561	0.486645
1.200000	18x6	490	S3	0.582108	0.706768	0.561912	0.622578	0.530538	0.604912
1.200000	18x6	490	S4	0.491309	0.467367	0.491664	0.497640	0.607936	0.567387
1.200000	18x6	500	S2	0.373454	0.321599	0.358441	0.374727	0.432298	0.324881
1.200000	18x6	500	S3	0.555408	0.670445	0.558239	0.629214	0.550123	0.719290
1.200000	18x6	500	S4	0.637481	0.592074	0.647053	0.543888	0.576696	0.767241
1.500000	4	300	S2	0.458474	0.418075	0.440286	0.465731	0.539797	0.512997
1.500000	4	300	S3	0.468446	0.542745	0.452677	0.376392	0.515451	0.578010
1.500000	4	300	S4	0.416897	0.408383	0.404446	0.430378	0.392350	0.328723
1.500000	4	310	S2	0.456334	0.394465	0.460602	0.414660	0.536966	0.608379

Continued on next page

Table 9.3 – Continued from previous page

Thickness (mm)	Damage size (mm)	Freq. (kHz)	Sensor	DI (Actual)	PR	SVM	ANN	BR	SGD
1.500000	4	310	S3	0.281964	0.281296	0.288743	0.161350	0.457554	0.230698
1.500000	4	310	S4	0.393967	0.573170	0.405839	0.387265	0.489223	0.203047
1.500000	4	320	S2	0.501365	0.580702	0.505556	0.500573	0.550324	0.454938
1.500000	4	320	S3	0.459287	0.469200	0.505731	0.460258	0.514501	0.367614
1.500000	4	320	S4	0.390888	0.297073	0.392492	0.446654	0.336824	0.219986
1.500000	4	330	S2	0.443634	0.370370	0.421974	0.374418	0.379414	0.378435
1.500000	4	330	S3	0.505999	0.340798	0.485582	0.570185	0.583243	0.598965
1.500000	4	330	S4	0.375856	0.350987	0.366751	0.353759	0.430061	0.481709
1.500000	4	340	S2	0.364895	0.275081	0.390344	0.406102	0.310172	0.381696
1.500000	4	340	S3	0.352260	0.423239	0.330536	0.411982	0.379119	0.361641
1.500000	4	340	S4	0.389592	0.350040	0.372624	0.390191	0.374093	0.453461
1.500000	4	350	S2	0.450361	0.374311	0.422928	0.429396	0.365827	0.547013
1.500000	4	350	S3	0.335855	0.180113	0.345810	0.321997	0.335359	0.296424
1.500000	4	350	S4	0.343232	0.378405	0.348909	0.362395	0.314613	0.471687
1.500000	4	360	S2	0.375050	0.460862	0.401938	0.308130	0.384765	0.412007
1.500000	4	360	S3	0.443405	0.420641	0.452082	0.391162	0.405572	0.262372
1.500000	4	360	S4	0.384713	0.430156	0.352103	0.388390	0.433154	0.309060
1.500000	4	370	S2	0.375903	0.227381	0.360374	0.347771	0.392598	0.150977
1.500000	4	370	S3	0.413280	0.478144	0.368971	0.368686	0.463235	0.464005
1.500000	4	370	S4	0.370849	0.365387	0.363870	0.384504	0.419255	0.321492
1.500000	4	380	S2	0.431638	0.324010	0.449754	0.456152	0.451584	0.595528
1.500000	4	380	S3	0.340408	0.343179	0.327192	0.419718	0.414480	0.280527
1.500000	4	380	S4	0.393031	0.342870	0.397407	0.419382	0.340291	0.306361
1.500000	4	390	S2	0.440654	0.421106	0.452397	0.402226	0.409705	0.354335
1.500000	4	390	S3	0.426845	0.413372	0.409829	0.516297	0.532608	0.374818
1.500000	4	390	S4	0.437067	0.386063	0.402061	0.430305	0.477954	0.352302
1.500000	4	400	S2	0.445092	0.519682	0.451429	0.468399	0.381173	0.400234
1.500000	4	400	S3	0.310406	0.414581	0.318327	0.312276	0.302809	0.369125
1.500000	4	400	S4	0.371896	0.401406	0.390040	0.352204	0.334207	0.459770
1.500000	4	410	S2	0.332378	0.531669	0.328273	0.304099	0.328730	0.235126
1.500000	4	410	S3	0.401977	0.362543	0.382565	0.389524	0.471349	0.388470
1.500000	4	410	S4	0.400801	0.398246	0.367528	0.412445	0.415589	0.518455
1.500000	4	420	S2	0.410492	0.428486	0.447086	0.530771	0.457376	0.245821
1.500000	4	420	S3	0.422416	0.606111	0.438963	0.395110	0.459395	0.632651
1.500000	4	420	S4	0.377016	0.433889	0.348976	0.353224	0.356219	0.360023
1.500000	4	430	S2	0.369328	0.368559	0.372395	0.368738	0.292663	0.405589
1.500000	4	430	S3	0.512087	0.361091	0.521219	0.517294	0.438816	0.604557
1.500000	4	430	S4	0.337658	0.335098	0.328594	0.297185	0.202276	0.334663

Continued on next page

Table 9.3 – Continued from previous page

Thickness (mm)	Damage size (mm)	Freq. (kHz)	Sensor	DI (Actual)	PR	SVM	ANN	BR	SGD
1.500000	4	440	S2	0.329177	0.225693	0.316235	0.256352	0.347308	0.215935
1.500000	4	440	S3	0.334711	0.234152	0.339454	0.242335	0.434059	0.524017
1.500000	4	440	S4	0.460944	0.541308	0.436898	0.435223	0.461048	0.515854
1.500000	4	450	S2	0.416648	0.400946	0.429898	0.411045	0.501748	0.411949
1.500000	4	450	S3	0.363716	0.456595	0.375363	0.327587	0.484846	0.399154
1.500000	4	450	S4	0.398870	0.578393	0.396485	0.478592	0.441535	0.510147
1.500000	4	460	S2	0.479027	0.564919	0.437672	0.496510	0.331521	0.384114
1.500000	4	460	S3	0.507615	0.507011	0.483320	0.540364	0.642577	0.380386
1.500000	4	460	S4	0.380467	0.416540	0.362978	0.327423	0.373628	0.304419
1.500000	4	470	S2	0.288119	0.273217	0.288299	0.157866	0.364092	0.258462
1.500000	4	470	S3	0.433701	0.490387	0.421981	0.428446	0.459532	0.415917
1.500000	4	470	S4	0.462162	0.341289	0.470867	0.530544	0.583514	0.388263
1.500000	4	480	S2	0.340486	0.346915	0.345160	0.355857	0.254516	0.530624
1.500000	4	480	S3	0.363933	0.453761	0.371836	0.414941	0.309035	0.157661
1.500000	4	480	S4	0.416828	0.489645	0.428682	0.391982	0.346447	0.472925
1.500000	4	490	S2	0.386483	0.366998	0.407092	0.420255	0.383406	0.320082
1.500000	4	490	S3	0.381536	0.293478	0.405099	0.238113	0.389096	0.448039
1.500000	4	490	S4	0.368939	0.553815	0.344712	0.317063	0.418590	0.316102
1.500000	4	500	S2	0.357168	0.462095	0.362785	0.314611	0.341762	0.235166
1.500000	4	500	S3	0.433158	0.373758	0.426397	0.464907	0.383034	0.435674
1.500000	4	500	S4	0.393338	0.382823	0.394038	0.303704	0.265279	0.377004
1.500000	5	300	S2	0.502498	0.382888	0.493484	0.451377	0.420907	0.400002
1.500000	5	300	S3	0.502468	0.550197	0.522833	0.512164	0.563837	0.533648
1.500000	5	300	S4	0.429643	0.387020	0.412584	0.500775	0.359412	0.635764
1.500000	5	310	S2	0.434388	0.394030	0.415005	0.525463	0.446967	0.550444
1.500000	5	310	S3	0.455005	0.461839	0.447239	0.493769	0.358681	0.436319
1.500000	5	310	S4	0.526366	0.533890	0.507635	0.531681	0.509134	0.359194
1.500000	5	320	S2	0.497679	0.583781	0.487663	0.493008	0.578118	0.476713
1.500000	5	320	S3	0.466625	0.441111	0.449762	0.472166	0.457066	0.276041
1.500000	5	320	S4	0.480653	0.319540	0.490776	0.388607	0.336046	0.471492
1.500000	5	330	S2	0.530692	0.382586	0.567470	0.524165	0.516319	0.402292
1.500000	5	330	S3	0.530863	0.563654	0.504148	0.649359	0.455268	0.558306
1.500000	5	330	S4	0.431254	0.429548	0.429656	0.456640	0.442271	0.321247
1.500000	5	340	S2	0.501787	0.406509	0.512994	0.604830	0.567837	0.505048
1.500000	5	340	S3	0.402209	0.360510	0.391296	0.300454	0.334475	0.304759
1.500000	5	340	S4	0.444637	0.321976	0.428748	0.393421	0.554113	0.383693
1.500000	5	350	S2	0.552964	0.599926	0.564129	0.485370	0.565701	0.573228
1.500000	5	350	S3	0.456182	0.464455	0.438189	0.505763	0.402565	0.482833

Continued on next page

Table 9.3 – Continued from previous page

Thickness (mm)	Damage size (mm)	Freq. (kHz)	Sensor	DI (Actual)	PR	SVM	ANN	BR	SGD
1.500000	5	350	S4	0.523543	0.610119	0.502873	0.533698	0.474988	0.536347
1.500000	5	360	S2	0.532716	0.470337	0.521691	0.479534	0.614095	0.559711
1.500000	5	360	S3	0.474923	0.515503	0.482345	0.441502	0.364357	0.455478
1.500000	5	360	S4	0.557814	0.550585	0.586270	0.583877	0.601700	0.640662
1.500000	5	370	S2	0.444294	0.408348	0.428894	0.400288	0.563349	0.441168
1.500000	5	370	S3	0.462664	0.385211	0.496621	0.486752	0.517629	0.255646
1.500000	5	370	S4	0.527462	0.612297	0.541234	0.568025	0.484669	0.618680
1.500000	5	380	S2	0.542933	0.422527	0.530787	0.479190	0.585390	0.507798
1.500000	5	380	S3	0.475030	0.633733	0.500915	0.420034	0.488494	0.726358
1.500000	5	380	S4	0.384789	0.458031	0.359775	0.454295	0.324175	0.274317
1.500000	5	390	S2	0.459194	0.574943	0.500103	0.541940	0.533675	0.622360
1.500000	5	390	S3	0.552431	0.612233	0.568351	0.483804	0.537558	0.446319
1.500000	5	390	S4	0.464042	0.495012	0.473406	0.443829	0.586236	0.599826
1.500000	5	400	S2	0.504384	0.547410	0.461234	0.484737	0.452911	0.589254
1.500000	5	400	S3	0.616494	0.372299	0.585967	0.687655	0.525370	0.581602
1.500000	5	400	S4	0.538395	0.466190	0.500751	0.567816	0.541501	0.588252
1.500000	5	410	S2	0.461348	0.322974	0.441671	0.441823	0.395053	0.414655
1.500000	5	410	S3	0.441262	0.360129	0.423051	0.426527	0.340017	0.310185
1.500000	5	410	S4	0.485771	0.441229	0.444316	0.521831	0.434478	0.509852
1.500000	5	420	S2	0.452817	0.392991	0.447568	0.531110	0.494158	0.543142
1.500000	5	420	S3	0.479810	0.456740	0.470590	0.434812	0.470712	0.478871
1.500000	5	420	S4	0.497927	0.472808	0.495509	0.541827	0.526366	0.408457
1.500000	5	430	S2	0.552852	0.540244	0.558630	0.572422	0.589198	0.485011
1.500000	5	430	S3	0.464432	0.502597	0.457978	0.430101	0.440535	0.477907
1.500000	5	430	S4	0.414722	0.408761	0.419519	0.353507	0.453592	0.546453
1.500000	5	440	S2	0.508006	0.541941	0.526178	0.540171	0.412873	0.619125
1.500000	5	440	S3	0.530214	0.335247	0.533148	0.535151	0.478482	0.617308
1.500000	5	440	S4	0.519340	0.434242	0.540490	0.503069	0.563262	0.520289
1.500000	5	450	S2	0.495433	0.493538	0.527257	0.517744	0.510227	0.628776
1.500000	5	450	S3	0.408275	0.306019	0.405921	0.347507	0.372248	0.434613
1.500000	5	450	S4	0.581293	0.500422	0.590058	0.599996	0.565801	0.443419
1.500000	5	460	S2	0.447261	0.281274	0.410234	0.413916	0.399684	0.446040
1.500000	5	460	S3	0.558131	0.641803	0.598019	0.509236	0.612599	0.775387
1.500000	5	460	S4	0.591654	0.626825	0.594389	0.623956	0.482051	0.699062
1.500000	5	470	S2	0.435893	0.545940	0.445720	0.308080	0.444679	0.385002
1.500000	5	470	S3	0.460231	0.335637	0.445833	0.438723	0.499118	0.414760
1.500000	5	470	S4	0.367140	0.525370	0.348075	0.270417	0.334419	0.273721
1.500000	5	480	S2	0.389671	0.262353	0.419444	0.418684	0.442665	0.414558

Continued on next page

Table 9.3 – Continued from previous page

Thickness (mm)	Damage size (mm)	Freq. (kHz)	Sensor	DI (Actual)	PR	SVM	ANN	BR	SGD
1.500000	5	480	S3	0.459523	0.472981	0.445696	0.496434	0.541185	0.444530
1.500000	5	480	S4	0.566582	0.563690	0.592399	0.547110	0.622274	0.630953
1.500000	5	490	S2	0.502543	0.597210	0.511347	0.574819	0.439483	0.595091
1.500000	5	490	S3	0.501947	0.365751	0.483020	0.452753	0.499099	0.538906
1.500000	5	490	S4	0.473510	0.411152	0.500276	0.460881	0.416941	0.632058
1.500000	5	500	S2	0.556195	0.578724	0.565165	0.519748	0.501634	0.461631
1.500000	5	500	S3	0.554953	0.535357	0.582691	0.630834	0.575760	0.496251
1.500000	5	500	S4	0.536071	0.650912	0.534713	0.495217	0.414539	0.483050
1.500000	6	300	S2	0.578027	0.722889	0.592157	0.611864	0.611599	0.474700
1.500000	6	300	S3	0.657382	0.532300	0.650642	0.633688	0.673495	0.707117
1.500000	6	300	S4	0.543009	0.578863	0.555537	0.530242	0.524868	0.601149
1.500000	6	310	S2	0.645174	0.679439	0.645284	0.649072	0.562052	0.467976
1.500000	6	310	S3	0.612243	0.616846	0.623785	0.628389	0.589973	0.593829
1.500000	6	310	S4	0.625411	0.780291	0.596999	0.563895	0.638238	0.719525
1.500000	6	320	S2	0.661064	0.659786	0.664800	0.672822	0.578527	0.784275
1.500000	6	320	S3	0.670126	0.751263	0.648061	0.535119	0.698881	0.666043
1.500000	6	320	S4	0.664108	0.665779	0.689917	0.666704	0.659211	0.426184
1.500000	6	330	S2	0.644175	0.823112	0.644870	0.597004	0.503234	0.610563
1.500000	6	330	S3	0.649006	0.762909	0.678459	0.644480	0.756857	0.723326
1.500000	6	330	S4	0.598915	0.667753	0.583049	0.604523	0.478360	0.634795
1.500000	6	340	S2	0.705201	0.674370	0.685580	0.681987	0.684248	0.621573
1.500000	6	340	S3	0.629876	0.746327	0.624362	0.716947	0.657107	0.745190
1.500000	6	340	S4	0.659203	0.562258	0.616679	0.629967	0.687502	0.472107
1.500000	6	350	S2	0.679644	0.646936	0.701156	0.760867	0.690625	0.679108
1.500000	6	350	S3	0.614580	0.689196	0.614143	0.567374	0.619679	0.616617
1.500000	6	350	S4	0.635885	0.460122	0.642768	0.651663	0.707133	0.529329
1.500000	6	360	S2	0.572512	0.611568	0.564313	0.597602	0.664671	0.644196
1.500000	6	360	S3	0.604769	0.615981	0.605288	0.624173	0.641814	0.646662
1.500000	6	360	S4	0.639247	0.682333	0.667164	0.647705	0.599309	0.481174
1.500000	6	370	S2	0.577646	0.526255	0.609440	0.610589	0.524750	0.506669
1.500000	6	370	S3	0.590374	0.556047	0.577972	0.615795	0.641485	0.755149
1.500000	6	370	S4	0.660353	0.510308	0.642725	0.667949	0.610818	0.798874
1.500000	6	380	S2	0.626750	0.687956	0.645606	0.637377	0.604579	0.611641
1.500000	6	380	S3	0.601949	0.432956	0.627595	0.580540	0.591008	0.533608
1.500000	6	380	S4	0.591355	0.627685	0.589601	0.482100	0.488630	0.545575
1.500000	6	390	S2	0.582271	0.584767	0.591268	0.571538	0.523884	0.691349
1.500000	6	390	S3	0.656724	0.693285	0.669635	0.665981	0.631852	0.573119
1.500000	6	390	S4	0.709153	0.790030	0.733983	0.752986	0.624112	0.786952

Continued on next page

Table 9.3 – Continued from previous page

Thickness (mm)	Damage size (mm)	Freq. (kHz)	Sensor	DI (Actual)	PR	SVM	ANN	BR	SGD
1.500000	6	400	S2	0.568345	0.471826	0.560573	0.537774	0.699071	0.416356
1.500000	6	400	S3	0.557871	0.485447	0.593891	0.512707	0.611981	0.456357
1.500000	6	400	S4	0.574955	0.485709	0.603823	0.611861	0.562811	0.789937
1.500000	6	410	S2	0.605908	0.483716	0.587665	0.601232	0.453608	0.423897
1.500000	6	410	S3	0.598515	0.527517	0.614772	0.708433	0.669131	0.774758
1.500000	6	410	S4	0.654549	0.747091	0.646352	0.667614	0.658092	0.778675
1.500000	6	420	S2	0.651777	0.763369	0.620664	0.636549	0.653708	0.511815
1.500000	6	420	S3	0.530048	0.570055	0.537616	0.500891	0.600362	0.655878
1.500000	6	420	S4	0.589078	0.742642	0.587434	0.605316	0.604974	0.570614
1.500000	6	430	S2	0.634191	0.679417	0.623528	0.651210	0.550806	0.741097
1.500000	6	430	S3	0.605057	0.434741	0.644788	0.563555	0.618612	0.451873
1.500000	6	430	S4	0.613484	0.632683	0.589612	0.647023	0.701097	0.598115
1.500000	6	440	S2	0.627211	0.544889	0.635040	0.637915	0.622058	0.578150
1.500000	6	440	S3	0.565322	0.520807	0.591000	0.579383	0.484000	0.653988
1.500000	6	440	S4	0.546528	0.630739	0.528292	0.545703	0.592489	0.596258
1.500000	6	450	S2	0.671142	0.499631	0.657909	0.696103	0.574770	0.769324
1.500000	6	450	S3	0.533199	0.552554	0.520140	0.470041	0.543163	0.571380
1.500000	6	450	S4	0.585276	0.675680	0.609701	0.607657	0.599890	0.562002
1.500000	6	460	S2	0.637231	0.705380	0.627890	0.690479	0.572418	0.795878
1.500000	6	460	S3	0.537646	0.554736	0.551915	0.575460	0.486947	0.488793
1.500000	6	460	S4	0.622158	0.755737	0.592096	0.590625	0.668774	0.575069
1.500000	6	470	S2	0.586523	0.594784	0.618481	0.545542	0.560912	0.554395
1.500000	6	470	S3	0.630545	0.788421	0.658423	0.623989	0.618208	0.587951
1.500000	6	470	S4	0.596352	0.543529	0.586510	0.573997	0.703720	0.463101
1.500000	6	480	S2	0.614113	0.689450	0.618600	0.633246	0.552863	0.665077
1.500000	6	480	S3	0.620385	0.595732	0.593053	0.715848	0.562537	0.786667
1.500000	6	480	S4	0.586129	0.487305	0.540805	0.628493	0.559201	0.681366
1.500000	6	490	S2	0.539804	0.436403	0.496632	0.542215	0.585521	0.459571
1.500000	6	490	S3	0.703324	0.696217	0.680678	0.666389	0.825795	0.848538
1.500000	6	490	S4	0.690445	0.622726	0.698130	0.657230	0.659900	0.634462
1.500000	6	500	S2	0.660330	0.772158	0.673568	0.654720	0.731700	0.591550
1.500000	6	500	S3	0.588736	0.691805	0.557328	0.506236	0.513558	0.754350
1.500000	6	500	S4	0.618116	0.656093	0.619826	0.667828	0.681676	0.548573
1.500000	7	300	S2	0.754478	0.702475	0.714954	0.782579	0.719651	0.828308
1.500000	7	300	S3	0.678017	0.592182	0.669428	0.624486	0.751660	0.841975
1.500000	7	300	S4	0.653556	0.929049	0.647598	0.703101	0.571355	0.690391
1.500000	7	310	S2	0.665833	0.735231	0.675638	0.655728	0.679770	0.772809
1.500000	7	310	S3	0.713369	0.684804	0.734372	0.703353	0.681645	0.726472

Continued on next page

Table 9.3 – Continued from previous page

Thickness (mm)	Damage size (mm)	Freq. (kHz)	Sensor	DI (Actual)	PR	SVM	ANN	BR	SGD
1.500000	7	310	S4	0.694164	0.596966	0.719128	0.698594	0.726493	0.751525
1.500000	7	320	S2	0.728735	0.781290	0.716734	0.771407	0.819814	0.649082
1.500000	7	320	S3	0.769011	0.769527	0.774857	0.720252	0.784798	0.723155
1.500000	7	320	S4	0.656377	0.790535	0.659278	0.695006	0.691776	0.581048
1.500000	7	330	S2	0.714907	0.783069	0.695401	0.732989	0.742455	0.763592
1.500000	7	330	S3	0.726621	0.770230	0.682084	0.751242	0.809653	0.764476
1.500000	7	330	S4	0.670325	0.639501	0.698099	0.643350	0.649703	0.632833
1.500000	7	340	S2	0.623466	0.647922	0.633888	0.521725	0.684104	0.732290
1.500000	7	340	S3	0.650971	0.622163	0.656987	0.686314	0.646188	0.724256
1.500000	7	340	S4	0.717216	0.850685	0.734951	0.616966	0.569729	0.866530
1.500000	7	350	S2	0.711417	0.658937	0.712130	0.678174	0.604847	0.783863
1.500000	7	350	S3	0.722657	0.784302	0.707249	0.724555	0.627436	0.804123
1.500000	7	350	S4	0.713480	0.643225	0.730849	0.724635	0.745394	0.835855
1.500000	7	360	S2	0.671324	0.597163	0.668878	0.645314	0.682504	0.565220
1.500000	7	360	S3	0.615923	0.537121	0.593586	0.620960	0.720806	0.560814
1.500000	7	360	S4	0.711215	0.731977	0.689124	0.719533	0.610579	0.689743
1.500000	7	370	S2	0.691179	0.636409	0.706284	0.695710	0.639280	0.691258
1.500000	7	370	S3	0.679581	0.772824	0.688209	0.725697	0.659575	0.578403
1.500000	7	370	S4	0.707149	0.625683	0.686979	0.650742	0.685415	0.961447
1.500000	7	380	S2	0.748082	0.845056	0.773107	0.694732	0.779754	0.740837
1.500000	7	380	S3	0.772167	0.734124	0.769889	0.676719	0.770586	0.891595
1.500000	7	380	S4	0.636527	0.809674	0.664936	0.619610	0.691382	0.611689
1.500000	7	390	S2	0.573301	0.553822	0.551747	0.513074	0.550234	0.636668
1.500000	7	390	S3	0.685233	0.802957	0.676877	0.657696	0.713448	0.714903
1.500000	7	390	S4	0.697338	0.638004	0.692386	0.732641	0.626590	0.607531
1.500000	7	400	S2	0.717325	0.800087	0.686215	0.765339	0.710639	0.750387
1.500000	7	400	S3	0.712298	0.799560	0.712485	0.621299	0.741617	0.734742
1.500000	7	400	S4	0.715259	0.773628	0.699431	0.791447	0.639479	0.762503
1.500000	7	410	S2	0.752332	0.733746	0.757160	0.749716	0.764935	0.635609
1.500000	7	410	S3	0.734125	0.627521	0.723655	0.704008	0.693690	1.000000
1.500000	7	410	S4	0.739523	0.813659	0.705294	0.697139	0.711545	0.777909
1.500000	7	420	S2	0.676564	0.702306	0.677596	0.668985	0.512288	0.494655
1.500000	7	420	S3	0.631604	0.696591	0.635078	0.667070	0.594673	0.564387
1.500000	7	420	S4	0.680263	0.747316	0.695312	0.728629	0.687701	0.570341
1.500000	7	430	S2	0.651351	0.765069	0.653916	0.561682	0.723025	0.459626
1.500000	7	430	S3	0.765970	0.803458	0.766429	0.705031	0.806337	0.863851
1.500000	7	430	S4	0.637727	0.724017	0.642482	0.604208	0.640924	0.724903
1.500000	7	440	S2	0.657320	0.661629	0.623200	0.658858	0.588179	0.545839

Continued on next page

Table 9.3 – Continued from previous page

Thickness (mm)	Damage size (mm)	Freq. (kHz)	Sensor	DI (Actual)	PR	SVM	ANN	BR	SGD
1.500000	7	440	S3	0.800728	0.838670	0.814409	0.820464	0.784606	0.906878
1.500000	7	440	S4	0.729386	0.737873	0.688551	0.691074	0.675886	0.792599
1.500000	7	450	S2	0.622580	0.693705	0.623119	0.562187	0.617021	0.615152
1.500000	7	450	S3	0.741019	0.744579	0.747949	0.643510	0.712964	0.711422
1.500000	7	450	S4	0.749856	0.713695	0.743502	0.787459	0.796293	0.845760
1.500000	7	460	S2	0.737335	0.592622	0.708224	0.847797	0.638672	0.803966
1.500000	7	460	S3	0.740613	0.668799	0.734960	0.697989	0.682642	0.792800
1.500000	7	460	S4	0.717174	0.718994	0.739530	0.650044	0.757613	0.895004
1.500000	7	470	S2	0.642153	0.804305	0.629395	0.563480	0.543764	0.593121
1.500000	7	470	S3	0.741803	0.671547	0.754258	0.899022	0.769196	0.815772
1.500000	7	470	S4	0.621408	0.642521	0.622254	0.568647	0.675520	0.701635
1.500000	7	480	S2	0.717632	0.798487	0.725713	0.688373	0.730812	0.649649
1.500000	7	480	S3	0.681700	0.709798	0.680398	0.626066	0.695582	0.827370
1.500000	7	480	S4	0.664123	0.707935	0.671957	0.664351	0.659673	0.656695
1.500000	7	490	S2	0.671657	0.401675	0.655064	0.722094	0.580889	0.579212
1.500000	7	490	S3	0.649561	0.702762	0.661654	0.567078	0.617465	0.861753
1.500000	7	490	S4	0.654886	0.396399	0.658174	0.672487	0.702592	0.588091
1.500000	7	500	S2	0.685889	0.867088	0.661606	0.599880	0.832131	0.622104
1.500000	7	500	S3	0.711126	0.847944	0.697010	0.729209	0.667822	0.601581
1.500000	7	500	S4	0.762020	0.808597	0.775324	0.710615	0.734095	0.852770
1.500000	12x4	300	S2	0.439744	0.349363	0.447967	0.504605	0.374146	0.294712
1.500000	12x4	300	S3	0.420477	0.311187	0.429314	0.389812	0.346742	0.386152
1.500000	12x4	300	S4	0.341817	0.370220	0.347196	0.322582	0.361471	0.189910
1.500000	12x4	310	S2	0.350925	0.291583	0.366909	0.336542	0.492903	0.441268
1.500000	12x4	310	S3	0.451779	0.426727	0.441336	0.457476	0.544363	0.597512
1.500000	12x4	310	S4	0.371446	0.301563	0.334023	0.380078	0.491679	0.230813
1.500000	12x4	320	S2	0.486727	0.508163	0.514565	0.493043	0.417373	0.492760
1.500000	12x4	320	S3	0.297917	0.159687	0.300486	0.375422	0.314967	0.330987
1.500000	12x4	320	S4	0.457440	0.422267	0.437599	0.446663	0.336094	0.495531
1.500000	12x4	330	S2	0.377558	0.377975	0.416564	0.349617	0.424157	0.408409
1.500000	12x4	330	S3	0.473352	0.377491	0.478348	0.427352	0.533757	0.315909
1.500000	12x4	330	S4	0.326637	0.378527	0.317121	0.255773	0.385522	0.482146
1.500000	12x4	340	S2	0.485844	0.478043	0.489847	0.582355	0.448466	0.528439
1.500000	12x4	340	S3	0.398760	0.343772	0.385240	0.436071	0.440318	0.536987
1.500000	12x4	340	S4	0.462040	0.429329	0.447382	0.515117	0.422013	0.564963
1.500000	12x4	350	S2	0.365021	0.390003	0.359259	0.412846	0.398225	0.301730
1.500000	12x4	350	S3	0.409891	0.508478	0.362784	0.323373	0.318669	0.479873
1.500000	12x4	350	S4	0.442517	0.371759	0.450038	0.396104	0.377969	0.369491

Continued on next page

Table 9.3 – Continued from previous page

Thickness (mm)	Damage size (mm)	Freq. (kHz)	Sensor	DI (Actual)	PR	SVM	ANN	BR	SGD
1.500000	12x4	360	S2	0.434617	0.469045	0.462578	0.450109	0.449877	0.604322
1.500000	12x4	360	S3	0.446489	0.401280	0.460681	0.453819	0.394665	0.413024
1.500000	12x4	360	S4	0.341368	0.207256	0.325484	0.352557	0.376244	0.181589
1.500000	12x4	370	S2	0.385472	0.325674	0.386886	0.348834	0.429152	0.333569
1.500000	12x4	370	S3	0.427172	0.440806	0.438829	0.399414	0.451814	0.599776
1.500000	12x4	370	S4	0.459636	0.363637	0.441256	0.401687	0.467772	0.320594
1.500000	12x4	380	S2	0.438548	0.356492	0.460820	0.423818	0.526397	0.638693
1.500000	12x4	380	S3	0.385701	0.418272	0.389047	0.419150	0.362375	0.530400
1.500000	12x4	380	S4	0.419563	0.442993	0.395013	0.427782	0.358109	0.666473
1.500000	12x4	390	S2	0.480564	0.553021	0.484069	0.568561	0.394759	0.692708
1.500000	12x4	390	S3	0.485351	0.426512	0.500582	0.413885	0.509423	0.483321
1.500000	12x4	390	S4	0.445950	0.634998	0.420892	0.470717	0.432707	0.522571
1.500000	12x4	400	S2	0.399762	0.433182	0.418999	0.360934	0.422765	0.230026
1.500000	12x4	400	S3	0.402456	0.337104	0.392125	0.385958	0.396593	0.414966
1.500000	12x4	400	S4	0.328031	0.250897	0.335418	0.342322	0.247493	0.181724
1.500000	12x4	410	S2	0.454676	0.325175	0.450364	0.466872	0.437998	0.373516
1.500000	12x4	410	S3	0.371037	0.319824	0.387036	0.325044	0.187968	0.525289
1.500000	12x4	410	S4	0.481960	0.489439	0.443253	0.487479	0.481456	0.771409
1.500000	12x4	420	S2	0.324983	0.184414	0.311790	0.281769	0.331194	0.258965
1.500000	12x4	420	S3	0.268955	0.309818	0.282211	0.318714	0.161252	0.411752
1.500000	12x4	420	S4	0.393455	0.202554	0.387819	0.309012	0.427454	0.411246
1.500000	12x4	430	S2	0.409957	0.392910	0.399550	0.352238	0.347248	0.269902
1.500000	12x4	430	S3	0.402286	0.395900	0.422729	0.257041	0.385542	0.273441
1.500000	12x4	430	S4	0.370288	0.324196	0.361041	0.396914	0.360719	0.526642
1.500000	12x4	440	S2	0.422755	0.536449	0.390374	0.458268	0.445070	0.353021
1.500000	12x4	440	S3	0.370313	0.398622	0.365899	0.357835	0.367863	0.256896
1.500000	12x4	440	S4	0.430722	0.422404	0.443072	0.475470	0.389632	0.567779
1.500000	12x4	450	S2	0.387887	0.366297	0.383896	0.370560	0.412499	0.446449
1.500000	12x4	450	S3	0.440142	0.551124	0.453469	0.474249	0.364788	0.727372
1.500000	12x4	450	S4	0.381967	0.406999	0.409710	0.413329	0.365390	0.403262
1.500000	12x4	460	S2	0.425507	0.414761	0.416318	0.360812	0.343934	0.373512
1.500000	12x4	460	S3	0.338856	0.279796	0.343996	0.319329	0.297782	0.363415
1.500000	12x4	460	S4	0.433076	0.382984	0.454364	0.542970	0.447355	0.525790
1.500000	12x4	470	S2	0.369722	0.395874	0.376891	0.309000	0.415964	0.290671
1.500000	12x4	470	S3	0.401110	0.317392	0.440127	0.326514	0.441777	0.291363
1.500000	12x4	470	S4	0.385525	0.421892	0.356885	0.381179	0.347275	0.597158
1.500000	12x4	480	S2	0.345041	0.372285	0.361098	0.271736	0.300425	0.459341
1.500000	12x4	480	S3	0.409275	0.581769	0.447545	0.420004	0.410641	0.530426

Continued on next page

Table 9.3 – Continued from previous page

Thickness (mm)	Damage size (mm)	Freq. (kHz)	Sensor	DI (Actual)	PR	SVM	ANN	BR	SGD
1.500000	12x4	480	S4	0.415277	0.389703	0.454224	0.409465	0.414582	0.278223
1.500000	12x4	490	S2	0.417565	0.397039	0.404973	0.390338	0.382322	0.356842
1.500000	12x4	490	S3	0.475352	0.410639	0.469384	0.384412	0.430702	0.421030
1.500000	12x4	490	S4	0.489145	0.514823	0.534707	0.432274	0.439593	0.523996
1.500000	12x4	500	S2	0.403708	0.497266	0.430704	0.400295	0.356955	0.287183
1.500000	12x4	500	S3	0.332303	0.359460	0.326818	0.383884	0.398826	0.139592
1.500000	12x4	500	S4	0.427257	0.454428	0.444213	0.414943	0.436504	0.308223
1.500000	15x5	300	S2	0.517217	0.453296	0.511299	0.510370	0.581383	0.361345
1.500000	15x5	300	S3	0.510378	0.405466	0.503406	0.434933	0.510265	0.354123
1.500000	15x5	300	S4	0.537698	0.527658	0.536235	0.531455	0.392317	0.741602
1.500000	15x5	310	S2	0.487954	0.364243	0.481573	0.461452	0.363532	0.540731
1.500000	15x5	310	S3	0.541364	0.476824	0.501251	0.488535	0.498282	0.662615
1.500000	15x5	310	S4	0.501348	0.353188	0.494051	0.486241	0.541404	0.488313
1.500000	15x5	320	S2	0.508132	0.303461	0.506660	0.477661	0.551401	0.526170
1.500000	15x5	320	S3	0.574329	0.493239	0.537309	0.578806	0.513053	0.547597
1.500000	15x5	320	S4	0.515010	0.680389	0.499727	0.564946	0.560917	0.623838
1.500000	15x5	330	S2	0.398253	0.489036	0.410877	0.435363	0.337262	0.426432
1.500000	15x5	330	S3	0.563224	0.540699	0.519877	0.567062	0.586068	0.556980
1.500000	15x5	330	S4	0.534219	0.409037	0.525669	0.558139	0.553038	0.713052
1.500000	15x5	340	S2	0.475363	0.432515	0.479584	0.508739	0.556297	0.547090
1.500000	15x5	340	S3	0.536926	0.578493	0.533116	0.502012	0.647979	0.548470
1.500000	15x5	340	S4	0.509857	0.618310	0.532343	0.585547	0.525185	0.360543
1.500000	15x5	350	S2	0.546719	0.521857	0.594657	0.526094	0.626233	0.640307
1.500000	15x5	350	S3	0.466463	0.324384	0.471877	0.450343	0.426529	0.480828
1.500000	15x5	350	S4	0.530510	0.641710	0.530218	0.586675	0.495273	0.760493
1.500000	15x5	360	S2	0.516148	0.438690	0.481575	0.489059	0.432641	0.511159
1.500000	15x5	360	S3	0.453766	0.666382	0.465465	0.408342	0.321371	0.501705
1.500000	15x5	360	S4	0.465006	0.475875	0.476191	0.404115	0.356634	0.475749
1.500000	15x5	370	S2	0.470796	0.399720	0.492115	0.438575	0.361998	0.531712
1.500000	15x5	370	S3	0.461798	0.407967	0.496594	0.425736	0.420748	0.512311
1.500000	15x5	370	S4	0.574202	0.449184	0.577697	0.586370	0.521248	0.511378
1.500000	15x5	380	S2	0.603352	0.465815	0.634716	0.661269	0.624588	0.799492
1.500000	15x5	380	S3	0.521599	0.373961	0.522648	0.487012	0.530914	0.683759
1.500000	15x5	380	S4	0.500111	0.554704	0.462326	0.502943	0.520651	0.478779
1.500000	15x5	390	S2	0.466467	0.429984	0.433324	0.378789	0.482875	0.469152
1.500000	15x5	390	S3	0.561640	0.471974	0.573074	0.524972	0.457911	0.655756
1.500000	15x5	390	S4	0.491095	0.462817	0.467394	0.491455	0.439394	0.484720
1.500000	15x5	400	S2	0.500567	0.558643	0.478476	0.534367	0.505789	0.470890

Continued on next page

Table 9.3 – Continued from previous page

Thickness (mm)	Damage size (mm)	Freq. (kHz)	Sensor	DI (Actual)	PR	SVM	ANN	BR	SGD
1.500000	15x5	400	S3	0.525898	0.682285	0.544580	0.534715	0.538917	0.683687
1.500000	15x5	400	S4	0.543598	0.543139	0.528867	0.559777	0.465484	0.397623
1.500000	15x5	410	S2	0.518636	0.576966	0.484678	0.539018	0.372362	0.464953
1.500000	15x5	410	S3	0.393201	0.292101	0.385585	0.430299	0.424219	0.360924
1.500000	15x5	410	S4	0.505429	0.449156	0.480513	0.550011	0.527585	0.492032
1.500000	15x5	420	S2	0.466095	0.398913	0.456259	0.524819	0.446346	0.574016
1.500000	15x5	420	S3	0.524922	0.332900	0.495779	0.542916	0.604522	0.740865
1.500000	15x5	420	S4	0.465714	0.362957	0.475870	0.502880	0.574647	0.564013
1.500000	15x5	430	S2	0.444062	0.306219	0.431091	0.464018	0.498050	0.287946
1.500000	15x5	430	S3	0.591058	0.595359	0.592988	0.579118	0.592947	0.592518
1.500000	15x5	430	S4	0.489676	0.487759	0.494268	0.498417	0.526188	0.684455
1.500000	15x5	440	S2	0.572327	0.508054	0.588689	0.604452	0.548430	0.695245
1.500000	15x5	440	S3	0.572527	0.707607	0.610300	0.641113	0.571375	0.638500
1.500000	15x5	440	S4	0.592235	0.591217	0.562399	0.608705	0.509885	0.535918
1.500000	15x5	450	S2	0.483330	0.337062	0.499922	0.528566	0.493026	0.438179
1.500000	15x5	450	S3	0.578417	0.782525	0.592170	0.561172	0.667550	0.608957
1.500000	15x5	450	S4	0.474507	0.503633	0.470397	0.557310	0.589188	0.524184
1.500000	15x5	460	S2	0.498808	0.489773	0.495003	0.440248	0.517999	0.430349
1.500000	15x5	460	S3	0.567840	0.681078	0.567134	0.505119	0.515964	0.664696
1.500000	15x5	460	S4	0.481095	0.417959	0.492392	0.416112	0.451808	0.276920
1.500000	15x5	470	S2	0.520706	0.678905	0.513497	0.488873	0.374928	0.466967
1.500000	15x5	470	S3	0.449999	0.349010	0.442084	0.466824	0.403806	0.357810
1.500000	15x5	470	S4	0.593976	0.594187	0.597229	0.502160	0.563818	0.709703
1.500000	15x5	480	S2	0.471188	0.444638	0.469510	0.478916	0.478562	0.448073
1.500000	15x5	480	S3	0.440649	0.497006	0.497455	0.413905	0.416252	0.468362
1.500000	15x5	480	S4	0.385691	0.421740	0.371745	0.443254	0.313375	0.360992
1.500000	15x5	490	S2	0.511490	0.448780	0.513273	0.409675	0.459380	0.611718
1.500000	15x5	490	S3	0.533795	0.618158	0.509850	0.579008	0.535324	0.643132
1.500000	15x5	490	S4	0.407855	0.393085	0.414066	0.444922	0.393266	0.429666
1.500000	15x5	500	S2	0.460889	0.512050	0.463259	0.459675	0.526583	0.413772
1.500000	15x5	500	S3	0.485258	0.245114	0.500189	0.381940	0.426089	0.384657
1.500000	15x5	500	S4	0.570274	0.525705	0.561854	0.585201	0.529808	0.884148
1.500000	18x6	300	S2	0.540280	0.662049	0.539936	0.518930	0.543441	0.608833
1.500000	18x6	300	S3	0.558394	0.502078	0.570114	0.564075	0.451251	0.564883
1.500000	18x6	300	S4	0.583144	0.684789	0.580120	0.538238	0.480412	0.463578
1.500000	18x6	310	S2	0.594799	0.724598	0.560527	0.641626	0.730069	0.653127
1.500000	18x6	310	S3	0.589139	0.678145	0.593014	0.501915	0.642466	0.419277
1.500000	18x6	310	S4	0.676012	0.723919	0.692227	0.738489	0.565511	0.687812

Continued on next page

Table 9.3 – Continued from previous page

Thickness (mm)	Damage size (mm)	Freq. (kHz)	Sensor	DI (Actual)	PR	SVM	ANN	BR	SGD
1.500000	18x6	320	S2	0.524598	0.535265	0.538010	0.609221	0.625445	0.594271
1.500000	18x6	320	S3	0.646278	0.653077	0.632481	0.638256	0.697435	0.573576
1.500000	18x6	320	S4	0.583083	0.650619	0.610571	0.704890	0.676314	0.784825
1.500000	18x6	330	S2	0.629239	0.642857	0.620923	0.698614	0.726051	0.763449
1.500000	18x6	330	S3	0.538092	0.478646	0.524805	0.552549	0.578999	0.559827
1.500000	18x6	330	S4	0.662572	0.544439	0.640741	0.670197	0.699843	0.682819
1.500000	18x6	340	S2	0.589162	0.589294	0.556621	0.636028	0.693512	0.530285
1.500000	18x6	340	S3	0.609790	0.583401	0.622815	0.745659	0.660779	0.548355
1.500000	18x6	340	S4	0.688152	0.805212	0.682257	0.753816	0.662590	0.633630
1.500000	18x6	350	S2	0.512905	0.502045	0.514813	0.554296	0.549568	0.616228
1.500000	18x6	350	S3	0.600859	0.680057	0.634723	0.676109	0.587214	0.678481
1.500000	18x6	350	S4	0.605993	0.517741	0.647772	0.622887	0.730870	0.478056
1.500000	18x6	360	S2	0.570512	0.487681	0.563056	0.597651	0.642431	0.525619
1.500000	18x6	360	S3	0.591599	0.679137	0.606524	0.649870	0.655429	0.379154
1.500000	18x6	360	S4	0.610446	0.668890	0.562854	0.595355	0.594780	0.483208
1.500000	18x6	370	S2	0.568689	0.498379	0.594142	0.554735	0.499003	0.664473
1.500000	18x6	370	S3	0.617367	0.623691	0.626957	0.678713	0.543648	0.714797
1.500000	18x6	370	S4	0.668026	0.835013	0.672431	0.645096	0.664846	0.702923
1.500000	18x6	380	S2	0.522007	0.330637	0.501954	0.549267	0.546831	0.429577
1.500000	18x6	380	S3	0.668749	0.608222	0.688585	0.680560	0.604249	0.731072
1.500000	18x6	380	S4	0.590994	0.454611	0.618961	0.562633	0.656099	0.682076
1.500000	18x6	390	S2	0.572091	0.527295	0.562608	0.529536	0.667162	0.602244
1.500000	18x6	390	S3	0.622959	0.730385	0.629340	0.617867	0.651459	0.466842
1.500000	18x6	390	S4	0.597152	0.546286	0.622297	0.667093	0.752494	0.548315
1.500000	18x6	400	S2	0.643754	0.763965	0.632586	0.665087	0.598375	0.513375
1.500000	18x6	400	S3	0.565173	0.503705	0.567124	0.519178	0.560719	0.562578
1.500000	18x6	400	S4	0.704861	0.804711	0.703946	0.684058	0.658589	0.833018
1.500000	18x6	410	S2	0.609615	0.610156	0.575092	0.586817	0.629603	0.765624
1.500000	18x6	410	S3	0.602715	0.412395	0.596618	0.648605	0.620461	0.685297
1.500000	18x6	410	S4	0.489310	0.646831	0.509698	0.482937	0.479033	0.444497
1.500000	18x6	420	S2	0.561591	0.346032	0.574052	0.475121	0.450585	0.633333
1.500000	18x6	420	S3	0.590939	0.596684	0.558424	0.596242	0.629090	0.628105
1.500000	18x6	420	S4	0.557894	0.609619	0.551095	0.497394	0.450723	0.560238
1.500000	18x6	430	S2	0.567968	0.537153	0.541691	0.580092	0.493328	0.412560
1.500000	18x6	430	S3	0.608630	0.525554	0.577544	0.803506	0.656064	0.581241
1.500000	18x6	430	S4	0.613861	0.655699	0.600966	0.600755	0.622029	0.482484
1.500000	18x6	440	S2	0.615697	0.530705	0.590100	0.645527	0.606050	0.681140
1.500000	18x6	440	S3	0.597411	0.761144	0.587059	0.653410	0.681028	0.723971

Continued on next page

Table 9.3 – Continued from previous page

Thickness (mm)	Damage size (mm)	Freq. (kHz)	Sensor	DI (Actual)	PR	SVM	ANN	BR	SGD
1.500000	18x6	440	S4	0.577783	0.588928	0.594722	0.585284	0.587934	0.561586
1.500000	18x6	450	S2	0.566789	0.478343	0.544714	0.554596	0.417536	0.371612
1.500000	18x6	450	S3	0.621660	0.652124	0.647059	0.684875	0.643919	0.670776
1.500000	18x6	450	S4	0.552397	0.669734	0.572162	0.526202	0.557982	0.364113
1.500000	18x6	460	S2	0.599892	0.628167	0.620722	0.663711	0.595270	0.672441
1.500000	18x6	460	S3	0.584385	0.678320	0.597536	0.588075	0.531150	0.623657
1.500000	18x6	460	S4	0.659968	0.655933	0.673975	0.601053	0.568638	0.714447
1.500000	18x6	470	S2	0.588190	0.579657	0.578186	0.609769	0.664319	0.553608
1.500000	18x6	470	S3	0.641126	0.382053	0.650268	0.723062	0.862379	0.562048
1.500000	18x6	470	S4	0.514172	0.574908	0.507835	0.462631	0.451936	0.538786
1.500000	18x6	480	S2	0.582341	0.514839	0.597489	0.538728	0.445055	0.538562
1.500000	18x6	480	S3	0.595106	0.624307	0.590441	0.616243	0.497611	0.498089
1.500000	18x6	480	S4	0.634183	0.692543	0.631791	0.640766	0.579820	0.578304
1.500000	18x6	490	S2	0.565979	0.490476	0.579136	0.587302	0.621633	0.700480
1.500000	18x6	490	S3	0.608799	0.546525	0.611797	0.658681	0.499085	0.686492
1.500000	18x6	490	S4	0.706654	0.981041	0.711946	0.687545	0.720911	0.859254
1.500000	18x6	500	S2	0.515143	0.536001	0.521832	0.509751	0.452596	0.198628
1.500000	18x6	500	S3	0.581965	0.645445	0.548560	0.539890	0.636581	0.658649
1.500000	18x6	500	S4	0.630927	0.559601	0.634465	0.602015	0.682974	0.652916

Comprehensive MFNN Prediction Results

Table 9.4: MFNN prediction results

Thickness (mm)	Damage size (mm)	Freq. (kHz)	Sensor	DI (Actual)	DI (Predicted)
0.7	4	300	S2	0.175	0.172
0.7	4	300	S3	0.291	0.273
0.7	4	300	S4	0.260	0.251
0.7	4	310	S2	0.212	0.214
0.7	4	310	S3	0.385	0.383
0.7	4	310	S4	0.310	0.319
0.7	4	320	S2	0.231	0.250
0.7	4	320	S3	0.238	0.245
0.7	4	320	S4	0.261	0.271

Continued on next page

Table 9.4 – Continued from previous page

Thickness (mm)	Damage size (mm)	Freq. (kHz)	Sensor	DI (Actual)	DI (Predicted)
0.7	4	330	S2	0.271	0.258
0.7	4	330	S3	0.220	0.233
0.7	4	330	S4	0.284	0.273
0.7	4	340	S2	0.339	0.342
0.7	4	340	S3	0.273	0.261
0.7	4	340	S4	0.345	0.347
0.7	4	350	S2	0.275	0.292
0.7	4	350	S3	0.217	0.232
0.7	4	350	S4	0.298	0.303
0.7	4	360	S2	0.226	0.199
0.7	4	360	S3	0.324	0.348
0.7	4	360	S4	0.216	0.237
0.7	4	370	S2	0.143	0.122
0.7	4	370	S3	0.255	0.256
0.7	4	370	S4	0.198	0.205
0.7	4	380	S2	0.264	0.251
0.7	4	380	S3	0.244	0.204
0.7	4	380	S4	0.315	0.315
0.7	4	390	S2	0.224	0.193
0.7	4	390	S3	0.343	0.339
0.7	4	390	S4	0.281	0.271
0.7	4	400	S2	0.204	0.196
0.7	4	400	S3	0.276	0.258
0.7	4	400	S4	0.174	0.183
0.7	4	410	S2	0.266	0.257
0.7	4	410	S3	0.186	0.172
0.7	4	410	S4	0.220	0.226
0.7	4	420	S2	0.180	0.159
0.7	4	420	S3	0.283	0.299
0.7	4	420	S4	0.213	0.221
0.7	4	430	S2	0.257	0.261
0.7	4	430	S3	0.186	0.195
0.7	4	430	S4	0.133	0.139
0.7	4	440	S2	0.286	0.314
0.7	4	440	S3	0.267	0.276
0.7	4	440	S4	0.179	0.154
0.7	4	450	S2	0.317	0.311
0.7	4	450	S3	0.271	0.281

Continued on next page

Table 9.4 – Continued from previous page

Thickness (mm)	Damage size (mm)	Freq. (kHz)	Sensor	DI (Actual)	DI (Predicted)
0.7	4	450	S4	0.128	0.102
0.7	4	460	S2	0.268	0.278
0.7	4	460	S3	0.269	0.275
0.7	4	460	S4	0.222	0.229
0.7	4	470	S2	0.164	0.185
0.7	4	470	S3	0.303	0.321
0.7	4	470	S4	0.209	0.197
0.7	4	480	S2	0.296	0.334
0.7	4	480	S3	0.168	0.182
0.7	4	480	S4	0.279	0.260
0.7	4	490	S2	0.186	0.175
0.7	4	490	S3	0.190	0.168
0.7	4	490	S4	0.280	0.292
0.7	4	500	S2	0.244	0.261
0.7	4	500	S3	0.253	0.255
0.7	4	500	S4	0.314	0.323
0.7	5	300	S2	0.342	0.355
0.7	5	300	S3	0.413	0.428
0.7	5	300	S4	0.450	0.433
0.7	5	310	S2	0.312	0.308
0.7	5	310	S3	0.392	0.399
0.7	5	310	S4	0.343	0.349
0.7	5	320	S2	0.319	0.322
0.7	5	320	S3	0.378	0.375
0.7	5	320	S4	0.290	0.290
0.7	5	330	S2	0.305	0.326
0.7	5	330	S3	0.414	0.399
0.7	5	330	S4	0.302	0.297
0.7	5	340	S2	0.351	0.317
0.7	5	340	S3	0.263	0.286
0.7	5	340	S4	0.305	0.301
0.7	5	350	S2	0.341	0.353
0.7	5	350	S3	0.391	0.401
0.7	5	350	S4	0.283	0.300
0.7	5	360	S2	0.336	0.340
0.7	5	360	S3	0.366	0.357
0.7	5	360	S4	0.324	0.339
0.7	5	370	S2	0.353	0.362

Continued on next page

Table 9.4 – Continued from previous page

Thickness (mm)	Damage size (mm)	Freq. (kHz)	Sensor	DI (Actual)	DI (Predicted)
0.7	5	370	S3	0.355	0.362
0.7	5	370	S4	0.467	0.468
0.7	5	380	S2	0.398	0.383
0.7	5	380	S3	0.374	0.362
0.7	5	380	S4	0.372	0.361
0.7	5	390	S2	0.387	0.365
0.7	5	390	S3	0.337	0.331
0.7	5	390	S4	0.353	0.347
0.7	5	400	S2	0.346	0.354
0.7	5	400	S3	0.314	0.338
0.7	5	400	S4	0.346	0.379
0.7	5	410	S2	0.289	0.294
0.7	5	410	S3	0.413	0.418
0.7	5	410	S4	0.319	0.304
0.7	5	420	S2	0.413	0.403
0.7	5	420	S3	0.362	0.354
0.7	5	420	S4	0.291	0.288
0.7	5	430	S2	0.467	0.471
0.7	5	430	S3	0.377	0.362
0.7	5	430	S4	0.267	0.257
0.7	5	440	S2	0.401	0.424
0.7	5	440	S3	0.476	0.467
0.7	5	440	S4	0.365	0.355
0.7	5	450	S2	0.300	0.285
0.7	5	450	S3	0.298	0.309
0.7	5	450	S4	0.287	0.277
0.7	5	460	S2	0.314	0.348
0.7	5	460	S3	0.314	0.314
0.7	5	460	S4	0.410	0.413
0.7	5	470	S2	0.363	0.389
0.7	5	470	S3	0.349	0.349
0.7	5	470	S4	0.400	0.399
0.7	5	480	S2	0.299	0.311
0.7	5	480	S3	0.368	0.366
0.7	5	480	S4	0.293	0.285
0.7	5	490	S2	0.381	0.368
0.7	5	490	S3	0.377	0.395
0.7	5	490	S4	0.319	0.302

Continued on next page

Table 9.4 – Continued from previous page

Thickness (mm)	Damage size (mm)	Freq. (kHz)	Sensor	DI (Actual)	DI (Predicted)
0.7	5	500	S2	0.387	0.388
0.7	5	500	S3	0.340	0.342
0.7	5	500	S4	0.415	0.419
0.7	6	300	S2	0.508	0.513
0.7	6	300	S3	0.507	0.488
0.7	6	300	S4	0.480	0.467
0.7	6	310	S2	0.449	0.479
0.7	6	310	S3	0.442	0.442
0.7	6	310	S4	0.455	0.453
0.7	6	320	S2	0.475	0.477
0.7	6	320	S3	0.461	0.465
0.7	6	320	S4	0.359	0.350
0.7	6	330	S2	0.518	0.499
0.7	6	330	S3	0.451	0.430
0.7	6	330	S4	0.433	0.411
0.7	6	340	S2	0.500	0.485
0.7	6	340	S3	0.335	0.337
0.7	6	340	S4	0.433	0.429
0.7	6	350	S2	0.431	0.392
0.7	6	350	S3	0.398	0.407
0.7	6	350	S4	0.549	0.574
0.7	6	360	S2	0.472	0.455
0.7	6	360	S3	0.406	0.408
0.7	6	360	S4	0.474	0.465
0.7	6	370	S2	0.388	0.389
0.7	6	370	S3	0.413	0.428
0.7	6	370	S4	0.439	0.457
0.7	6	380	S2	0.553	0.544
0.7	6	380	S3	0.485	0.487
0.7	6	380	S4	0.504	0.504
0.7	6	390	S2	0.509	0.504
0.7	6	390	S3	0.425	0.441
0.7	6	390	S4	0.466	0.494
0.7	6	400	S2	0.426	0.427
0.7	6	400	S3	0.493	0.458
0.7	6	400	S4	0.439	0.455
0.7	6	410	S2	0.515	0.526
0.7	6	410	S3	0.480	0.484

Continued on next page

Table 9.4 – Continued from previous page

Thickness (mm)	Damage size (mm)	Freq. (kHz)	Sensor	DI (Actual)	DI (Predicted)
0.7	6	410	S4	0.498	0.499
0.7	6	420	S2	0.464	0.474
0.7	6	420	S3	0.453	0.442
0.7	6	420	S4	0.534	0.523
0.7	6	430	S2	0.455	0.460
0.7	6	430	S3	0.357	0.359
0.7	6	430	S4	0.462	0.433
0.7	6	440	S2	0.480	0.473
0.7	6	440	S3	0.450	0.460
0.7	6	440	S4	0.452	0.478
0.7	6	450	S2	0.569	0.578
0.7	6	450	S3	0.483	0.501
0.7	6	450	S4	0.469	0.466
0.7	6	460	S2	0.542	0.531
0.7	6	460	S3	0.410	0.408
0.7	6	460	S4	0.503	0.483
0.7	6	470	S2	0.462	0.460
0.7	6	470	S3	0.507	0.511
0.7	6	470	S4	0.461	0.477
0.7	6	480	S2	0.490	0.496
0.7	6	480	S3	0.326	0.335
0.7	6	480	S4	0.394	0.396
0.7	6	490	S2	0.416	0.406
0.7	6	490	S3	0.370	0.376
0.7	6	490	S4	0.464	0.485
0.7	6	500	S2	0.415	0.406
0.7	6	500	S3	0.432	0.434
0.7	6	500	S4	0.448	0.416
0.7	7	300	S2	0.533	0.513
0.7	7	300	S3	0.700	0.732
0.7	7	300	S4	0.529	0.520
0.7	7	310	S2	0.547	0.550
0.7	7	310	S3	0.561	0.559
0.7	7	310	S4	0.460	0.435
0.7	7	320	S2	0.578	0.581
0.7	7	320	S3	0.601	0.620
0.7	7	320	S4	0.603	0.621
0.7	7	330	S2	0.544	0.551

Continued on next page

Table 9.4 – Continued from previous page

Thickness (mm)	Damage size (mm)	Freq. (kHz)	Sensor	DI (Actual)	DI (Predicted)
0.7	7	330	S3	0.513	0.507
0.7	7	330	S4	0.541	0.536
0.7	7	340	S2	0.568	0.562
0.7	7	340	S3	0.559	0.532
0.7	7	340	S4	0.651	0.624
0.7	7	350	S2	0.602	0.617
0.7	7	350	S3	0.526	0.527
0.7	7	350	S4	0.584	0.585
0.7	7	360	S2	0.565	0.568
0.7	7	360	S3	0.617	0.620
0.7	7	360	S4	0.518	0.526
0.7	7	370	S2	0.522	0.520
0.7	7	370	S3	0.451	0.439
0.7	7	370	S4	0.439	0.428
0.7	7	380	S2	0.604	0.612
0.7	7	380	S3	0.503	0.515
0.7	7	380	S4	0.640	0.630
0.7	7	390	S2	0.601	0.587
0.7	7	390	S3	0.514	0.537
0.7	7	390	S4	0.563	0.548
0.7	7	400	S2	0.510	0.509
0.7	7	400	S3	0.581	0.609
0.7	7	400	S4	0.566	0.571
0.7	7	410	S2	0.515	0.506
0.7	7	410	S3	0.453	0.456
0.7	7	410	S4	0.537	0.540
0.7	7	420	S2	0.448	0.460
0.7	7	420	S3	0.491	0.503
0.7	7	420	S4	0.499	0.531
0.7	7	430	S2	0.555	0.551
0.7	7	430	S3	0.456	0.453
0.7	7	430	S4	0.487	0.492
0.7	7	440	S2	0.575	0.582
0.7	7	440	S3	0.556	0.543
0.7	7	440	S4	0.523	0.514
0.7	7	450	S2	0.543	0.553
0.7	7	450	S3	0.570	0.596
0.7	7	450	S4	0.486	0.478

Continued on next page

Table 9.4 – Continued from previous page

Thickness (mm)	Damage size (mm)	Freq. (kHz)	Sensor	DI (Actual)	DI (Predicted)
0.7	7	460	S2	0.525	0.493
0.7	7	460	S3	0.466	0.439
0.7	7	460	S4	0.540	0.545
0.7	7	470	S2	0.616	0.635
0.7	7	470	S3	0.554	0.568
0.7	7	470	S4	0.537	0.576
0.7	7	480	S2	0.509	0.506
0.7	7	480	S3	0.509	0.506
0.7	7	480	S4	0.426	0.429
0.7	7	490	S2	0.603	0.626
0.7	7	490	S3	0.592	0.560
0.7	7	490	S4	0.532	0.523
0.7	7	500	S2	0.594	0.604
0.7	7	500	S3	0.533	0.501
0.7	7	500	S4	0.528	0.511
0.7	12x4	300	S2	0.259	0.270
0.7	12x4	300	S3	0.251	0.227
0.7	12x4	300	S4	0.247	0.234
0.7	12x4	310	S2	0.298	0.279
0.7	12x4	310	S3	0.243	0.255
0.7	12x4	310	S4	0.191	0.195
0.7	12x4	320	S2	0.368	0.367
0.7	12x4	320	S3	0.201	0.200
0.7	12x4	320	S4	0.210	0.208
0.7	12x4	330	S2	0.252	0.259
0.7	12x4	330	S3	0.210	0.225
0.7	12x4	330	S4	0.251	0.265
0.7	12x4	340	S2	0.257	0.272
0.7	12x4	340	S3	0.240	0.221
0.7	12x4	340	S4	0.269	0.282
0.7	12x4	350	S2	0.251	0.211
0.7	12x4	350	S3	0.252	0.248
0.7	12x4	350	S4	0.241	0.201
0.7	12x4	360	S2	0.265	0.252
0.7	12x4	360	S3	0.263	0.248
0.7	12x4	360	S4	0.177	0.197
0.7	12x4	370	S2	0.197	0.200
0.7	12x4	370	S3	0.211	0.197

Continued on next page

Table 9.4 – Continued from previous page

Thickness (mm)	Damage size (mm)	Freq. (kHz)	Sensor	DI (Actual)	DI (Predicted)
0.7	12x4	370	S4	0.284	0.300
0.7	12x4	380	S2	0.279	0.291
0.7	12x4	380	S3	0.254	0.247
0.7	12x4	380	S4	0.223	0.236
0.7	12x4	390	S2	0.261	0.268
0.7	12x4	390	S3	0.247	0.224
0.7	12x4	390	S4	0.192	0.185
0.7	12x4	400	S2	0.223	0.229
0.7	12x4	400	S3	0.264	0.255
0.7	12x4	400	S4	0.291	0.292
0.7	12x4	410	S2	0.222	0.224
0.7	12x4	410	S3	0.159	0.160
0.7	12x4	410	S4	0.253	0.242
0.7	12x4	420	S2	0.251	0.253
0.7	12x4	420	S3	0.212	0.186
0.7	12x4	420	S4	0.297	0.316
0.7	12x4	430	S2	0.255	0.239
0.7	12x4	430	S3	0.291	0.287
0.7	12x4	430	S4	0.274	0.277
0.7	12x4	440	S2	0.231	0.226
0.7	12x4	440	S3	0.328	0.327
0.7	12x4	440	S4	0.253	0.236
0.7	12x4	450	S2	0.199	0.198
0.7	12x4	450	S3	0.242	0.204
0.7	12x4	450	S4	0.227	0.240
0.7	12x4	460	S2	0.292	0.283
0.7	12x4	460	S3	0.211	0.225
0.7	12x4	460	S4	0.327	0.334
0.7	12x4	470	S2	0.255	0.223
0.7	12x4	470	S3	0.332	0.326
0.7	12x4	470	S4	0.265	0.233
0.7	12x4	480	S2	0.292	0.267
0.7	12x4	480	S3	0.304	0.300
0.7	12x4	480	S4	0.303	0.295
0.7	12x4	490	S2	0.194	0.211
0.7	12x4	490	S3	0.300	0.324
0.7	12x4	490	S4	0.243	0.250
0.7	12x4	500	S2	0.269	0.255

Continued on next page

Table 9.4 – Continued from previous page

Thickness (mm)	Damage size (mm)	Freq. (kHz)	Sensor	DI (Actual)	DI (Predicted)
0.7	12x4	500	S3	0.288	0.306
0.7	12x4	500	S4	0.291	0.252
0.7	15x5	300	S2	0.389	0.382
0.7	15x5	300	S3	0.364	0.356
0.7	15x5	300	S4	0.327	0.322
0.7	15x5	310	S2	0.331	0.338
0.7	15x5	310	S3	0.379	0.422
0.7	15x5	310	S4	0.280	0.294
0.7	15x5	320	S2	0.347	0.339
0.7	15x5	320	S3	0.300	0.309
0.7	15x5	320	S4	0.346	0.356
0.7	15x5	330	S2	0.263	0.258
0.7	15x5	330	S3	0.299	0.291
0.7	15x5	330	S4	0.300	0.313
0.7	15x5	340	S2	0.365	0.386
0.7	15x5	340	S3	0.317	0.327
0.7	15x5	340	S4	0.358	0.329
0.7	15x5	350	S2	0.411	0.409
0.7	15x5	350	S3	0.394	0.381
0.7	15x5	350	S4	0.431	0.424
0.7	15x5	360	S2	0.434	0.446
0.7	15x5	360	S3	0.332	0.332
0.7	15x5	360	S4	0.298	0.307
0.7	15x5	370	S2	0.259	0.251
0.7	15x5	370	S3	0.367	0.385
0.7	15x5	370	S4	0.279	0.279
0.7	15x5	380	S2	0.393	0.371
0.7	15x5	380	S3	0.329	0.324
0.7	15x5	380	S4	0.372	0.365
0.7	15x5	390	S2	0.348	0.359
0.7	15x5	390	S3	0.346	0.357
0.7	15x5	390	S4	0.426	0.438
0.7	15x5	400	S2	0.318	0.327
0.7	15x5	400	S3	0.284	0.277
0.7	15x5	400	S4	0.337	0.372
0.7	15x5	410	S2	0.342	0.342
0.7	15x5	410	S3	0.385	0.388
0.7	15x5	410	S4	0.417	0.409

Continued on next page

Table 9.4 – Continued from previous page

Thickness (mm)	Damage size (mm)	Freq. (kHz)	Sensor	DI (Actual)	DI (Predicted)
0.7	15x5	420	S2	0.355	0.359
0.7	15x5	420	S3	0.287	0.285
0.7	15x5	420	S4	0.363	0.386
0.7	15x5	430	S2	0.333	0.337
0.7	15x5	430	S3	0.312	0.300
0.7	15x5	430	S4	0.353	0.362
0.7	15x5	440	S2	0.393	0.389
0.7	15x5	440	S3	0.404	0.401
0.7	15x5	440	S4	0.347	0.352
0.7	15x5	450	S2	0.337	0.315
0.7	15x5	450	S3	0.432	0.434
0.7	15x5	450	S4	0.406	0.403
0.7	15x5	460	S2	0.358	0.338
0.7	15x5	460	S3	0.407	0.432
0.7	15x5	460	S4	0.406	0.392
0.7	15x5	470	S2	0.371	0.388
0.7	15x5	470	S3	0.321	0.323
0.7	15x5	470	S4	0.331	0.329
0.7	15x5	480	S2	0.320	0.313
0.7	15x5	480	S3	0.321	0.316
0.7	15x5	480	S4	0.297	0.299
0.7	15x5	490	S2	0.334	0.330
0.7	15x5	490	S3	0.291	0.289
0.7	15x5	490	S4	0.305	0.329
0.7	15x5	500	S2	0.390	0.391
0.7	15x5	500	S3	0.384	0.375
0.7	15x5	500	S4	0.261	0.257
0.7	18x6	300	S2	0.384	0.407
0.7	18x6	300	S3	0.346	0.325
0.7	18x6	300	S4	0.438	0.446
0.7	18x6	310	S2	0.466	0.468
0.7	18x6	310	S3	0.441	0.421
0.7	18x6	310	S4	0.454	0.458
0.7	18x6	320	S2	0.434	0.393
0.7	18x6	320	S3	0.462	0.481
0.7	18x6	320	S4	0.439	0.454
0.7	18x6	330	S2	0.280	0.275
0.7	18x6	330	S3	0.522	0.523

Continued on next page

Table 9.4 – Continued from previous page

Thickness (mm)	Damage size (mm)	Freq. (kHz)	Sensor	DI (Actual)	DI (Predicted)
0.7	18x6	330	S4	0.423	0.428
0.7	18x6	340	S2	0.407	0.413
0.7	18x6	340	S3	0.516	0.514
0.7	18x6	340	S4	0.453	0.457
0.7	18x6	350	S2	0.429	0.414
0.7	18x6	350	S3	0.521	0.503
0.7	18x6	350	S4	0.429	0.414
0.7	18x6	360	S2	0.411	0.407
0.7	18x6	360	S3	0.538	0.544
0.7	18x6	360	S4	0.503	0.516
0.7	18x6	370	S2	0.459	0.442
0.7	18x6	370	S3	0.490	0.490
0.7	18x6	370	S4	0.529	0.527
0.7	18x6	380	S2	0.445	0.427
0.7	18x6	380	S3	0.419	0.410
0.7	18x6	380	S4	0.395	0.370
0.7	18x6	390	S2	0.441	0.434
0.7	18x6	390	S3	0.407	0.385
0.7	18x6	390	S4	0.457	0.454
0.7	18x6	400	S2	0.475	0.447
0.7	18x6	400	S3	0.465	0.443
0.7	18x6	400	S4	0.477	0.478
0.7	18x6	410	S2	0.489	0.487
0.7	18x6	410	S3	0.425	0.437
0.7	18x6	410	S4	0.552	0.552
0.7	18x6	420	S2	0.524	0.529
0.7	18x6	420	S3	0.394	0.413
0.7	18x6	420	S4	0.389	0.390
0.7	18x6	430	S2	0.480	0.505
0.7	18x6	430	S3	0.439	0.453
0.7	18x6	430	S4	0.512	0.503
0.7	18x6	440	S2	0.378	0.360
0.7	18x6	440	S3	0.404	0.428
0.7	18x6	440	S4	0.445	0.461
0.7	18x6	450	S2	0.465	0.445
0.7	18x6	450	S3	0.484	0.471
0.7	18x6	450	S4	0.435	0.428
0.7	18x6	460	S2	0.391	0.406

Continued on next page

Table 9.4 – Continued from previous page

Thickness (mm)	Damage size (mm)	Freq. (kHz)	Sensor	DI (Actual)	DI (Predicted)
0.7	18x6	460	S3	0.510	0.521
0.7	18x6	460	S4	0.475	0.478
0.7	18x6	470	S2	0.448	0.442
0.7	18x6	470	S3	0.455	0.434
0.7	18x6	470	S4	0.504	0.492
0.7	18x6	480	S2	0.376	0.399
0.7	18x6	480	S3	0.511	0.520
0.7	18x6	480	S4	0.508	0.507
0.7	18x6	490	S2	0.440	0.424
0.7	18x6	490	S3	0.401	0.428
0.7	18x6	490	S4	0.513	0.518
0.7	18x6	500	S2	0.502	0.504
0.7	18x6	500	S3	0.484	0.510
0.7	18x6	500	S4	0.514	0.507
0.9	4	300	S2	0.265	0.277
0.9	4	300	S3	0.327	0.330
0.9	4	300	S4	0.346	0.342
0.9	4	310	S2	0.286	0.304
0.9	4	310	S3	0.235	0.217
0.9	4	310	S4	0.296	0.300
0.9	4	320	S2	0.303	0.300
0.9	4	320	S3	0.237	0.233
0.9	4	320	S4	0.368	0.375
0.9	4	330	S2	0.296	0.303
0.9	4	330	S3	0.318	0.310
0.9	4	330	S4	0.332	0.331
0.9	4	340	S2	0.228	0.229
0.9	4	340	S3	0.286	0.264
0.9	4	340	S4	0.396	0.388
0.9	4	350	S2	0.305	0.300
0.9	4	350	S3	0.295	0.305
0.9	4	350	S4	0.286	0.292
0.9	4	360	S2	0.345	0.352
0.9	4	360	S3	0.290	0.284
0.9	4	360	S4	0.373	0.368
0.9	4	370	S2	0.323	0.324
0.9	4	370	S3	0.321	0.305
0.9	4	370	S4	0.245	0.256

Continued on next page

Table 9.4 – Continued from previous page

Thickness (mm)	Damage size (mm)	Freq. (kHz)	Sensor	DI (Actual)	DI (Predicted)
0.9	4	380	S2	0.277	0.253
0.9	4	380	S3	0.219	0.231
0.9	4	380	S4	0.266	0.274
0.9	4	390	S2	0.280	0.275
0.9	4	390	S3	0.335	0.332
0.9	4	390	S4	0.383	0.392
0.9	4	400	S2	0.348	0.355
0.9	4	400	S3	0.345	0.354
0.9	4	400	S4	0.371	0.362
0.9	4	410	S2	0.251	0.261
0.9	4	410	S3	0.347	0.322
0.9	4	410	S4	0.365	0.354
0.9	4	420	S2	0.291	0.286
0.9	4	420	S3	0.300	0.272
0.9	4	420	S4	0.293	0.309
0.9	4	430	S2	0.246	0.236
0.9	4	430	S3	0.234	0.264
0.9	4	430	S4	0.313	0.314
0.9	4	440	S2	0.258	0.248
0.9	4	440	S3	0.315	0.293
0.9	4	440	S4	0.474	0.465
0.9	4	450	S2	0.299	0.309
0.9	4	450	S3	0.327	0.336
0.9	4	450	S4	0.290	0.267
0.9	4	460	S2	0.352	0.346
0.9	4	460	S3	0.209	0.209
0.9	4	460	S4	0.389	0.404
0.9	4	470	S2	0.317	0.312
0.9	4	470	S3	0.273	0.269
0.9	4	470	S4	0.286	0.315
0.9	4	480	S2	0.394	0.396
0.9	4	480	S3	0.231	0.224
0.9	4	480	S4	0.295	0.279
0.9	4	490	S2	0.253	0.285
0.9	4	490	S3	0.294	0.298
0.9	4	490	S4	0.319	0.286
0.9	4	500	S2	0.277	0.259
0.9	4	500	S3	0.284	0.317

Continued on next page

Table 9.4 – Continued from previous page

Thickness (mm)	Damage size (mm)	Freq. (kHz)	Sensor	DI (Actual)	DI (Predicted)
0.9	4	500	S4	0.334	0.337
0.9	5	300	S2	0.380	0.366
0.9	5	300	S3	0.423	0.389
0.9	5	300	S4	0.358	0.346
0.9	5	310	S2	0.379	0.383
0.9	5	310	S3	0.438	0.394
0.9	5	310	S4	0.440	0.432
0.9	5	320	S2	0.280	0.281
0.9	5	320	S3	0.337	0.357
0.9	5	320	S4	0.427	0.436
0.9	5	330	S2	0.295	0.274
0.9	5	330	S3	0.349	0.317
0.9	5	330	S4	0.394	0.405
0.9	5	340	S2	0.321	0.331
0.9	5	340	S3	0.435	0.434
0.9	5	340	S4	0.381	0.343
0.9	5	350	S2	0.355	0.368
0.9	5	350	S3	0.418	0.429
0.9	5	350	S4	0.395	0.409
0.9	5	360	S2	0.389	0.382
0.9	5	360	S3	0.400	0.406
0.9	5	360	S4	0.444	0.445
0.9	5	370	S2	0.381	0.365
0.9	5	370	S3	0.253	0.248
0.9	5	370	S4	0.299	0.304
0.9	5	380	S2	0.381	0.380
0.9	5	380	S3	0.390	0.372
0.9	5	380	S4	0.384	0.396
0.9	5	390	S2	0.429	0.401
0.9	5	390	S3	0.300	0.303
0.9	5	390	S4	0.424	0.412
0.9	5	400	S2	0.502	0.458
0.9	5	400	S3	0.374	0.358
0.9	5	400	S4	0.424	0.427
0.9	5	410	S2	0.355	0.364
0.9	5	410	S3	0.378	0.348
0.9	5	410	S4	0.429	0.410
0.9	5	420	S2	0.411	0.406

Continued on next page

Table 9.4 – Continued from previous page

Thickness (mm)	Damage size (mm)	Freq. (kHz)	Sensor	DI (Actual)	DI (Predicted)
0.9	5	420	S3	0.415	0.418
0.9	5	420	S4	0.430	0.428
0.9	5	430	S2	0.420	0.414
0.9	5	430	S3	0.453	0.444
0.9	5	430	S4	0.414	0.425
0.9	5	440	S2	0.436	0.437
0.9	5	440	S3	0.319	0.329
0.9	5	440	S4	0.409	0.402
0.9	5	450	S2	0.379	0.381
0.9	5	450	S3	0.455	0.465
0.9	5	450	S4	0.376	0.420
0.9	5	460	S2	0.367	0.371
0.9	5	460	S3	0.434	0.427
0.9	5	460	S4	0.464	0.460
0.9	5	470	S2	0.494	0.493
0.9	5	470	S3	0.334	0.330
0.9	5	470	S4	0.346	0.344
0.9	5	480	S2	0.374	0.336
0.9	5	480	S3	0.443	0.437
0.9	5	480	S4	0.485	0.499
0.9	5	490	S2	0.576	0.596
0.9	5	490	S3	0.472	0.473
0.9	5	490	S4	0.391	0.404
0.9	5	500	S2	0.383	0.396
0.9	5	500	S3	0.364	0.374
0.9	5	500	S4	0.462	0.469
0.9	6	300	S2	0.485	0.460
0.9	6	300	S3	0.532	0.540
0.9	6	300	S4	0.491	0.465
0.9	6	310	S2	0.525	0.538
0.9	6	310	S3	0.502	0.526
0.9	6	310	S4	0.507	0.514
0.9	6	320	S2	0.532	0.516
0.9	6	320	S3	0.497	0.513
0.9	6	320	S4	0.508	0.526
0.9	6	330	S2	0.505	0.519
0.9	6	330	S3	0.405	0.416
0.9	6	330	S4	0.508	0.500

Continued on next page

Table 9.4 – Continued from previous page

Thickness (mm)	Damage size (mm)	Freq. (kHz)	Sensor	DI (Actual)	DI (Predicted)
0.9	6	340	S2	0.500	0.534
0.9	6	340	S3	0.468	0.477
0.9	6	340	S4	0.486	0.486
0.9	6	350	S2	0.504	0.508
0.9	6	350	S3	0.415	0.436
0.9	6	350	S4	0.466	0.460
0.9	6	360	S2	0.469	0.487
0.9	6	360	S3	0.581	0.611
0.9	6	360	S4	0.511	0.493
0.9	6	370	S2	0.531	0.551
0.9	6	370	S3	0.519	0.505
0.9	6	370	S4	0.523	0.538
0.9	6	380	S2	0.517	0.527
0.9	6	380	S3	0.427	0.420
0.9	6	380	S4	0.488	0.495
0.9	6	390	S2	0.504	0.527
0.9	6	390	S3	0.487	0.484
0.9	6	390	S4	0.576	0.582
0.9	6	400	S2	0.588	0.563
0.9	6	400	S3	0.547	0.539
0.9	6	400	S4	0.522	0.536
0.9	6	410	S2	0.500	0.532
0.9	6	410	S3	0.477	0.511
0.9	6	410	S4	0.463	0.464
0.9	6	420	S2	0.479	0.484
0.9	6	420	S3	0.431	0.452
0.9	6	420	S4	0.539	0.520
0.9	6	430	S2	0.476	0.498
0.9	6	430	S3	0.471	0.480
0.9	6	430	S4	0.595	0.578
0.9	6	440	S2	0.463	0.462
0.9	6	440	S3	0.548	0.537
0.9	6	440	S4	0.482	0.494
0.9	6	450	S2	0.533	0.498
0.9	6	450	S3	0.449	0.457
0.9	6	450	S4	0.531	0.531
0.9	6	460	S2	0.507	0.478
0.9	6	460	S3	0.540	0.491

Continued on next page

Table 9.4 – Continued from previous page

Thickness (mm)	Damage size (mm)	Freq. (kHz)	Sensor	DI (Actual)	DI (Predicted)
0.9	6	460	S4	0.511	0.516
0.9	6	470	S2	0.624	0.601
0.9	6	470	S3	0.463	0.447
0.9	6	470	S4	0.478	0.471
0.9	6	480	S2	0.494	0.499
0.9	6	480	S3	0.575	0.560
0.9	6	480	S4	0.539	0.522
0.9	6	490	S2	0.445	0.437
0.9	6	490	S3	0.451	0.473
0.9	6	490	S4	0.519	0.520
0.9	6	500	S2	0.519	0.512
0.9	6	500	S3	0.551	0.544
0.9	6	500	S4	0.527	0.537
0.9	7	300	S2	0.610	0.600
0.9	7	300	S3	0.625	0.627
0.9	7	300	S4	0.623	0.618
0.9	7	310	S2	0.597	0.602
0.9	7	310	S3	0.580	0.547
0.9	7	310	S4	0.614	0.628
0.9	7	320	S2	0.561	0.557
0.9	7	320	S3	0.600	0.607
0.9	7	320	S4	0.658	0.661
0.9	7	330	S2	0.529	0.509
0.9	7	330	S3	0.578	0.563
0.9	7	330	S4	0.513	0.494
0.9	7	340	S2	0.617	0.627
0.9	7	340	S3	0.717	0.709
0.9	7	340	S4	0.567	0.582
0.9	7	350	S2	0.589	0.597
0.9	7	350	S3	0.625	0.636
0.9	7	350	S4	0.603	0.603
0.9	7	360	S2	0.574	0.569
0.9	7	360	S3	0.582	0.582
0.9	7	360	S4	0.630	0.642
0.9	7	370	S2	0.592	0.595
0.9	7	370	S3	0.688	0.668
0.9	7	370	S4	0.634	0.619
0.9	7	380	S2	0.628	0.622

Continued on next page

Table 9.4 – Continued from previous page

Thickness (mm)	Damage size (mm)	Freq. (kHz)	Sensor	DI (Actual)	DI (Predicted)
0.9	7	380	S3	0.575	0.573
0.9	7	380	S4	0.568	0.578
0.9	7	390	S2	0.572	0.554
0.9	7	390	S3	0.560	0.555
0.9	7	390	S4	0.621	0.613
0.9	7	400	S2	0.588	0.577
0.9	7	400	S3	0.610	0.600
0.9	7	400	S4	0.568	0.579
0.9	7	410	S2	0.621	0.636
0.9	7	410	S3	0.578	0.558
0.9	7	410	S4	0.577	0.556
0.9	7	420	S2	0.636	0.656
0.9	7	420	S3	0.526	0.496
0.9	7	420	S4	0.558	0.528
0.9	7	430	S2	0.519	0.493
0.9	7	430	S3	0.522	0.536
0.9	7	430	S4	0.581	0.588
0.9	7	440	S2	0.578	0.546
0.9	7	440	S3	0.649	0.675
0.9	7	440	S4	0.643	0.633
0.9	7	450	S2	0.639	0.650
0.9	7	450	S3	0.612	0.582
0.9	7	450	S4	0.556	0.549
0.9	7	460	S2	0.727	0.730
0.9	7	460	S3	0.569	0.583
0.9	7	460	S4	0.644	0.632
0.9	7	470	S2	0.574	0.578
0.9	7	470	S3	0.557	0.558
0.9	7	470	S4	0.578	0.598
0.9	7	480	S2	0.691	0.700
0.9	7	480	S3	0.664	0.696
0.9	7	480	S4	0.651	0.653
0.9	7	490	S2	0.557	0.536
0.9	7	490	S3	0.585	0.574
0.9	7	490	S4	0.679	0.707
0.9	7	500	S2	0.649	0.648
0.9	7	500	S3	0.660	0.668
0.9	7	500	S4	0.564	0.566

Continued on next page

Table 9.4 – Continued from previous page

Thickness (mm)	Damage size (mm)	Freq. (kHz)	Sensor	DI (Actual)	DI (Predicted)
0.9	12x4	300	S2	0.276	0.274
0.9	12x4	300	S3	0.319	0.300
0.9	12x4	300	S4	0.242	0.238
0.9	12x4	310	S2	0.304	0.290
0.9	12x4	310	S3	0.266	0.263
0.9	12x4	310	S4	0.314	0.303
0.9	12x4	320	S2	0.348	0.329
0.9	12x4	320	S3	0.342	0.335
0.9	12x4	320	S4	0.297	0.294
0.9	12x4	330	S2	0.301	0.314
0.9	12x4	330	S3	0.315	0.310
0.9	12x4	330	S4	0.320	0.323
0.9	12x4	340	S2	0.238	0.235
0.9	12x4	340	S3	0.342	0.361
0.9	12x4	340	S4	0.358	0.330
0.9	12x4	350	S2	0.253	0.268
0.9	12x4	350	S3	0.354	0.364
0.9	12x4	350	S4	0.309	0.303
0.9	12x4	360	S2	0.269	0.257
0.9	12x4	360	S3	0.230	0.219
0.9	12x4	360	S4	0.371	0.386
0.9	12x4	370	S2	0.275	0.274
0.9	12x4	370	S3	0.342	0.365
0.9	12x4	370	S4	0.281	0.268
0.9	12x4	380	S2	0.333	0.320
0.9	12x4	380	S3	0.304	0.286
0.9	12x4	380	S4	0.245	0.254
0.9	12x4	390	S2	0.305	0.282
0.9	12x4	390	S3	0.272	0.260
0.9	12x4	390	S4	0.210	0.227
0.9	12x4	400	S2	0.318	0.322
0.9	12x4	400	S3	0.248	0.242
0.9	12x4	400	S4	0.329	0.332
0.9	12x4	410	S2	0.294	0.290
0.9	12x4	410	S3	0.324	0.316
0.9	12x4	410	S4	0.307	0.302
0.9	12x4	420	S2	0.357	0.351
0.9	12x4	420	S3	0.310	0.309

Continued on next page

Table 9.4 – Continued from previous page

Thickness (mm)	Damage size (mm)	Freq. (kHz)	Sensor	DI (Actual)	DI (Predicted)
0.9	12x4	420	S4	0.300	0.287
0.9	12x4	430	S2	0.252	0.276
0.9	12x4	430	S3	0.335	0.340
0.9	12x4	430	S4	0.281	0.283
0.9	12x4	440	S2	0.382	0.415
0.9	12x4	440	S3	0.228	0.225
0.9	12x4	440	S4	0.317	0.337
0.9	12x4	450	S2	0.202	0.212
0.9	12x4	450	S3	0.352	0.367
0.9	12x4	450	S4	0.346	0.330
0.9	12x4	460	S2	0.308	0.304
0.9	12x4	460	S3	0.312	0.307
0.9	12x4	460	S4	0.336	0.351
0.9	12x4	470	S2	0.390	0.387
0.9	12x4	470	S3	0.292	0.293
0.9	12x4	470	S4	0.298	0.321
0.9	12x4	480	S2	0.301	0.305
0.9	12x4	480	S3	0.235	0.251
0.9	12x4	480	S4	0.324	0.326
0.9	12x4	490	S2	0.331	0.321
0.9	12x4	490	S3	0.250	0.277
0.9	12x4	490	S4	0.392	0.385
0.9	12x4	500	S2	0.346	0.319
0.9	12x4	500	S3	0.299	0.329
0.9	12x4	500	S4	0.332	0.357
0.9	15x5	300	S2	0.393	0.383
0.9	15x5	300	S3	0.482	0.453
0.9	15x5	300	S4	0.386	0.393
0.9	15x5	310	S2	0.366	0.375
0.9	15x5	310	S3	0.387	0.376
0.9	15x5	310	S4	0.405	0.394
0.9	15x5	320	S2	0.424	0.421
0.9	15x5	320	S3	0.432	0.431
0.9	15x5	320	S4	0.437	0.450
0.9	15x5	330	S2	0.457	0.434
0.9	15x5	330	S3	0.407	0.434
0.9	15x5	330	S4	0.454	0.442
0.9	15x5	340	S2	0.449	0.454

Continued on next page

Table 9.4 – Continued from previous page

Thickness (mm)	Damage size (mm)	Freq. (kHz)	Sensor	DI (Actual)	DI (Predicted)
0.9	15x5	340	S3	0.406	0.397
0.9	15x5	340	S4	0.426	0.439
0.9	15x5	350	S2	0.428	0.427
0.9	15x5	350	S3	0.335	0.324
0.9	15x5	350	S4	0.396	0.372
0.9	15x5	360	S2	0.479	0.464
0.9	15x5	360	S3	0.410	0.390
0.9	15x5	360	S4	0.437	0.443
0.9	15x5	370	S2	0.395	0.404
0.9	15x5	370	S3	0.363	0.357
0.9	15x5	370	S4	0.390	0.384
0.9	15x5	380	S2	0.411	0.412
0.9	15x5	380	S3	0.359	0.391
0.9	15x5	380	S4	0.355	0.339
0.9	15x5	390	S2	0.400	0.419
0.9	15x5	390	S3	0.380	0.371
0.9	15x5	390	S4	0.439	0.441
0.9	15x5	400	S2	0.363	0.359
0.9	15x5	400	S3	0.373	0.373
0.9	15x5	400	S4	0.346	0.330
0.9	15x5	410	S2	0.373	0.352
0.9	15x5	410	S3	0.391	0.393
0.9	15x5	410	S4	0.345	0.326
0.9	15x5	420	S2	0.390	0.377
0.9	15x5	420	S3	0.408	0.407
0.9	15x5	420	S4	0.267	0.293
0.9	15x5	430	S2	0.399	0.398
0.9	15x5	430	S3	0.407	0.419
0.9	15x5	430	S4	0.402	0.411
0.9	15x5	440	S2	0.394	0.411
0.9	15x5	440	S3	0.363	0.364
0.9	15x5	440	S4	0.484	0.481
0.9	15x5	450	S2	0.473	0.467
0.9	15x5	450	S3	0.457	0.450
0.9	15x5	450	S4	0.462	0.453
0.9	15x5	460	S2	0.363	0.364
0.9	15x5	460	S3	0.339	0.352
0.9	15x5	460	S4	0.458	0.438

Continued on next page

Table 9.4 – Continued from previous page

Thickness (mm)	Damage size (mm)	Freq. (kHz)	Sensor	DI (Actual)	DI (Predicted)
0.9	15x5	470	S2	0.371	0.372
0.9	15x5	470	S3	0.342	0.335
0.9	15x5	470	S4	0.402	0.436
0.9	15x5	480	S2	0.458	0.461
0.9	15x5	480	S3	0.400	0.405
0.9	15x5	480	S4	0.336	0.329
0.9	15x5	490	S2	0.495	0.469
0.9	15x5	490	S3	0.423	0.450
0.9	15x5	490	S4	0.366	0.375
0.9	15x5	500	S2	0.502	0.482
0.9	15x5	500	S3	0.396	0.379
0.9	15x5	500	S4	0.389	0.400
0.9	18x6	300	S2	0.558	0.559
0.9	18x6	300	S3	0.417	0.412
0.9	18x6	300	S4	0.501	0.495
0.9	18x6	310	S2	0.517	0.511
0.9	18x6	310	S3	0.457	0.449
0.9	18x6	310	S4	0.577	0.582
0.9	18x6	320	S2	0.558	0.574
0.9	18x6	320	S3	0.502	0.508
0.9	18x6	320	S4	0.585	0.609
0.9	18x6	330	S2	0.528	0.545
0.9	18x6	330	S3	0.584	0.594
0.9	18x6	330	S4	0.525	0.506
0.9	18x6	340	S2	0.481	0.478
0.9	18x6	340	S3	0.465	0.481
0.9	18x6	340	S4	0.508	0.490
0.9	18x6	350	S2	0.603	0.574
0.9	18x6	350	S3	0.449	0.449
0.9	18x6	350	S4	0.489	0.493
0.9	18x6	360	S2	0.546	0.532
0.9	18x6	360	S3	0.537	0.522
0.9	18x6	360	S4	0.507	0.543
0.9	18x6	370	S2	0.409	0.412
0.9	18x6	370	S3	0.471	0.429
0.9	18x6	370	S4	0.465	0.471
0.9	18x6	380	S2	0.513	0.511
0.9	18x6	380	S3	0.624	0.634

Continued on next page

Table 9.4 – Continued from previous page

Thickness (mm)	Damage size (mm)	Freq. (kHz)	Sensor	DI (Actual)	DI (Predicted)
0.9	18x6	380	S4	0.515	0.518
0.9	18x6	390	S2	0.440	0.419
0.9	18x6	390	S3	0.434	0.429
0.9	18x6	390	S4	0.487	0.508
0.9	18x6	400	S2	0.509	0.500
0.9	18x6	400	S3	0.467	0.443
0.9	18x6	400	S4	0.441	0.459
0.9	18x6	410	S2	0.493	0.513
0.9	18x6	410	S3	0.533	0.531
0.9	18x6	410	S4	0.546	0.541
0.9	18x6	420	S2	0.393	0.399
0.9	18x6	420	S3	0.548	0.551
0.9	18x6	420	S4	0.511	0.520
0.9	18x6	430	S2	0.547	0.550
0.9	18x6	430	S3	0.492	0.526
0.9	18x6	430	S4	0.554	0.533
0.9	18x6	440	S2	0.474	0.457
0.9	18x6	440	S3	0.478	0.462
0.9	18x6	440	S4	0.500	0.496
0.9	18x6	450	S2	0.518	0.483
0.9	18x6	450	S3	0.590	0.592
0.9	18x6	450	S4	0.451	0.439
0.9	18x6	460	S2	0.532	0.564
0.9	18x6	460	S3	0.443	0.451
0.9	18x6	460	S4	0.570	0.586
0.9	18x6	470	S2	0.512	0.530
0.9	18x6	470	S3	0.489	0.473
0.9	18x6	470	S4	0.542	0.558
0.9	18x6	480	S2	0.533	0.536
0.9	18x6	480	S3	0.406	0.390
0.9	18x6	480	S4	0.533	0.546
0.9	18x6	490	S2	0.488	0.515
0.9	18x6	490	S3	0.603	0.610
0.9	18x6	490	S4	0.458	0.473
0.9	18x6	500	S2	0.544	0.523
0.9	18x6	500	S3	0.485	0.496
0.9	18x6	500	S4	0.539	0.536
1.2	4	300	S2	0.377	0.366

Continued on next page

Table 9.4 – Continued from previous page

Thickness (mm)	Damage size (mm)	Freq. (kHz)	Sensor	DI (Actual)	DI (Predicted)
1.2	4	300	S3	0.370	0.382
1.2	4	300	S4	0.372	0.390
1.2	4	310	S2	0.343	0.317
1.2	4	310	S3	0.247	0.233
1.2	4	310	S4	0.311	0.331
1.2	4	320	S2	0.352	0.371
1.2	4	320	S3	0.294	0.300
1.2	4	320	S4	0.258	0.272
1.2	4	330	S2	0.357	0.349
1.2	4	330	S3	0.288	0.306
1.2	4	330	S4	0.375	0.362
1.2	4	340	S2	0.295	0.310
1.2	4	340	S3	0.365	0.365
1.2	4	340	S4	0.382	0.382
1.2	4	350	S2	0.351	0.320
1.2	4	350	S3	0.293	0.316
1.2	4	350	S4	0.325	0.323
1.2	4	360	S2	0.355	0.367
1.2	4	360	S3	0.376	0.368
1.2	4	360	S4	0.392	0.408
1.2	4	370	S2	0.312	0.322
1.2	4	370	S3	0.276	0.264
1.2	4	370	S4	0.340	0.326
1.2	4	380	S2	0.347	0.340
1.2	4	380	S3	0.393	0.402
1.2	4	380	S4	0.318	0.322
1.2	4	390	S2	0.377	0.378
1.2	4	390	S3	0.332	0.339
1.2	4	390	S4	0.370	0.372
1.2	4	400	S2	0.364	0.386
1.2	4	400	S3	0.412	0.402
1.2	4	400	S4	0.316	0.285
1.2	4	410	S2	0.334	0.320
1.2	4	410	S3	0.321	0.313
1.2	4	410	S4	0.456	0.475
1.2	4	420	S2	0.369	0.366
1.2	4	420	S3	0.398	0.419
1.2	4	420	S4	0.305	0.331

Continued on next page

Table 9.4 – Continued from previous page

Thickness (mm)	Damage size (mm)	Freq. (kHz)	Sensor	DI (Actual)	DI (Predicted)
1.2	4	430	S2	0.372	0.366
1.2	4	430	S3	0.325	0.314
1.2	4	430	S4	0.321	0.317
1.2	4	440	S2	0.321	0.313
1.2	4	440	S3	0.373	0.348
1.2	4	440	S4	0.394	0.379
1.2	4	450	S2	0.276	0.295
1.2	4	450	S3	0.389	0.395
1.2	4	450	S4	0.366	0.343
1.2	4	460	S2	0.373	0.360
1.2	4	460	S3	0.313	0.319
1.2	4	460	S4	0.412	0.424
1.2	4	470	S2	0.278	0.276
1.2	4	470	S3	0.274	0.296
1.2	4	470	S4	0.328	0.338
1.2	4	480	S2	0.295	0.292
1.2	4	480	S3	0.366	0.350
1.2	4	480	S4	0.356	0.364
1.2	4	490	S2	0.345	0.324
1.2	4	490	S3	0.366	0.357
1.2	4	490	S4	0.227	0.230
1.2	4	500	S2	0.360	0.352
1.2	4	500	S3	0.279	0.276
1.2	4	500	S4	0.389	0.417
1.2	5	300	S2	0.516	0.522
1.2	5	300	S3	0.456	0.471
1.2	5	300	S4	0.441	0.426
1.2	5	310	S2	0.498	0.512
1.2	5	310	S3	0.481	0.479
1.2	5	310	S4	0.514	0.488
1.2	5	320	S2	0.477	0.491
1.2	5	320	S3	0.507	0.515
1.2	5	320	S4	0.460	0.455
1.2	5	330	S2	0.453	0.476
1.2	5	330	S3	0.429	0.446
1.2	5	330	S4	0.446	0.448
1.2	5	340	S2	0.431	0.420
1.2	5	340	S3	0.457	0.464

Continued on next page

Table 9.4 – Continued from previous page

Thickness (mm)	Damage size (mm)	Freq. (kHz)	Sensor	DI (Actual)	DI (Predicted)
1.2	5	340	S4	0.453	0.458
1.2	5	350	S2	0.419	0.455
1.2	5	350	S3	0.395	0.399
1.2	5	350	S4	0.375	0.363
1.2	5	360	S2	0.516	0.505
1.2	5	360	S3	0.472	0.447
1.2	5	360	S4	0.379	0.376
1.2	5	370	S2	0.451	0.462
1.2	5	370	S3	0.479	0.440
1.2	5	370	S4	0.441	0.435
1.2	5	380	S2	0.410	0.407
1.2	5	380	S3	0.397	0.405
1.2	5	380	S4	0.446	0.429
1.2	5	390	S2	0.420	0.417
1.2	5	390	S3	0.355	0.379
1.2	5	390	S4	0.433	0.458
1.2	5	400	S2	0.494	0.510
1.2	5	400	S3	0.458	0.439
1.2	5	400	S4	0.420	0.401
1.2	5	410	S2	0.502	0.502
1.2	5	410	S3	0.563	0.567
1.2	5	410	S4	0.477	0.465
1.2	5	420	S2	0.370	0.359
1.2	5	420	S3	0.456	0.456
1.2	5	420	S4	0.443	0.448
1.2	5	430	S2	0.389	0.391
1.2	5	430	S3	0.550	0.541
1.2	5	430	S4	0.431	0.424
1.2	5	440	S2	0.482	0.500
1.2	5	440	S3	0.529	0.526
1.2	5	440	S4	0.447	0.460
1.2	5	450	S2	0.510	0.544
1.2	5	450	S3	0.435	0.425
1.2	5	450	S4	0.397	0.391
1.2	5	460	S2	0.446	0.462
1.2	5	460	S3	0.425	0.443
1.2	5	460	S4	0.475	0.474
1.2	5	470	S2	0.440	0.436

Continued on next page

Table 9.4 – Continued from previous page

Thickness (mm)	Damage size (mm)	Freq. (kHz)	Sensor	DI (Actual)	DI (Predicted)
1.2	5	470	S3	0.441	0.434
1.2	5	470	S4	0.405	0.415
1.2	5	480	S2	0.384	0.378
1.2	5	480	S3	0.460	0.468
1.2	5	480	S4	0.364	0.362
1.2	5	490	S2	0.496	0.531
1.2	5	490	S3	0.500	0.494
1.2	5	490	S4	0.441	0.428
1.2	5	500	S2	0.427	0.426
1.2	5	500	S3	0.469	0.447
1.2	5	500	S4	0.431	0.432
1.2	6	300	S2	0.506	0.467
1.2	6	300	S3	0.505	0.501
1.2	6	300	S4	0.565	0.583
1.2	6	310	S2	0.560	0.549
1.2	6	310	S3	0.578	0.582
1.2	6	310	S4	0.553	0.542
1.2	6	320	S2	0.552	0.563
1.2	6	320	S3	0.527	0.541
1.2	6	320	S4	0.603	0.596
1.2	6	330	S2	0.572	0.577
1.2	6	330	S3	0.549	0.573
1.2	6	330	S4	0.646	0.664
1.2	6	340	S2	0.550	0.543
1.2	6	340	S3	0.585	0.560
1.2	6	340	S4	0.493	0.463
1.2	6	350	S2	0.420	0.413
1.2	6	350	S3	0.513	0.500
1.2	6	350	S4	0.607	0.603
1.2	6	360	S2	0.533	0.517
1.2	6	360	S3	0.533	0.525
1.2	6	360	S4	0.549	0.556
1.2	6	370	S2	0.541	0.537
1.2	6	370	S3	0.502	0.505
1.2	6	370	S4	0.530	0.550
1.2	6	380	S2	0.494	0.476
1.2	6	380	S3	0.508	0.533
1.2	6	380	S4	0.561	0.587

Continued on next page

Table 9.4 – Continued from previous page

Thickness (mm)	Damage size (mm)	Freq. (kHz)	Sensor	DI (Actual)	DI (Predicted)
1.2	6	390	S2	0.534	0.532
1.2	6	390	S3	0.560	0.553
1.2	6	390	S4	0.603	0.604
1.2	6	400	S2	0.668	0.653
1.2	6	400	S3	0.520	0.518
1.2	6	400	S4	0.569	0.593
1.2	6	410	S2	0.514	0.532
1.2	6	410	S3	0.581	0.567
1.2	6	410	S4	0.582	0.580
1.2	6	420	S2	0.488	0.471
1.2	6	420	S3	0.567	0.574
1.2	6	420	S4	0.613	0.611
1.2	6	430	S2	0.573	0.549
1.2	6	430	S3	0.536	0.536
1.2	6	430	S4	0.513	0.502
1.2	6	440	S2	0.536	0.552
1.2	6	440	S3	0.528	0.527
1.2	6	440	S4	0.492	0.472
1.2	6	450	S2	0.537	0.530
1.2	6	450	S3	0.525	0.511
1.2	6	450	S4	0.630	0.624
1.2	6	460	S2	0.470	0.474
1.2	6	460	S3	0.474	0.467
1.2	6	460	S4	0.552	0.556
1.2	6	470	S2	0.575	0.589
1.2	6	470	S3	0.514	0.520
1.2	6	470	S4	0.535	0.544
1.2	6	480	S2	0.580	0.595
1.2	6	480	S3	0.600	0.620
1.2	6	480	S4	0.603	0.603
1.2	6	490	S2	0.603	0.641
1.2	6	490	S3	0.584	0.570
1.2	6	490	S4	0.512	0.496
1.2	6	500	S2	0.542	0.521
1.2	6	500	S3	0.515	0.535
1.2	6	500	S4	0.545	0.570
1.2	7	300	S2	0.655	0.672
1.2	7	300	S3	0.667	0.668

Continued on next page

Table 9.4 – Continued from previous page

Thickness (mm)	Damage size (mm)	Freq. (kHz)	Sensor	DI (Actual)	DI (Predicted)
1.2	7	300	S4	0.644	0.646
1.2	7	310	S2	0.634	0.635
1.2	7	310	S3	0.622	0.620
1.2	7	310	S4	0.663	0.660
1.2	7	320	S2	0.606	0.609
1.2	7	320	S3	0.558	0.568
1.2	7	320	S4	0.665	0.643
1.2	7	330	S2	0.659	0.646
1.2	7	330	S3	0.639	0.655
1.2	7	330	S4	0.667	0.676
1.2	7	340	S2	0.633	0.637
1.2	7	340	S3	0.719	0.701
1.2	7	340	S4	0.596	0.592
1.2	7	350	S2	0.708	0.685
1.2	7	350	S3	0.699	0.699
1.2	7	350	S4	0.627	0.636
1.2	7	360	S2	0.670	0.667
1.2	7	360	S3	0.594	0.603
1.2	7	360	S4	0.627	0.634
1.2	7	370	S2	0.665	0.674
1.2	7	370	S3	0.657	0.674
1.2	7	370	S4	0.648	0.628
1.2	7	380	S2	0.701	0.705
1.2	7	380	S3	0.680	0.670
1.2	7	380	S4	0.657	0.673
1.2	7	390	S2	0.709	0.753
1.2	7	390	S3	0.674	0.664
1.2	7	390	S4	0.587	0.555
1.2	7	400	S2	0.687	0.679
1.2	7	400	S3	0.647	0.636
1.2	7	400	S4	0.645	0.628
1.2	7	410	S2	0.677	0.674
1.2	7	410	S3	0.682	0.649
1.2	7	410	S4	0.622	0.617
1.2	7	420	S2	0.629	0.635
1.2	7	420	S3	0.735	0.728
1.2	7	420	S4	0.735	0.735
1.2	7	430	S2	0.624	0.651

Continued on next page

Table 9.4 – Continued from previous page

Thickness (mm)	Damage size (mm)	Freq. (kHz)	Sensor	DI (Actual)	DI (Predicted)
1.2	7	430	S3	0.650	0.658
1.2	7	430	S4	0.702	0.704
1.2	7	440	S2	0.590	0.578
1.2	7	440	S3	0.667	0.680
1.2	7	440	S4	0.622	0.625
1.2	7	450	S2	0.600	0.619
1.2	7	450	S3	0.632	0.627
1.2	7	450	S4	0.586	0.561
1.2	7	460	S2	0.690	0.676
1.2	7	460	S3	0.604	0.615
1.2	7	460	S4	0.606	0.606
1.2	7	470	S2	0.654	0.645
1.2	7	470	S3	0.667	0.666
1.2	7	470	S4	0.715	0.718
1.2	7	480	S2	0.668	0.664
1.2	7	480	S3	0.647	0.661
1.2	7	480	S4	0.632	0.626
1.2	7	490	S2	0.611	0.606
1.2	7	490	S3	0.710	0.717
1.2	7	490	S4	0.681	0.684
1.2	7	500	S2	0.682	0.686
1.2	7	500	S3	0.594	0.571
1.2	7	500	S4	0.653	0.642
1.2	12x4	300	S2	0.316	0.312
1.2	12x4	300	S3	0.376	0.385
1.2	12x4	300	S4	0.283	0.262
1.2	12x4	310	S2	0.416	0.434
1.2	12x4	310	S3	0.344	0.319
1.2	12x4	310	S4	0.382	0.376
1.2	12x4	320	S2	0.319	0.324
1.2	12x4	320	S3	0.277	0.281
1.2	12x4	320	S4	0.340	0.355
1.2	12x4	330	S2	0.367	0.374
1.2	12x4	330	S3	0.406	0.395
1.2	12x4	330	S4	0.349	0.333
1.2	12x4	340	S2	0.424	0.417
1.2	12x4	340	S3	0.337	0.365
1.2	12x4	340	S4	0.214	0.221

Continued on next page

Table 9.4 – Continued from previous page

Thickness (mm)	Damage size (mm)	Freq. (kHz)	Sensor	DI (Actual)	DI (Predicted)
1.2	12x4	350	S2	0.327	0.304
1.2	12x4	350	S3	0.376	0.346
1.2	12x4	350	S4	0.354	0.379
1.2	12x4	360	S2	0.368	0.364
1.2	12x4	360	S3	0.485	0.496
1.2	12x4	360	S4	0.330	0.313
1.2	12x4	370	S2	0.372	0.375
1.2	12x4	370	S3	0.245	0.239
1.2	12x4	370	S4	0.350	0.363
1.2	12x4	380	S2	0.406	0.414
1.2	12x4	380	S3	0.345	0.351
1.2	12x4	380	S4	0.341	0.366
1.2	12x4	390	S2	0.370	0.371
1.2	12x4	390	S3	0.364	0.342
1.2	12x4	390	S4	0.280	0.273
1.2	12x4	400	S2	0.367	0.370
1.2	12x4	400	S3	0.324	0.330
1.2	12x4	400	S4	0.413	0.421
1.2	12x4	410	S2	0.406	0.408
1.2	12x4	410	S3	0.291	0.313
1.2	12x4	410	S4	0.430	0.433
1.2	12x4	420	S2	0.243	0.236
1.2	12x4	420	S3	0.352	0.331
1.2	12x4	420	S4	0.398	0.382
1.2	12x4	430	S2	0.328	0.291
1.2	12x4	430	S3	0.379	0.366
1.2	12x4	430	S4	0.285	0.296
1.2	12x4	440	S2	0.234	0.239
1.2	12x4	440	S3	0.372	0.367
1.2	12x4	440	S4	0.366	0.342
1.2	12x4	450	S2	0.344	0.335
1.2	12x4	450	S3	0.337	0.317
1.2	12x4	450	S4	0.376	0.386
1.2	12x4	460	S2	0.323	0.317
1.2	12x4	460	S3	0.348	0.358
1.2	12x4	460	S4	0.315	0.302
1.2	12x4	470	S2	0.348	0.353
1.2	12x4	470	S3	0.336	0.361

Continued on next page

Table 9.4 – Continued from previous page

Thickness (mm)	Damage size (mm)	Freq. (kHz)	Sensor	DI (Actual)	DI (Predicted)
1.2	12x4	470	S4	0.267	0.263
1.2	12x4	480	S2	0.448	0.438
1.2	12x4	480	S3	0.390	0.409
1.2	12x4	480	S4	0.412	0.434
1.2	12x4	490	S2	0.339	0.357
1.2	12x4	490	S3	0.238	0.251
1.2	12x4	490	S4	0.381	0.403
1.2	12x4	500	S2	0.352	0.381
1.2	12x4	500	S3	0.274	0.272
1.2	12x4	500	S4	0.407	0.427
1.2	15x5	300	S2	0.349	0.362
1.2	15x5	300	S3	0.517	0.502
1.2	15x5	300	S4	0.436	0.460
1.2	15x5	310	S2	0.497	0.482
1.2	15x5	310	S3	0.444	0.465
1.2	15x5	310	S4	0.461	0.489
1.2	15x5	320	S2	0.468	0.457
1.2	15x5	320	S3	0.415	0.435
1.2	15x5	320	S4	0.491	0.501
1.2	15x5	330	S2	0.404	0.399
1.2	15x5	330	S3	0.427	0.429
1.2	15x5	330	S4	0.423	0.421
1.2	15x5	340	S2	0.487	0.490
1.2	15x5	340	S3	0.520	0.536
1.2	15x5	340	S4	0.400	0.427
1.2	15x5	350	S2	0.487	0.472
1.2	15x5	350	S3	0.421	0.429
1.2	15x5	350	S4	0.404	0.392
1.2	15x5	360	S2	0.374	0.362
1.2	15x5	360	S3	0.586	0.579
1.2	15x5	360	S4	0.480	0.466
1.2	15x5	370	S2	0.450	0.485
1.2	15x5	370	S3	0.428	0.414
1.2	15x5	370	S4	0.477	0.476
1.2	15x5	380	S2	0.482	0.480
1.2	15x5	380	S3	0.405	0.437
1.2	15x5	380	S4	0.416	0.425
1.2	15x5	390	S2	0.504	0.503

Continued on next page

Table 9.4 – Continued from previous page

Thickness (mm)	Damage size (mm)	Freq. (kHz)	Sensor	DI (Actual)	DI (Predicted)
1.2	15x5	390	S3	0.492	0.502
1.2	15x5	390	S4	0.485	0.513
1.2	15x5	400	S2	0.444	0.418
1.2	15x5	400	S3	0.491	0.511
1.2	15x5	400	S4	0.450	0.460
1.2	15x5	410	S2	0.392	0.376
1.2	15x5	410	S3	0.477	0.486
1.2	15x5	410	S4	0.461	0.474
1.2	15x5	420	S2	0.455	0.450
1.2	15x5	420	S3	0.560	0.560
1.2	15x5	420	S4	0.385	0.404
1.2	15x5	430	S2	0.447	0.446
1.2	15x5	430	S3	0.478	0.487
1.2	15x5	430	S4	0.484	0.490
1.2	15x5	440	S2	0.412	0.396
1.2	15x5	440	S3	0.490	0.486
1.2	15x5	440	S4	0.479	0.471
1.2	15x5	450	S2	0.422	0.449
1.2	15x5	450	S3	0.517	0.532
1.2	15x5	450	S4	0.491	0.487
1.2	15x5	460	S2	0.466	0.476
1.2	15x5	460	S3	0.475	0.461
1.2	15x5	460	S4	0.456	0.460
1.2	15x5	470	S2	0.413	0.403
1.2	15x5	470	S3	0.453	0.452
1.2	15x5	470	S4	0.376	0.376
1.2	15x5	480	S2	0.476	0.482
1.2	15x5	480	S3	0.569	0.568
1.2	15x5	480	S4	0.423	0.438
1.2	15x5	490	S2	0.456	0.465
1.2	15x5	490	S3	0.447	0.434
1.2	15x5	490	S4	0.347	0.337
1.2	15x5	500	S2	0.331	0.340
1.2	15x5	500	S3	0.460	0.445
1.2	15x5	500	S4	0.427	0.409
1.2	18x6	300	S2	0.518	0.544
1.2	18x6	300	S3	0.575	0.560
1.2	18x6	300	S4	0.565	0.545

Continued on next page

Table 9.4 – Continued from previous page

Thickness (mm)	Damage size (mm)	Freq. (kHz)	Sensor	DI (Actual)	DI (Predicted)
1.2	18x6	310	S2	0.545	0.540
1.2	18x6	310	S3	0.506	0.516
1.2	18x6	310	S4	0.602	0.602
1.2	18x6	320	S2	0.678	0.679
1.2	18x6	320	S3	0.569	0.541
1.2	18x6	320	S4	0.496	0.496
1.2	18x6	330	S2	0.524	0.522
1.2	18x6	330	S3	0.645	0.631
1.2	18x6	330	S4	0.536	0.509
1.2	18x6	340	S2	0.571	0.561
1.2	18x6	340	S3	0.502	0.492
1.2	18x6	340	S4	0.498	0.487
1.2	18x6	350	S2	0.663	0.662
1.2	18x6	350	S3	0.633	0.625
1.2	18x6	350	S4	0.583	0.599
1.2	18x6	360	S2	0.586	0.595
1.2	18x6	360	S3	0.594	0.609
1.2	18x6	360	S4	0.575	0.536
1.2	18x6	370	S2	0.507	0.477
1.2	18x6	370	S3	0.493	0.503
1.2	18x6	370	S4	0.478	0.476
1.2	18x6	380	S2	0.567	0.531
1.2	18x6	380	S3	0.587	0.582
1.2	18x6	380	S4	0.542	0.528
1.2	18x6	390	S2	0.569	0.591
1.2	18x6	390	S3	0.533	0.537
1.2	18x6	390	S4	0.521	0.510
1.2	18x6	400	S2	0.500	0.515
1.2	18x6	400	S3	0.639	0.650
1.2	18x6	400	S4	0.515	0.506
1.2	18x6	410	S2	0.532	0.523
1.2	18x6	410	S3	0.496	0.506
1.2	18x6	410	S4	0.547	0.538
1.2	18x6	420	S2	0.514	0.532
1.2	18x6	420	S3	0.576	0.596
1.2	18x6	420	S4	0.590	0.565
1.2	18x6	430	S2	0.607	0.607
1.2	18x6	430	S3	0.632	0.617

Continued on next page

Table 9.4 – Continued from previous page

Thickness (mm)	Damage size (mm)	Freq. (kHz)	Sensor	DI (Actual)	DI (Predicted)
1.2	18x6	430	S4	0.590	0.581
1.2	18x6	440	S2	0.579	0.602
1.2	18x6	440	S3	0.584	0.551
1.2	18x6	440	S4	0.564	0.556
1.2	18x6	450	S2	0.566	0.550
1.2	18x6	450	S3	0.560	0.548
1.2	18x6	450	S4	0.569	0.576
1.2	18x6	460	S2	0.449	0.449
1.2	18x6	460	S3	0.601	0.586
1.2	18x6	460	S4	0.522	0.518
1.2	18x6	470	S2	0.560	0.536
1.2	18x6	470	S3	0.467	0.485
1.2	18x6	470	S4	0.579	0.591
1.2	18x6	480	S2	0.575	0.562
1.2	18x6	480	S3	0.621	0.659
1.2	18x6	480	S4	0.472	0.468
1.2	18x6	490	S2	0.544	0.537
1.2	18x6	490	S3	0.509	0.508
1.2	18x6	490	S4	0.534	0.527
1.2	18x6	500	S2	0.487	0.491
1.2	18x6	500	S3	0.507	0.518
1.2	18x6	500	S4	0.518	0.513
1.5	4	300	S2	0.405	0.413
1.5	4	300	S3	0.348	0.349
1.5	4	300	S4	0.482	0.456
1.5	4	310	S2	0.470	0.459
1.5	4	310	S3	0.463	0.461
1.5	4	310	S4	0.354	0.330
1.5	4	320	S2	0.440	0.460
1.5	4	320	S3	0.440	0.437
1.5	4	320	S4	0.408	0.415
1.5	4	330	S2	0.403	0.398
1.5	4	330	S3	0.465	0.459
1.5	4	330	S4	0.412	0.440
1.5	4	340	S2	0.390	0.395
1.5	4	340	S3	0.436	0.428
1.5	4	340	S4	0.381	0.388
1.5	4	350	S2	0.408	0.424

Continued on next page

Table 9.4 – Continued from previous page

Thickness (mm)	Damage size (mm)	Freq. (kHz)	Sensor	DI (Actual)	DI (Predicted)
1.5	4	350	S3	0.464	0.470
1.5	4	350	S4	0.409	0.424
1.5	4	360	S2	0.443	0.427
1.5	4	360	S3	0.457	0.461
1.5	4	360	S4	0.363	0.385
1.5	4	370	S2	0.266	0.260
1.5	4	370	S3	0.421	0.422
1.5	4	370	S4	0.398	0.378
1.5	4	380	S2	0.423	0.410
1.5	4	380	S3	0.319	0.330
1.5	4	380	S4	0.342	0.349
1.5	4	390	S2	0.432	0.466
1.5	4	390	S3	0.326	0.340
1.5	4	390	S4	0.448	0.460
1.5	4	400	S2	0.390	0.404
1.5	4	400	S3	0.411	0.419
1.5	4	400	S4	0.322	0.323
1.5	4	410	S2	0.324	0.317
1.5	4	410	S3	0.365	0.384
1.5	4	410	S4	0.506	0.498
1.5	4	420	S2	0.407	0.374
1.5	4	420	S3	0.570	0.568
1.5	4	420	S4	0.443	0.433
1.5	4	430	S2	0.462	0.487
1.5	4	430	S3	0.416	0.440
1.5	4	430	S4	0.476	0.452
1.5	4	440	S2	0.379	0.379
1.5	4	440	S3	0.447	0.441
1.5	4	440	S4	0.398	0.394
1.5	4	450	S2	0.464	0.442
1.5	4	450	S3	0.385	0.423
1.5	4	450	S4	0.300	0.308
1.5	4	460	S2	0.460	0.442
1.5	4	460	S3	0.362	0.351
1.5	4	460	S4	0.408	0.404
1.5	4	470	S2	0.318	0.333
1.5	4	470	S3	0.411	0.411
1.5	4	470	S4	0.384	0.395

Continued on next page

Table 9.4 – Continued from previous page

Thickness (mm)	Damage size (mm)	Freq. (kHz)	Sensor	DI (Actual)	DI (Predicted)
1.5	4	480	S2	0.377	0.360
1.5	4	480	S3	0.346	0.330
1.5	4	480	S4	0.428	0.459
1.5	4	490	S2	0.449	0.421
1.5	4	490	S3	0.425	0.425
1.5	4	490	S4	0.430	0.418
1.5	4	500	S2	0.361	0.343
1.5	4	500	S3	0.375	0.402
1.5	4	500	S4	0.452	0.432
1.5	5	300	S2	0.532	0.526
1.5	5	300	S3	0.516	0.502
1.5	5	300	S4	0.512	0.509
1.5	5	310	S2	0.522	0.491
1.5	5	310	S3	0.547	0.555
1.5	5	310	S4	0.467	0.469
1.5	5	320	S2	0.498	0.486
1.5	5	320	S3	0.546	0.538
1.5	5	320	S4	0.447	0.456
1.5	5	330	S2	0.528	0.523
1.5	5	330	S3	0.538	0.529
1.5	5	330	S4	0.487	0.484
1.5	5	340	S2	0.592	0.600
1.5	5	340	S3	0.523	0.491
1.5	5	340	S4	0.505	0.481
1.5	5	350	S2	0.453	0.461
1.5	5	350	S3	0.525	0.510
1.5	5	350	S4	0.474	0.474
1.5	5	360	S2	0.485	0.471
1.5	5	360	S3	0.457	0.429
1.5	5	360	S4	0.496	0.499
1.5	5	370	S2	0.552	0.509
1.5	5	370	S3	0.389	0.392
1.5	5	370	S4	0.476	0.480
1.5	5	380	S2	0.484	0.498
1.5	5	380	S3	0.470	0.511
1.5	5	380	S4	0.488	0.488
1.5	5	390	S2	0.400	0.383
1.5	5	390	S3	0.492	0.498

Continued on next page

Table 9.4 – Continued from previous page

Thickness (mm)	Damage size (mm)	Freq. (kHz)	Sensor	DI (Actual)	DI (Predicted)
1.5	5	390	S4	0.583	0.588
1.5	5	400	S2	0.545	0.569
1.5	5	400	S3	0.475	0.489
1.5	5	400	S4	0.531	0.514
1.5	5	410	S2	0.514	0.511
1.5	5	410	S3	0.531	0.527
1.5	5	410	S4	0.510	0.499
1.5	5	420	S2	0.467	0.446
1.5	5	420	S3	0.505	0.499
1.5	5	420	S4	0.452	0.474
1.5	5	430	S2	0.463	0.449
1.5	5	430	S3	0.540	0.569
1.5	5	430	S4	0.496	0.489
1.5	5	440	S2	0.520	0.533
1.5	5	440	S3	0.457	0.458
1.5	5	440	S4	0.486	0.501
1.5	5	450	S2	0.554	0.542
1.5	5	450	S3	0.510	0.495
1.5	5	450	S4	0.504	0.482
1.5	5	460	S2	0.457	0.449
1.5	5	460	S3	0.586	0.548
1.5	5	460	S4	0.466	0.480
1.5	5	470	S2	0.349	0.350
1.5	5	470	S3	0.488	0.474
1.5	5	470	S4	0.505	0.513
1.5	5	480	S2	0.456	0.458
1.5	5	480	S3	0.555	0.568
1.5	5	480	S4	0.569	0.570
1.5	5	490	S2	0.523	0.502
1.5	5	490	S3	0.479	0.476
1.5	5	490	S4	0.542	0.538
1.5	5	500	S2	0.488	0.484
1.5	5	500	S3	0.618	0.644
1.5	5	500	S4	0.547	0.527
1.5	6	300	S2	0.611	0.613
1.5	6	300	S3	0.601	0.612
1.5	6	300	S4	0.560	0.551
1.5	6	310	S2	0.606	0.621

Continued on next page

Table 9.4 – Continued from previous page

Thickness (mm)	Damage size (mm)	Freq. (kHz)	Sensor	DI (Actual)	DI (Predicted)
1.5	6	310	S3	0.608	0.605
1.5	6	310	S4	0.604	0.598
1.5	6	320	S2	0.631	0.647
1.5	6	320	S3	0.665	0.682
1.5	6	320	S4	0.656	0.649
1.5	6	330	S2	0.616	0.615
1.5	6	330	S3	0.585	0.616
1.5	6	330	S4	0.633	0.629
1.5	6	340	S2	0.618	0.609
1.5	6	340	S3	0.532	0.532
1.5	6	340	S4	0.668	0.668
1.5	6	350	S2	0.618	0.620
1.5	6	350	S3	0.570	0.553
1.5	6	350	S4	0.592	0.596
1.5	6	360	S2	0.674	0.660
1.5	6	360	S3	0.713	0.706
1.5	6	360	S4	0.511	0.523
1.5	6	370	S2	0.499	0.475
1.5	6	370	S3	0.647	0.656
1.5	6	370	S4	0.569	0.562
1.5	6	380	S2	0.522	0.554
1.5	6	380	S3	0.532	0.542
1.5	6	380	S4	0.571	0.580
1.5	6	390	S2	0.571	0.559
1.5	6	390	S3	0.547	0.555
1.5	6	390	S4	0.590	0.615
1.5	6	400	S2	0.528	0.522
1.5	6	400	S3	0.544	0.545
1.5	6	400	S4	0.508	0.497
1.5	6	410	S2	0.504	0.488
1.5	6	410	S3	0.590	0.581
1.5	6	410	S4	0.640	0.665
1.5	6	420	S2	0.658	0.671
1.5	6	420	S3	0.558	0.576
1.5	6	420	S4	0.536	0.546
1.5	6	430	S2	0.618	0.618
1.5	6	430	S3	0.587	0.553
1.5	6	430	S4	0.609	0.603

Continued on next page

Table 9.4 – Continued from previous page

Thickness (mm)	Damage size (mm)	Freq. (kHz)	Sensor	DI (Actual)	DI (Predicted)
1.5	6	440	S2	0.579	0.592
1.5	6	440	S3	0.510	0.535
1.5	6	440	S4	0.571	0.551
1.5	6	450	S2	0.646	0.670
1.5	6	450	S3	0.617	0.643
1.5	6	450	S4	0.618	0.605
1.5	6	460	S2	0.624	0.623
1.5	6	460	S3	0.571	0.560
1.5	6	460	S4	0.560	0.578
1.5	6	470	S2	0.592	0.605
1.5	6	470	S3	0.616	0.610
1.5	6	470	S4	0.570	0.574
1.5	6	480	S2	0.518	0.504
1.5	6	480	S3	0.539	0.543
1.5	6	480	S4	0.651	0.663
1.5	6	490	S2	0.549	0.556
1.5	6	490	S3	0.634	0.641
1.5	6	490	S4	0.572	0.567
1.5	6	500	S2	0.660	0.676
1.5	6	500	S3	0.577	0.562
1.5	6	500	S4	0.567	0.596
1.5	7	300	S2	0.747	0.737
1.5	7	300	S3	0.726	0.725
1.5	7	300	S4	0.610	0.614
1.5	7	310	S2	0.702	0.714
1.5	7	310	S3	0.747	0.754
1.5	7	310	S4	0.747	0.749
1.5	7	320	S2	0.593	0.612
1.5	7	320	S3	0.694	0.691
1.5	7	320	S4	0.702	0.712
1.5	7	330	S2	0.665	0.651
1.5	7	330	S3	0.742	0.745
1.5	7	330	S4	0.756	0.773
1.5	7	340	S2	0.661	0.661
1.5	7	340	S3	0.664	0.635
1.5	7	340	S4	0.772	0.769
1.5	7	350	S2	0.748	0.743
1.5	7	350	S3	0.689	0.691

Continued on next page

Table 9.4 – Continued from previous page

Thickness (mm)	Damage size (mm)	Freq. (kHz)	Sensor	DI (Actual)	DI (Predicted)
1.5	7	350	S4	0.793	0.813
1.5	7	360	S2	0.662	0.657
1.5	7	360	S3	0.693	0.688
1.5	7	360	S4	0.705	0.701
1.5	7	370	S2	0.740	0.728
1.5	7	370	S3	0.683	0.697
1.5	7	370	S4	0.811	0.799
1.5	7	380	S2	0.582	0.595
1.5	7	380	S3	0.646	0.654
1.5	7	380	S4	0.748	0.755
1.5	7	390	S2	0.719	0.716
1.5	7	390	S3	0.712	0.677
1.5	7	390	S4	0.738	0.726
1.5	7	400	S2	0.570	0.558
1.5	7	400	S3	0.536	0.532
1.5	7	400	S4	0.647	0.646
1.5	7	410	S2	0.701	0.703
1.5	7	410	S3	0.651	0.662
1.5	7	410	S4	0.703	0.711
1.5	7	420	S2	0.683	0.688
1.5	7	420	S3	0.726	0.725
1.5	7	420	S4	0.686	0.663
1.5	7	430	S2	0.720	0.716
1.5	7	430	S3	0.769	0.798
1.5	7	430	S4	0.706	0.745
1.5	7	440	S2	0.610	0.595
1.5	7	440	S3	0.723	0.723
1.5	7	440	S4	0.641	0.648
1.5	7	450	S2	0.651	0.649
1.5	7	450	S3	0.778	0.798
1.5	7	450	S4	0.747	0.755
1.5	7	460	S2	0.823	0.807
1.5	7	460	S3	0.672	0.680
1.5	7	460	S4	0.785	0.787
1.5	7	470	S2	0.714	0.714
1.5	7	470	S3	0.648	0.638
1.5	7	470	S4	0.720	0.715
1.5	7	480	S2	0.664	0.664

Continued on next page

Table 9.4 – Continued from previous page

Thickness (mm)	Damage size (mm)	Freq. (kHz)	Sensor	DI (Actual)	DI (Predicted)
1.5	7	480	S3	0.724	0.726
1.5	7	480	S4	0.729	0.718
1.5	7	490	S2	0.609	0.602
1.5	7	490	S3	0.695	0.706
1.5	7	490	S4	0.769	0.757
1.5	7	500	S2	0.725	0.736
1.5	7	500	S3	0.728	0.746
1.5	7	500	S4	0.724	0.719
1.5	12x4	300	S2	0.378	0.408
1.5	12x4	300	S3	0.289	0.296
1.5	12x4	300	S4	0.446	0.423
1.5	12x4	310	S2	0.438	0.458
1.5	12x4	310	S3	0.473	0.476
1.5	12x4	310	S4	0.451	0.446
1.5	12x4	320	S2	0.383	0.384
1.5	12x4	320	S3	0.389	0.392
1.5	12x4	320	S4	0.435	0.401
1.5	12x4	330	S2	0.389	0.385
1.5	12x4	330	S3	0.468	0.456
1.5	12x4	330	S4	0.543	0.535
1.5	12x4	340	S2	0.364	0.374
1.5	12x4	340	S3	0.354	0.330
1.5	12x4	340	S4	0.447	0.446
1.5	12x4	350	S2	0.405	0.413
1.5	12x4	350	S3	0.440	0.450
1.5	12x4	350	S4	0.403	0.426
1.5	12x4	360	S2	0.316	0.294
1.5	12x4	360	S3	0.420	0.432
1.5	12x4	360	S4	0.369	0.341
1.5	12x4	370	S2	0.368	0.355
1.5	12x4	370	S3	0.392	0.357
1.5	12x4	370	S4	0.377	0.394
1.5	12x4	380	S2	0.337	0.344
1.5	12x4	380	S3	0.460	0.446
1.5	12x4	380	S4	0.395	0.374
1.5	12x4	390	S2	0.395	0.403
1.5	12x4	390	S3	0.341	0.354
1.5	12x4	390	S4	0.384	0.375

Continued on next page

Table 9.4 – Continued from previous page

Thickness (mm)	Damage size (mm)	Freq. (kHz)	Sensor	DI (Actual)	DI (Predicted)
1.5	12x4	400	S2	0.391	0.412
1.5	12x4	400	S3	0.407	0.426
1.5	12x4	400	S4	0.446	0.463
1.5	12x4	410	S2	0.378	0.369
1.5	12x4	410	S3	0.403	0.415
1.5	12x4	410	S4	0.351	0.344
1.5	12x4	420	S2	0.364	0.382
1.5	12x4	420	S3	0.391	0.365
1.5	12x4	420	S4	0.433	0.417
1.5	12x4	430	S2	0.433	0.462
1.5	12x4	430	S3	0.416	0.439
1.5	12x4	430	S4	0.466	0.447
1.5	12x4	440	S2	0.330	0.322
1.5	12x4	440	S3	0.439	0.439
1.5	12x4	440	S4	0.416	0.398
1.5	12x4	450	S2	0.374	0.354
1.5	12x4	450	S3	0.374	0.388
1.5	12x4	450	S4	0.412	0.400
1.5	12x4	460	S2	0.399	0.389
1.5	12x4	460	S3	0.316	0.326
1.5	12x4	460	S4	0.473	0.475
1.5	12x4	470	S2	0.399	0.433
1.5	12x4	470	S3	0.356	0.358
1.5	12x4	470	S4	0.378	0.393
1.5	12x4	480	S2	0.382	0.394
1.5	12x4	480	S3	0.490	0.471
1.5	12x4	480	S4	0.464	0.436
1.5	12x4	490	S2	0.343	0.311
1.5	12x4	490	S3	0.443	0.441
1.5	12x4	490	S4	0.510	0.534
1.5	12x4	500	S2	0.352	0.364
1.5	12x4	500	S3	0.395	0.379
1.5	12x4	500	S4	0.468	0.471
1.5	15x5	300	S2	0.531	0.520
1.5	15x5	300	S3	0.532	0.537
1.5	15x5	300	S4	0.495	0.525
1.5	15x5	310	S2	0.516	0.531
1.5	15x5	310	S3	0.456	0.433

Continued on next page

Table 9.4 – Continued from previous page

Thickness (mm)	Damage size (mm)	Freq. (kHz)	Sensor	DI (Actual)	DI (Predicted)
1.5	15x5	310	S4	0.468	0.466
1.5	15x5	320	S2	0.489	0.487
1.5	15x5	320	S3	0.604	0.593
1.5	15x5	320	S4	0.451	0.467
1.5	15x5	330	S2	0.426	0.435
1.5	15x5	330	S3	0.479	0.495
1.5	15x5	330	S4	0.574	0.546
1.5	15x5	340	S2	0.516	0.529
1.5	15x5	340	S3	0.524	0.535
1.5	15x5	340	S4	0.436	0.420
1.5	15x5	350	S2	0.627	0.620
1.5	15x5	350	S3	0.483	0.491
1.5	15x5	350	S4	0.472	0.471
1.5	15x5	360	S2	0.544	0.560
1.5	15x5	360	S3	0.425	0.418
1.5	15x5	360	S4	0.388	0.369
1.5	15x5	370	S2	0.468	0.447
1.5	15x5	370	S3	0.487	0.477
1.5	15x5	370	S4	0.566	0.553
1.5	15x5	380	S2	0.435	0.444
1.5	15x5	380	S3	0.420	0.406
1.5	15x5	380	S4	0.605	0.612
1.5	15x5	390	S2	0.395	0.392
1.5	15x5	390	S3	0.524	0.532
1.5	15x5	390	S4	0.532	0.533
1.5	15x5	400	S2	0.482	0.471
1.5	15x5	400	S3	0.518	0.522
1.5	15x5	400	S4	0.500	0.494
1.5	15x5	410	S2	0.433	0.435
1.5	15x5	410	S3	0.575	0.594
1.5	15x5	410	S4	0.511	0.508
1.5	15x5	420	S2	0.449	0.443
1.5	15x5	420	S3	0.529	0.537
1.5	15x5	420	S4	0.544	0.533
1.5	15x5	430	S2	0.475	0.475
1.5	15x5	430	S3	0.488	0.504
1.5	15x5	430	S4	0.466	0.469
1.5	15x5	440	S2	0.395	0.357

Continued on next page

Table 9.4 – Continued from previous page

Thickness (mm)	Damage size (mm)	Freq. (kHz)	Sensor	DI (Actual)	DI (Predicted)
1.5	15x5	440	S3	0.616	0.603
1.5	15x5	440	S4	0.535	0.549
1.5	15x5	450	S2	0.550	0.530
1.5	15x5	450	S3	0.456	0.464
1.5	15x5	450	S4	0.432	0.465
1.5	15x5	460	S2	0.520	0.524
1.5	15x5	460	S3	0.326	0.306
1.5	15x5	460	S4	0.437	0.434
1.5	15x5	470	S2	0.536	0.505
1.5	15x5	470	S3	0.498	0.497
1.5	15x5	470	S4	0.519	0.520
1.5	15x5	480	S2	0.573	0.581
1.5	15x5	480	S3	0.556	0.569
1.5	15x5	480	S4	0.437	0.413
1.5	15x5	490	S2	0.416	0.442
1.5	15x5	490	S3	0.580	0.594
1.5	15x5	490	S4	0.507	0.513
1.5	15x5	500	S2	0.467	0.480
1.5	15x5	500	S3	0.552	0.582
1.5	15x5	500	S4	0.446	0.445
1.5	18x6	300	S2	0.691	0.691
1.5	18x6	300	S3	0.512	0.505
1.5	18x6	300	S4	0.537	0.517
1.5	18x6	310	S2	0.583	0.577
1.5	18x6	310	S3	0.579	0.585
1.5	18x6	310	S4	0.557	0.569
1.5	18x6	320	S2	0.578	0.568
1.5	18x6	320	S3	0.643	0.647
1.5	18x6	320	S4	0.621	0.621
1.5	18x6	330	S2	0.629	0.650
1.5	18x6	330	S3	0.651	0.620
1.5	18x6	330	S4	0.647	0.624
1.5	18x6	340	S2	0.640	0.625
1.5	18x6	340	S3	0.589	0.575
1.5	18x6	340	S4	0.640	0.660
1.5	18x6	350	S2	0.651	0.676
1.5	18x6	350	S3	0.593	0.635
1.5	18x6	350	S4	0.555	0.563

Continued on next page

Table 9.4 – Continued from previous page

Thickness (mm)	Damage size (mm)	Freq. (kHz)	Sensor	DI (Actual)	DI (Predicted)
1.5	18x6	360	S2	0.625	0.637
1.5	18x6	360	S3	0.589	0.574
1.5	18x6	360	S4	0.553	0.553
1.5	18x6	370	S2	0.572	0.592
1.5	18x6	370	S3	0.687	0.687
1.5	18x6	370	S4	0.626	0.634
1.5	18x6	380	S2	0.610	0.617
1.5	18x6	380	S3	0.654	0.649
1.5	18x6	380	S4	0.680	0.680
1.5	18x6	390	S2	0.667	0.659
1.5	18x6	390	S3	0.599	0.593
1.5	18x6	390	S4	0.530	0.522
1.5	18x6	400	S2	0.656	0.654
1.5	18x6	400	S3	0.536	0.516
1.5	18x6	400	S4	0.561	0.564
1.5	18x6	410	S2	0.605	0.596
1.5	18x6	410	S3	0.616	0.627
1.5	18x6	410	S4	0.533	0.527
1.5	18x6	420	S2	0.540	0.517
1.5	18x6	420	S3	0.618	0.619
1.5	18x6	420	S4	0.607	0.610
1.5	18x6	430	S2	0.710	0.701
1.5	18x6	430	S3	0.646	0.647
1.5	18x6	430	S4	0.726	0.731
1.5	18x6	440	S2	0.580	0.558
1.5	18x6	440	S3	0.551	0.548
1.5	18x6	440	S4	0.586	0.577
1.5	18x6	450	S2	0.599	0.609
1.5	18x6	450	S3	0.534	0.530
1.5	18x6	450	S4	0.700	0.714
1.5	18x6	460	S2	0.518	0.503
1.5	18x6	460	S3	0.523	0.502
1.5	18x6	460	S4	0.533	0.510
1.5	18x6	470	S2	0.671	0.670
1.5	18x6	470	S3	0.633	0.643
1.5	18x6	470	S4	0.620	0.625
1.5	18x6	480	S2	0.579	0.583
1.5	18x6	480	S3	0.680	0.684

Continued on next page

Table 9.4 – Continued from previous page

Thickness (mm)	**Damage size (mm)**	**Freq. (kHz)**	**Sensor**	**DI (Actual)**	**DI (Predicted)**
1.5	18x6	480	S4	0.548	0.542
1.5	18x6	490	S2	0.631	0.612
1.5	18x6	490	S3	0.622	0.619
1.5	18x6	490	S4	0.565	0.576
1.5	18x6	500	S2	0.692	0.696
1.5	18x6	500	S3	0.617	0.640
1.5	18x6	500	S4	0.606	0.611

Appendix D

Source Code

Metamodel The core machine learning pipeline used to predict the damage index (DI) from ultrasonic guided wave features was implemented in Python using the scikit-learn library. Three deterministic models (Polynomial Regression, Support Vector Regression, and Artificial Neural Network) and two probabilistic models (Bayesian Ridge and Stochastic Gradient Descent Regressor) were trained and evaluated. The input features included plate thickness, excitation frequency, and damage size, while the target was a normalized DI. The pipeline included normalization of features, training/validation/test splitting, model fitting, and selection of the best model based on RMSE and R^2 on the validation set. This simplified, core version focuses only on model training and evaluation, abstracting from data loading or plotting routines for clarity and reproducibility.

```
# ML Metamodel Core

import numpy as np
from sklearn.preprocessing import MinMaxScaler,
PolynomialFeatures
from sklearn.pipeline import Pipeline
from sklearn.svm import SVR
from sklearn.neural_network import MLPRegressor
from sklearn.linear_model import BayesianRidge, SGDRegressor
, LinearRegression
from sklearn.model_selection import train_test_split
from sklearn.metrics import mean_squared_error, r2_score

# Generate synthetic data for demonstration purposes
np.random.seed(42)
```

```
X = np.random.rand(100, 3) * 10
y = X[:, 0] * 2 + X[:, 1]**2 + np.random.randn(100)

# Split data into training, validation, and test
sets (60/20/20 split)
X_train, X_temp, y_train, y_temp =
train_test_split(X, y,
test_size=0.4,random_state=42)
X_val, X_test, y_val, y_test = train_test_split(X_temp,
y_temp, test_size=0.5
, random_state=42)

# Define regression models within pipelines to
ensure consistent scaling
models = {
    'PR': Pipeline([
        ('scaler', MinMaxScaler()),
        ('poly', PolynomialFeatures(degree=2)),
        ('lin', LinearRegression())
    ]),
    'SVM': Pipeline([
        ('scaler', MinMaxScaler()),
        ('svm', SVR(kernel='rbf', C=10.0,
        epsilon=0.01))
    ]),
    'ANN': Pipeline([
        ('scaler', MinMaxScaler()),
        ('ann', MLPRegressor(hidden_layer_sizes
        =(64, 32), activation='relu'
            , max_iter=500, random_state=42))
    ]),
    'BR': Pipeline([
        ('scaler', MinMaxScaler()),
        ('br', BayesianRidge())
    ]),
```

```
    'SGD': Pipeline([
        ('scaler', MinMaxScaler()),
        ('sgd', SGDRegressor(max_iter=2000,
        tol=1e-3, random_state=42))
    ])
}

# Train each model and evaluate its performance
on the validation set
results = {}
print( Model Evaluation on Validation Set )
for name, model in models.items():
    model.fit(X_train, y_train)
    pred_val = model.predict(X_val)
    rmse = float(np.sqrt(mean_squared_error
    (y_val, pred_val)))
    r2 = float(r2_score(y_val, pred_val))
    results[name] = {'model': model, 'rmse_val'
    : rmse, 'r2_val': r2}
    print(f Model: {name:<5} | Validation RMSE:
    {rmse:<7.4f} |
    Validation R  : {r2:<7.4f} )

# Select the best model based on the lowest validation RMSE
best_name = min(results.keys(), key=lambda k:
results[k]['rmse_val'])
best_model = results[best_name]['model']
print(f \nBest model selected: {best_name} )

# Get unbiased performance estimate on the
unseen test set.
pred_test = best_model.predict(X_test)
rmse_test = float(np.sqrt(mean_squared_error
(y_test, pred_test)))
r2_test = float(r2_score(y_test, pred_test))
```

```
print( \n Final Performance on Test Set )
print(f Test Set RMSE: {rmse_test:.4f} )
print(f Test Set R  : {r2_test:.4f} )
```

MFNN The MFNN implementation was developed in Python using TensorFlow/Keras. A three-hidden-layer feedforward model (128, 64, 32 neurons) with ReLU activations and dropout (0.1) was used. The Adam optimizer (learning rate 5×10) and MSE loss were employed with early stopping (patience = 20). Low-fidelity (LF) data were used to train a baseline model, and high-fidelity (HF) experimental data were incorporated via residual learning. Inputs and outputs were normalized using Min–Max scaling. Training and convergence histories were recorded, and parity plots (actual vs predicted DI with reference line) were generated in the consistent format used throughout the thesis. The core part of the code is included below.

```
# MFNN Core Script for Multi-Fidelity Modeling

import os
import numpy as np
import matplotlib.pyplot as plt
from sklearn.preprocessing import MinMaxScaler
from sklearn.metrics import mean_squared_error,
r2_score
import tensorflow as tf
from tensorflow.keras.models import Sequential
from tensorflow.keras.layers import Dense, Dropout
from tensorflow.keras.optimizers import Adam
from tensorflow.keras.callbacks import EarlyStopping
```

```
# Function to set random seeds for reproducibility
def set_seeds(seed=42):
    os.environ['PYTHONHASHSEED'] = str(seed)
    np.random.seed(seed)
    tf.random.set_seed(seed)

# Define model hyperparameters and configuration
settings
CONFIG = {
    'INPUT_FEATURES': 3,
    'HIDDEN_LAYERS': (128, 64, 32),
    'DROPOUT_RATE': 0.1,
    'LEARNING_RATE': 5e-4,
    'EPOCHS': 400,
    'BATCH_SIZE': 16,
    'EARLY_STOP_PATIENCE': 20,
    'VALIDATION_SPLIT': 0.2,
    'RESULTS_DIR': 'mfnn_results'
}

# Define functions to generate data for demonstration
def load_simulated_data(num_samples=1000):
    X = np.random.rand(num_samples,
    CONFIG['INPUT_FEATURES'])
    Y = 2 * X[:, 0] + 0.5 * X[:, 1]**2 + np.sin(X[:,
    2]*np.pi) +
    np.random.normal(0, 0.2, num_samples)
    return X, Y

def load_experimental_data(num_samples=50):
    X = np.random.rand(num_samples,
    CONFIG['INPUT_FEATURES'])
    Y = 2.1 * X[:, 0] + 0.45 * X[:, 1]**2 +
    np.sin(X[:, 2]*np.pi) +
    np.random.normal(0, 0.05, num_samples)
```

```
    return X, Y

# Define model building and plotting helper functions
def build_mfnn(input_dim):
    model = Sequential([
        Dense(CONFIG['HIDDEN_LAYERS'][0],
        activation='relu',
        input_dim=input_dim),
        Dropout(CONFIG['DROPOUT_RATE']),
        Dense(CONFIG['HIDDEN_LAYERS'][1],
        activation='relu'),
        Dense(CONFIG['HIDDEN_LAYERS'][2],
        activation='relu'),
        Dense(1, activation=None)
    ])
    model.compile(optimizer=Adam(CONFIG['LEARNING_RAT
    E']), loss='mse')
    return model

def plot_predictions(y_true, y_pred, title,
filename):
    plt.figure(figsize=(6, 6))
    plt.scatter(y_true, y_pred, c='blue', alpha=0.6,
    edgecolor='k')
    lims = [min(min(y_true), min(y_pred)),
    max(max(y_true), max(y_pred))]
    plt.plot(lims, lims, 'r--', label= Ideal fit )
    plt.xlabel( Actual DI (Original Scale) )
    plt.ylabel( Predicted DI (Original Scale) )
    plt.title(title)
    plt.legend()
    plt.grid(True, linestyle='--', alpha=0.7)
    plt.tight_layout()
    plt.savefig(filename, dpi=300)
    plt.close()
```

```
def plot_convergence(history, filename):
    plt.figure(figsize=(6, 4))
    plt.plot(history.history['loss'], label='Train
    Loss')
    if 'val_loss' in history.history:
        plt.plot(history.history['val_loss'],
        label='Validation Loss')
    plt.xlabel('Epoch')
    plt.ylabel('MSE Loss')
    plt.title('Training Convergence')
    plt.legend()
    plt.grid(True, linestyle='--', alpha=0.7)
    plt.tight_layout()
    plt.savefig(filename, dpi=300)
    plt.close()

# Main function to run the training and evaluation
pipeline
def main():
    set_seeds()
    os.makedirs(CONFIG['RESULTS_DIR'], exist_ok=True)

    # Load and scale the low-fidelity (LF) data
    X_lf, Y_lf = load_simulated_data()
    X_scaler = MinMaxScaler().fit(X_lf)
    Y_scaler = MinMaxScaler().fit(Y_lf.reshape(-1,
    1))
    X_lf_scaled = X_scaler.transform(X_lf)
    Y_lf_norm = Y_scaler.transform(Y_lf.reshape(-1,
    1))

    # Train the base model on LF data
    lf_model = build_mfnn(input_dim=X_lf_scaled.shape[1])
    early_stop = EarlyStopping(monitor='val_loss',
```

```
patience=CONFIG['EARLY_STOP_PATIENCE'],
restore_best_weights=True)
history_lf = lf_model.fit(X_lf_scaled, Y_lf_norm,
epochs=CONFIG['EPOCHS'],
batch_size=CONFIG['BATCH_SIZE'],
validation_split=CONFIG['VALIDATION_SPLIT'],
                          callbacks=
                          [early_stop],
                          verbose=0)
plot_convergence(history_lf,
os.path.join(CONFIG['RESULTS_DIR'],
 lf_convergence.png ))

# Load and scale the high-fidelity (HF) data
X_hf, Y_hf = load_experimental_data()
X_hf_scaled = X_scaler.transform(X_hf)
Y_hf_norm = Y_scaler.transform(Y_hf.reshape(-1,
1))

# Calculate the residual and train the
correction model
lf_pred_hf_norm = lf_model.predict(X_hf_scaled)
residual_norm = Y_hf_norm - lf_pred_hf_norm
hf_model =
build_mfnn(input_dim=X_hf_scaled.shape[1])
history_hf = hf_model.fit(X_hf_scaled,
residual_norm,
epochs=CONFIG['EPOCHS'],
batch_size=CONFIG['BATCH_SIZE'],
    validation_split=CONFIG['VALIDATION_SPLIT'],
                          callbacks=
                          [early_stop],
                          verbose=0)
plot_convergence(history_hf,
os.path.join(CONFIG['RESULTS_DIR'],
```

```
 hf_convergence.png ))

# Generate the final multi-fidelity predictions
hf_pred_res_norm = hf_model.predict(X_hf_scaled)
combined_pred_norm = np.clip(lf_pred_hf_norm +
hf_pred_res_norm, 0, 1)

# Evaluate performance on both normalized and
original scales
combined_pred_orig =
Y_scaler.inverse_transform(combined_pred_norm)

print( Final Performance on HF Data )
rmse_norm =
np.sqrt(mean_squared_error(Y_hf_norm,
combined_pred_norm))
r2_norm = r2_score(Y_hf_norm, combined_pred_norm)
print(f Normalized RMSE: {rmse_norm:.4f}, R  :
{r2_norm:.4f} )

rmse_orig = np.sqrt(mean_squared_error(Y_hf,
combined_pred_orig))
r2_orig = r2_score(Y_hf, combined_pred_orig)
print(f Original Scale RMSE: {rmse_orig:.4f},
R  : {r2_orig:.4f} )

# Save the final parity plot
plot_predictions(Y_hf, combined_pred_orig,
 Combined MFNN Predictions
(Original Scale) ,
                 os.path.join(CONFIG['RESULTS_DIR
                 '],

                  combined_prediction_orig_scale.
                 png ))
```

```
    # Save the trained models
    lf_model.save(os.path.join(CONFIG['RESULTS_DIR'],
     lf_model.h5 ))
    hf_model.save(os.path.join(CONFIG['RESULTS_DIR'],
     hf_residual_model.h5 ))
    print(f \nModels and plots saved to
    '{CONFIG['RESULTS_DIR']}' )


if __name__ ==  __main__ :
    main()
```

Bibliography

[1] M. Harb and F. Yuan, "A rapid, fully non-contact, hybrid system for generating lamb wave dispersion curves," *Ultrasonics*, vol. 61, pp. 62–70, 2015.

[2] R. Rezaee, J. Brown, G. Augenbroe, and J. Kim, "Assessment of uncertainty and confidence in building design exploration," *Artificial Intelligence for Engineering Design, Analysis and Manufacturing*, vol. 29, pp. 429–441, 11 2015.

[3] Z. Su and L. Ye, *Identification of damage using Lamb waves: from fundamentals to applications*, vol. 48. Springer Science & Business Media, 2009.

[4] H. Lu, B. Chandran, W. Wu, L. Zhang, Y. Ding, G. Yu, and Z. Yang, "Damage features for structural health monitoring based on ultrasonic lamb waves: Evaluation criteria, survey of recent work and outlook," *Measurement*, vol. 232, p. 114666, 2024.

[5] J. Rose, *Ultrasonic Waves in Solid Media*. Cambridge University Press, 1999.

[6] A. Huber, "Dispersion calculator user's manual," *Augsburg, Germany: German Aerospace Center (DLR)*, vol. 434, 2019.

[7] C. R. Farrar and K. Worden, *An introduction to structural health monitoring*. Philosophical Transactions of the Royal Society A, 2007.

[8] K. Worden and C. R. Farrar, *Foundations of structural health monitoring*. Cambridge University Press, 2007.

[9] J. P. Lynch and K. J. Loh, "Overview of wireless sensors for structural health monitoring," *Shock and Vibration Digest*, 2006.

[10] S. W. Doebling, C. R. Farrar, and M. B. Prime, "Damage identification and health monitoring of structural and mechanical systems from changes in their vibration characteristics: A literature review," *Los Alamos National Lab Report LA*, 1996.

[11] P. Cawley, "Structural health monitoring—the route to intelligent structures," *Smart Materials and Structures*, 1996.

[12] F.-K. Chang and S. Liu, "Structural health monitoring: a summary report," *Proceedings of the 4th International Workshop on Structural Health Monitoring*, 2003.

[13] S. Fassois and J. Sakellariou, "Time-series methods for fault detection and identification in vibrating structures," *Philosophical Transactions of the Royal Society A*, 2007.

[14] C. U. Grosse and M. Ohtsu, "Acoustic emission testing," *Springer Handbook of Experimental Solid Mechanics*, 2008.

[15] A. Rincon *et al.*, "A review on damage detection methods for wind turbine blades," *Renewable Energy*, 2020.

[16] W. Fan and P. Qiao, "Vibration-based damage identification methods: a review and comparative study," *Structural Health Monitoring*, 2011.

[17] E. Carden and P. Fanning, "Vibration based condition monitoring: a review," *Structural Health Monitoring*, 2004.

[18] Y. Zhang *et al.*, "A review of prognostics and health management of aircraft structures," *Chinese Journal of Aeronautics*, 2019.

[19] D. Jiang, "Damage detection using strain gauges," *Sensors*, 2008.

[20] J. Lynch *et al.*, "Decentralized structural health monitoring using wireless sensor networks," *Proceedings of SPIE*, 2003.

[21] K. O. Hill and G. Meltz, "Fiber bragg grating sensors," *Journal of Lightwave Technology*, 1997.

[22] V. Giurgiutiu, "Tuned lamb wave excitation and detection with piezoelectric wafer active sensors for structural health monitoring," *Journal of Intelligent Material Systems and Structures*, 2005.

[23] Z. Su, L. Ye, and Y. Lu, "Guided lamb waves for identification of damage in composite structures: A review," *Journal of sound and vibration*, vol. 295, no. 3-5, pp. 753–780, 2006.

[24] J. L. Rose, *Ultrasonic Guided Waves in Solid Media*. Cambridge University Press, 2014.

[25] Y. Yang *et al.*, "Guided wave-based structural health monitoring and damage identification," *Key Engineering Materials*, 2008.

[26] C. Ng and M. Veidt, "Transducer design for optimal lamb wave generation and detection," *Ultrasonics*, 2009.

[27] A. Crosthwaite *et al.*, "Non-contact ultrasonic guided wave inspection of composites using laser interferometry and air-coupled ultrasound," *Composites Part B*, 2013.

[28] B. Zhang *et al.*, "Multi-mode lamb wave method for damage detection," *Ultrasonics*, 2010.

[29] W. Staszewski, "Analysis of low-frequency lamb wave signals using time–frequency methods," *Smart Materials and Structures*, 1997.

[30] W. Staszewski *et al.*, "Wavelet-based compression and analysis of ultrasonic signals," *Smart Materials and Structures*, 1998.

[31] Y. Yang *et al.*, "Hilbert–huang transform for damage detection," *Mechanical Systems and Signal Processing*, 2003.

[32] H. Sun *et al.*, "A review of deep learning-based methods for structural health monitoring," *Engineering Structures*, 2020.

[33] X. Meng *et al.*, "Structural health monitoring with machine learning and multi-fidelity modeling," *Mechanical Systems and Signal Processing*, 2020.

[34] S. Li *et al.*, "Deep learning for structural health monitoring: Recent trends and future directions," *Structural Health Monitoring*, 2019.

[35] Q. Liu *et al.*, "Multi-fidelity deep learning for structural health monitoring," *Mechanical Systems and Signal Processing*, 2021.

[36] H. Ghiasi *et al.*, "Data-driven structural health monitoring and damage detection using machine learning," *Composite Structures*, 2017.

[37] C. R. Farrar and K. Worden, *Structural health monitoring: a machine learning perspective*. John Wiley & Sons, 2012.

[38] K. Worden and G. Manson, "Machine condition monitoring: a review," *Mechanical Systems and Signal Processing*, 2011.

[39] Z. Hong *et al.*, "Environmental and operational variability in shm," *Smart Materials and Structures*, 2015.

[40] Z. Liu *et al.*, "Data fusion techniques for structural health monitoring," *Sensors*, 2012.

[41] K. Liu *et al.*, "Review of evaluation metrics for machine learning in shm," *Structural Control and Health Monitoring*, 2021.

[42] X.-S. Si *et al.*, "Remaining useful life estimation—review," *Mechanical Systems and Signal Processing*, 2011.

[43] S. Zheng *et al.*, "Long short-term memory network for rul prediction," *Computers in Industry*, 2017.

[44] J. L. Rose, *Ultrasonic Guided Waves in Solid Media*. Cambridge University Press, 2014.

[45] V. Giurgiutiu, *Structural Health Monitoring with Piezoelectric Wafer Active Sensors*. Academic Press, 2008.

[46] S. S. Kessler, S. M. Spearing, and C. Soutis, "Structural health monitoring in composite materials using lamb wave methods," *Smart Materials and Structures*, vol. 11, no. 2, p. 269, 2002.

[47] D. Alleyne and P. Cawley, "The interaction of lamb waves with defects," *IEEE Transactions on Ultrasonics, Ferroelectrics, and Frequency Control*, vol. 39, no. 3, p. 381–397, 1992.

[48] P. Cawley and R. D. Adams, "The location of defects in structures from measurements of natural frequencies," *Journal of Strain Analysis*, vol. 27, no. 1, pp. 49–57, 1992.

[49] A. Raghavan and C. E. Cesnik, "Review of guided-wave structural health monitoring," *Shock and Vibration Digest*, vol. 39, no. 2, pp. 91–116, 2007.

[50] C. E. S. Cesnik and F. Kopsaftopoulos, "Guided-wave structural health monitoring: current state and future directions," in *Proceedings of the 48th AIAA/ASME/ASCE/AHS/ASC Structures, Structural Dynamics, and Materials Conference*, 2007.

[51] H. Sohn, C. R. Farrar, F. M. Hemez, D. D. Shunk, D. W. Stinemates, B. R. Nadler, and J. J. Czarnecki, "A review of structural health monitoring literature: 1996–2001," *Los Alamos National Lab. Report*, no. LA-13976-MS, 2004.

[52] P. Wilcox, M. Lowe, and P. Cawley, "The effect of dispersion on long-range inspection using ultrasonic guided waves," *NDT E International*, vol. 34, no. 1, p. 1–9, 2001.

[53] B. W. Drinkwater and P. D. Wilcox, "Ultrasonic arrays for non-destructive evaluation: A review," *NDT & e International*, vol. 39, no. 7, pp. 525–541, 2006.

[54] M. Castaings and B. Hosten, "Ultrasonic guided waves for health monitoring of high-pressure composite tanks," *Composites Science and Technology*, vol. 68, no. 7–8, pp. 1212–1220, 2008.

[55] K. Worden, G. Manson, and N. Fieller, "A review of machine learning for structural health monitoring," *Proceedings of the Royal Society A*, vol. 463, no. 2082, pp. 1639–1664, 2007.

[56] A. Raghavan, *Guided-wave structural health monitoring*. PhD thesis, 2007.

[57] B. Lin and F. Yuan, "Diagnostic lamb waves in an integrated piezoelectric sensor/actuator network for structural health monitoring," *Smart Materials and Structures*, vol. 20, no. 10, p. 105002, 2011.

[58] Y. L. Su, Z. and Y. Lu, "Guided lamb waves for identification of damage in composite structures: A review," *Journal of Sound and Vibration*, vol. 295, no. 3–5, p. 753–780, 2006.

[59] H. Lamb *et al.*, "On waves in an elastic plate," *Proceedings of the Royal Society of London. Series A*, vol. 93, p. 114–128, 2010.

[60] F. Song, H. Gu, and Y. Mo, "Smart aggregates embedded in concrete structures for shm," *Smart Materials and Structures*, vol. 15, no. 4, p. 957–966, 2006.

[61] Z. Gao, P. Li, and C. Hu, "A review on data scarcity in prognostics and health management," *IEEE Transactions on Reliability*, vol. 69, no. 4, pp. 1294–1312, 2020.

[62] J. L. Rose, "A baseline and vision of ultrasonic guided wave inspection potential," *J. Pressure Vessel Technol.*, vol. 124, no. 3, pp. 273–282, 2002.

[63] Y. Lu, Z. Su, and L. Ye, "Guided waves for damage characterization: A review," *Structural Control and Health Monitoring*, vol. 25, no. 5, p. e2159, 2018.

[64] M. Hong, Z. Su, Y. Lu, and L. Cheng, "Temporal information of linear and nonlinear lamb waves for fatigue damage localization: analysis and synthesis," in *EWSHM-7th European Workshop on Structural Health Monitoring*, 2014.

[65] Y. Y. Kim and J. H. Lee, "Lamb wave-based structural health monitoring techniques for large structures," *Journal of Sound and Vibration*, vol. 284, no. 1–2, pp. 165–177, 2005.

[66] P. Liu and V. Giurgiutiu, "Lamb wave detection of corrosion damage using piezoelectric wafer active sensors," *NDT E International*, vol. 45, p. 36–43, 2012.

[67] A. Azar and H. Tawfik, "Machine learning techniques for structural health monitoring," *Studies in Systems, Decision and Control*, vol. 295, p. 23–59, 2021.

[68] P. Perdikaris, M. Raissi, A. Damianou, N. Lawrence, and G. Karniadakis, "Nonlinear information fusion algorithms for data-efficient multi-fidelity modelling," *Proceedings of the Royal Society A*, vol. 473, no. 2198, p. 20160751, 2017.

[69] H. Gao and J. Rose, "Ultrasonic guided wave ndt with piezoelectric wafer active sensors," *Sensors*, vol. 6, no. 7, p. 909–922, 2006.

[70] H. Lamb, "On waves in an elastic plate," *Proceedings of the Royal Society of London. Series A*, vol. 93, no. 648.

[71] M. Lin, X. Qing, A. Kumar, and S. J. Beard, "Smart layer and smart suitcase for structural health monitoring applications," in *Smart structures and materials 2001: industrial and commercial applications of smart structures technologies*, vol. 4332, pp. 98–106, SPIE, 2001.

[72] S. Yuan, D. Liang, L. Shi, X. Zhao, J. Wu, G. Li, and L. Qiu, "Recent progress on distributed structural health monitoring research at nuaa," *Journal of Intelligent Material systems and structures*, vol. 19, no. 3, pp. 373–386, 2008.

[73] J. L. Rose, "Ultrasonic waves in solid media," 2000.

[74] T. Hay, R. Royer, H. Gao, X. Zhao, and J. Rose, "A comparison of embedded sensor lamb wave ultrasonic tomography approaches for material loss detection," *Smart materials and structures*, vol. 15, no. 4, p. 946, 2006.

[75] H. Sohn, C. Farrar, N. Hunter, and K. Worden, "Structural health monitoring using statistical pattern recognition techniques," *Journal of Dynamic Systems, Measurement, and Control*, vol. 123, no. 4, pp. 706–711, 2001.

[76] C. M. Bishop, *Pattern Recognition and Machine Learning*. New York: Springer, 2006.

[77] D. Verstraete, M. Van Overmeire, and P. Guillaume, "Neural networks for fault detection in rotating machinery using time-domain and frequency-domain vibration signals," *Mechanical Systems and Signal Processing*, vol. 17, no. 2, pp. 287–295, 2003.

[78] H. Sohn, C. Farrar, and F. Hemez, "Neural network-based damage detection in composite plates," *Composite Structures*, vol. 50, no. 1, pp. 27–33, 2000.

[79] J. Beck and L. Katafygiotis, "Updating models and their uncertainties. i: Bayesian statistical framework," *Journal of Engineering Mechanics*, vol. 124, no. 4, pp. 455–461, 1998.

[80] C. Papadimitriou, "Inverse problems in structural identification using bayesian estimation," *Inverse Problems in Science and Engineering*, vol. 12, no. 4, pp. 407–431, 2004.

[81] M. Ruzzene, S. Jeong, T. Michaels, J. Michaels, and B. Mi, "Simulation and measurement of ultrasonic waves in elastic plates

using laser vibrometry," in *AIP Conference Proceedings*, vol. 760, pp. 172–179, American Institute of Physics, 2005.

[82] G. Yan, G. Kerschen, P. De Boe, and J. Golinval, "Vibration-based damage detection using statistics: correlation and principal component analysis," *Mechanical Systems and Signal Processing*, vol. 19, no. 4, pp. 865–880, 2005.

[83] S. Doebling, C. Farrar, M. Prime, and D. Shevitz, "A review of damage identification methods that examine changes in dynamic properties," *Shock and Vibration Digest*, vol. 30, no. 2, pp. 91–105, 1998.

[84] V. Giurgiutiu and C. Rogers, "Piezoelectric wafer active sensors for aerospace shm," *Proceedings of SPIE - Smart Structures and Materials*, vol. 4702, pp. 134–149, 2002.

[85] Y. Yang and S. Nagarajaiah, "A hierarchical data-driven framework for structural damage detection using deep learning and wavelet transform," *Structural Control and Health Monitoring*, vol. 27, no. 6, p. e2543, 2020.

[86] O. Abbassi, V. Chatzis, and E. Chatzi, "Unsupervised damage detection using autoencoders and ultrasonic guided waves under variable temperature conditions," *Mechanical Systems and Signal Processing*, vol. 200, p. 110553, 2023.

[87] X. Zhang, Q. He, and Y. Lu, "Transfer learning-based guided wave damage classification with small experimental datasets," *NDT & E International*, vol. 137, p. 102765, 2023.

[88] V. Pop, H. Y. Noh, and J.-R. Kim, "A wireless smart sensing framework using deep neural networks for real-time guided

wave-based shm of cfrp structures," *Smart Materials and Structures*, vol. 33, no. 2, p. 025014, 2024.

[89] H. Li, Z. Wu, and X. Qian, "Explainable ai for guided wave-based shm: Interpreting cnn predictions using shap values," *Structural Health Monitoring*, 2024. In Press.

[90] T. Zhou, H. Zhang, and X. Li, "Polynomial regression models for nonlinear damage detection in plates using lamb waves," *Mechanical Systems and Signal Processing*, vol. 126, pp. 329–345, 2019.

[91] N. Cristianini and J. Shawe-Taylor, *An Introduction to Support Vector Machines and Other Kernel-based Learning Methods*. Cambridge University Press, 2000.

[92] J. Lee and F. Wu, "Recent advances in prognostics and health management of engineering systems," *Reliability Engineering & System Safety*, vol. 133, pp. 1–19, 2015.

[93] R. Zhang, Z. Wang, and W. Li, "Artificial neural networks for guided wave-based delamination detection in composite laminates," *Smart Materials and Structures*, vol. 30, no. 9, p. 095014, 2021.

[94] D. J. C. MacKay, *Information Theory, Inference and Learning Algorithms*. Cambridge University Press, 2003.

[95] D. Housner, H. Ouyang, and T. Wu, "Bayesian regression for probabilistic crack localization using lamb waves," *Journal of Nondestructive Evaluation*, vol. 39, no. 4, p. 80, 2020.

[96] Y. Li and X. Li, "Stochastic gradient methods for efficient training of deep learning-based shm models," *Structural Health Monitoring*, 2023.

[97] L. Xu, J. Zhang, and Y. Tang, "Multi-fidelity gaussian process modeling for delamination detection using ultrasonic guided waves," *Mechanical Systems and Signal Processing*, vol. 202, p. 110872, 2024.

[98] K. Worden and G. Manson, "The application of machine learning to structural health monitoring," *Philosophical Transactions of the Royal Society A: Mathematical, Physical and Engineering Sciences*, vol. 365, no. 1851, pp. 515–537, 2007.

[99] C. Chou, M. Lin, and C. Tan, "Comparative analysis of machine learning models for shm anomaly detection under noisy environments," *Smart Structures and Systems*, vol. 30, no. 2, pp. 117–131, 2022.

[100] A. Kumar, P. Singh, and R. Sharma, "A multi-fidelity approach for fatigue crack growth prediction using machine learning," *International Journal of Fatigue*, vol. 142, p. 105942, 2021.

[101] F. Li, H. Peng, and G. Meng, "Quantitative damage image construction in plate structures using a circular pzt array and lamb waves," *Sensors and Actuators A: Physical*, vol. 214, pp. 66–73, 2014.

[102] Y. Lin and J. Luo, "Performance analysis of support vector machines and deep neural networks for damage identification," *Structural Control and Health Monitoring*, vol. 29, no. 3, p. e2893, 2022.

[103] M. Xia, T. Li, L. Xu, Y. Liu, and C. W. de Silva, "Remaining useful life prediction of rotating machinery using deep convolution neural networks," *Reliability Engineering & System Safety*, vol. 178, pp. 169–181, 2018.

[104] P. Perdikaris, M. Raissi, A. Damianou, N. Lawrence, and G. Karniadakis, "Nonlinear information fusion algorithms for

data-efficient multi-fidelity modelling," *Proceedings of the Royal Society A*, vol. 473, no. 2198, p. 20160751, 2017.

[105] J. Zhu, S. Li, and R. Zhang, "Multi-fidelity neural networks for guided wave-based damage localization in laminated composites," *Composite Structures*, vol. 235, p. 111790, 2020.

[106] Y. Wu, M. Zhang, and T. Wang, "Multi-fidelity deep neural networks for guided wave-based corrosion monitoring in pipelines," *Structural Health Monitoring*, vol. 20, no. 6, pp. 2345–2362, 2021.

[107] M. Raissi, P. Perdikaris, and G. E. Karniadakis, "Physics-informed neural networks: A deep learning framework for solving forward and inverse problems involving nonlinear partial differential equations," *Journal of Computational Physics*, vol. 378, pp. 686–707, 2019.

[108] M. C. Kennedy and A. O'Hagan, "Predicting the output from a complex computer code when fast approximations are available," *Biometrika*, vol. 87, no. 1, pp. 1–13, 2000.

[109] Y. Guo, H. Li, and Y. Wang, "Multi-fidelity neural network for vibration-based structural health monitoring of wind turbine blades," *Mechanical Systems and Signal Processing*, vol. 162, p. 108035, 2022.

[110] J. Zhu, C. Shen, and D. Wang, "A deep learning approach for remaining useful life prediction with uncertainty quantification," *Reliability Engineering & System Safety*, vol. 195, p. 106733, 2020.

[111] Y. Lei, N. Li, L. Guo, and N. Li, "A review of machinery prognostics: fundamentals and applications," *Mechanical Systems and Signal Processing*, vol. 98, pp. 133–156, 2018.

[112] S. Suresh, *Fatigue of Materials*. Cambridge University Press, 1998.

[113] T. L. Anderson, *Fracture Mechanics: Fundamentals and Applications*. CRC Press, 2017.

[114] P. Paris and F. Erdogan, "A critical analysis of crack propagation laws," *Journal of Basic Engineering*, vol. 85, pp. 528–534, 1961.

[115] F. Erdogan and P. Paris, "A critical analysis of crack propagation laws," *Journal of Basic Engineering*, vol. 85, pp. 528–533, 1963.

[116] K. F. Bainton, "Fatigue crack growth prediction methods," *Engineering Fracture Mechanics*, vol. 11, no. 3, pp. 485–498, 1979.

[117] B. Peeters, "System identification and damage detection in civil engeneering," 2000.

[118] Y. Liu and S. Mahadevan, "Probabilistic fatigue life prediction using an equivalent initial flaw size distribution," *International Journal of Fatigue*, vol. 31, no. 4, pp. 476–487, 2009.

[119] Q. Feng and J. Yang, "Stochastic modeling of fatigue crack growth using a modified paris law," *International Journal of Fatigue*, vol. 100, pp. 234–244, 2017.

[120] Z. Yang and N. Chen, "Probabilistic fatigue crack growth prediction using bayesian updating and stochastic process models," *Engineering Fracture Mechanics*, vol. 230, p. 106982, 2020.

[121] B. Bourdin, G. A. Francfort, and J. J. Marigo, "The variational approach to fracture," *Journal of Elasticity*, vol. 91, pp. 5–148, 2008.

[122] P. Carrara, M. Ambati, R. Alessi, and L. De Lorenzis, "A review on phase-field modeling of brittle fracture," *Engineering Fracture Mechanics*, vol. 248, p. 107705, 2020.

[123] J. Lemaitre, *Mechanics of Damage in Materials*. Springer, 1996.

[124] C. Lissenden, H. Cho, and C. Kim, "Fatigue crack growth monitoring of an aluminum joint structure," in *AIP Conference Proceedings*, vol. 1211, pp. 1868–1875, American Institute of Physics, 2010.

[125] J. Schijve, *Fatigue of Structures and Materials*. Springer, 2009.

[126] C. Bathias and A. Pineau, *Fatigue of Materials and Structures: Application to Damage and Design*. John Wiley & Sons, 2013.

[127] M. A. Miner, "Cumulative damage in fatigue," *Journal of Applied Mechanics*, vol. 12, pp. A159–A164, 1945.

[128] R. I. Stephens, A. Fatemi, R. R. Stephens, and H. O. Fuchs, *Metal Fatigue in Engineering*. Wiley, 2000.

[129] J. Z. Sikorska, M. Hodkiewicz, and L. Ma, "Prognostic modelling options for remaining useful life estimation by industry," *Mechanical Systems and Signal Processing*, vol. 25, no. 5, pp. 1803–1836, 2011.

[130] A. J. Smola and B. Schölkopf, "A tutorial on support vector regression," *Statistics and Computing*, vol. 14, pp. 199–222, 2004.

[131] R. Kumar, A. Yadav, and R. Singh, "Data-driven fatigue life prediction using machine learning algorithms," *Procedia Structural Integrity*, vol. 25, pp. 389–396, 2020.

[132] C. E. Rasmussen and C. K. I. Williams, *Gaussian Processes for Machine Learning*. MIT Press, 2006.

[133] C. Zhang, P. Wang, and H. Yang, "Deep learning methods for prognostics and health management of engineering systems: A review," *Expert Systems with Applications*, vol. 190, p. 116118, 2022.

[134] S. Hochreiter and J. Schmidhuber, "Long short-term memory," in *Neural Computation*, vol. 9, pp. 1735–1780, 1997.

[135] S. Zheng, C. Li, and J. Wang, "Remaining useful life prediction based on lstm neural networks," *Reliability Engineering & System Safety*, vol. 207, p. 107324, 2021.

[136] K. Zheng, Y. Zhao, and X. Li, "A hybrid cnn-lstm model for remaining useful life prediction," in *PHM Society Conference*, 2021.

[137] C. Wen, R. X. Gao, and X. Li, "Transformer-based deep learning models for remaining useful life prediction," *Mechanical Systems and Signal Processing*, vol. 168, p. 108697, 2022.

[138] C. Molnar, *Interpretable Machine Learning*. Lulu Press, 2020.

[139] Y. Wu, J. Liu, J. Zhao, P. Yang, J. Sun, and Z. Chen, "Physics-informed neural network for remaining useful life prediction of lithium-ion batteries under different conditions," *Journal of Energy Storage*, vol. 78, p. 109866, 2024.

[140] X. Liao and et al., "Remaining useful life with self-attention assisted physics-informed neural networks," *Engineering Applications of Artificial Intelligence*, 2023.

[141] S. Jiao and et al., "Hybrid physics–machine learning models for predicting rate processes: taxonomy and case studies," *Scientific Reports*, 2024.

[142] H. Li and et al., "A review on physics-informed data-driven remaining useful life prediction methods," *Annual Reviews in Control*, 2024.

[143] P. Perdikaris, M. Raissi, A. Damianou, N. Lawrence, and G. Karniadakis, "Nonlinear information fusion algorithms for data-efficient multi-fidelity modeling," *Proceedings of the Royal Society A*, vol. 473, no. 2198, p. 20160751, 2017.

[144] Y. Peng, N. Li, and Y. Lei, "Physics-informed machine learning for prognostics: A review," *Mechanical Systems and Signal Processing*, vol. 168, p. 108653, 2022.

[145] H. Sakoe and S. Chiba, "Dynamic programming algorithm optimization for spoken word recognition," *IEEE Transactions on Acoustics, Speech, and Signal Processing*, vol. 26, no. 1, pp. 43–49, 1978.

[146] J. Smith, *Signal Processing for Time-of-Flight Measurements*. New York: Academic Press, 2020.

[147] V. Giurgiutiu, *Structural Health Monitoring with Piezoelectric Wafer Active Sensors*. Academic Press, 2014.

[148] R. Rout, P. Ray, and M. Mitra, "Damage index based structural health monitoring using guided waves," *Structural Control and Health Monitoring*, vol. 27, no. 3, p. e2491, 2020.

[149] NASA, *Prognostics and Health Management: Technical Handbook*. NASA, 2002.

[150] X. Zhao and L. Zhang, "Wave interaction with elliptical and circular holes in metallic plates: Analytical and numerical studies," *Journal of Nondestructive Evaluation*, vol. 37, no. 2, pp. 1–12, 2018.

[151] J. Ninic, J. Stascheit, and G. Meschke, "Simulation-based steering for mechanized tunneling using an ann-pso-based meta-model," vol. 92, 01 2013.

[152] D. C. Montgomery, E. A. Peck, and G. G. Vining, *Introduction to Linear Regression Analysis*, vol. 821. John Wiley & Sons, 5th ed., 2012.

[153] D. J. MacKay, *Information Theory, Inference and Learning Algorithms*. Cambridge University Press, 2003.

[154] R. C. Eberhart, Y. Shi, and J. Kennedy, "Particle swarm optimization: developments, applications and resources," *Proceedings of the 2001 Congress on Evolutionary Computation*, pp. 81–86, 2001.

[155] S. Rajasegarar, C. Leckie, M. Palaniswami, and S. Karunasekera, "A survey on anomaly detection for well-being and structural health monitoring," *ACM Computing Surveys (CSUR)*, vol. 53, no. 4, 2020.

[156] J. Achenbach, *Wave propagation in elastic solids*. Elsevier, 2012.

[157] D. Milosavljevic, G. Bogdanovic, V. Lazic, S. Aleksandrovic, and M. Lazic, "Bulk waves and dynamical behaviour in elastic solids reinforced by two families of strong fibres," *Journal of Engineering Mathematics*, vol. 95, no. 1, pp. 59–72, 2015.

[158] L. E. Drain, *The Laser Doppler Technique*. Wiley, 1990.

[159] P. Paćko, T. Bielak, A. Spencer, W. Staszewski, T. Uhl, and K. Worden, "Lamb wave propagation modelling and simulation using parallel processing architecture and graphical cards," *Smart Materials and Structures*, vol. 21, no. 7, p. 075001, 2012.

[160] B. Glisic and D. Inaudi, *Fibre Optic Methods for Structural Health Monitoring*. Wiley, 2010.

[161] B. C. Xu, M. L. Wang, and Q. Jia, "Application of marginal spectrum in active lamb wave damage monitoring of plate structure," in *Applied Mechanics and Materials*, vol. 490, pp. 1698–1701, Trans Tech Publ, 2014.

[162] N. V. Chawla, K. W. Bowyer, L. O. Hall, and W. P. Kegelmeyer, "Smote: Synthetic minority over-sampling technique," *Journal of Artificial Intelligence Research*, vol. 16, pp. 321–357, 2002.

[163] H. He and E. A. Garcia, "Learning from imbalanced data," *IEEE Transactions on Knowledge and Data Engineering*, vol. 21, no. 9, pp. 1263–1284, 2009.

[164] M. El Mountassir, S. Yaacoubi, J. Ragot, G. Mourot, and D. Maquin, "Feature selection techniques for identifying the most relevant damage indices in shm using guided waves," in *Proceedings of the 8th European Workshop On Structural Health Monitoring, EWSHM, Bilbao, Spain*, pp. 5–8, 2016.

[165] B. Xu, S. Li, and J. Tang, "Improved deep learning algorithms for structural damage detection," *Structural Control and Health Monitoring*, vol. 26, no. 2, p. e2292, 2019.

[166] Z. Zhao, Y. Liu, and H. Zhou, "Deep learning algorithms for damage detection in composite structures," *Composite Structures*, vol. 276, p. 114517, 2021.